UNIVERSIDADE D
COIMBRA

Eduardo Luís Gonçalves Salgado

Properties of the Hadron-Quark Phase Diagram in Symmetric and Asymmetric Strongly Interacting Matter

Thesis submitted to the University of Coimbra in fulfilment of the requirements for the Master's Degree in Physics under the scientific supervision of Professor Pedro Fernando Simões Costa.

September of 2025

1 2  9 0

UNIVERSIDADE D
COIMBRA

Properties of the Hadron-Quark Phase Diagram in Symmetric and Asymmetric Strongly Interacting Matter

Author:
Eduardo Luís Gonçalves Salgado

Supervisor:
Prof. Pedro Fernando Simões Costa

Jury:
Prof. João Miguel Carvalho Alves Moreira
Prof. Pedro Fernando Simões Costa
Dr. Rainer Stiele

President of the Jury:
Prof. Paulo de Jesus Henriques da Silva

Dissertation submitted in partial fulfilment of the requirements for the Master's Degree in Physics.

Coimbra, September 2025

Acknowledgments

I am deeply grateful to my supervisor, Prof. Pedro Costa, for guiding me throughout the exciting and (very!) broad theme of phase diagrams of strongly interacting matter. I thank him for his valuable advice and discussions, the careful reading of this thesis and helpful suggestions, as well as his patience and support during tedious debugging sessions.

I also wish to thank Prof. Constança Providência for generously sharing all the codes related to the hadronic models, which were crucial for the development of this project. I am grateful for her careful reading and useful suggestions regarding Chapter 7, and I have greatly benefited from her expertise on nuclear matter and neutron stars.

My gratitude extends to the many professors who taught me during my bachelor's and master's studies. In particular, I thank Prof. Fernando Nogueira, Prof. João Rosa, and Prof. Brigitte Hiller for their excellent lectures and stimulating discussions. I am also grateful to Prof. Orlando Oliveira and Prof. Paulo Silva for welcoming me to the world of lattice QCD and for many valuable discussions, which significantly enriched sections of Chapter 3.

This thesis has also benefited from the friendly and ambitious environment of the Department of Physics. I thank my "older" friends, Simão Gonçalves, Thalis Silva, and João Cartaxo, with whom I have shared many jokes, challenges, and physics problems since my bachelor's. To my newer friends: Inês d'Oliveira and Pedro Carmo, who always welcomed me with great energy in the master's room; Inês Sequeira, with whom I shared countless conversations about cosmology, music, business ideas, and the frustrations of using Mathematica; to Hugo Fernandes, for his friendship and whom I proudly watched growing as a physicist every day; and Ana Bensabat, for her kindness, for sharing my passion for physics, and from whom I have learned so much about food, programming, people and the world.

Last but not least, I want to thanks my parents — specially my mother — and my sister, for all their love, unwavering support, and for making my life so much more colourful.

Resumo

Este trabalho visa estudar a transição de fase entre a matéria hadrónica e a matéria de quarks através da construção de uma fase mista em matéria com simetria de isospin e também em matéria com assimetria de isospin, sendo esta última, um cenário relevante para as colisões de iões pesados. Impomos a conservação do número bariónico e de isospin, bem como estranheza nula; o equilíbrio entre as duas fases é imposto pela condição de Gibbs.

No setor hadrónico, são utilizados modelos relativistas de campo médio, do tipo Walecka não-lineares, estendidos para incluir o octeto bariónico. Já a fase de quarks é descrita pelo modelo de Polyakov-Nambu-Jona-Lasinio (PNJL), em 2+1 sabores, com interações vetoriais. Estas interações vetoriais entre quarks são parametrizadas pela razão de acoplamentos G_V/G_S, que se variam para avaliar o seu impacto.

A partir desta abordagem, obtêm-se trajetórias isentrópicas, ao longo das quais se extraem quantidades físicas de grande interesse, como a velocidade do som e os cumulantes das flutuações do número bariónico.

Os resultados obtidos concordam qualitativamente com estudos anteriores, revelam também, uma diferença clara entre as trajetórias isentrópicas que passam relativamente perto do ponto crítico (CEP) e aquelas que estão mais afastadas do CEP. Em particular, as trajetórias próximas do CEP exibem um arrefecimento acentuado, enquanto as trajetórias com menor entropia por barião tendem a aumentar a sua temperatura.

Por sua vez, as interações vetoriais deslocam a transição de fase para densidades mais elevadas e afetam a magnitude da descontinuidade que ocorre na transição hadrão-quark. Mesmo para um acoplamento vetorial reduzido ($G_V/G_S = 0.1$), observa-se que o limite conforme é ultrapassado para densidades elevadas; é então proposto um procedimento adicional para restringir o valor de G_V/G_S.

A inclusão de hiperões faz deslocar a transição para densidades ainda maiores e reduz de forma significativa a temperatura de entrada na fase mista para as trajetórias com maior entropia por barião. Estas conclusões têm implicações diretas nos observáveis sensíveis à fase mista em colisões de iões pesados relativistas.

Abstract

We investigate the hadron-quark phase transition within a two-phase construction for both isospin-symmetric and isospin-asymmetric matter under conditions relevant to heavy-ion collisions. We impose conservation of baryon number and isospin and require vanishing net strangeness; phase equilibrium is imposed via the Gibbs condition.

For the hadronic sector we employ non-linear Walecka-type relativistic mean-field models extended to include the full baryon octet. The deconfined phase is described by the 2+1-flavour Polyakov-Nambu-Jona-Lasinio (PNJL) model that includes vector interactions, which are parametrised by the coupling ratio G_V/G_S and varied to assess their impact.

From this approach, we compute isentropic trajectories and extract quantities of interest along them, specifically the speed of sound and cumulants of net-baryon number fluctuations.

Our results are qualitatively consistent with earlier studies but reveal clear distinctions between isentropic trajectories that pass relatively near the CEP and those that do not. In particular, isentropes close to the CEP exhibit pronounced cooling, whereas lower entropy per baryon trajectories tend to increase their temperature.

Vector interactions shift the phase transition to higher densities and modify the magnitude of the discontinuity that occurs in the hadron-quark phase transition. Even for a reduced vector coupling ($G_V/G_S = 0.1$), the conformal limit is violated at high density; we propose a procedure to further constrain G_V/G_S.

The inclusion of hyperons shifts the transition to yet higher densities and substantially lowers the onset temperature for high-entropy isentropes. These findings have direct implications for observables sensitive to the mixed phase in heavy-ion collisions.

“мир спасет красота!”

– Ф. М. Достоевского, *Идиот*

Contents

List of Acronyms

QCD	Quantum Chromodynamics´
QGP	Quark–Gluon Plasma
CEP	Critical End Point
LQCD	Lattice Quantum Chromodynamics
HIC	Heavy-Ion Collision
fRG	Functional Renormalisation Group
DSE	Dyson–Schwinger Equation
BEC	Bose–Einstein Condensate
BCS	Bardeen–Cooper–Schrieffer
QED	Quantum Electrodynamics
RGE	Renormalisation Group Equation
DIS	Deep Inelastic Scattering
NJL	Nambu–Jona-Lasinio
PNJL	Polyakov–Nambu–Jona-Lasinio
LSZ	Lehmann–Symanzik–Zimmerman
MFA	Mean–Field Approximation
EoS	Equation of State
KMT	Kobayashi–Maskawa–'t Hooft
NLW	Non–Linear Walecka

List of Figures

List of Tables

Chapter 1

Introduction

And now for something completely different ...

– John Cleese, *Monty Python's Flying Circus*

Quantum chromodynamics (QCD) is the established theory describing the strong interaction between quarks and gluons. In QCD the strong force emerges from the exchange of colour and anti-colour charges. In the absence of medium effects, only colour-neutral hadrons — bound states of quarks and gluons — are observed in detectors. This phenomenon, known as **colour confinement**, reflects the intrinsically non-perturbative and non-linear nature of the theory. Another essential feature of QCD is **dynamical chiral symmetry breaking**, which gives rise to a non-zero quark-antiquark condensate and generates constituent (dynamical) quark masses. Understanding the mechanisms behind confinement and mass generation remains one of the central open problems in contemporary theoretical physics.

Under extreme conditions (high temperature, large baryon density, strong external fields, etc.) the properties of the QCD vacuum can change such that confinement and/or dynamical chiral symmetry breaking are (partially) restored; the resulting deconfined phase of quarks and gluons is called the **quark-gluon plasma** (QGP). State-of-the-art lattice QCD calculations indicate that the thermal transition at vanishing baryon chemical potential ($\mu_B = 0$) is not a true phase transition but a smooth crossover [5–10]. Lattice methods become unreliable at high baryon density because of the fermion sign problem, and several speculative scenarios have been advanced for that region; see Refs. [1, 11] for reviews. One commonly discussed possibility is a first-order transition at large μ_B originating from a **critical end point** (CEP), where the transition becomes second order. This scenario is supported by effective QCD models and by functional, first-principles methods (see, e.g., [12–15] and references therein).

A central goal of contemporary heavy-ion physics is to map the QCD phase diagram: to determine whether a CEP exists and to map any first-order transition region at large baryon chemical potential. Experimental programs targeting these questions include the Beam En-

ergy Scan (BES) at RHIC [12], the present HADES campaign (FAIR Phase-0) [16], and the forthcoming CBM experiment at FAIR [17]. These efforts employ a range of observables (e.g., fluctuations of conserved charges, flow coefficients, and dilepton spectra) to probe both chiral restoration and deconfinement. The experimental establishment of a CEP would be a landmark result, providing decisive guidance to theory and future explorations of QCD matter.

A first-order hadron-quark transition at large baryon chemical potential implies a mixed-phase region in which portions of the system have undergone the transition while others remain as hadrons. A common strategy to study this regime is a two-phase model that treats hadronic and quark degrees of freedom separately and matches them through appropriate phase-equilibrium conditions. This approach has long been employed to describe the phase transition in neutron-star matter in weak equilibrium [18–21] and has also been applied to heavy-ion collision studies, in particular for asymmetric matter [22–27]. The roles of isoscalar-vector and isovector-vector interactions in shifting the transition and modifying the mixed phase have been investigated in Refs. [28, 29].

The combined effects of vector interactions, isospin asymmetry and thermal excitations on strongly interacting matter evolving along isentropic trajectories in the mixed phase have not, to our knowledge, been studied systematically. These joint contributions influence the onset and extent of the hadron-quark coexistence region and the approximately adiabatic evolution of the fireball produced in heavy-ion collisions, leaving imprints on observables such as conserved-charge fluctuations and the momentum spectra of produced hadrons. In this work we address this gap by analysing isentropic trajectories in the QCD phase diagram and their derived properties — in particular, the speed of sound and net-baryon number fluctuations — across a range of scenarios relevant to heavy-ion experiments.

Discussion Layout

This thesis is structured as follows: In Ch. 2, we review the early motivation for the existence of the hadron-quark transition, the conjectured features of a modern quantum chromodynamics (QCD) phase diagram, and established as well as recent results on the chiral and deconfinement phase transitions and the critical end point (CEP). We also provide an overview of the different stages of a heavy-ion collision and summarize recent results from the BES-II experiment. In Ch. 3, we outline the development of QCD, highlight important concepts related to symmetry, and deconstruct its Lagrangian. In Ch. 4, we introduce the main framework used in this work: quantum field theory at finite temperature. In Ch. 5, we present the Polyakov–Nambu–Jona-Lasinio (PNJL) model employed to describe quark matter. The role of the discrete centre symmetry of QCD and its relation to colour deconfinement are discussed. In Ch. 6, we focus on nuclear matter, beginning with the early Walecka model and later non-linear Walecka–type models. The possible emergence of hyperons and the associated “hyperon puzzle” are also examined. In Ch. 7, we describe the parametrisation sets employed and extend previous analyses. We study the impact of quark vector interactions on both symmetric and asymmetric matter

in the phase diagram and along isentropic trajectories. We further analyse their influence on the speed of sound and net-baryon number fluctuations. The effects due to hyperonic degrees of freedom and their emergence along isentropes is also analysed. Finally, in Ch. 8, we summarise the main conclusions and outline directions for future work.

Chapter 2

QCD Phase Diagram

Men of science are not dependent on the ideas of a single man, but on the combined wisdom of thousands of men [...]

– Ernest Rutherford [1]

In this chapter, we provide a concise overview of the current state of knowledge on the QCD phase diagram, encompassing both theoretical predictions and eventual empirical evidence for the critical end point, chiral symmetry restoration and deconfinement transitions. We also discuss the role of isospin asymmetry in quark and hadronic matter. Following this survey, we present a contemporary rendition of the QCD phase diagram and examine the liquid–gas phase transition in nuclear matter. Given its central importance to this work, we then review both the experimental and theoretical aspects of heavy-ion collisions, with particular emphasis on how measurements of conserved-charge number fluctuations can reveal critical behaviour in QCD matter. We conclude the chapter with a summary of recent results from the BES-II experiment at RHIC.

2.1 Hadron-Quark Phase Transition

Extreme conditions of high temperature and/or density are expected to drive strongly interacting matter into new thermodynamical phases. The mass and radii of hadrons are characterised by the intrinsic parameter of QCD, $\Lambda_{\mathrm{QCD}} \approx 200$ MeV. For physical processes with a momentum scale well above Λ_{QCD}, hadrons are observed as colour singlets of more elementary particles. If matter is compressed such that inter-nuclear distances are comparable or below to $\Lambda_{\mathrm{QCD}}^{-1} \approx 1$ fm, the wave-function of hadrons overlaps each other, meaning that these no longer exists as isolated asymptotic states and the relevant degrees of freedom of QCD vacuum are taken over by more elementary particles such as quarks and gluons.

[1] As quoted in [30].

Equilibrium thermodynamics shows that the particle number density ρ increases with temperature T as $\rho \propto T^3$, meaning that the inter-particle distance scales as $\propto T^{-1}$. Similarly, an increase in the baryon density ρ_B leads to a decrease of the average distance between particles according to $\propto \rho_B^{-1/3}$, which can also be concluded from dimensional analysis. Thus, it becomes natural to conjecture that a phase transition may occur at high enough density and/or temperature, and a phase boundary surface can emerge in the plane of T and ρ_B separating hadrons from new states of matter.

This assumption was realised shortly after the introduction of asymptotic freedom and confinement as properties of QCD by Collins and Perry in [31] questioning the presence of weakly interacting quark matter at large baryon density in stellar objects such as neutron stars. In the same year, the idea of a phase diagram for QCD was proposed by Cabibbo and Parisi in [32] based on the conjecture of a limiting temperature for stable hadronic matter — the **Hagendorn temperature** [33]. For an historical overview of QCD phase diagrams see [34]

Phases transitions can be identified by observing variations in a selected **order parameter** associated with symmetries present in the system. For example, in a ferromagnetic material, the magnetization is the order parameter, and it has a non-zero value below the Curie temperature and zero above it. Transitions can be classified into three main types:

- **First-order phase transition.** The first derivative of Gibbs free energy with respect to some thermodynamical variable exhibits a discontinuity, according to Ehrenfest's classification scheme. Furthermore, two phases I and II may co-exist at some constant temperature T_m with different values of entropy, S_{I} and S_{II}, respectively, in a mix-phase regime, in which percentages of the system have completed the transitions, while other have not. Therefore, the mix-phase is accompanied by release or absorption of heat by the system quantised by the latent heat $\Delta Q_L = T_m(S_{\mathrm{II}} - S_{\mathrm{I}})$ during the phase transition. Furthermore, at the critical point, the order parameter exhibits a discontinuity from zero to a non-zero value or vice-versa, and the correlation length is finite.

- **Second-order phase transition.** The second derivative of the Gibbs free energy with respect to some thermodynamical variable is the lowest derivative to exhibit a discontinuity, according to Ehrenfest's classification scheme. Near the critical point, they exhibit a power law, which can be described by the critical exponents, and the correlation length diverges, meaning that all the system is at the same thermodynamical phase. For this type of transitions, there is a clear, continuous vanishing of the order parameter at the critical point and the transition is complete.

- **Crossover.** The transition between thermodynamical phases occurs smoothly, i.e., without the presence of discontinuities in the thermodynamical quantities. This type of transition occurs in a region of the phase diagram rather than at a critical line, meaning that the transition boundary needed to be specified. In this case, one often defines a *pseudo*-critical point where the rate of change of the order parameter (or its susceptibility) is maximal,

but the order parameter itself does not strictly vanish.

The transition from hadronic matter to the QGP (see Sec. 2.3), is known as the **hadron-quark phase transition** (or QCD phase transition). There are two essential aspects of the QCD phase transitions: deconfinement and chiral restoration, which will be discussed below. In this section we will describe the main features and motivations behind each of this transitions, and highlight recent results related to their classification.

2.1.1 Hagedorn Temperature and Deconfinement

It is empirically known that the density of mesons states $\rho_M(E)$ at large energy E grows exponentially. With increasing energy of the system, new higher-energy particles are produced rather than increasing the energy of existing states. This leads to an increase in the entropy instead of temperature, in which the latter is held at limiting value T_H^M called Hagedorn temperature for mesons. The density $\rho_M(E)$ reads,

$$\rho_M(E) \approx \exp\left(\frac{E}{T_H^M}\right). \tag{2.1}$$

Systems with zero baryon density, the mesonic partition function is

$$\mathcal{Z}_M = \int \mathrm{d}E\, \rho_M(E) e^{-E/T}, \tag{2.2}$$

which diverges for $T > T_H^M$. Hagedorn interpreted this phenomenological parameter T_H^M as the upper limit of the physically possible temperature. Later on, an alternative interpretation was proposed suggesting that a phase transition to a state with more fundamental degrees of freedom should occur at critical temperature $T_c^M = T_H^M$ [32].

Similar arguments can be applied at finite baryon density. In this case, a chemical potential μ_B is added to the previous Boltzmann factor, and Eq. (2.2) becomes

$$\mathcal{Z}_B = \int \mathrm{d}E\, \rho_B(E) e^{-(E-\mu_B)/T}, \tag{2.3}$$

with $\rho_B(E) \approx \exp(E/T_H')$, as suggested by experimental measurements [35]. Now, the critical temperature, T_c^B, is given by

$$T_c^B(\mu_B) = \left(1 - \frac{\mu_B}{E_0}\right) T_H^B, \tag{2.4}$$

where E_0 is a phenomenological parameter. As discussed in [36], since the Hagedorn spectrum $\rho_B(E)$ is only valid in the limit of large energies, the corresponding transition Hagedorn temperature is independent of μ_B, thus the parameter E_0 is added above in order to make the dependence on μ_B explicit.

Relation (2.4) expresses that for each value of μ_B there is a corresponding transition temperature for a new thermodynamical phase. As μ_B increases the transition temperature T_c^B decreases linearly. On the other hand, in the low density regime $\mu_B \ll T$, the thermal degrees

of freedom are dominated by meson states, and the deconfinement transition is characterised by T_c^M rather than T_c^B, meaning that T_c^H must be approximately constant for increasing μ_B. At higher values of μ_B, contributions from excited baryon states become more significant indicating that a transitional point in the $T-\mu_B$ plane must appear where baryons importance is greater than that of mesons. This behaviour is also supported by heavy-ion collision experiments [37–42] and recent numerical simulations from **lattice QCD** (LQCD) [43–45] which have shown that T_c decreases slowly, about 10% for μ_B from 0 to 400 MeV, while for μ_B in the range $400-800$ MeV an approximate linear behaviour is observed. Eventually, assuming $T_H^B > T_H$, the two lines of constant T_c^M and decreasing T_c^B cross leading to a triple-point of coexistent of hadronic and the new states of matter resultant from the increasing temperature and/or baryon density.

Although the picture of hadrons percolating at the Hagedorn temperature [46,47] to describe the deconfinement of quarks is intuitive, it is necessary to develop a field description of deconfinement in agreement with QCD. This can be achieved by considering a global *centre symmetry* Z_3 of the pure $SU(3)$ Yang-Mills using the expectation value of the so-called **Polyakov loop**, Φ as an order parameter for deconfinement [48]. The centre symmetry and the parameter Φ will be discussed in much detail in Ch. 5. Here, it is only essential to mention that a confined phase is characterised by $\langle\Phi\rangle = 0$ and a deconfined phase by $\langle\Phi\rangle \neq 0$, as required by the Elitzur's theorem [49] for the spontaneous breaking of the centre symmetry. When dynamical quarks are considered the centre symmetry is broken explicitly, so that the expectation value of the Polyakov loop never vanishes and it reduces to an approximate order parameter. This breaking of the centre symmetry is enlarged at high density regimes of QCD matter, obscuring the theoretical concept of quark deconfinement. In other words, deconfinement is most well defined in the limit of infinite quark masses. Nevertheless, in most situations the Polyakov loop has proven to be useful to study the nature of the deconfinement transition in cases with heavy quarks [50], even at physical masses [51–54], as well as at smaller than physical quark masses [55]. Furthermore, provided the centre symmetry is only mildly broken, one may define an approximate critical temperature — the ***pseudo*-critical temperature**, T_{pc}. In the present work this symmetry will also be considered as an (approximate) order parameter for deconfinement.

In order to locate the deconfinement pseudo-critical temperature different approaches can be taken. One can study the inflexion point of $\Phi(T,\mu_B^*)$ or the peak position of the $\partial\Phi(T,\mu_B^*)/\partial T$ at some fixed value of $\mu_B = \mu_B^*$, or several other observables derived form this. In particular, determining the peak position of the static quark entropy with temperature at fixed μ_B as shown to be advantageous to locate the crossover temperature over the **Polyakov loop susceptibility**, generally defined as

$$\chi_\Phi = V\left(\left\langle|\Phi|^2\right\rangle - \langle|\Phi|\rangle^2\right), \tag{2.5}$$

where V represents spatial volume. In full QCD calculations with approximate physical quark masses, chiral features (see the following subsection) dominate over deconfinement and, instead of a clean signature of the transition, one obtains a broad width for the deconfinement crossover.

The **static quark entropy**, defined as

$$S_Q(T,\mu_B) = -\left(\frac{\partial F_Q(T,\mu_B)}{\partial T}\right)_{\mu=\mu_B^*}, \tag{2.6}$$

for some fixed $\mu_B = \mu_B^*$ and with the static quark free energy,

$$F_Q = -T \ln \langle \Phi \rangle , \tag{2.7}$$

is less scheme dependent than the Polyakov loop and it defines a crossover temperature which coincides with the chiral transition temperature even in situations of physical quark masses.

Besides the Polyakov loop, there have been indications that support the idea of using the difference of the gluon and ghost propagator to identify the confinement-deconfinement transition in the $SU(3)$ gauge group [56, 57]. However, despite intense theoretical effort, an exact deconfinement order parameter has not yet been found, and various proposal candidates turned out to be unsuccessful (see [58, 59] for several examples). This absence for a satisfactory order parameter could be connected with the lack of a strict definition of confinement (see Sec. 3.3 for further exploration of confinement in QCD).

2.1.2 Chiral Phase Transition

A second important aspect of QCD phase transitions is related to the restoration of chiral symmetry. This symmetry is exact for massless quarks, and the Lagrangian of QCD is invariant under $SU(N_f)_R \times SU(N_f)_L$ transformations. The quark masses, however, should not be understood as an actual physical mass, since they cannot be measured directly with scattering processes due to confinement. Instead, masses of the different quark flavours are obtained from theoretical calculations such as LQCD simulations in which they are tuned to match ratios of precise experimentally measured quantities such as hadronic masses. The discrepancy between the masses of quarks (see Table 2.1) and the baryons raises a distinction between **current** (or bare) m_q and the **constituent** (or dynamical) M_q quark mass which should be approximately 1/3 of the average mass of nucleons. This difference is explained by the spontaneous breaking of chiral symmetry whose order parameter is the chiral condensate $\left\langle \bar{\psi}\psi \right\rangle$, which will also be discussed in the context of symmetries of the QCD Lagrangian in section 3.2.

The breaking of chiral symmetry and, consequently, the value of M_q, is connected with the zero-point oscillation energy of quarks and anti-quarks. This is given by,

$$\Omega = -2N_f N_c \int^{\Lambda} \frac{d^3p}{(2\pi)^3} \left(p^2 + M_q^2\right)^{1/2}, \tag{2.8}$$

where N_f and N_c are the number of colours and flavours considered respectively, and Λ is an ultraviolet cut-off to regularise the divergent integral. Since M_q is not a physical constant, but determined dynamically from QCD interactions, this zero-point energy cannot be discarded. This can be better understood by evaluating the integral (2.8). Changing variables as $p \rightarrow$

Quark	**Current mass** [35]
Up (u)	2.16 ± 0.07 MeV
Down (d)	4.70 ± 0.07 MeV
Strange (s)	93.5 ± 0.8 MeV
Charm (c)	1.2730 ± 0.0046 GeV
Bottom (b)	4.183 ± 0.007 GeV
Top (t)	172.57 ± 0.29 GeV

Table 2.1: The *up*, *down* and *strange* quark masses are given in the modified minimal subtraction ($\overline{\text{MS}}$) scheme at $\mu \approx 2$ GeV. The *charm* and *bottom* masses are $\overline{\text{MS}}$ masses renormalised at the $\overline{\text{MS}}$ mass. The *top* quark is extracted from event kinematics.

p/Λ and $M_q \to M_q/\Lambda$, with Λ sufficiently large such that $M_q/\Lambda \ll 1$, we obtain from Taylor expanding (2.8) that

$$\Omega = -N_f N_c \frac{\Lambda^4}{4\pi^2}\left[1 + \left(\frac{M_q}{\Lambda}\right)^2 + O\left(\left(\frac{M_q}{\Lambda}\right)^4\right)\right], \tag{2.9}$$

where the negative sign associated with the term $(M/\Lambda)^2$ indicates that the minimisation of Ω favours large M_q values, and thus, the breaking of chiral symmetry. With increasing μ_B, the low-energy states become progressively occupied by quarks, leading to the formation of a Fermi sphere. Owing to the Pauli exclusion principle, these occupied states no longer contribute to the phase-space integration in Eq. (2.8). As a consequence, the mechanism responsible for dynamical symmetry breaking is weakened, and the chiral phase transition is expected to give rise to a phase boundary in the T–μ_B plane, analogous to the deconfinement transition.

The behaviour for increasing temperature is identical. At high temperatures, thermal excitations leads to a population of a large number of states regardless of the ground state configuration. The energy difference between the symmetric and broken phase becomes less significant in comparison with the available thermal energy, and chiral restoration occurs at a certain critical temperature value, thus contributing to the boundary curve in the $T - \mu_B$ plane. In both cases, chiral restoration is accompanied by the melting of the order parameter $\left\langle \bar{\psi}\psi \right\rangle$, i.e., $\left\langle \bar{\psi}\psi \right\rangle = 0$.

In contrast to the poorly studied observables related to deconfinement at $\mu_B \neq 0$, the chiral transition has been well established for small μ_B [43,60,61]. The identification of the crossover to a chiral restored phase can be made by localising the peak position of the chiral susceptibility[2],

$$\chi_{\bar{\psi}\psi} = \frac{T}{V}\frac{\partial^2 \ln \mathcal{Z}}{\partial m_f^2}, \tag{2.10}$$

for flavour $f = u, d, s$.

[2]Another common definition of the chiral-crossover line is the temperature at which the chiral condensate changes most rapidly, i.e. the inflection point satisfying $\mathrm{d}^2 \left\langle \bar{\psi}\psi \right\rangle / \mathrm{d}T^2 = 0$.

2.1.3 Where We Stand

The exploration of the QCD phase diagram proceeds along theoretical and experimental lines: theoretically via LQCD simulations, hydrodynamic and functional methods, and effective theories of QCD; experimentally via astrophysical observations of neutron stars and measurements from particle colliders.

Crossover Transition

At $\mu_B = 0$, LQCD simulations with physical quark masses have shown that the hadron-quark transition is a smooth crossover [5–10]. Due to the absence of a real transition, the crossover temperature will be dependent on the definition used, leading a range of values for it. State-of-the-art calculations, based on the observables related to the chiral symmetry (e.g. chiral condensate and its susceptibilities) indicate that this smooth crossover takes place at the pseudo-critical temperature, $T_{pc} = 155 - 158$ MeV [43,44]. This behaviour is also supported by the phenomenology and experiments of heavy-ion collisions [44,62,63]. However, the presence of additional external parameters, such as non-vanishing μ_B, may change the nature of this transition.

Although LQCD simulations are limited by the fermion sign problem, various extrapolation methods enable investigation of the regime of small baryon chemical potential μ_B (see Subsec. 3.3.2). Currently, numerical results indicate that the crossover transition persists up to $\mu_B/T \leq 3$ [44,64,65], but recently an indication of a narrowing of the crossover towards large μ_B was observed in [45]. This narrowing might be an indication for the presence of a first-order phase transition between hadronic matter to a quark-gluon plasma at larger μ_B.

Quenched and Chiral Limits

In the quenched limit (infinite quark masses) LQCD results have shown the existence of a weak first-order transition from confined to deconfined matter [66]. On the other hand, in the chiral limit, a first or second-order phase transition is expected to take place depending on the number of quark flavours and their relative masses to each other [10,67,68].

In Fig. 2.1 the current understanding of the different natures of the chiral transition for a $N_f = (2+1)$ phase diagram is displayed. For two vanishing light quark masses ($m_u = m_d = 0$) at $\mu_B = 0$, chiral restoration through a second-order phase transition has been well established by LQCD simulations [7,10], where it has been determined to occur at a critical temperature $T_c = 132 - 134$ MeV [7,69] from LQCD simulations, while a larger value of $T_c = 142.6$ MeV [70] was predicted using **functional renormalisation group** (fRG) methods. However, the presence of a tricritical point $(T^{\text{tri}}, \mu_B^{\text{tri}})$, connecting the second to the first-order transition at larger values of μ_B, is still expected with base on numerical models calculations and on universality arguments [67,71–75].

The nature of this transition has not yet been settled. Although LQCD calculations support that the critical phenomena at $N_f = 2$ should belong to the $O(4)$ universal class, the possible

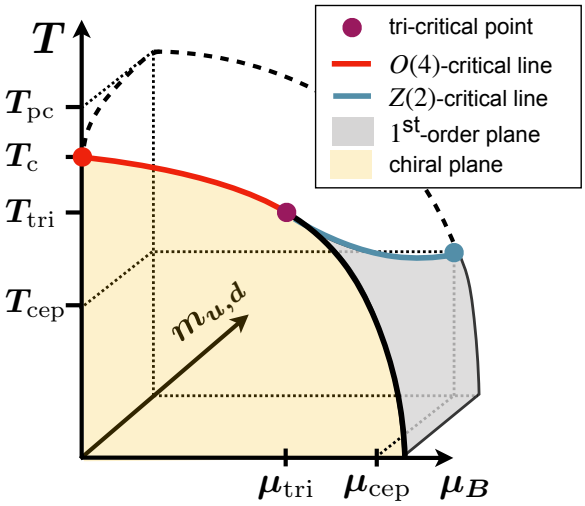

Figure 2.1: Sketch of the QCD phase diagram based on the chiral restoration transition for various temperatures (T), baryon chemical potential (μ_B) and degenerate light quark masses ($m_u = m_d$). See the text for more detail.[3]

restoration of the axial symmetry $U_A(1)$ (see Sec. 3.2) below T_c remains controversial, meaning that the possibility for a larger symmetry group cannot be discarded [67, 76–83].

Critical End Point

In the case of $m_s \gg m_u = m_d \neq 0$, the second-order phase transition is taken over by a crossover, as discussed above, and reduced to the chiral CEP which belongs to the $3d$, $Z(2)$ universality class. Locating the CEP in realistic scenarios is of great importance for our understanding of the QCD phase diagram, and has been the subject of intensive theoretical and experimental study over the last decades.

Recent results on the position of the CEP for $N_f = (2+1)$ flavours have been obtained from various theoretical approaches. Results from fRG methods and **Dyson-Schwinger equations** (DSEs), including variations thereof, are mutually consistent and converge as truncation order is increased, yielding a CEP in the region $(T^{\mathrm{CEP}}, \mu_B^{\mathrm{CEP}}) = (100-110, 600-650)$ MeV [15, 84–87]. This region for the CEP location has also been supported by LQCD calculations using the Padé approximation to the logarithm of the QCD grand-canonical partition function and analysis of the Lee-Yang singularities, as introduced in [88]. Applying this method, the CEP has been estimated to be $(T^{\mathrm{CEP}}, \mu_B^{\mathrm{CEP}}) = (100, 580)$ MeV in [89]. A much lower value for μ_B^{CEP} was recently obtained in Ref. [90], where the CEP was determined to be at $(T^{\mathrm{CEP}}, \mu_B^{\mathrm{CEP}}) = (105^{+8}_{-18}, 422^{+80}_{-35})$ MeV. However, as explained by the authors, it is expected that cut-off effects move the chemical potential towards larger values of around $\mu_B^{\mathrm{CEP}} \approx 650$ MeV.

Several effective models of QCD predict a first-order phase transition originating from the CEP (for recent reviews, see Refs. [12, 13]). However, the inclusion of a repulsive vector–channel

[3] Not shown in the figure but by including the strange quark flavour at all vanishing masses ($m_u = m_d = m_s = 0$) it is predicted that a first-order transition should occur at all values of μ_B [73].

interaction can substantially shift the CEP (see [91] and references therein) and, if sufficiently strong, can smooth out the first-order transition into a crossover [91–94]. This same interaction also reduces the extent of the **co-existence (binodal) region** in the phase diagram [95]. Despite its crucial role in both neutron-star structure calculations [94, 96] and the mapping of the QCD phase diagram, the sign and density dependence of the vector coupling remain poorly constrained. While one can fix its vacuum value by reproducing the vacuum masses of vector mesons, there is no firm constraint for its magnitude or medium dependence at finite baryon density.

Interplay of Chiral restoration and Deconfinement

The analogous response of the chiral restoration and deconfinement transitions to changes in temperature and density suggests an intrinsic connection between these two phenomena.

LQCD simulations at vanishing baryon chemical potential ($\mu_B = 0$) support this conjecture [6]: both the chiral condensate and the Polyakov loop undergo, respectively, a rapid decrease and increase over the same temperature range, indicating a simultaneous chiral-symmetry restoration and deconfinement crossover. This coincidence led early phase-diagram models — such as the prototype phase diagram revisited in [97] — to suggest a strict correspondence between the two transitions.

This relationship has also been investigated using an effective model for symmetric quark matter [98], which confirmed earlier observations [99] regarding the crossing of the chiral and deconfinement transitions. Furthermore, an analysis of the impact of vector interactions — associated with the mixing between gluon and quark degrees of freedom — revealed that the chiral transition strongly influences deconfinement. While the crossing temperature remains largely unaffected, the corresponding chemical potential increases significantly at large vector couplings. A similar interplay has been observed in the case of the strange quark chiral crossover in the absence of vector interactions, where the deconfinement crossover displays a kink.

Nonetheless, an exact relation between chiral restoration and deconfinement have remained a long standing problem in QCD.

A Modern QCD Phase Diagram

Different modern versions of the QCD phase diagrams have been proposed, e.g., some assuming the presence of a first-order phase transition, others, a crossover even at large densities. With the current available theoretical and experimental knowledge selecting one among many others has not been possible. A widely supported scenario for a phase diagram is shown in Fig. 2.2. Here, the CEP point is considered, separating the crossover from the first-order chiral symmetry restoration phase transition. Another first-order liquid-gas phase transition for nuclear matter is also present which will be discussed in the next section. With increasing density, as mentioned in Subsec. 2.1.1, the deconfinement transition becomes more blurred due to a decrease in the barrier for QCD string breaking; this is represented by the colour gradation in Fig. 2.2.

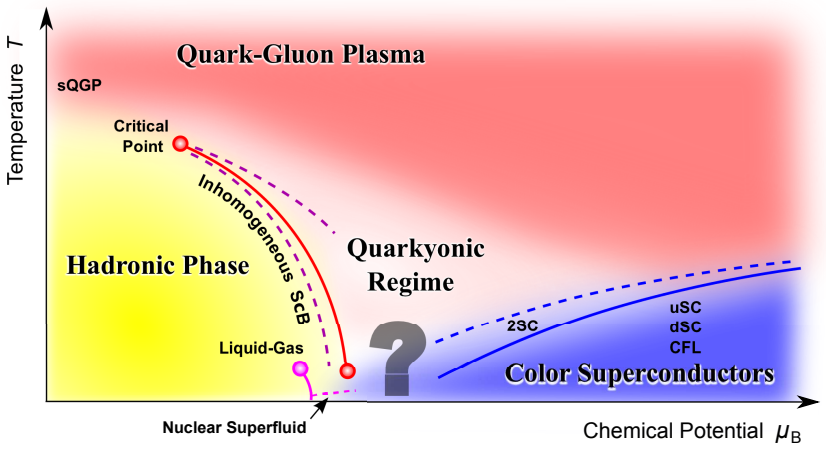

Figure 2.2: A modern picture of the QCD phase diagram for isospin-symmetric matter, including conjectured thermodynamical phases at high baryon chemical potential. The figure is taken from [1].

Four major regions can be identified: the hadronic phase, quark-gluon plasma, quarkyonic regime and colour superconductors. Also a big question mark defines an unknown region of high density and low temperature. In **quarkyonic regimes** the system is still in the confined phase with hadrons being the relevant degrees of freedom, but pressure becomes sensitive to quarks through inter-baryonic interactions. **Colour superconducting phase**, at much larger densities, is based on the **Bardeen-Cooper-Schrieffer** (BCS) theory of superconductivity [100] where here pairs of quarks (i.e., diquarks) are connected by one-gluon exchange. Given the speculative nature and the lack of experimental exploration at these last two regimes, we shall not further explore their properties and phase transitions therein; the interested reader is referred to [1] for a more broad and detailed review. Instead, we focus on the hadronic phase, the QGP, the chiral and deconfinement transition in the following sections and throughout this work.

Isospin-Asymmetry Effects

The isospin-symmetric case of QCD matter has been only discussed so far. However, this scenario has to be considered for a full understanding of the QCD phase diagram and given its relevancy in **heavy-ion collisions** (HICs) [101] and astrophysics, such as cold neutron stars [102, 103] and the early evolution of the Universe [104]. Isospin density is given by

$$\rho_3 = \frac{\rho_u - \rho_d}{2}, \tag{2.11}$$

where ρ_u, ρ_d, are the net densities of each quark flavour. While the baryon density measures the excess of strongly interacting matter over anti-matter, the isospin density quantifies the asymmetry between the up and down quark flavours or, equivalently, the difference between the density of protons and neutrons in the system (see Subsec. 2.2.2). Experimentally, particle colliders have only achieved small asymmetries so far. On the other hand, the low proton content in neutron stars makes them valuable laboratories to study not only the effects of high baryon

density but also of those for high isospin-asymmetries in QCD matter, meaning that precision neutron star observation and gravitational-wave astronomy offer important sources to constrain the QCD phase diagram along the ρ_3 axis.

Isospin-asymmetric matter at finite baryon density modifies the chiral phase transition. Increasing the isospin chemical potential $\mu_3 = \mu_u - \mu_d$ lowers the CEP temperature and reduces the extent of the **spinodal region**[4] [95, 105, 106] — an effect further enhanced by the inclusion of vector interactions, as discussed previously. Chiral perturbation theory yields the same trends [107–109], and fRG analyses confirm them [110].

At $T = 0$, when the isospin chemical potential exceeds the critical value $\mu_3^c = m_\pi$, there is sufficient energy to produce charged pions, driving pion condensation and the formation of a **Bose-Einstein condensate** (BEC) of charged pions. LQCD simulations at finite isospin asymmetry — both for $\mu_B = 0$ [111,112] and for small μ_B [113] — have shown that the chiral crossover persists at small μ_3, and that the pion-condensation onset line intersects the chiral-restoration line at a triple point; beyond that intersection the two phenomena occur simultaneously. A similar tendency has also been observed in a related study using the Nambu–Jona-Lasinio model for two-flavour and two-colour QCD [114]. Chiral perturbation theory has also predicted that the transition to the pion condensate phase is of second-order with universality class $O(2)$ [107], which have been confirmed by LQCD [111]. However, while the former predicts a monotonous rise of $\mu_3^c(T)$ with temperature, the latter have shown evidence for a flattening of this curve around the zero-density deconfinement crossover, suggesting that deconfinement is stronger than the condensation mechanism, and that in the QGP phase pions cannot be created by increasing μ_3 above $T \approx 160$ MeV [111, 115, 116]. An analysis of the renormalised Polyakov loop has also indicated that the deconfinement crossover temperature decreases and smoothly penetrates into the pion condensation phase, favouring the scenario where the deconfinement transition connects continuously to the BEC-BCS-superconductivity crossover [111].

2.2 Liquid-Gas Phase Transition

Hadronic matter is expected to undergo two major phase transitions: the hadron-quark phase transition, discussed in the previous section, and the **liquid-gas phase transition** at low temperatures and high baryon densities as shown in Fig. 2.2. In contrast to the former, the existence of a critical point for the liquid-gas transition has been confirmed by the available, in both symmetric and asymmetric nuclear matter, multi-fragmentation data and the survey of the nuclear caloric curve in nucleus-nucleus and hadron-nucleus reactions [117–121] (see also [122] for a recent review).

The presence of a liquid-gas transition is generally true for any system of 3-dimensional self-bound fermions. In opposition to second-order phase transitions, which are related to a global symmetry and its spontaneous breaking, first-order transitions do not change the symmetry

[4] The spinodal region denotes the range of densities and temperatures where the system is mechanically unstable, leading to a phase separation into a dense and dilute phase.

pattern. Instead, the latter is related with a mixture of two phases with different densities. The reasons for this transition can be understood intuitively from the saturation properties of nuclear matter[5]. At $T = 0$ and below the saturation density ρ_0, it is energetically more favourable for the nucleons to pile up into an isolated nuclear liquid droplets, surrounded by vacuum, with the nuclei being though as droplets or clumps of this liquid with a local density ρ_0. For increasing temperature, the droplets swell, reducing the local density, and the nuclear liquid droplets are evaporated in to what was formerly the vacuum. This evaporation creates a phase mixture of liquid droplets with (local) density $\rho_\ell < \rho_0$ and a nuclear gas with density $\rho_g < \rho_\ell$; right at the first-order phase transition these two phases can coexist in space. Eventually, at some critical temperature T_c^{l-g}, $\rho_\ell = \rho_g \equiv \rho_B^c$ and the distinction between hadronic liquid and gas disappears.

2.2.1 Symmetric Nuclear Matter

As mentioned above, the existence of a first-order liquid-gas phase transition of nuclear matter has been better established theoretically and it is one of the few experimentally accessible aspects of the phase structure of strongly interacting matter at low temperature. A recent empirical estimate of the critical end point yields [121]

$$T_c^{l-g} = 17.9 \pm 0.4\text{MeV}, \quad \rho_B^c = 0.06 \pm 0.01\text{fm}^{-3}. \tag{2.12}$$

This critical end point is connected by first-order phase transition line ending at $T = 0$ with the empirical values of $\rho_0 = 0.16$ fm^{-3} and a binding energy per nucleon of $\epsilon_B \approx 16$ MeV. Theoretically, this results have been also extensively supported by phenomenological relativistic mean field models (e.g. the Walecka model) [1, 123–127] and the relativistic Hartree-Fock approach based on the nucleon-nucleon potential [128–130]. Moreover, first principle approach methods such as LQCD calculations via effective theories [131–134], fRG methods [135] and DSEs [136] have not only showed good agreement with the experimental location of the liquid-gas critical point, but also to quantitatively describe this transition directly from QCD and to derive analytic expressions for ϵ_B and ρ_0.

2.2.2 Asymmetric Nuclear Matter

Recently, the isospin-asymmetric nuclear matter case, i.e., when the density of neutrons and proton differs, has been the subject of a lot of experimental efforts [120, 137–140] and theoretical activity (see the reviews [122, 141, 142]) given its relevancy to both nuclear physics and astrophysics.

[5] In nuclear physics, saturation refers to the empirical observation that the binding energy per nucleon in bulk nuclear matter attains a maximum (at a local **saturation density** ρ_0) and thereafter remains essentially constant as the nucleon number grows. This behaviour stands in contrast to long-range interactions — such as gravity — where the net binding continues to increase with total mass. Saturation arises from the form of nucleon-nucleon interactions, which features a strong, short-range repulsive core followed by an intermediate-range attractive component. As a result, each nucleon in a dense nucleus interacts significantly only with a limited number of neighbour nucleons, so that adding further nucleons leaves the average interaction energy per particle essentially unchanged.

Various theoretical approaches [143–149] converge on two principal effects of isospin asymmetry on the nuclear liquid–gas phase transition. First, both the critical temperature and the critical density are suppressed, causing a marked contraction of the spinodal region — an effect analogous to the reduction of the chiral symmetry restoration point under isospin imbalance. The reason for this decrease are primarily attributed to an increase in the symmetry energy, which quantifies the energy cost of deviating from equal numbers of protons and neutrons in nuclear matter. From the semi-empirical mass formula proposed by Bethe and Weizsäcker [150,151] the expressions of increasing isospin-asymmetry is to reduce the total biding energy per nucleon, making the system less bound and thus lowering the critical parameters. Furthermore, it leads to an increase of repulsive interactions among like nucleons (neutron-neutron and proton-proton), suppressing density fluctuations, thus narrowing the range of conditions under which the system is unstable to phase separation. The second feature is the so-called **isospin distillation**, in which the phase separation process tends to produce a liquid phase that is more symmetric (closer to equal numbers of protons and neutrons) and a gas phase that is more neutron rich [152]. This behaviour has also been explored in the context of two-phase model in [153].

2.3 Heavy-Ion Collisions

The experimental realisation of the QCD phase diagram is strongly related with HICs. Given the applications of this work to analyse their results, we shall make a short introduction to the different stages of a HIC, namely, to the QGP, its experimental observables as well as recent empirical results. The **Relativistic Heavy Ion Collider** (RHIC), located at Brookhaven National Laboratory, and the **Large Hadron Collider** (LHC) at the European Organization for Nuclear Research (CERN) are prominent examples of ion-colliders using particles such as Au (gold) and Pb (lead). While the LHC results are at low densities, RHIC has been able to access larger values of μ_B. Nonetheless, there are new upcoming facilities that will allow one to reach even higher densities. Some examples are the **Compressed Baryonic Matter experiment** (CBM) at the Facility for Antiproton and Ion Research (FAIR) [154] and the **J-PARC Heavy-Ion project** (J-PARC-HI) at the Japan Proton Accelerator Research Complex (J-PARC) [155].

2.3.1 Stages of a Heavy-Ion Collision

A HIC consist on the collision of two beams of nuclei accelerated to relativistic velocities. When the two beams collide, they form a hot **fireball** characterised by an energy density ϵ and temperature T. Due to conservation of baryon number — while neglecting dissipative effects due to viscosity, heat conduction and charge diffusion — the evolution of the fireball undergoes an adiabatic expansion moved by pressure gradients along **isentropes**, i.e., trajectories of constant entropy per baryon (s/ρ_B). The higher the centre-of-mass energy of the collision the higher is s/ρ_B. Furthermore, the evolution of the fireball can be separated into three major stages:

- **Pre-thermalisation.** An initial non-thermalised state with strongly correlated field called **glasma** is produced. This is commonly treated in the **colour glass condensate** framework (see [156,157] for a detailed review). A major challenge of this stage is the description of the different momentum scales composed by valence and sea quarks as well as gluons. Due to its non-thermalised nature, the glasma state is not accessible using LQCD.

- **QGP.** As the fireball evolves, further fragmentation of partons into quarks and gluons leads to the formation of the QGP[6] in which (total or partial) deconfinement and chiral symmetry restoration occurs. Contrary to early ideas about the QGP — expected to behave similar to an electromagnetic plasma — the system remains strongly coupled over a large temperature range above T_{pc} (represented in Fig. 2.2 by the label "sQGP"). This is reflected in the interaction measure or trace anomaly computed in LQCD as the difference between energy density and pressure, normalised by temperature,

$$I = \frac{\epsilon - 3P}{T^4}, \tag{2.13}$$

  which by definition vanishes for an ideal gas of massless quarks and gluons. This strong interacting plasma has been shown to endure up to $T \approx 200$ MeV (about 20% above T_{pc}), where the value of I peaks, before thermal contributions become more significant and the interaction falls off with increasing temperature [3]. The conclusion of a strongly interacting QGP close to T_{pc} is also supported from the experimental point of view as the colliders and the computation of shear and bulk viscosities using hydrodynamical simulations[7] to fit empirical results, have shown that even at $\approx 2T_{pc}$ the QGP is strongly coupled [159]. For further discussion on the properties of the QGP and relativistic hydrodynamical simulations see [160–163].

- **Freeze-out.** The QGP expands and lowers its temperature, simultaneously. When it reaches the QCD transition temperature, deconfined quarks and gluons recombine to form colour-neutral hadrons. At this points, **chemical freeze-out** occurs, and the chemical abundance of hadrons is determined. Nonetheless, the exchange of energy and momentum can prevail until **kinetic freeze-out** takes place.

Whether the QGP stage and the following transition to hadrons can be treated as a thermalised state remains an open question. Only if such is verified, LQCD can be applied to study this regime reliably.

2.3.2 Fluctuations and Critical Behaviour

Measurements of not only the first-order moments of hadron production data, but also higher ones provide essential information about the nature of QCD phase transitions, namely, on the

[6] The term QGP was first coined by Shuryak in [158].

[7] For a strongly coupled system with a mean free-path comparable or lower than the corresponding de Broglie wavelength of particles, the treatment as a fluid is appropriate, and one then can describe properties of the QGP by solving hydrodynamic equations.

(conjectured) location of the CEP, as they can be directly connected to the QCD partition function, $\mathcal{Z}$, via conserved charge number susceptibilities in the grand canonical ensemble [12].

Let $P(X)$ be the probability distribution function of an integer stochastic variable X satisfying $\sum_X P(N) = 1$. The ***n*th-order moment** of $P(X)$ is defined by [164]

$$\langle X^n \rangle = \sum_X X^n P(X). \tag{2.14}$$

Another useful type of quantities characterising $P(X)$ are the ***n*th-order cumulants** $\kappa_n(X)$. Generally, the $\kappa_n(X)$ are defined as the coefficients in the Maclaurin series, [164]

$$\kappa_n(X) = \left(\frac{\partial^n \ln G(\omega)}{\partial \omega^n} \right)_{\omega=0}, \tag{2.15}$$

of the moment generating function

$$G(\omega) = \sum_X P(X) e^{\omega X} = \left\langle e^{\omega X} \right\rangle, \tag{2.16}$$

where ω is a continuous variable that parametrises G.

For a thermodynamical system of volume V and temperature T, $G(\omega)$ is replaced by the $\mathcal{Z}(V,T,\mu)$, where μ is a chemical potential vector introduced to conserve, on average, e.g., the baryon number, electric charge and strangeness, i.e. $\mu = (B, Q, S)$. The susceptibilities and cumulants of a net-charged number (N_q) distributions can be related as

$$\chi_n^{(q)} \equiv \left(\frac{\partial^n \left(P/T^4 \right)}{\partial (\mu_q/T)^n} \right)_T = \left(\frac{1}{VT^3} \frac{\partial^n \ln \mathcal{Z}(V,T,\mu)}{\partial (\mu_q/T)^n} \right)_T = \left(\frac{\kappa_n(N_q)}{VT^3} \right)_T, \tag{2.17}$$

where $q \in \{B, Q, S\}$. Up to 4th order, cumulants of a distribution are given by

$$\kappa_1(N_q) = \left(\frac{\partial \ln \mathcal{Z}(V,T,\mu)}{\partial (\mu_q/T)} \right)_T = \langle N_q \rangle, \tag{2.18}$$

$$\kappa_2(N_q) = \left(\frac{\partial^2 \ln \mathcal{Z}(V,T,\mu)}{\partial (\mu_q/T)^2} \right)_T = \left\langle (\delta N_q)^2 \right\rangle, \tag{2.19}$$

$$\kappa_3(N_q) = \left(\frac{\partial^3 \ln \mathcal{Z}(V,T,\mu)}{\partial (\mu_q/T)^3} \right)_T = \left\langle (\delta N_q)^3 \right\rangle, \tag{2.20}$$

$$\kappa_4(N_q) = \left(\frac{\partial^4 \ln \mathcal{Z}(V,T,\mu)}{\partial (\mu_q/T)^4} \right)_T = \left\langle (\delta N_q)^4 \right\rangle - 3 \left\langle (\delta N_q)^2 \right\rangle^2, \tag{2.21}$$

with $\delta N_q \equiv N_q - \langle N_q \rangle$.

Cumulants have useful properties in describing the fluctuations of physical systems [164]. For example, from Eq. (2.19) one can define the mean M and variance σ^2 of N_q, respectively as

$$\mathrm{M} = \kappa_1(N_q), \quad \sigma^2 \equiv \kappa_2(N_q). \tag{2.22}$$

Additionally, one can also introduce the **kurtosis** K and **skewness** Σ of the conserved charge distribution N_q,

$$\mathrm{K}(N_q) = \frac{\kappa_4(N_2)}{(\kappa_2(N_q))^2}, \quad \Sigma(N_q) = \frac{\kappa_3(N_q)}{(\kappa_2(N_q))^{3/2}}, \tag{2.23}$$

which quantify, respectively, how peak/broad and asymmetric the net-charge number distribution is in relation to a Gaussian distribution, for which all cumulants for $n \geq 3$ vanish.

Experimental measurements of cumulants such as net-proton, net-charge, and net-kaon are expected to carry significant information about the fireball, and to further probe the nature of the QCD phase diagram. Fluctuations are studied by measuring the variances of the event-by-event observables such as multiplicities or mean transverse momenta of particles: a given observable is measured on an event-by-event basis and its fluctuations are studied for the ensemble of events [12].

The reason for measuring higher-order cumulants in HICs is two-folded. Firstly, is the location of the CEP. If present, the second-order transition nature of the CEP is characterised by a divergent correlation length ξ of the order parameter, in this case the chiral condensate. The singular, critical contribution of the CEP to cumulants would manifest in a *non-monotonic* dependence of an experimentally varied parameter, e.g. the collision energy or ion size, as the critical point is passed by during beam energy scan [165, 166]. In realistic HICs the finite size and expansion rate of the produced medium — far from the thermodynamical limit in which the phase transition is defined — cuts-off the divergence of ξ. However, as pointed out in Ref. [167], higher-order cumulants are much more sensitive to ξ, making them attractive experimental observables. Secondly, the measurement of higher-order fluctuations of conserved charges in HICs provide an independent estimate of the chemical freeze-out point, and be used in comparison to results from LQCD [168, 169].

Cumulants are extensive quantities dependent on the volume V, as shown in (2.17), which can ben be poorly known. For this reason, the dependence on V is removed by taking ratios of cumulants (or susceptibilities) instead. In this work, we shall focus on the nth-order net-baryon number susceptibility $\chi_B^n(T, \mu_B) \equiv \chi_n(N_B)$, and, in particular, the following ratios

$$\frac{\chi_B^3(T,\mu_B)}{\chi_B^1(T,\mu_B)} = \frac{\Sigma(N_B)\sigma^3}{\mathrm{M}}, \quad \frac{\chi_B^4(T,\mu_B)}{\chi_B^2(T,\mu_B)} = \mathrm{K}(N_B)\sigma^2. \tag{2.24}$$

The analysis of these ratios has also been done previously in the literature (see, e.g. Ref. [98, 170]).

In summary, the presence of a CEP in the QCD phase diagram should result in non-monotonic behaviour of parameters such as cumulants. Finite system size suppresses the divergence of the correlation length ξ near the CEP. Higher-order cumulants are more sensitive probes of a first-order phase transition. Quantitative characterization of non-monotonic features is difficult because they depend sensitively on the QCD equation of state near a possible CEP — notably on the CEP's location and its strength. Consequently, theoretical models play a crucial

role both in interpreting experimental data and in informing viscous hydrodynamics simulations.

2.3.3 Recent Results from the BES-II Experiment

Recently the STAR collaboration at RHIC reported precision measurements of net-proton number fluctuations from the **Beam Energy Scan experiment** (BES-II). The BES-II results present cumulants (and factorial cumulants) up to fourth order for Au+Au collisions in collider runs at $\sqrt{s_{NN}} = 7.7 - 27$ GeV (approximately $\mu_B = 400 - 150$ MeV) [40, 171]; fixed-target (FXT) measurements extend the coverage down to $\sqrt{s_{NN}} \approx 3$ GeV. When combined with previous runs, the experimental program provides data spanning roughly $3 \leq \sqrt{s_{NN}} \leq 200$ GeV (corresponding to μ_B values of order $25 - 750$ MeV) [172].

The recent results have reported a monotonic decrease towards lower $\sqrt{s_{NN}}$ (increasing μ_B) for κ_2/κ_1 cumulants ratios. While this effect has been previously observed in the BES-I experiment and attributed to baryon number conservation [173], an excess over the baseline[8] can be seen, which would be consistent with the presence of the CEP. Moreover, measurements of $n = 4$ factorial cumulant data have shown a dip at $\sqrt{s_{NN}} \approx 19$ GeV, again, in qualitative agreement with the equilibrium critical point predictions [174, 175]. However, further data at $\sqrt{s_{NN}} < 7.7$ GeV from the RHIC fixed-target program and/or future at experiments, like FAIR, will be necessary to establish the presence of critical behaviour and provide insights into the nature of correlations in HICs [172]. Despite these indications, no conclusive statement on the CEP existence/location has been made so far.

[8] The baseline refers to the reference expectation for fluctuation observables, namely, the cumulants of net-particle multiplicity distributions—under non-critical physicals conditions. This is typically obtained either from simpler systems like proton-proton collisions or from non-critical models by assuming that proton and anti-proton multiplicities follow simple statistics such as Poisson or binomial. The evaluation of the baseline is essential to identify anomalous (or critical) behaviour in the data.

Chapter 3

The Strong Interaction

> *As usual when you discover something new, the response comes in three waves. First, this is nonsense. Second, this is trivial. Third, this is important, and we did it before you did.*
>
> – Freeman J. Dyson[1]

In this chapter, we begin with a short review of the historical background leading to the acceptance of quantum chromodynamics as the theory of the strong force. Next, we analyse its Lagrangian and symmetries. Finally, we discuss the confinement problem and explore how lattice gauge theories can probe strongly coupled regimes. We also outline the limitations of this approach, present recent results, and motivate the use of effective field theories as an alternative framework.

3.1 Historical Background

Our familiarity with the accurate predictions of quantum field theory in describing fundamental interactions, makes it easy to overlook the theoretical and philosophical challenges that early physicists faced. Examining the stages of their approach — including the confusions and proposals along the way — offers valuable insight into our ongoing quest for ever more refined theories.

In this section, we briefly review the steps that led to the success of quantum field theory and the emergence of our current theory of the strong interaction.

3.1.1 Beginnings

During the early 1960s, particle physics witnessed rapid experimental progress, with new discoveries emerging regularly. However, this surge in experimental data was not matched by

[1] In *The Prisoner's Dilemma,* https://www.ias.edu/ideas/2012/dyson-prisoners-dilemma

theoretical advances. Among the four known fundamental interactions, only gravity and electromagnetism were well understood, while the forces governing the nucleus remained poorly described [176].

The discovery of the neutron [177] established that nuclei consist of neutrons and protons, and pointed to the presence of a fundamental interaction that overcomes the electromagnetic repulsion between protons, thereby holding the nucleons together — the strong nuclear force. In 1935, Yukawa proposed that the nuclear force could be described by the exchange of a spinless particle between nucleons — a meson [178]. Following Yukawa, different non-relativistic potential models were developed: Woods Saxon-potential [179], Paris potential [180], Bonn potential [181]. Within this framework, a decent description of the nuclear structure was possible, and phenomena such as the α-decay or stellar structure could be understood.

Experimentally, it had become possible for collisions at relativistic regimes, but the use of non-relativistic potentials was inappropriate to cover these. Early attempts to construct a perturbative field theory, based on local interactions of Yukawa type employing pion and nucleon fields, could not handle the large coupling constants that appeared in calculations. Moreover, with the discovery of new particles, it became clear that there was nothing so special about the nucleon or the pion [182].

Quantum field theory was originally developed for a quantised treatment of the electromagnetic field. **Quantum electrodynamics** (QED) successfully explained features such as the Lamb shift and the anomalous magnetic momentum of the electrons. In the case of the weak interactions, Fermi's four-fermion interaction provided an accurate phenomenological theory of β-decay by means of perturbation theory. In spite of the early successes of field theory, the renormalisation procedure — required to obtain physical meaningful results — was questioned about its logical consistency and physical interpretation [183]. Landau and Pomeranchuk [184] claimed that QED was inconsistent, given the appearance of poles in the ultraviolet region (**Landau pole**), and that this phenomena would occur in all field theories [185].

The ***S*-matrix theory** and **bootstrap models** emerged as alternative theoretical frameworks to field theory in order to describe the strong interaction. This approach was based on the assumption of the existence of a unique S-matrix that obeyed principles such as unitarity and analyticity, without the need for a fundamental microscopic Hamiltonian or equations of motion [186]. In order to deal with the increasing number of new found resonances "Nuclear Democracy" [187] was proclaimed: all particles were equally fundamental, existing as dynamical bound states of each other.

3.1.2 Quark Model

The search for a classification scheme for the increasing number of stable hadrons and resonances begin in the 1950's [188–190]. Experimental results showed that many hadrons shared similar masses, charges, and other quantum numbers, suggesting an underlying structure. The introduction of the new quantum number *strangeness* and the success of the **Nishijima–Gell-**

Mann formula [191,192] indicated the existence of a larger symmetry that extended the isospin symmetry, known to be a very good symmetry of the strong force.

The discovery of the "**Eightfold Way**" by Gell-Mann [193] and Ne'eman [194] allowed for a more fundamental interpretation of the Nishijima–Gell-Mann and the mass pattern of the baryons and mesons. In this model, the isospin symmetry, $SU(2)$, and *strangeness*, $U(1)$ were embedded in a larger group $SU(3)$, representing a much more predictive symmetry: the *flavour* symmetry, $SU(3)_f$. The $SU(3)_f$ symmetry was found to be only approximately conserved by the strong interaction, implying that the meson and baryon spectra do not form exactly degenerate multiplets of this group.

Gell-Mann [195] and Zweig [196] pointed out that the observed hadronic spectrum could be understood on the assumptions that these particles are bound states built from three different types, or flavours, of a more fundamental constituent named by **quarks**: *up*, *down* and *strange*. The baryonic spectrum could be reproduced if baryons were composed of three quarks, while the spectrum of the mesons indicated that only two (a quark-antiquark pair) were required. A remarkable success of the $SU(3)_f$ quark model was the prediction, including the mass, of the baryon $\Omega^- = |sss\rangle$, later experimentally observed [197].

In 1969, Björken [198] showed that if nucleons contained more fundamental point-like constituents, the cross section of scattering experiments should obey scaling laws in the deep-inelastic region. **Deep inelastic scattering** (DIS) experiments at SLAC (Stanford Linear Accelerator) confirmed the appearance of scaling, providing evidence for the existence of quarks [199].

3.1.3 Colour Space

The early quark model faced various difficulties after its introduction:

- **Spin-statistic problem.** Consider the state

$$\left|\Omega^-(J^P = 3/2^+)\right\rangle = |sss\rangle\,|\uparrow\uparrow\uparrow\rangle\,, \tag{3.1}$$

  for which the wave-function can be factorized as

$$\Psi_{\Omega^-} = \psi_{\text{space}}\psi_{\text{spin}}\psi_{\text{flavour}}, \tag{3.2}$$

  the product of wave-functions in the space, spin and the internal flavour-$SU(3)$ symmetry. The flavour-spin component is completely symmetric under the exchange of quarks and/or spins, and the spatial component of the wave-function is symmetric in the ground state ($L = 0$). Thus Ψ_{Ω^-} is symmetric. This violates the Pauli principle, which states that the wave-function for fermions must be anti-symmetric.

- **Momentum balance in DIS.** The momentum sum rule of the proton constituents was

expected to be +1. However, the integration.

$$\int_0^1 \mathrm{d}x \, \Big(x[u(x) + \bar{u}(x) + d(x) + \bar{d}(x) + s(x) + \bar{s}(x)]\Big) \approx 0.5, \tag{3.3}$$

as remarked in [200], indicating that besides quarks there must exist another (neutral) constituent in the proton.

- **Neutral pion decay.** The electromagnetic decay rate of $\pi^0 \to \gamma\gamma$ predicted by the quark model was only 1/9 of the experimentally observed value.

To compensate the missing half of the proton momentum a new bosonic neutral particle was introduced: the **gluon**. With the additional gluon distribution function $g(x)$ the sum rule becomes

$$\int_0^1 \mathrm{d}x \, \Big(x[u(x) + \bar{u}(x) + d(x) + \bar{d}(x) + s(x) + \bar{s}(x) + g(x)]\Big) = 1, \tag{3.4}$$

Following Greenberg [201], Bogoluybov, Struminsky, Tavkhelidze [202], Han and Nambu [203] and Miyamoto [204], Fritzsch Gell-Mann and Bardeen [205] a new quantum number called *colour* solved several of the remaining problems above. Each quark is described by a *red (r)*, *green (g)*, *blue (b)* quark, and the three colours can be transformed by the exact colour-$SU(3)$ symmetry, $SU(3)_c$. The decay rate is nine times larger with coloured quarks agreeing with experiments [205]. Additionally, the quark wave-function of the Ω^- baryon acquires the colour-space function,

$$\psi_{\text{colour}} = \frac{1}{\sqrt{6}}(rgb - rbg + brg - bgr + gbr - grb), \tag{3.5}$$

which is anti-symmetric under the exchange of two quarks, and a colour singlet, since colour exists as an intrinsic property of hadrons. Thus, Ψ_{Ω^-} is factorised as

$$\Psi_{\Omega^-} = \psi_{\text{space}}\psi_{\text{spin}}\psi_{\text{flavour}}\psi_{\text{colour}}. \tag{3.6}$$

In 1972, Gell-Mann and Fritzsch formulated the colour symmetry as a gauge group attempting to understand the empirical observation that coloured quarks appear confined, but never in a free state. They proposed that quarks would interact by the exchange of gauge bosons (gluons) in a colour octet. This gauge theory was called QCD [206].

3.1.4 Asymptotic Freedom

The work on the renormalisability of Yang-Mills theory by t'Hooft [207] re-introduced the interest on non-Abelian gauge theories to the physics community. Kenneth Wilson revived the renormalisation group approach [208], first introduced by Stueckelberg and Petermann [209], clarifying many misunderstandings related to the renormalisation program in field theory.

After the successful description of the electroweak force by Glasgow [210], Salam [211] and Weinberg [212], the Yang-Mills theory was seen to provide a natural framework to construct fundamental interactions mediated by vector bosons. Yet, no field theory was able to describe

the scaling behaviour observed at SLAC in 1969.

The coupling constant, that sets the strength of a given interaction, changes at different energy scales. This variation — the running of the coupling constant — can be understood by means of the renormalisation group approach. For a non-Abelian gauge theory, the coupling satisfies the following **renormalisation group equation** (RGE):

$$\beta(\alpha_s) \equiv \mu_R^2 \frac{\mathrm{d}\alpha_s(\mu_R^2)}{\mathrm{d}\mu_R^2} = -(b_0\alpha_s^2 + b_1\alpha_s^3 + \dots), \tag{3.7}$$

where $\beta(\alpha)$ encodes the dependence of the coupling parameter α_s with an (unphysical) renormalisation energy scale μ_R, and b_0, b_1, are refereed to as 1-loop and 2-loop β-function coefficients, respectively. In many theories, such as QED, the β-function is positive, meaning that the coupling increases with the energetic scale. For example, the fine-structure constant is at the energy of 100 GeV about 10% larger than at much lower energies.

Already in 1965, V. Vanyashin and M. Terentyev [213] found a negative sign in the charge renormalisation of charged vector mesons, which in terms of the $SU(2)$ gauge field theory implied that the β-function was negative at 1-loop. They regarded this result as "absurd" and attributed the cause to the non-renormalisability of the theory. In 1969, Khriplovich [214] correctly computed the β-function for the $SU(2)$ Yang-Mills theory. Again, β was found to be negative and he concluded that the interaction is weaker at short distances.

In 1973, D. Gross and F. Wilczek [215] and, independently, D. Politzer [216] computed the 1-loop β-function for the non-Abelian Yang-Mills theory up to 1-loop corrections. They planned to prove that local field theory could not explain scaling, meaning that field theory was not an appropriate framework to describe the strong force. First, they demonstrated that the vanishing of the effective coupling at short distances — **asymptotic freedom** — was required to explain scaling. Second, they would show that no asymptotically free field theory existed [182].

The non-Abelian nature of QCD requires that not only quark 1-loops must be considered, but also the contribution from the self-interaction of gluons (see Fig. 3.1). The quark 1-loop will give rise to a positive contribution to the β-function (**screening**) while the contribution from 1-loop gluon diagrams will be negative (**anti-screening**).

(a) (b)

Figure 3.1: Quark (a) and gluon (b) 1-loop diagrams contributing to the QCD β-function. (Drawn with *JaxoDraw* [2].)

The solution of the 1-loop RGE obtained in [215,216] for the $SU(3)$ Yang-Mills theory reads

$$\alpha_s(\mu_R^2) = \frac{1}{b_0 \ln\left(\frac{\mu_R^2}{\Lambda_{\rm QCD}^2}\right)}, \quad b_0 = \frac{1}{12\pi}(33 - 2n_f), \tag{3.8}$$

where n_f is the number of quark flavours. Here, $\Lambda_{\rm QCD}$ is the so-called **QCD scale parameter**. It is a constant of integration, which defines the energy range where the non-perturbative dynamics starts to dominate, and the (perturbatively defined) coupling diverges.

From (3.8), as long as, the number of observed flavours obeys

$$n_f < \frac{33}{2}, \tag{3.9}$$

the β-function is negative. Thus, the coupling constant decreases with increasing energy scales ($\alpha_s \to 0$, for $\mu_R^2 \to \infty$), meaning that the interaction between quarks becomes weaker at short distances and they behave as almost free particles. Asymptotic freedom is a unique feature of non-Abelian gauge theories that explains this scaling behaviour at small distances. Demonstrating this property was a milestone in the search for a dynamical theory of hadrons, and the acceptance of QCD as the theory of strong interactions quickly permeated the scientific community.

Conversely, at larger distances the coupling becomes so strong that isolating a quark from a hadron is impossible, since it is energetically more favourable to create a quark-antiquark pair. This mechanism is known as **confinement**. Confinement is confirmed in LQCD calculations [217], but it has not yet been derived rigorously from first principles [218]. A more detailed discussion of the confinement phenomenon is presented in Sec. 3.3.

3.2 QCD Lagrangian

In this section, we analyse the QCD Lagrangian with a special focus on its symmetries. We examine the requirement for gauge invariance and explore the implications of chiral symmetry breaking. Additionally, we provide a brief overview of the $U(1)_A$ problem and the topological structure characteristic of non-Abelian theories. A summary of the internal continuous symmetries is presented in Table 3.1.

3.2.1 Gauge Symmetry

Yang–Mills Lagrangians are constructed to be invariant under gauge transformations. This built-in symmetry reflects the gauge principle, which requires that conserved quantities are maintained not only globally but also locally. In other words, a conserved charge cannot vanish at one location and reappear at another without an ordinary notion of continuity; any movement of charge must be accompanied by an corresponding current. **Noether's theorem** formalizes this idea by linking local symmetries to conservation laws. Therefore, the Lagrangian must

remain invariant under gauge transformations that depend arbitrarily on space and time, a requirement that constrains the form of interactions between fields.

The Lagrangian of QCD is based on the $SU(3)$ Yang-Mills theory:

$$\mathcal{L} = \bar{\psi}^i_\alpha \left(i\gamma^\mu D_\mu - m_\alpha\right) \delta_{ij} \psi^j_\alpha - \frac{1}{4} G^a_{\mu\nu} G^{\mu\nu}_a - \theta\omega, \tag{3.10}$$

where α is the quark-flavour index from 1 to N_f (*up*, *down*, *strange*, *charm*, ...). In most cases only the lightest quarks will be considered ($N_f = 3$). The index a is the colour index in adjoint representation from 1 to $N_c^2 - 1$, while i and j refer to the colour indices in the fundamental representation from 1 to N_c.

Matter Field Term

The first term in (3.10) encloses the dynamical and mass term of quark fields, ψ^i_α. Under the requirement of gauge invariance, the quark fields may transform in the fundamental representation as

$$\psi(x) \longrightarrow U(x)\psi(x), \tag{3.11}$$

where $U(x) = \exp(i\alpha^a(x)T_a) \in SU(3)_c$. Similarly, to maintain local gauge invariance, the ordinary partial derivative is replaced by the covariant derivative, which incorporates the gauge fields into the theory

$$D_\mu = \partial_\mu - i g_s A^a_\mu T_a, \tag{3.12}$$

guaranteeing that $D_\mu\psi(x)$ transforms homogeneously (covariantly),

$$D_\mu\psi(x) \longrightarrow U(x) D_\mu \psi(x), \quad U(x) \in SU(3)_c \tag{3.13}$$

similarly to ψ. Here, the (gluon) gauge field is given by a multiplet of vector fields, $A_\mu = A^a_\mu T_a$ on the Minkowski space where T_a is a local orthonormal basis in the Lie algebra of $SU(3)_c$, defined as

$$T_a = \frac{\lambda_a}{2}, \tag{3.14}$$

in which λ_a are the 3×3 **Gell-Mann matrices** satisfying

$$\lambda_a = \lambda_a^\dagger, \qquad \mathrm{Tr}(\lambda_a \lambda_b) = 2\delta_{ab}. \tag{3.15}$$

The Gell-Mann matrices act on the colour indices and define the correspondent Lie algebra through the commutation relations

$$[\lambda_a, \lambda_b] = 2i f_{abc} \lambda_c, \tag{3.16}$$

where f_{abc} are the (real and anti-symmetric) structure constants.

In a more geometric sense, the covariant derivative introduces an additional structure —

namely, a connection — on a manifold that allows us to compare fields at different points, even when these fields are expressed in different local phases. This connection defines a rule for parallel transport, ensuring that the derivative remains consistent with the local gauge symmetry of the theory.

Pure Yang-Mills Term

Naturally, the presence of gauge fields leads us to consider an additional interaction term. This is expressed with the second term in (3.10), which represents the **pure Yang-Mills** part of the Lagrangian. The local components of gluon field strength tensor, $G_{\mu\nu} = G^a_{\mu\nu} T_a$, are given by

$$G^a_{\mu\nu} = \partial_\mu A^a_\nu - \partial_\nu A^a_\mu + g_s f_{abc} A^b_\mu A^c_\nu, \tag{3.17}$$

where, g_s is the strong coupling constant of the quark-gluon interaction, related with α_s by $g_s^2 = 2\pi\alpha_s$. In contrast to QED, where the gauge group is Abelian, U(1), and the structure constants vanish ($f_{abc} = 0$) — implying that the photon fields commute — the non-Abelian nature of QCD's $SU(3)$ symmetry introduces an additional term in the gluon field strength tensor (3.17). This extra term is responsible for the self-interaction of the gluonic fields. When the QCD Lagrangian (3.10) is expanded using (3.17), it naturally produces three-gluon and four-gluon vertex interactions (see Fig. 3.2).

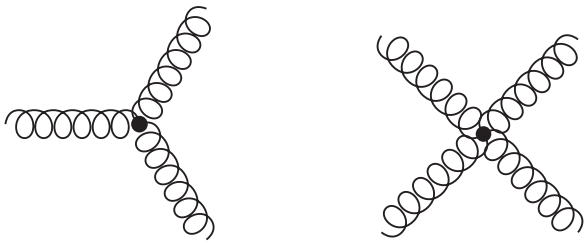

(a) (b)

Figure 3.2: Three-gluon (a) and four-gluon (b) vertices illustrating the self-coupling inherent in non-Abelian QCD. (Drawn with *JaxoDraw* [2].)

The gluon fields transform in the adjoint representation following the gauge transformation law

$$A_\mu \longrightarrow U(x)\left(A_\mu - \frac{1}{ig_s}\partial_\mu\right)U^\dagger(x), \tag{3.18}$$

such that $G_{\mu\nu}$ transforms homogeneously under the gauge action:

$$G_{\mu\nu} \longrightarrow U(x) G_{\mu\nu} U^\dagger(x), \tag{3.19}$$

ensuring that the pure Yang-Mills part is gauge invariant.

For completeness, it should be noticed that the inclusion of a mass term for gauge fields,

$$M^2 A_\mu A^\mu, \tag{3.20}$$

would violate gauge invariance explicitly. For this reason, gauge bosons must be massless. Indeed, this is known to be the case for photons. On the other hand, the $W^{\pm}, Z^0$ bosons, that mediate the electroweak interactions, carry a non-vanishing mass. The reasons for this is due to the breaking of the $SU(2)$ symmetry that describes these bosons by the **Higgs mechanism**.

CP-Violating Term

The last term in (3.10) corresponds to a charge-parity (CP) violation term. The ***CP*-symmetry** states that the laws of physics must remain the same even if a particle is changed by its anti-particle while inverting its spatial coordinates. In 1964, the **Fitch-Cronin experiment** showed that weak interactions violate this symmetry [219].

The constant θ is called the **vacuum angle**, while the **winding number density** ω, is given by

$$\omega = \frac{g_s^2}{32\pi^2} G^a_{\mu\nu} \tilde{G}^{\mu\nu}_a, \tag{3.21}$$

with $\tilde{G}^{\mu\nu}_a = \frac{1}{2}\varepsilon^{\mu\nu\rho\sigma} G_{a,\rho\sigma}$ the dual of the field strength. Currently, there is no reason for θ to be vanishingly small or QCD to preserve CP-symmetry, and so, from a gauge invariance point of view, the last parity-violating term can be included in (3.10). A non-zero θ should give rise to a neutron electric dipole momentum. Current experiments set an upper bound of $|\theta| < 10^{-10}$ [220], meaning that CP-violation does not have a considerable impact in most circumstances. Neither the θ-term played a significant role on the development of QCD. Explaining the smallness of θ despite the large amount of CP-violation in the weak sector is the so-called **strong *CP*-problem**.

In far from equilibrium situations, θ may acquire a non-zero value (locally) corresponding to pseudo-scalar condensation, meaning that the CP-violation by the strong force could be possibly detected in relativistic heavy-ion collision [221, 222]. Furthermore, the topological susceptibility, defined by [223]

$$\chi_t \equiv \frac{1}{4} \left\langle \left(\varepsilon^{\mu\nu\rho\sigma} G^a_{\mu\nu} G_{a\,\rho\sigma} \right) \left(\varepsilon^{\alpha\beta\gamma\delta} G^b_{\alpha\beta} G_{b,\gamma\delta} \right) \right\rangle, \tag{3.22}$$

is non-vanishing and related with the η' meson mass by the **Witten-Veneziano relation** [224, 225],

$$\chi_t = \frac{F_\pi^2}{12} (m_\eta^2 + m_{\eta'}^2 - 2m_K^2), \tag{3.23}$$

where F_π is the pion decay constant. So, if $\varepsilon^{\mu\nu\rho\sigma} G^a_{\mu\nu} G_{a\,\rho\sigma}$ had no effect then $\chi_t = 0$ and the mass of η' would be small. Thus, the in-medium $m_{\eta'}$ mass could provide information about the topological structure of the QCD-vacuum.

3.2.2 Flavour Symmetry

An important (approximate) symmetry of the Lagrangian (3.10) is related to the flavour space. Since the gauge part of (3.10) is not sensitive to the flavour sector, we can focus on the fermionic terms.

The spinors can be projected into two chiral sectors,

$$\psi_R = \frac{1+\gamma_5}{2}\psi, \quad \psi_L = \frac{1-\gamma_5}{2}\psi, \tag{3.24}$$

where ψ_R, ψ_L are commonly called **right-handed** and **left-handed** fields, respectively. Thus, the fermionic part can then be decomposed as

$$\bar{\psi}(i\gamma^\mu D_\mu - m)\psi = \psi_R i\gamma^\mu D_\mu \psi_L + \psi_L i\gamma^\mu D_\mu \psi_R - \psi_R m\psi_L + \psi_L m\psi_R, \tag{3.25}$$

where the colour and flavour indices were suppressed to simplify the notation. The mass matrix m acts on the flavour space, and its form will depend on the choice of the quark fields basis. If each chiral field is independently transformed as

$$\psi_R \longrightarrow V_R\psi_R, \quad \psi_L \longrightarrow V_L\psi_L, \tag{3.26}$$

where $V_R, V_L \in U(N_f)$, thus, it is always possible to replace

$$m \longrightarrow V_R^\dagger m V_L, \tag{3.27}$$

such that the matrix m is diagonal and its eigenvalues are real, non-negative and ordered as $0 \leq m_u \leq m_d \leq \cdots \leq m_t$, i.e.,

$$m = \begin{pmatrix} m_u & & \\ & m_d & \\ & & \ddots \end{pmatrix}. \tag{3.28}$$

In the limit of massless flavours (**chiral limit**), the right- and left-handed components are completely disconnected from each other, forbidding any mixing between ψ_R and ψ_L in the Lagrangian. This means that for massless quarks, the Lagrangian of QCD is invariant under the following symmetry transformations,

$$U(N_f)_R \times U(N_f)_L \simeq SU(N_f)_R \times SU(N_f)_L \times U(1)_V \times U(1)_A. \tag{3.29}$$

The Noether's currents associated with these symmetries are (up to a sign)

$$J_R^{\mu,\alpha} = \bar{\psi}_R\gamma^\mu t^\alpha \psi_R, \quad J_L^{\mu,\alpha} = \bar{\psi}_L\gamma^\mu t^\alpha \psi_L, \tag{3.30}$$

where t^α, with $\alpha = 1, \ldots, N_f^2 - 1$, form a basis of the $SU(N_f)$ Lie algebra. The generators of the group transformations (charges) are obtained by

$$\begin{aligned} Q_{R/L}^\alpha &= \int \mathrm{d}^3x \; J_{R/L}^{0,\alpha}(x) \\ &= \int \mathrm{d}^3x \; \bar{\psi}_{R/L}\gamma^0 t^\alpha \psi_{R/L}. \end{aligned} \tag{3.31}$$

Instead of these charges one often uses the combinations

$$Q_V^\alpha = Q_R^\alpha + Q_L^\alpha, \quad Q_A^\alpha = Q_R^\alpha - Q_L^\alpha, \tag{3.32}$$

corresponding to the vector and axial-vector transformations, respectively.

Chiral Symmetry

The first component in (3.29), the $SU(N_f)_R \times SU(N_f)_L$ symmetry group, is the so-called **chiral symmetry**. The implications of this symmetry on the hadronic spectrum were first studied by Nambu [226]. At low energies, there is a small energy gap: the smallest eigenvalue spectrum of the Hamiltonian is the pion with $m_\pi \approx 135$ MeV which is small compared to the mass of the proton, $m_p \approx 938$ MeV. Nambu pointed out that this is a consequence of the dynamical breaking of the chiral symmetry due to the strong interaction; chiral symmetry is not manifest in the low energy hadron spectrum regime.

By definition, symmetry breaking occurs if the charge that generates the symmetry transformation does not annihilate the ground state (vacuum). In the case of chiral symmetry, the generator of the axial transformation, Q_A^α, this means that [227]

$$Q_A^\alpha |\Omega\rangle \neq 0, \tag{3.33}$$

where $|\Omega\rangle$ is the vacuum. If condition (3.33) is satisfied, vacuum is said to be degenerate. More precisely, we should say that $Q_A^\alpha |\Omega\rangle$ does not exist in Hilbert space, because its norm is infinite [228]. The same definition can be expressed in a different form: there must exist some operator such that

$$\langle\Omega| [Q_A^\alpha, \mathcal{O}] |\Omega\rangle \neq 0, \tag{3.34}$$

which, again, expresses that symmetry generated by the charge Q_A^α is spontaneously broken in the vacuum. The expectation value above can thus be used as order parameter, since it would be zero if $|\Omega\rangle$ was a singlet. The simplest form for the operator is

$$\mathcal{O} = \bar{\psi} t^\alpha \psi, \tag{3.35}$$

implying that the **chiral condensate** $\left\langle \bar{\psi}\psi \right\rangle$ can be used as an order parameter,

$$\left\langle \bar{\psi}\psi \right\rangle = \left\langle \bar{\psi}_L \psi_R + \bar{\psi}_R \psi_L \right\rangle \neq 0. \tag{3.36}$$

The chiral condensate is invariant under the $SU(N_f)_V$ transformations generated by Q_V^β. Thus, when chiral symmetry is broken by $\left\langle \bar{\psi}\psi \right\rangle \neq 0$, the symmetry group is reduced as

$$SU(N_f)_R \times SU(N_f)_L \longrightarrow SU(N_f)_V, \tag{3.37}$$

in which $SU(N_f)_V$ is related to the **isospin conservation**. This symmetry is, however, only

approximate in nature, because quarks have different masses. It is almost respected in the two flavour case ($m_u \approx m_d$), but severely broken when including the *strange* quark[2].

According to **Goldstone's theorem** [229], the spontaneous breaking of a continuous global symmetry leads to the emergence of massless scalar fields, known as **Nambu-Goldstone bosons** (NG bosons). The number of NG bosons is given by the dimension of the coset manifold G/H, where G is the original symmetry group and H is the subgroup under which the vacuum remains invariant. In the case of chiral symmetry, $G = SU(N_f)_L \times SU(N_f)_R$ and $H = SU(N_f)_V$, leading to $\dim(G/H) = N_f^2 - 1$ NG bosons. For the three light quarks ($N_f = 3$), this corresponds to the eight mesons in the pseudo-scalar octet.

Although these mesons share the quantum numbers of NG bosons, they are not massless and are instead classified as ***pseudo*-NG bosons**. This mass arises because the quark masses are non-zero, meaning the QCD Lagrangian (3.10) is only approximately chiral symmetric, causing the NG bosons to acquire a finite mass.

The quark masses appearing in (3.10) are not the masses of free quarks but rather those inside hadrons. Due to asymptotic freedom, these masses depend on the energy scale: they are large at low momentum scales and decrease at high momentum scales. Since quarks are confined and do not exist as asymptotic (physical) states, their masses cannot be directly measured through scattering processes. Consequently, quark masses are not observables in QCD and lack direct physical meaning. Therefore, when discussing quark masses, it is crucial to specify the renormalisation scheme and scale used. The most common choice in QCD perturbation theory is the modified minimal subtraction ($\overline{\text{MS}}$) scheme at a renormalisation scale of $\mu \approx 2$ GeV. Quark masses can be determined using techniques such as chiral perturbation theory, QCD sum rules, or lattice QCD simulations[3].

The $\mathbf{U(1)_A}$ Anomaly

Apart from the chiral symmetry, the QCD Lagrangian (3.10) also exhibits the $U(1)_V \times U(1)_A$ symmetry. The $U(1)_V$ part corresponds to the **conservation of baryon number** which is remains unbroken except in the colour-superconductor phase at asymptotically high density [230]. On the other hand, the symmetry breaking of the $U(1)_A$ symmetry should imply the existence of an additional massless boson due to the NG theorem. The lightest meson in the iso-singlet pseudo-scalar meson is the η' particle with a mass of $m_{\eta'} \approx 935$ MeV, that is too heavy to be the NG boson. In fact, for the η' meson to be the expected NG boson, it would have to satisfy $m_{\eta'} < \sqrt{3} m_{\pi^0}$ [231]. Why the η' meson is so heavy and why the NG bosons corresponding to the axial $U(1)$ symmetry is missing is known as the $\mathbf{U(1)_A}$ **problem** or the $\boldsymbol{\eta - \eta'}$ **puzzle**.

[2]For a long time, it was believed that the strong force strictly conserves isospin symmetry. This would imply that $m_u = m_d$, meaning that the mass difference between protons and neutrons would be solely due to the electromagnetic interaction. Since the electromagnetic self-energy of the proton is larger than that of the neutron, one would expect the proton to be heavier than the neutron, which is not the case. Thus, even if the electromagnetic interaction is "turned off," the quark masses must differ.

[3]Consult the section *Quark Masses* in [35] for more details.

The solution to the $U(1)$ problem comes from the fact that the axial vector current associated with this symmetry is **anomalous**. In other words, an extra term appears in the conservation law for the singlet axial current,

$$\partial_\mu J_A^\mu = 2i\,\bar{\psi}(m\gamma_5)\psi + \frac{g_s^2}{16\pi^2}\,\varepsilon^{\mu\nu\rho\sigma}\,G^a_{\mu\nu}\,G_{a\,\rho\sigma}, \tag{3.38}$$

which arises to cancel ultraviolet divergences. Even in the chiral limit ($m \to 0$), the axial current is not conserved.

It is important to note that the anomalous term in (3.38) can be written as a total derivative,

$$\varepsilon^{\mu\nu\rho\sigma}\,G^a_{\mu\nu}\,G_{a\,\rho\sigma} = \partial_\mu K^\mu, \quad \text{with} \quad K^\mu = \varepsilon^{\mu\nu\rho\sigma}\left(A^a_\nu\,G^a_{\rho\sigma} - \frac{1}{3}g_s f^{abc}\,A^a_\nu\,A^b_\rho\,A^c_\sigma\right), \tag{3.39}$$

where K^μ is the **Chern-Simons current**. One might expect that, as a total derivative, the anomaly would vanish at the space-time boundaries, rendering the η particle as light as the pions. However, because K^μ is not gauge-invariant, the necessary boundary conditions for partial integration are not satisfied. Consequently, the existence of a light pseudo-scalar cannot be inferred.

The resolution of the $U(1)$ problem is intimately connected with the topological structure of non-Abelian interactions. In fact, a topologically non-trivial, localised gauge configuration, as described in [232], exhibits a fixed value for the integral

$$\int \mathrm{d}^4x\,\partial_\mu K_\mu = \frac{32\pi^2}{g_s^2}, \tag{3.40}$$

indicating that the corresponding Chern-Simons term cannot be gauged away and does not vanish at infinity. Such localised gauge configurations in space and time are known as **instantons**. As demonstrated by 't Hooft [233, 234], instantons give rise to interactions that explicitly break the axial $U(1)$ symmetry, thereby preventing the existence of an additional Goldstone boson. Moreover, the contributions from instantons account for a significant fraction of the masses of the η and η' mesons, explaining their large mass values.

Symmetry	Transformation	Current	Realisation
$U(1)_V$	$\psi \to e^{-i\varepsilon}\psi$	$J_\mu = \bar{\psi}\gamma_\mu\psi$	Baryon number conservation (conserved)
$U(1)_A$	$\psi \to e^{-i\gamma_5\varepsilon}\psi$	$J_\mu = \bar{\psi}\gamma_\mu\gamma_5\psi$	$U(1)_A$ problem (anomalous)
$SU(N_f)_V$	$\psi \to e^{-i\theta^\alpha t_\alpha}\psi$	$J^\alpha_\mu = \bar{\psi}\gamma_\mu t^\alpha\psi$	*Eightfold Way* (approximate)
$SU(N_f)_A$	$\psi \to e^{-i\gamma_5\theta^\alpha t_\alpha}\psi$	$J^\alpha_\mu = \bar{\psi}\gamma_\mu\gamma_5 t^\alpha\psi$	Nambu-Goldstone bosons (spontaneously broken)
$SU(3)_c$	$\psi \to e^{-i\theta^a T_a}\psi$	$J^a_\mu = \bar{\psi}\gamma_\mu T^a\psi$	Colour charge conservation (conserved)

Table 3.1: Summary of internal continuous symmetries in QCD. Here, T_a denote the eight generators of the $SU(3)_c$ (colour) Lie algebra, while t_a form the basis of the $SU(N_f)$ (flavour) Lie algebra.

3.3 The Confinement Problem

The property of asymptotic freedom in QCD allows for a quantitative understanding of the strong force at large energy scales using a perturbative approach. In the low-energy (infrared) regime, however, the increasing coupling strength invalidates perturbative methods. Non-perturbative techniques are therefore required to address the observational fact that quarks and gluons do not appear as isolated, asymptotic states. As mentioned above, this phenomenon is commonly referred to as confinement.

Defining confinement precisely is challenging because its interpretation can vary with context. One common approach is to identify confinement with the presence of a linearly rising potential between a static quark-antiquark pair. Yet, if confinement were defined solely by a potential that increases indefinitely with separation, QCD would not qualify as confining since, at sufficiently large distances, quark-antiquark pair production causes the potential to flatten.

Another common definition identifies confinement with the absence of colour-charged asymptotic states, implying that only colour-singlet states are physical — referred to as **colour confinement**. While this definition is consistent with the general intuition behind confinement, it encounters conceptual challenges in the context of gauge-Higgs theories.

In this class of theories, two distinct phases can be identified. One phase exhibits a linearly rising potential between quarks, which eventually saturates due to vacuum polarisation effects; this phase is commonly referred to as the *confinement-like* phase, as it closely resembles the behaviour observed in QCD. The other phase, in contrast, lacks these features, with quark interactions being entirely short-ranged and of Yukawa type; this is known as the *Higgs-like* phase.

However, as demonstrated in Refs. [235, 236], it is always possible to trace a path between any two points in the phase diagram along which all local gauge-invariant observables, as well as their products, vary analytically. This observation implies that a discontinuous transition from

a colour-singlet spectrum in the confinement-like region to a colour non-singlet spectrum in the Higgs-like region is discarded. Consequently, if confinement is defined solely in terms of colour neutrality, gauge-Higgs theories would necessarily also qualify as confining.

In this work, the confining phase is identified by the unbroken status of the so-called centre symmetry. The meaning and significance of this symmetry will be elaborated in Ch. 5.

When dealing with strongly interacting (non-perturbative) systems, several methods can be employed, each with its own theoretical and practical challenges. For example, the DSEs lead to an infinite tower of coupled integral equations, which must be truncated or approximated in practical applications (see, e.g., [223,237–241]). Functional renormalization group methods offer another powerful approach by solving a hierarchy of differential flow equations for the Green's or vertex functions of the system (see, e.g., [242]). However, the most widely used method for studying QCD in the non-perturbative regime is lattice gauge theory. Given the importance of LQCD results at low energies, a brief introduction to this method is provided in the following section.

3.3.1 LQCD at Zero Temperature

The lattice gauge theory[4] approach was developed in 1974 by Wilson [243] while developing a mechanism for total confinement of quarks. In his proposal, gauge and matter fields are described on a discrete lattice Euclidean space-time. This discretisation naturally regularizes the theory in the ultraviolet by introducing a cutoff, $\Lambda = 1/a$, where a is the lattice spacing. Calculations in lattice gauge theory are typically performed using the path-integral formulation of quantum field theory.

There are two main reasons for employing an Euclidean rather than a Minkowski description:

- **Numerical stability.** The oscillatory factor $\exp(iS)$ in the Minkowski path integral is replaced by $\exp(-S^E)$ in the Euclidean formulation, where S^E corresponds to the Euclidean action, which is real and bounded from below. This transformation allows $\exp(-S^E)$ to be interpreted as a Boltzmann factor, facilitating the use of standard computational techniques from statistical mechanics and providing better numerical stability, especially for Monte Carlo integration[5];

- **Preservation of symmetry.** In four-dimensional Euclidean space-time, a discrete subgroup of the $SO(4)$ symmetry is preserved by the lattice. In contrast, a lattice formulation of Minkowski space does not retain any remnant of the $SO(3,1)$ symmetry because the non-compact nature of $SO(3,1)$ (due to the Lorentz boosts) cannot be accommodated by a finite lattice.

The transformation from Minkowski to Euclidean space is carried out via the so-called **Wick rotation**,

$$t \longrightarrow i\tau, \tag{3.41}$$

[4] For a more detailed introduction to the formalism and numerical methods, see [217].
[5] For a focused discussion on Monte Carlo methods in quantum field theory, see [244].

where τ denotes the Euclidean time coordinate. Any fields defined in the Minkowski space are replaced by an equivalent field which is a function of the Euclidean variable x_μ, for $\mu = 0, 1, 2, 3$. As mentioned above, the Euclidean action is obtained by transforming $iS \to -S^E$. Moreover, since the Lorentz group is replaced by the rotation group in four dimensions the Euclidean γ-matrices, γ_μ^E are required to satisfy the algebra

$$\{\gamma_\mu^E, \gamma_\nu^E\} = 2\delta_{\mu\nu}, \tag{3.42}$$

where $\gamma_i^E = -i\gamma_i$ and $\gamma_0^E = \gamma_0$ (cf. App. A.2 for more details).

The transition from the continuum to the lattice is straightforward. Space-time coordinates are replaced by points on the lattice, specified by a tuple of four integer numbers $n \equiv (n_1, n_2, n_3, n_4)$, where, by convention, the last value denotes the Euclidean time component. Thus,

$$x_\mu = n_\mu a. \tag{3.43}$$

Moreover, each variable is scaled by the lattice spacing a to their canonical dimension. Matter fields $\psi(n)$ reside on the lattice sites. Gauge transformations can also be incorporated in a discrete space-time lattice, where a matter field transforms similarly to the continuum case (see (3.11)),

$$\hat{\psi}(n) \longrightarrow U(n)\hat{\psi}, \tag{3.44}$$

where $U(n) = \exp\left(i\alpha^a(n)T_a\right)$ is defined separately on each site, and the superscript on each field indicates that these are dimensionless quantities.

The formulation of gauge theories on a finite lattice demands that gauge invariance must be satisfied. The naive straightforward approach of starting with the gauge invariant fermionic action and discretise it, would led to violation of gauge invariance at higher orders of the lattice spacing, that is, gauge invariance is not satisfied in a lattice framework by directly discretising the covariant derivative, D_μ.

Instead of adding a vector field, such as in the continuum formulation, in order to compare fields at different lattice sites in a gauge invariant way[6] a lattice version of the so-called Wilson line is defined connecting neighbouring sites.

In the continuum, the **Wilson line** is defined by[7]

$$W_P(x, y) = \mathcal{P} \exp\left(ig \int_y^x A_\mu^a(z) T_a \, \mathrm{d}z^\mu\right), \tag{3.45}$$

along the path P from y^μ and x^μ. Here, $\mathcal{P}$ is the **path-ordering operator**, necessary for non-Abelian groups since the group generators at different points do not commute. Under local

[6] See the final paragraph in the *Matter field term* part in subsection 3.2.1.

[7] The Wilson line can be defined in any representation using $A_\mu^a T_a^R$, but to keep our treatment simple we restrict to the fundamental representation.

gauge transformations, the Wilson line is required to transform as

$$W_P(x,y) \longrightarrow U(x)W_P(x,y)U^{-1}(y), \tag{3.46}$$

where $U(x)$ and $U(y)$ are elements of $SU(N)$. From transformation laws (3.11) and (3.46) it is easy to see that the combination $\bar{\psi}(x)W_P(x,y)\psi(y)$ is gauge invariant.

In particular, if $x = y$, we obtain a contour integral named **Wilson loop**

$$W_P^{loop} = \mathrm{Tr}\left\{\mathcal{P}\exp\left(ig\oint_P A_\mu^a(z)T_a\ \mathrm{d}z^\mu\right)\right\}, \tag{3.47}$$

where the trace, given its cyclic properties, was introduced to preserve gauge invariance.

On the lattice, the discrete version of the Wilson line is straightforward. A new field $W_\mu(n)$ is defined with a transformation law similar to (3.46),

$$W_\mu(n) \longrightarrow U(n)W_\mu(n))U^{-1}(n+\hat{\mu}), \tag{3.48}$$

where $\hat{\mu}$ denotes a vector of norm a pointing along the μ direction. Again, it is clear that the product $\bar{\psi}(n)W_\mu(n)\psi(n+\hat{\mu})$ is gauge invariant. As previously said, the $W_\mu(n)$ field can be thought to live between neighbouring lattice sites. For this reason, $W_\mu(n)$ are often called **link variables** or **link fields**. It is also convenient to define

$$W_{-\mu}(n) = W_\mu^\dagger(n-\hat{\mu}). \tag{3.49}$$

To reproduce the results in the continuum, when one takes the limit $a \to 0$ (**continuum limit**), we write

$$W_\mu(n) = \exp\left(igaA_\mu^a(n)T_a\right). \tag{3.50}$$

On the lattice, the path ordered exponential (3.45) becomes a product of link variables along a path connect any two sites,

$$W_P(n,m) = \prod_{\ell\in P} W_\ell, \tag{3.51}$$

where W_ℓ denotes a link variable on the path P connecting site n and m. Thus, the Wilson loop reads

$$W_P^{loop}(n,m) = \mathrm{Tr}\prod_{\ell\in C} W_\ell, \tag{3.52}$$

with P some closed path on the lattice. From the transformation property (3.48) any closed loop of link variables is a gauge invariant object. Of particular importance, the smallest (non-trivial) loop that can be constructed is the unit square. This object is called a **plaquette** and it is defined by

$$W_{\mu\nu}(n) \equiv W_\mu(n)W_\nu(n+\hat{\mu})W_\mu^\dagger(n+\hat{\nu})W_\nu^\dagger(n). \tag{3.53}$$

The importance of the Wilson loop, when attempting to understand confinement, becomes

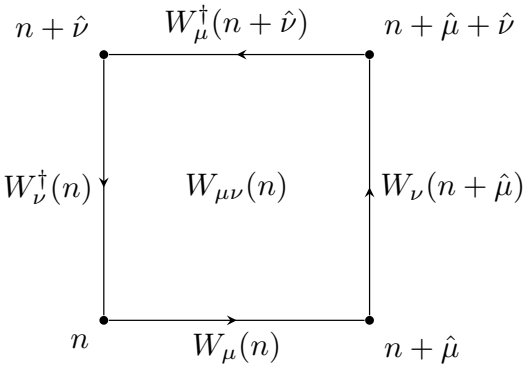

Figure 3.3: The plaquette $W_{\mu\nu}(n)$ with base at n lying in the $\mu\nu$-plane.

clear if one computes its expectation values. As demonstrated by Brown and Weisberger [245] the static potential $V(r)$ between a heavy quark and antiquark pair, separated by a relative distance r, can be obtained from the expectation value of the Wilson loop $W_P^{loop}(r,t)$ as

$$\left\langle W_P^{loop}(r,t)\right\rangle \approx \exp(-V(r)t) + \ldots, \tag{3.54}$$

where P is a rectangular loop with spatial extent r and temporal extent t, and the ellipses denote contributions from excited states. Thus, $V(r)$ can be obtained from studying the limit

$$V(r) = \lim_{t\to\infty} V(r,t) = \ln\left(\frac{\langle W(r,t)\rangle}{\langle W(r,t+1)\rangle}\right). \tag{3.55}$$

Excited-state contributions and the explicit t-dependence are exponentially suppressed at large Euclidean time; consequently $V(r)$ can be extracted from the plateau that develops in $V(r,t)$ for fixed r as $t\to\infty$.

Further generalisations to include spin-dependent relativistic correction were first made by Eichten and Feinberg [246]. Alternative derivations have been carried out subsequently by Peskin [247], Gromes [248], Barchielli, Montaldi and Prosperi [249, 250]. A more detailed treatment of all derivations involved can be found in [251].

In the limit of infinitely heavy quarks, early lattice simulations, without including effects from dynamical quark fields (called the **quenched approximation**), shows that QCD predicts the static inter-quark potential to rise linearly for increasing quark-antiquark displacement (see, e.g., Fig. 3 in Ref. [252]). This linear behaviour supports a **flux-tube** picture of confinement: for small quarks separation, asymptotic freedom predicts that the chromoelectric and chromomagnetic fields should spread out in space leading to a Coulomb-like potential. On the other hand, for a large separation these colour electric and magnetic fields are squeezed into narrow flux tubes connecting the quark-antiquark pair and increasing the energy in the potential. Moreover, the flux-tube picture provides an explanation why mesons resonances are observed to follow (approximately) a linear relation between the angular momentum and the mass-squared, the

so-called **Regge trajectories** [253]. This relation can be predicted if the quark-antiquark pair behaves as a string-like object; the formation of a flux-tube offers a possible answer how a string-like object emerges from QCD. The presence of flux-tube structure was supported by various studies, more recently in [254].

An infinite amount of energy is required to separate quarks to an infinite distance. Yet, what is observed, e.g. in meson decay, is the formation of new quark-antiquark pairs. Thus, for sufficiently large quark separations the flux-tube or QCD string must break because it is energetically more favourable to produce a new quark-antiquark pair; then quarks are never seen as isolated asymptotic states. This process is called **hadronisation** or **string breaking** which translates into a flattening or saturation of the quark potential into two meson masses. String breaking can be observed in LQCD simulations when dynamical quark fields are included which screen the colour field of the static quark. See Refs. [254, 255] for recent results.

The dynamics responsible for flux-tube formation, and the mechanism underlying confinement, remain open questions that have been the subject of intensive study in recent years. Various mechanisms have been proposed (see Ref. [218] for an overview). Moreover, the question of the deconfinement transition cannot be separated from any proposed picture of confinement: any viable mechanism should also be able to accommodate deconfinement.

One promising class of proposals uses the topological structure of the QCD vacuum and, in particular, the percolation of centre vortices [256, 257]. Centre vortices are closed two-dimensional surfaces in four-dimensional spacetime that carry topological charge. Several recent studies have explored their role in non-perturbative QCD [258–261]. The removal of vortices from lattice configurations has been reported to destroy multiple non-perturbative features: for example, the infrared enhancement of the gluon propagator at low momenta — which distinguishes the non-perturbative regime from the perturbative one — disappears in vortex-removed configurations, suggesting a loss of confinement [259, 262–264]. Similarly, vortex removal has been observed to produce degeneracies in the hadron spectrum, consistent with a restoration of chiral symmetry [265].

Despite these encouraging results, and until non-Abelian gauge theories can be solved analytically, the mechanism of confinement will remain a subject of active debate and investigation.

3.3.2 LQCD at Finite Temperature

At zero temperature, numerical calculations from LQCD simulations provide a strong support that QCD accounts for quark confinement. The natural question arises whether quark confinement prevails at high temperature and/or density.

As discussed in the previous chapter, LQCD calculations have shown that the transition from hadronic matter to a deconfined quark–gluon plasma at $\mu_B = 0$ is an analytic, smooth crossover [51], occurring at a pseudo-critical temperature of approximately $155-158$ MeV [43,44]. This smooth behaviour is reflected in bulk thermodynamic quantities such as the internal energy and entropy. Figure 3.4 illustrates this behaviour for full LQCD simulations with $(2 + 1)$-

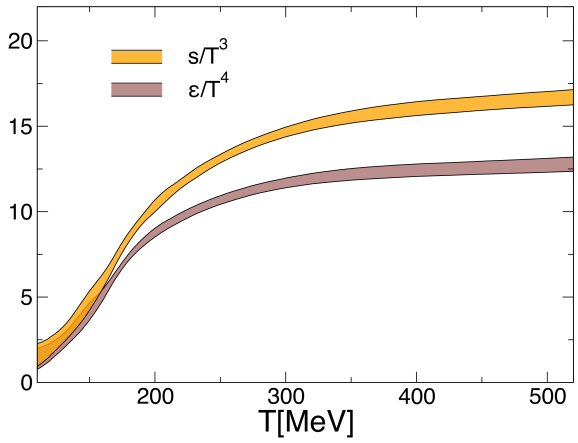

Figure 3.4: Entropy and energy densities, normalised by appropriate powers of T, as functions of temperature from $(2+1)$-flavour LQCD simulations. The bands represent continuum-extrapolated results, with their widths indicating the associated systematic uncertainties. Figure adapted from Ref. [3].

flavour dynamical quarks. In contrast to results obtained in the pure Yang–Mills case (see, e.g., Ref. [266]), both the energy and entropy densities vary continuously with increasing temperature, a characteristic feature of a crossover transition. Notably, the effective number of physical degrees of freedom increases rapidly within the temperature range $\lesssim 100$ MeV, signalling the liberation of colour degrees of freedom. Further details can be found in Ref. [3] and references therein.

Although finite temperature simulations are achievable, direct exploration of systems at high μ_B using LQCD simulations are constrained to small baryon densities due to the infamous **fermion sign problem**: the presence of a non-zero chemical potential leads to a complex fermion determinant for real chemical potential. Since the determinant enters in the $\exp(-S)$ factor when computing correlation on some observable, the usual Monte Carlo techniques cannot be employed because this factor cannot be interpreted as a Boltzmann weight factor due to the requirement of being positive. Several strategies have been adopted to extrapolate from zero or imaginary chemical potentials, such as analytic continuation or expanding the partition function using a Taylor series around $\mu_B = 0$ [267–271].

Nevertheless, the above extrapolation techniques tend to be limited by non-analyticities and may break at higher order terms of the expansion.[8] An alternative approach is to use an effective field theory of QCD that describes (at least, qualitatively) the behaviour of hadronic and quark matter for large chemical potentials while at the same time avoids the highly demanding computations of LQCD simulations. In the present work, this approach will be adopted.

[8] A recent review of some of the extrapolation techniques used in LQCD is made in [272].

3.3.3 Effective Models

What is an effective theory[9]? The basic idea of effective fields theories is to approximate the original (full) Lagrangian by a simpler effective Lagrangian composed only of the active light degrees of freedom, which may not necessarily correspond to the elementary particles. The effective Lagrangian is only valid at a chosen energy scale and may be of a non-renormalisable theory. Nevertheless, loop-diagrams can be included and physical results can be obtained.

The separation of heavy from light degrees of freedom relies on two fundamental ideas. First, the **decoupling theorem** (or **Appelquist–Carazzone theorem** [274]) states that the effects of heavy fields enter the low-energy theory only through renormalisable constants or through non-renormalisable effective interactions that are suppressed by powers of the heavy particle mass. Second, the renormalization group approach developed by Wilson [275] provides a systematic method to separate degrees of freedom above and below a chosen energy scale, effectively integrating out short-distance effects leaving an effective field theory for the light degrees of freedom.

Both the Standard Model and General Relativity are examples of effective field theories. The Standard Model, despite being renormalisable, is expected to break down at the gravitational energy scale and does not account for phenomena such as neutrino masses. On the other hand, General Relativity, non-renormalisable, is believed to be the low-energy effective theory emerging from a more fundamental theory of quantum gravity. In a broader sense, all current theories can be viewed as effective theories, valid only up to a defined energy scale.

An effective field Lagrangian should be constructed in order to match predictions from the full theory and results from experiment, as well as the symmetries of the full Lagrangian. In particular, an effective theory of QCD should highlight the approximate chiral symmetry and a mechanics for its spontaneous breaking [276].

[9] For an general introduction to the theme of effective field theories see [273].

Chapter 4

Thermal Quantum Field Theory

In this house, we obey the laws of thermodynamics!

– Homer Simpson, *The Simpsons*

The study of extreme environments characterized by high temperature and/or density requires extending the conventional zero-temperature QFT formalism to a finite-temperature (and, when relevant, finite-density) framework. Such in-medium field theories play a central role in particle and nuclear physics, as well as in cosmology. The pioneering work was carried work by Matsubara [277] within a non-relativistic context. Extensions to a relativistic framework were later developed by Fradkin [278], Bernard [279], Weinberg [280], Dolan and Jackiw [281].

Thermal field theory admits two largely complementary formulations — real-time and imaginary-time — but here we concentrate exclusively on the latter[1]. This formalism is constructed by assuming thermal equilibrium from the outset, and by exploiting the formal analogy between the Boltzmann operator $e^{-\beta H}$ appearing in thermal expectation values and the time-evolution operator of zero-temperature QFT. This framework is ideally suited for computing static, bulk thermodynamic observables.

In this chapter we begin with a review of quantum statistical mechanics and then develop the Matsubara (imaginary-time) formalism. We introduce the mean-field approximation — which will be employed throughout this work — and derive the grand-canonical potential of a Dirac gas in a self-consistent mean-field background.

4.1 Quantum Statistical Mechanics

In this section we review basic definitions in statistical mechanics. The derivation and interpretation of the full equilibrium density matrix is given.

[1] For a comprehensive review of the real-time and the imaginary-time approaches, see [282].

4.1.1 Statistical Ensembles

An **ensemble** is an idealisation composed of a large (or even infinite) number of virtual copies of a system, which represents a possible state of the real system. In other words, since tracking the exact micro-state of a system is not always possible, a set of many copies of the system, each with a different micro-state but all sharing the same macro-constraints, in which the system could be is considered in a probabilistic way. Observable quantities are then computed as ensemble averages. Three common ensembles can be identified:

- **Microcanonical ensemble.** Describes an isolated system of fixed energy, volume and particle number, where each micro-state has exactly the same energy.
- **Canonical ensemble.** Describes a closed system in contact with a heat reservoir with which can exchange energy. Temperature, volume and particle number is fixed, and the probability of micro-state i with energy E_i is

$$p_i = \frac{1}{Z} e^{-E_i/T}, \tag{4.1}$$

  where Z is the canonical ensemble partition function.
- **Grand-canonical ensemble.** Describes a system that can exchange both energy and particles. In this ensemble temperature, volume and chemical potential μ are fixed quantities. The probability of micro-state i with energy E_i and particle number N_i is given by

$$p_i = \frac{1}{\mathcal{Z}} e^{-(E_i - \mu N_i)/T}, \tag{4.2}$$

  where $\mathcal{Z}$ is the grand-canonical partition function.

In a relativistic quantum system, where particles can be created and destroyed, it becomes convenient to make use of the grand-canonical ensemble to compute observables. For that reason we shall focus on using this type of ensemble throughout this work.

4.1.2 Density Operator and the Partition Function

The primary objects of interest in zero-temperature QFT are the elements of the scattering or **S-matrix** related to vacuum expectation values of a set of time-ordered operator through the **Lehmann–Symanzik–Zimmerman reduction** (LSZ) (see e.g [223, 283]). These operators act on the vacuum to produce asymptotic states of particles in infinitely early and late times ($t \to \pm\infty$). From a quantum mechanical point of view, the vacuum state can be seen as a pure state, and expectation values can be constructed from pure states, only accounting for quantum fluctuations.

In a medium, statistical fluctuations emerge and the asymptotic states become only statistically specified[2]. For that reason, we are interested in averaging the rates of the processes over

[2]Furthermore, the presence of a thermal bath induces random interactions which do not preserve any state;

initial (or final) states with the corresponding probabilities. If the medium is composed by initial state $|i\rangle$ with weights $p_i(t)$ at time t, the expectation value of an observable $\mathcal{O}$, combining both quantum and statistical fluctuations, is defined by

$$\langle \mathcal{O}(t) \rangle \equiv \sum_i \langle i|\mathcal{O}|i\rangle \, p_i(t). \tag{4.3}$$

The above expression can also be re-written in terms of the **density operator**, defined as

$$\boldsymbol{\rho}(t) = \sum_i p_i(t) \, |i\rangle \, \langle i| \, , \tag{4.4}$$

where the unit-norm state $|i\rangle$ form an orthonormal basis and p_i is the probability of finding the state $|i\rangle$ in the ensemble (e.g. by (4.2)). Thus, (4.3) is equivalently defined as

$$\langle \mathcal{O}(t) \rangle = \mathcal{Z}^{-1} \mathrm{Tr} \left(\boldsymbol{\rho}(t) \mathcal{O}(t) \right), \tag{4.5}$$

where the normalisation parameter $\mathcal{Z}$, given by

$$\mathcal{Z} = \mathrm{Tr} \, \boldsymbol{\rho}, \tag{4.6}$$

defines the grand-canonical partition function.

In order to evaluate the expectation value of $\mathcal{O}$ at some later time t' ($t' > t$), the **time-evolution operator** $U(t')$ is applied:

$$\boldsymbol{\rho}(t') = U(t') \boldsymbol{\rho}(t) U^\dagger(t'), \quad U(t') = e^{-iH(t'-t)}, \tag{4.7}$$

where H is the Hamiltonian of the system and it has been abbreviated $U(t') \equiv U(t', t)$ and $U^\dagger(t') \equiv U(t, t')$. Then $\langle \mathcal{O}(t') \rangle$ reads

$$\langle \mathcal{O}(t') \rangle = \mathrm{Tr} \left(\boldsymbol{\rho}(t) U^\dagger(t') \mathcal{O}(t') U(t') \right), \tag{4.8}$$

in which the cyclic property of trace has been used.

That $\boldsymbol{\rho}(t)$ satisfies the time-evolution equation,

$$i \frac{\mathrm{d}\boldsymbol{\rho}}{\mathrm{d}t} = [H, \boldsymbol{\rho}], \tag{4.9}$$

is easy to verify. If the thermal equilibrium of the system is assumed, $\boldsymbol{\rho}$ must be independent of time, meaning that $[H, \boldsymbol{\rho}] = 0$. Thus, the density operator must be a function of operators $\mathcal{O}_i$ that commute with the Hamiltonian for all $i = 1, 2, \ldots,$

$$\boldsymbol{\rho} = \boldsymbol{\rho}(\mathcal{O}_1, \mathcal{O}_2, \ldots), \quad [H, \mathcal{O}_i] = 0; \tag{4.10}$$

namely, the asymptotic states, in which particles would be free of scattering interaction. Thus, the LSZ reduction formula cannot be applied to separate the asymptotic states from the space-time region where interaction takes place [282, 284].

namely, $\mathcal{O}_i$ are conserved quantities. More can be said about $\boldsymbol{\rho}$ if $\mathcal{O}_i$ are additively conserved quantities, such as energy, momentum and conserved charges in general. In that case, any $\mathcal{O}_i$ can be expressed as the direct sum of conserved quantities for the subsystems I, II, ...,

$$\mathcal{O}_i = \mathcal{O}_i^{(\mathrm{I})} + \mathcal{O}_i^{(\mathrm{II})} + \dots . \tag{4.11}$$

This property is necessary in order that the usual macroscopic thermodynamic limit can be taken. Moreover, $\boldsymbol{\rho}$ can be decomposed as the product

$$\boldsymbol{\rho} = \boldsymbol{\rho}^{(\mathrm{I})} \times \boldsymbol{\rho}^{(\mathrm{II})} \times \dots , \tag{4.12}$$

for each subsystem. The only function of $\mathcal{O}_i$ satisfying both (4.11) and (4.12) is the exponential[3],

$$\boldsymbol{\rho} = \frac{1}{\mathcal{Z}} e^{-c_i \mathcal{O}_i}, \tag{4.13}$$

where c_i are constants, and $\mathcal{Z}$ is given by

$$\mathcal{Z} = \mathrm{Tr}\, e^{-c_i \mathcal{O}_i}, \tag{4.14}$$

obtained by applying the identity $\mathrm{Tr}\,\boldsymbol{\rho} = 1$. Additionally, $\mathcal{O}_i$ are required to be Hermitian.

When special relativity is considered, the conserved quantities are the four-momentum P_μ, boost and rotations given by the generator of the Lorentz group $J_{\mu\nu}$, and a set of charges Q_a related to continuous internal symmetry groups of the system. Thus, the density operator reads

$$\boldsymbol{\rho} = \mathcal{Z}^{-1} \exp\left(-c_\mu P^\mu - c_{\mu\nu} J^{\mu\nu} - c_a Q_a\right). \tag{4.15}$$

Since boost, J_{0i}, do not commute with the Hamiltonian, the general density operator in (4.15) does not describe a system at equilibrium.

Useful information about $\langle P^\mu \rangle$ and $\langle J^{\mu\nu} \rangle$ can be obtained from $\boldsymbol{\rho}$ by considering a proper Lorentz transformation[4] $x^\mu \to \Lambda^\mu_{\ \nu} x^\nu$ with corresponding unitary operator $U(\Lambda)$ on the Hilbert space. Thus, $\boldsymbol{\rho}$ transform as

$$\begin{aligned}
\boldsymbol{\rho} \longrightarrow U(\Lambda)\boldsymbol{\rho}U^\dagger(\Lambda) &= \mathcal{Z}^{-1} \exp\left(-c_\mu U(\Lambda) P^\mu U^\dagger(\Lambda) - c_{\mu\nu} U(\Lambda) J^{\mu\nu} U^\dagger(\Lambda) - c_a U(\Lambda) Q_a U^\dagger(\Lambda)\right) \\
&= \mathcal{Z}^{-1} \exp\left(-\Lambda^\mu_{\ \alpha} c_\mu P^\alpha - c_{\mu\nu} \Lambda^\mu_{\ \alpha} \Lambda^\nu_{\ \beta} J^{\alpha\beta} - c_a Q_a\right) \\
&= \mathcal{Z}^{-1} \exp\left(-\Lambda^\alpha_{\ \mu} c_\alpha P^\mu - \Lambda^\alpha_{\ \mu} \Lambda^\beta_{\ \nu} c_{\alpha\beta} J^{\mu\nu} - c_a Q_a\right),
\end{aligned} \tag{4.16}$$

where the indices have been re-labelled in the last expression. Therefore, applying a Lorentz

[3] Notice that repeated indices correspond to a summation.

[4] Here, a proper Lorentz transformation is defined by $\Lambda^0_{\ 0} \geq 1$ and $\det \Lambda = 1$.

transformation on $\boldsymbol{\rho}$ is equivalent to transform

$$c_\mu \longrightarrow \Lambda_\mu^{\ \alpha} c_\alpha \quad \text{and} \quad c_{\mu\nu} \longrightarrow \Lambda_\mu^{\ \alpha} \Lambda_\nu^{\ \beta} c_{\alpha\beta}. \tag{4.17}$$

Thus, since P^μ is a vector and $J^{\mu\nu}$ a rank-two tensor, Lorentz covariance implies that

$$\langle P^\mu \rangle = f_1 c^\mu + f_2 c^{\mu\alpha} c_\alpha, \quad \langle J^{\mu\nu} \rangle = f_3 c^{\mu\nu}, \tag{4.18}$$

with f_1, f_2 and f_3 functions of the Lorentz invariant quantities c_a, $c_\mu c^\mu$, $c_{\mu\nu} c^{\mu\nu}$, $c_{\mu\nu} c^\nu c_\alpha c^{\mu\alpha}$. As mentioned above, boost transformations do not commute with the Hamiltonian. Thus, an equilibrium system requires that $c_{0j} = 0$, so (4.18) becomes

$$\langle P^\mu \rangle = f_1 c^\mu + f_2 c^{\mu j} c_j, \quad \left\langle J^{ij} \right\rangle = f_3 c^{ij}; \tag{4.19}$$

in particular, the spatial components of P^μ give

$$\left\langle P^i \right\rangle = f_1 c^i + f_2 c^{ij} c_j. \tag{4.20}$$

From the two expression above, it can be seen that setting $c^i = 0$ corresponding to having a system with vanishing average momentum. Moreover, if $c^{ij} = 0$, the system has a null average angular momentum. In this work angular momentum will not be considered, and so we shall follow our discussion having set $c^{ij} = 0$; then,

$$\boldsymbol{\rho} = \mathcal{Z}^{-1} \exp\left(-c_\mu P^\mu - c_a Q_a\right). \tag{4.21}$$

The convergence of the trace in the property $\operatorname{Tr} \boldsymbol{\rho} = 1$ implies that $c_0 > 0$ and $c_i c_i < c_0^2$. To better see this, the exponential argument in (4.21) can be expanded as

$$-c_\mu P^\mu = -c_0 E(P^i) + c_i P^i. \tag{4.22}$$

where energy $E(P^i) \approx |P^i|$ at large momentum (so mass can be neglected). Now, as $|P^i| \to \infty$, the exponent behaves as $-|P^i| \left(c_0 - |c_i| \cos\theta\right)$: if $c_0 > |c_i|$, then the Boltzmann weight decays fast enough to make the trace convergent for every direction θ, even for vanishing charges; on the other hand, if $c_0 \leq |c_i|$ there are directions in the space of states where the exponent fails to go to $-\infty$, and does not converge. Thus, there must exist a Lorentz transformation that moves to the rest-frame of the system where $c^\mu = (c^0, 0, 0, 0)$ and $P^i = 0$. Let $c^0 \equiv \beta = 1/T$ and $c_a \equiv -\beta \mu_a$. Therefore, the rest-frame equilibrium density operator in the absence of angular momentum contributions is

$$\boldsymbol{\rho} = \mathcal{Z}^{-1} \exp\left(-\beta \left(H - \mu_a Q_a\right)\right), \tag{4.23}$$

with

$$\mathcal{Z} = \mathrm{Tr} \exp\left(-\beta\left(H - \mu_a Q_a\right)\right), \tag{4.24}$$

as often encountered in the literature. The inverse temperature (β) and the chemical potentials (μ_a) variables can be thought as Lagrange multipliers, constraining the evolution of the system with time. While β determines the mean energy of the system, μ_a is related to the conservation of some charge, e.g. a set of number operators (baryonic number, electric charge, isospin, ...).

Notice that, applying (4.23) when computing $\langle\mathcal{O}\rangle$ in (4.3) (or (4.5)) yields the correct results at zero-temperature QFT:

$$\langle\mathcal{O}\rangle = \mathcal{Z}^{-1} \sum_i e^{-\beta(E_n - \mu_i Q_i)} \langle i|\, \mathcal{O}\, |i\rangle, \tag{4.25}$$

and, by taking the limit $\beta \to \infty$ ($T \to 0$), we recover the zero-temperature case result $\langle\mathcal{O}\rangle = \langle\Omega|\mathcal{O}|\Omega\rangle$, where $|i=0\rangle \equiv |\Omega\rangle$ is the interacting ground-state.

It will also be useful to define (up to an irrelevant constant) the **grand-canonical potential**:

$$\Omega = -\frac{T}{V} \ln \mathcal{Z}(\beta), \tag{4.26}$$

where V denotes volume.

The partition function (or equivalently, the density matrix) is the most important function in thermodynamics and statistical mechanics, as it allows to extract all the thermodynamics properties of the system. For example, in the infinite volume limit, pressure P, particle density ρ_i, entropy density s, and energy density ϵ can be obtained by [283, 285]

$$P = \frac{\partial\left(T \ln \mathcal{Z}\right)}{\partial V} = -\frac{\partial(V\Omega)}{\partial V}, \tag{4.27a}$$

$$\rho_i = \frac{1}{V}\frac{\partial\left(T \ln \mathcal{Z}\right)}{\partial \mu_i} = -\frac{\partial\Omega}{\partial \mu_i}, \tag{4.27b}$$

$$s = \frac{1}{V}\frac{\partial\left(T \ln \mathcal{Z}\right)}{\partial T} = -\frac{\partial\Omega}{\partial T}, \tag{4.27c}$$

$$\epsilon = -P + Ts + \mu_i \rho_i. \tag{4.27d}$$

4.1.3 The Matsubara Formalism

There are two main approaches to QFT: the method of second quantisation and the method of functional integrals. Although both methods should lead to the same conclusions, function integrals have become more convenient for dealing with a variety of situations, such as non-perturbative phenomena. For this reason, this approach is widely adopted in lattice gauge theory. Here, the path-integral method will be used to study the effects of temperature and/or density in QFT.

Connection to Imaginary-Time

In order to write a functional integral representation of the density operator and partition function, we move our focus to Eq. 4.8. Writing it in the field basis[5]

$$\langle \mathcal{O}(t') \rangle = \sum_{i,j,k,\ell} \langle \varphi_i | U(t') | \varphi_j \rangle \, \rho_{jk} \, \langle \varphi_k | \, U^\dagger(t') \, | \varphi_\ell \rangle \, \mathcal{O}_{i\ell}, \tag{4.28}$$

where $\rho_{jk} = \langle \varphi_j | \boldsymbol{\rho} | \varphi_k \rangle$ and $\mathcal{O}_{\ell i} = \langle \varphi_\ell | \mathcal{O} | \varphi_i \rangle$. The functional integral representation of the matrix elements of the time-evolution operator (up to an irrelevant normalisation constant) reads [283]

$$\begin{aligned} \langle \varphi_i | U(t') | \varphi_j \rangle &= \left\langle \varphi_i | e^{-iH(t'-t)} | \varphi_j \right\rangle \\ &= \int \mathrm{D}\pi_a \int_{\varphi_a(t,\mathbf{x})=\varphi_j}^{\varphi_a(t',\mathbf{x})=\varphi_i} \mathrm{D}\varphi_a \exp\left\{ i \int_t^{t'} \mathrm{d}t \int \mathrm{d}^3x \, (\mathcal{L} + \mu_a \mathcal{Q}_a(\pi_a, \varphi_a)) \right\}, \end{aligned} \tag{4.29}$$

where π denotes the conjugate momentum, $\mathcal{H}$ is the Hamiltonian density, $\mathcal{Q}_a$ are conserved charge densities (if present), and $\mathcal{L}$ is the Lagrangian density, which related with the Hamiltonian density by the Legendre transformation,

$$\mathcal{L} = \pi \frac{\partial \varphi}{\partial t} - \mathcal{H}. \tag{4.30}$$

The integration measures on φ and π are defined as

$$\mathrm{D}\varphi = \prod_{t,\mathbf{x}} \mathrm{d}\varphi(t,\mathbf{x}), \quad \mathrm{D}\pi = \prod_{t,\mathbf{x}} \frac{\mathrm{d}\pi(t,\mathbf{x})}{2\pi}. \tag{4.31}$$

The conjugate momentum π can be obtain from the Lagrangian density by

$$\pi = \frac{\partial \mathcal{L}}{\partial(\partial\varphi/\partial_t)}, \tag{4.32}$$

In the case of $\mathcal{H}$ has a quadratic, linear and/or constant term with respect to π, the integral over π can be computed as a Gaussian integral. Since this is commonly the case for physical theories of interest we will assume it to be true through this work. Integrating over π, one obtains the Lagrangian path-integral representation of (4.29)

$$\langle \varphi_i | U(t') | \varphi_j \rangle = \left\langle \varphi_i | e^{-iH(t'-t)} | \varphi_j \right\rangle = \int_{\varphi_a(t,\mathbf{x})=\varphi_j(\mathbf{x})}^{\varphi_a(t',\mathbf{x})=\varphi_i(\mathbf{x})} \mathrm{D}\varphi_a \; e^{iS[\varphi_a]}, \tag{4.33}$$

where the action S is given in terms of the Lagrangian density $\mathcal{L}$ by

$$S[\varphi_a] = \int_t^{t'} \mathrm{d}t \int \mathrm{d}^3x \; \left(\mathcal{L}(\varphi, \partial_\mu \varphi) + \mu_a \mathcal{Q}_a \right). \tag{4.34}$$

[5] Here, φ denotes a generic field (bosonic or fermionic); the discussion does not depend explicitly on its spin or Lorentz indices.

Identically, we obtain for the other matrix element

$$\left\langle \varphi_k | U^\dagger(t') | \varphi_\ell \right\rangle = \left\langle \varphi_k | e^{iH(t'-t)} | \varphi_\ell \right\rangle = \int_{\varphi_b(t,\mathbf{x})=\varphi_\ell(\mathbf{x})}^{\varphi_b(t',\mathbf{x})=\varphi_k(\mathbf{x})} \mathrm{D}\varphi_b \; e^{iS[\varphi_b]}. \tag{4.35}$$

Therefore, the expectation value in (4.28) becomes

$$\langle \mathcal{O}(t') \rangle = \sum_{i,j,k,\ell} \int_{\varphi_a(t,\mathbf{x})=\varphi_j(\mathbf{x})}^{\varphi_a(t',\mathbf{x})=\varphi_i(\mathbf{x})} \mathrm{D}\varphi_a \int_{\varphi_b(t,\mathbf{x})=\varphi_\ell(\mathbf{x})}^{\varphi_b(t',\mathbf{x})=\varphi_k(\mathbf{x})} \mathrm{D}\varphi_b \; e^{i(S[\varphi_a]-S[\varphi_b])} \rho_{jk} \mathcal{O}_{li}. \tag{4.36}$$

The matrix element ρ_{jk} can also be expressed in a functional integral representation. From the thermal equilibrium density operator obtained in (4.23) one can readily recognised the resemblance to the time-evolution operator in (4.33) by considering an imaginary-time variable,

$$\tau = it, \tag{4.37}$$

and identifying the interval $[t, t']$ with $[0, \beta]$. This transformation forms the essence of the **Matsubara formalism** [277]. The transformation from real-time to imaginary-time is known as **Wick rotation**, and it allow us to study relativistic field theories in Minkowski space from a related construction in Euclidean space, where techniques of statistical mechanics can be employed. However, in this transformation, one needs to be careful not to cross any pole singularity.

Therefore, using the Matsubara formalism, the density operator in functional form reads

$$\rho_{jk} = \mathcal{Z}^{-1} \int \mathrm{D}\pi_E \int_{\varphi_E(0,\mathbf{x})=\varphi_k(\mathbf{x})}^{\varphi_E(\beta,\mathbf{x})=\pm\varphi_j(\mathbf{x})} \mathrm{D}\varphi_E \; e^{-S_E[\pi_E,\varphi_E]} = \mathcal{Z}^{-1} \int_{\varphi_E(0,\mathbf{x})=\varphi_k(\mathbf{x})}^{\varphi_E(\beta,\mathbf{x})=\pm\varphi_j(\mathbf{x})} \mathrm{D}\varphi_E \; e^{-S_E[\varphi_E]}, \tag{4.38}$$

and the partition function (4.24) is

$$\mathcal{Z} = N \int \mathrm{D}\pi_E \int_{\varphi_E(0,\mathbf{x})=\varphi_j(\mathbf{x})}^{\varphi_E(\beta,\mathbf{x})=\pm\varphi_j(\mathbf{x})} \mathrm{D}\varphi_E \; e^{-S_E[\pi_E,\varphi_E]} = \int_{\varphi_E(0,\mathbf{x})=\varphi_j(\mathbf{x})}^{\varphi_E(\beta,\mathbf{x})=\pm\varphi_j(\mathbf{x})} \mathrm{D}\varphi_E \; e^{-S_E[\varphi_E]}, \tag{4.39}$$

where N is a normalisation constant, and the integration over π_E was taken under the condition discussed above. Here, S_E denotes the Euclidean action equivalent of (4.34) given by

$$S_E[\pi_E, \varphi_E] = \int_0^\beta \mathrm{d}\tau \int \mathrm{d}^3x \; \left(i\pi_E \frac{\partial \varphi_E}{\partial \tau} - \mathcal{H}_E + \mu_a \mathcal{Q}_a \right), \tag{4.40}$$

or, if π_E was integrated out,

$$S_E[\varphi_E] = \int_0^\beta \mathrm{d}\tau \int \mathrm{d}^3x \; \left(\mathcal{L}_E + \mu_a \mathcal{Q}_a \right). \tag{4.41}$$

The field at $\tau = \beta$ is equal to $\pm\varphi_j$, where the upper sign enforces *periodic boundary conditions* and the lower one an *anti-periodic boundary condition*. As we shall see in a moment, the former condition will be applied to bosons, while the latter to fermions.

Thermal Green's Function and Matsubara Frequencies

An important set of expectations values to compute are the Green's functions of the theory. In finite-temperature QFT, one can define the so-called **thermal Green's functions** or n-point correlation function of the theory for a generic field operator $\Phi(\mathbf{x}, \tau)$ by

$$\langle \mathcal{T} \left(\Phi(\tau_1, \mathbf{x}_1) \dots \Phi(\tau_n, \mathbf{x}_n) \right) \rangle \equiv \sum_i \langle i | \mathcal{T} \left(\Phi(\tau_1, \mathbf{x}_1) \dots \Phi(\tau_n, \mathbf{x}_n) \right) | i \rangle \,, \tag{4.42}$$

or in trace form,

$$\langle \mathcal{T} \left(\Phi(\tau_1, \mathbf{x}_1) \dots \Phi(\tau_n, \mathbf{x}_n) \right) \rangle = \mathcal{Z}^{-1} \mathrm{Tr} \left\{ \boldsymbol{\rho} \mathcal{T} \left(\Phi(\tau_1, \mathbf{x}_1) \dots \Phi(\tau_n, \mathbf{x}_n) \right) \right\} . \tag{4.43}$$

Here $\mathcal{T}$ denotes the **imaginary-time ordering operator**, that acts as (in analogy to the real-time case)

$$\mathcal{T} \left(\Phi(\tau_1, \mathbf{x}_1) \Phi(\tau_2, \mathbf{x}_2) \right) = \begin{cases} \phi(\tau_1, \mathbf{x}_1) \phi(\tau_2, \mathbf{x}_2) \theta(\tau_1 - \tau_2) + \phi(\tau_2, \mathbf{x}_2) \phi(\tau_1, \mathbf{x}_1), & \text{for } \Phi = \phi, \\ \psi(\tau_1, \mathbf{x}_1) \psi(\tau_2, \mathbf{x}_2) \theta(\tau_1 - \tau_2) - \psi(\tau_2, \mathbf{x}_2) \psi(\tau_1, \mathbf{x}_1), & \text{for } \Phi = \psi, \end{cases} \tag{4.44}$$

where ϕ and ψ are bosonic and fermionic fields, respectively, and θ is the step-function. The negative sign for fermions arises from the anti-commutation relations, required to respect the fundamental spin-statistics theorem [223].

In particular, for $n = 2$, one can define the **thermal propagator** G_β,

$$G_\beta(\tau_1, \mathbf{x}_1; \tau_2, \mathbf{x}_2) \equiv \langle \mathcal{T} \left(\Phi(\tau_1, \mathbf{x}_1) \Phi(\tau_2, \mathbf{x}_2) \right) \rangle = \mathcal{Z}^{-1} \mathrm{Tr} \left\{ \boldsymbol{\rho} \mathcal{T} \left(\Phi(\tau_1, \mathbf{x}_1) \Phi(\tau_2, \mathbf{x}_2) \right) \right\} . \tag{4.45}$$

The presence of the trace in expectation-value computations motivates considering cases in which the system returns to its initial state after a given time interval. For that reason, we are interested in knowing the behaviour of G_β after a period β in imaginary-time. Let τ be an instant where that $0 < \tau < \beta$. The thermal propagator reads

$$\begin{aligned} G_\beta(\tau, \mathbf{x}_1; 0, \mathbf{x}_2) &= \mathcal{Z}^{-1} \mathrm{Tr} \left\{ \boldsymbol{\rho} \mathcal{T} \left(\Phi(\tau, \mathbf{x}_1) \Phi(0, \mathbf{x}_2) \right) \right\} \\ &= \mathcal{Z}^{-1} \mathrm{Tr} \left\{ e^{-\beta H'} \Phi(\tau, \mathbf{x}_1) \Phi(0, \mathbf{x}_2) \right\} \\ &= \mathcal{Z}^{-1} \mathrm{Tr} \left\{ \underbrace{e^{-\beta H'} e^{\beta H'}}_{\mathbb{1}} \Phi(0, \mathbf{x}_2) e^{-\beta H'} \Phi(\tau, \mathbf{x}_1) \right\} \\ &= \mathcal{Z}^{-1} \mathrm{Tr} \left\{ e^{-\beta H'} \Phi(\beta, \mathbf{x}_2) \Phi(\tau, \mathbf{x}_1) \right\} \\ &= \pm \mathcal{Z}^{-1} \mathrm{Tr} \left\{ \boldsymbol{\rho} \mathcal{T} \left(\Phi(\tau, \mathbf{x}_1) \Phi(\beta, \mathbf{x}_2) \right) \right\} , \end{aligned} \tag{4.46}$$

where the cyclic properties of the trace where used, and that

$$\Phi(\beta, \mathbf{x}_2) = e^{\beta H'} \Phi(0, \mathbf{x}_2) e^{-\beta H'} , \tag{4.47}$$

with $H' \equiv H - \mu_a Q_a$, in analogy to the real-time Heisenberg time-evolution expression $\Phi(t, \mathbf{x}_2) = e^{itH}\Phi(0, \mathbf{x}_2)e^{-itH}$. Therefore,

$$G_\beta(\tau, \mathbf{x}_1; 0, \mathbf{x}_2) = \pm G_\beta(\tau, \mathbf{x}_1; \beta, \mathbf{x}_2), \tag{4.48}$$

again, with the positive and negative sign associated with bosonic and fermionic fields, respectively. Relation (4.48) implies *periodic boundary conditions* for bosons,

$$\phi(0, \mathbf{x}) = \phi(\beta, \mathbf{x}), \tag{4.49}$$

and *anti-periodic boundary conditions* for fermions,

$$\psi(0, \mathbf{x}) = -\psi(\beta, \mathbf{x}), \tag{4.50}$$

in the thermal case. Notice that the anti-periodicity of fermion fields is consistent with the trace operation in the partition function, i.e., that the system returns to the original state after a period β. Since the negative sign of ψ is just an overall phase, the right-hand side of (4.50) describes the same physical state as the left-hand side.

Due to the (anti-)periodicity of the thermal propagators, the fields are only allowed to take discrete frequencies. This can better be seen by Fourier expanding each field (with a conserved charge):

$$\phi(\tau, \mathbf{x}) = \frac{1}{\sqrt{TV}} \sum_n \sum_{\mathbf{k}} e^{i(\mathbf{k}\cdot\mathbf{x} + (\omega_n + i\mu)\tau)} \tilde{\phi}_n(\mathbf{k}), \tag{4.51}$$

$$\psi(\tau, \mathbf{x}) = \frac{1}{\sqrt{TV}} \sum_n \sum_{\mathbf{p}} e^{i(\mathbf{p}\cdot\mathbf{x} + (\omega_n + i\mu)\tau)} \tilde{\psi}_n(\mathbf{p}). \tag{4.52}$$

From the bosonic and fermionic boundary conditions (4.49) and (4.50), one finds that only the discrete frequencies

$$\omega_n = \begin{cases} 2\pi n T - i\mu, , & n \in \mathbf{Z} \quad \text{(bosons)}, \\ (2n+1)\pi T - i\mu, & n \in \mathbf{Z} \quad \text{(fermions)}, \end{cases} \tag{4.53}$$

contribute to the thermal propagator. These frequencies are known as **Matsubara frequencies**, and they are the main modification in comparison to (ordinary) zero-temperature QFT; all other definitions — including Green's functions and Feynman rules — remain unchanged. One can draw a close analogy between the emergence of discrete Matsubara frequencies (and hence quantised energy levels) and the quantisation of a particle confined within a box. This correspondence arises because, in the Matsubara formalism, Euclidean time is compactified onto a circle of circumference β of a "tube" with its axis along the spatial direction, so that the topology of space-time changes from

$$\mathbf{R}^4 = \mathbf{R}^1 \times \mathbf{R}^3, \tag{4.54}$$

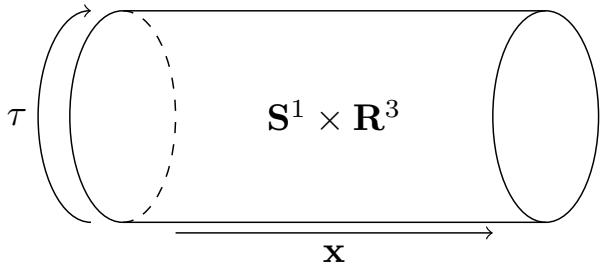

Figure 4.1: In the Matsubara formalism, the topology of space-time can be viewed as a cylinder whose radius is proportional to $1/T$. At $T = 0$, the radius goes to infinity and the flat topology is recovered.

where both spatial and temporal directions are open intervals and on an equal footing, to

$$\mathbf{S}^1 \times \mathbf{R}^3, \tag{4.55}$$

in which the Euclidean time direction is periodic (see Fig. 4.1). In the zero-temperature limit $T \to 0$ ($\beta \to \infty$), the radius of this "tube" $\mathbf{S}^1 \times \mathbf{R}^3$ diverges, the flat topology is recovered, and the discrete Matsubara modes coalesce into a continuum, just as the energy spectrum of a free particle in an unbounded domain is continuous.

4.2 Mean-Field Approximation

It will be of our interest to include four or more point interactions in the Lagrangians of the following chapters (e.g. in Ch. 5 with the **Nambu-Jona-Lasinio** (NJL) and the **Polyakov-Nambu-Jona-Lasinio** (PNJL) models). This would require one to evaluate quantum corrections of the theory, from one or higher loop diagrams. In the **mean-field approximation** (MFA), we simplify our treatment by neglecting loop corrections, and assume that fermions are taken to move independently in a mean-field. It has been demonstrated that the MFA yields results in close agreement with those obtained when one-loop corrections are included [286].

In this section we briefly introduce the fundamentals of the MFA and the background-field method.

4.2.1 Effective Action

In QFT one often defines the so-called generating functional of the fully connected Green's functions, given by [227]

$$W[J] \equiv -i \ln Z[J], \tag{4.56}$$

where, here, Z is the generating functional, which generates the Green's functions of the theory,

$$Z[J] = N \int \mathrm{D}\phi \, \exp\left(iS[\phi] + i \int \mathrm{d}^4x J(x)\phi(x) \right), \tag{4.57}$$

with N a normalisation constant, such that $Z[0] = 1$, and $J(x)$ is an external source of the field $\phi(x)$. One can obtain n-point correlation function by taking multiple functional derivatives of W (or Z) with respect to $J(x_i)$ at different points [227]:

$$\left(\frac{\delta^n W[J]}{\delta J(x_1)\dots\delta J(x_n)}\right)_{J=0} = \frac{(-i)^n}{\mathcal{Z}[J]}\left(\frac{\delta^n Z[J]}{\delta J(x_1)\dots\delta J(x_n)}\right)_{J=0} = \langle 0|\,\mathcal{T}\left(\phi(x_1)\dots\phi(x_n)\right)|0\rangle\,. \quad (4.58)$$

In particular, by setting $n = 1$, one can define the so-called **classical field**, $\phi_c(x)$,

$$\frac{\delta W[J]}{\delta J(x)} = \frac{-i}{Z[J]}\frac{\delta Z[J]}{\delta J(x)} = \langle\phi\rangle_J \equiv \phi_c(x). \quad (4.59)$$

When $J = 0$, due to Poincaré invariance and the uniqueness of the true ground state in the Hilbert space, $\phi_c(x)$ must be a constant, i.e., $\phi_c(x) = \phi_c$; more specifically, $\phi_c = 0$, if there is no spontaneous symmetry breaking, and $\phi_c \neq 0$, if any symmetry was spontaneously broken [223].

Furthermore, we can define from the Legendre transform of $W[J]$ the functional

$$\Gamma[\phi_c] \equiv W[J] - \int \mathrm{d}^3x\; J(x)\phi_c(x), \quad (4.60)$$

known as the **effective action**. The vertices of this functional correspond to one-particle irreducible (1PI) diagrams, i.e., those correlation functions whose diagrammatic representation cannot be separated into two disconnected pieces by cutting any single internal propagator. In $\Gamma[\phi]$, quantum fluctuations of all fields have been integrated out. Thus, $\Gamma[\phi]$ can be used at tree-level to yield Green's functions including all quantum correction [223].

4.2.2 Background Fields and MFA

A useful away to compute $\Gamma[\phi_c]$, while including fluctuations of the field, is through the **background field method** [223], where one evaluates 1PI diagrams in the theory by splitting the field into an arbitrary, non-dynamical[6], background-field ϕ_b and a field $\eta(x)$ containing addition quantum fluctuations,

$$\phi(x) = \phi_b(x) + \eta(x). \quad (4.61)$$

Here, we take $\phi_b(x) = \phi_c$. Inserting the above in $W[J]$, and Taylor expanding around ϕ_c, we obtain:

$$\begin{aligned} W[J] = &\int \mathrm{d}^4x\;\left(\mathcal{L}[\phi_c] + J(x)\phi_c(x)\right) \\ &+ \int \mathrm{d}^4x\;\left[\left(\frac{\delta\mathcal{L}[\phi]}{\delta\phi(x)}\right)_{\phi=\phi_c} + J(x)\right]\eta(x) \\ &+ \frac{1}{2}\int \mathrm{d}^4x\,\mathrm{d}^4y\;\left(\frac{\delta^2\mathcal{L}[\phi]}{\delta\phi(x)\delta\phi(y)}\right)_{\phi=\phi_c}\eta(x)\eta(y) + \dots \end{aligned} \quad (4.62)$$

[6] Here, non-dynamical means that ϕ_b is not integrated over in the path integral.

As one can see, the first term is independent of any fluctuating field. For the second term we first notice that

$$\frac{\delta Z[J]}{\delta\phi(x)} = 0, \tag{4.63}$$

because the generating functional, being a functional of the source $J(x)$. should be invariant under an infinitesimal change of the field ϕ (supposing that the integration measure is invariant likewise). Thus, we obtain the equations of motion

$$\frac{\delta S[\phi]}{\delta\phi(x)} = \frac{\delta\mathcal{L}[\phi]}{\delta\phi(x)} = -J(x), \tag{4.64}$$

and the second term in Eq. (4.62) vanishes.

Applying expansion (4.62) in (4.56), we obtain

$$\begin{aligned} Z[J] = N\exp\left(iS[\phi_c] + i\int \mathrm{d}^4x\; J(x)\phi_c(x)\right) \\ \times\int \mathrm{D}\eta\exp\left(\frac{i}{2}\int \mathrm{d}^4x\,\mathrm{d}^4y\;\eta(x)\eta(y)\left(\frac{\delta\mathcal{L}[\phi]}{\delta\phi(x)\delta\phi(y)}\right)_{\phi=\phi_c} + \dots\right), \end{aligned} \tag{4.65}$$

Neglecting the correction terms in ellipsis, the path integral over η has the form of a Gaussian integral and can be integrated exactly:

$$Z[J] \approx N\exp\left(iS[\phi_c] + i\int \mathrm{d}^4x\; J(x)\phi_c(x)\right)\left[\det\left(\frac{\delta^2\mathcal{L}}{\delta\phi(x)\phi(y)}\right)_{\phi=\phi_c}\right]^{-1/2}, \tag{4.66}$$

where the power $-1/2$ will be $+1$ if fermions are considered instead. Substituting this in (4.56), one obtains from (4.60) that

$$\Gamma[\phi_c] \approx S[\phi_c] - \frac{i}{2}\ln\det\left(\frac{\delta^2\mathcal{L}}{\delta\phi(x)\phi(y)}\right)_{\phi=\phi_c}, \tag{4.67}$$

representing the 1-loop approximation of the effective action. The first term corresponds to the classical action, while the second one are the first quantum corrections to the theory. The MFA is obtained by neglecting the contributions of the second and above terms, and setting

$$\tilde{\Gamma}[\phi_c] \equiv S[\phi_c], \tag{4.68}$$

where the tilde indicates that our quantity is defined in a mean-field.

4.2.3 Dirac Gas in a Mean-Field Potential

We now apply the mean-field approach to compute the grand-canonical potential of a (Dirac) fermion gas in the presence of mean-field interactions. As mentioned at the beginning of this chapter, this will be particular important to simplify the discussion using Lagrangians of the following chapters.

Within the MFA, the Lagrangian of a fermionic system can always written in the form [287]

$$\begin{aligned}\tilde{\mathcal{L}} &= \bar{\psi}\left[i\gamma^{\mu}\left(\partial_{\mu}+iV_0\delta^0_{\mu}\right)-(m+S)\right]\psi+U(S,V_0)\\ &= \bar{\psi}\left(i\gamma^{\mu}D_{\mu}-m^*\right)\psi+U,\end{aligned} \tag{4.69}$$

where $D_\mu = \partial_\mu + iV_0\delta^0_\mu$, which can be interpreted as a covariant derivative, and $m^* = m + S$ as an effective mass. The constants S and V_0 are the vacuum expectation values of the scalar and vector auxiliary $S(x)$ and $V_\mu(x)$, respectively,

$$S \equiv \langle S(x)\rangle\,, \quad V_0 = \langle V_0(x)\rangle\,. \tag{4.70}$$

Notice that $\langle V_i(x)\rangle = 0$ on account for rotation symmetry. The mean-field potential $U(S, V_0)$ is independent of $\psi(x)$ and x_μ, but can be constructed from S and V_0. The auxiliary fields have been used in the context of linearising terms in the Lagrangian, e.g., by transforming a four-fermion interaction into a two-point interaction, in which the bosonic auxiliary fields are introduced to couple with the fermions, and then to treat the auxiliary fields in the MFA. Various examples can be found in [287], but we will also see it later by linearising product of operators in the Lagrangian.

Within the imaginary-time formalism, Eq. (4.69) reads

$$\tilde{\mathcal{L}} = \bar{\psi}\left(-\gamma^0(\partial_\tau + V_0) + i\gamma_i\partial_i - m^*\right)\psi + U, \tag{4.71}$$

where γ_μ are the Euclidean gamma matrices introduced in (3.42) (the superscript E has been dropped for a shorter notation). The correspondent Hamiltonian (density) can be obtained using (4.30), with the Euclidean conjugate momentum Π

$$\Pi = -i\frac{\partial\tilde{\mathcal{L}}}{\partial(\partial_\tau\psi)} = i\psi^\dagger. \tag{4.72}$$

Hence,

$$\tilde{\mathcal{H}} = i\Pi\partial_\tau\psi - \tilde{\mathcal{L}} = \bar{\psi}(-i\gamma_i\partial_i + \gamma^0 V_0 + m^*)\psi - U. \tag{4.73}$$

Additionally, the Lagrangian $\tilde{\mathcal{L}}$ has a conserved charge given by

$$Q = \int \mathrm{d}^3x\; j^0 = \int \mathrm{d}^3x\; \bar{\psi}\gamma^0\psi. \tag{4.74}$$

Thus, Eq. (4.39) yields the partition function

$$\begin{aligned}\tilde{\mathcal{Z}} &= N\int i\,\mathrm{D}\psi^\dagger\int \mathrm{D}\psi\exp\left(\int_0^\beta \mathrm{d}\tau\int \mathrm{d}^3x\,\left(i\Pi\partial_\tau-\mathcal{H}+\mu\bar{\psi}\gamma^0\psi\right)\right)\\ &= N\int i\,\mathrm{D}\psi^\dagger\int \mathrm{D}\psi\exp\left(\int_0^\beta \mathrm{d}\tau\int \mathrm{d}^3x\,\bar{\psi}\left(-\gamma^0(\partial_\tau+V_0)+i\gamma_i\partial_i-m^*+\mu\gamma^0\right)\psi\right)\exp(\beta VU)\\ &= N\int i\,\mathrm{D}\psi^\dagger\int \mathrm{D}\psi\exp\left(\int_0^\beta \mathrm{d}\tau\int \mathrm{d}^3x\,i\psi^\dagger\left(i\partial_\tau+\alpha_i\partial_i+i\gamma^0m^*-i\mu^*\right)\psi\right)\exp(\beta VU),\end{aligned} \tag{4.75}$$

where $\alpha_i=\gamma^0\gamma_i$ and μ^* is the effective chemical potential defined by

$$\mu^*=\mu-V_0. \tag{4.76}$$

It will be useful to re-write the path integral in terms of dimensionless variables for the next step. Thus, by scaling each variables with the appropriate power of β according to their canonical dimensional, we introduce the dimensionless quantities:

$$\hat{\psi}=\beta^{3/2}\psi,\quad \hat{\tau}=\beta^{-1}\tau,\quad \hat{x}_i=\beta^{-1}x_i,\quad \hat{\mu^*}=\beta\mu^*,\quad \hat{m^*}=\beta m^*. \tag{4.77}$$

Hence,

$$\tilde{\mathcal{Z}}=N\int i\,\mathrm{D}\hat{\psi}^\dagger\int \mathrm{D}\hat{\psi}\exp\left(\int_0^1 \mathrm{d}\hat{\tau}\int \mathrm{d}^3\hat{x}_i\,i\hat{\psi}^\dagger\left(i\hat{\partial}_\tau+\alpha_i\hat{\partial}_i+i\gamma^0\hat{m^*}-i\hat{\mu^*}\right)\hat{\psi}\right)\exp(\beta VU) \tag{4.78}$$

Since the integral above is a Gaussian integral, it can be performed immediately using the relation

$$\int \mathrm{d}\eta_1^\dagger\,\mathrm{d}\eta_1\ldots\mathrm{d}\eta_N^\dagger\,\mathrm{d}\eta_N e^{\eta^\dagger A\eta}=\det A, \tag{4.79}$$

where $\eta_i^\dagger$ and η_i are independent Grassman variables, and A is $N\times N$ matrix. Therefore,

$$\begin{aligned}\ln\tilde{\mathcal{Z}}(\beta) &= \ln N+\beta VU+\ln\det_{n,p_i,\delta,I}\left(i\left[\hat{\partial}_\tau-\hat{\mu^*}+\boldsymbol{\alpha}\cdot\hat{\mathbf{p}}+\gamma^0\hat{m^*}\right]\right)\\ &= \ln N+\beta VU+\ln\det_{n,p_i,\delta,I}\left(i\beta\left[\partial_\tau-\mu^*+\boldsymbol{\alpha}\cdot\mathbf{p}+\gamma^0m^*\right]\right)\end{aligned} \tag{4.80}$$

where $\boldsymbol{\alpha}\cdot\mathbf{p}=\alpha_ip_i$ with $p_i=-i\partial_i$. Notice that the third and fourth term produce the Dirac operator. The determinant mus be taken over all indices: the Dirac indices δ, momentum p_i, frequency n and other possible indices that might exist I.

The determinant is given by the product of the eigenvalues of the operator acting in the space of functions satisfying the anti-periodic boundary conditions on $[0,\beta]$. The eigenfunction of $\partial_\tau-\mu^*+\alpha_ip_i+\gamma^0m^*$ have the form $\exp(i\omega_n\tau)\exp(ip_ix_i)\Psi(\mathbf{p})$, where ω_n are the Matsubara frequencies and $\Psi(\mathbf{p})$ are the eigenfunctions satisfying of the Dirac operator, whose eigenvalues

are given by $\pm E(\mathbf{p})$, where

$$E(\mathbf{p}) = \sqrt{\mathbf{p}^2 + m^{*2}}, \quad \mathbf{p}^2 \equiv p_i p_j \delta^{ij}, \tag{4.81}$$

corresponding to the two possible spin projections. Therefore, the eigenvalues of $\partial_\tau - \mu^* + \alpha_i p_i + \gamma^0 m^*$ are

$$\lambda^{\pm}_{\mathbf{p},n} = i\omega_n - \mu^* + E(\mathbf{p}). \tag{4.82}$$

Taking the determinant over the Dirac indices (δ), and using the relation $\ln\det A = \mathrm{Tr}\ln A$, we obtain

$$\ln\tilde{\mathcal{Z}}(\beta) = \ln N + \beta VU + 2\sum_{n,\mathbf{p},I}\left\{\ln\left[\beta(i\omega_n - \mu^* + E(\mathbf{p}))\right] + \ln\left[\beta(i\omega_n - \mu^* - E(\mathbf{p}))\right]\right\}. \tag{4.83}$$

Since n runs over both positive and negative integers, this expression can be written in an explicit real form

$$\begin{aligned}\ln\tilde{\mathcal{Z}}(\beta) =& \ln N + \beta VU \\ &+ 2\sum_{n,\mathbf{p},I}\left\{\ln\left[(2n+1)^2\pi^2 + \beta^2(E-\mu^*)^2\right] + \ln\left[(2n+1)^2\pi^2 + \beta^2(E+\mu^*)^2\right]\right\}.\end{aligned} \tag{4.84}$$

The sum over n diverges. To extract the β and μ^* dependent parts, we consider the logarithm in the form[7]

$$\begin{aligned}\sum_{n,\mathbf{p},I}\left\{\ln\left[(2n+1)^2\pi^2 + \beta^2(E\pm\mu^*)^2\right]\right\} =& \ln\left(1 + (2n+1)^2\pi^2\right) \\ &+ \int_1^{\beta^2(E\pm\mu)^2} \mathrm{d}x^2 \frac{1}{(2n+1)^2\pi^2 + x^2}.\end{aligned} \tag{4.85}$$

Summing over n by making use of

$$\sum_{n=-\infty}^{\infty} \frac{1}{(n-a)(n-b)} = \frac{\pi\left[\cot(\pi a) - \cot(\pi b)\right]}{b-a}, \tag{4.86}$$

one finds that

$$\sum_{n=-\infty}^{\infty} \frac{1}{(2n+1)^2\pi^2 + x^2} = \frac{1}{x}\left(\frac{1}{2} - \frac{1}{e^x+1}\right). \tag{4.87}$$

Finally, integrating over x, and replacing the sum in the standard way

$$\sum_{\mathbf{p}} \longrightarrow V\int \frac{\mathrm{d}^3p}{(2\pi)^3}, \tag{4.88}$$

[7] Here, we follow the method of [283].

we obtain

$$\ln \tilde{\mathcal{Z}}(\beta) = \ln N + \beta V U + 2V \sum_I \int \frac{\mathrm{d}^3 p}{(2\pi)^3} \left[-\beta E(\mathbf{p}) + \ln(1 + e^{-\beta(E+\mu^*)}) + \ln(1 + e^{-\beta(E-\mu^*)}) \right], \tag{4.89}$$

whose grand-canonical potential $\tilde{\Omega}$ is given by

$$\tilde{\Omega} = \Omega_0 - U - 2T \sum_I \int \frac{\mathrm{d}^3 p}{(2\pi)^3} \left[-\beta E(\mathbf{p}) + \ln(1 + e^{-\beta(E+\mu^*)}) + \ln(1 + e^{-\beta(E-\mu^*)}) \right] \tag{4.90}$$

where $\Omega_0 = -\frac{T}{V} \ln N$ is a constant chosen so that pressure and energy density are zero in vacuum. The factor of 2 comes naturally from the spin-1/2 nature of fermions, and the contributions from particles (μ) and anti-particles ($-\mu$) are explicit with the two logarithm terms. Moreover, a contribution from the zero-point energy ($-\beta E$) is present.

Chapter 5

The (Polyakov–) Nambu–Jona-Lasinio Model

Things fall apart; the centre cannot hold;

– W.B. Yeats, *The Second Coming*

At the end of Ch. 3, we noted that effective QCD models provide a valuable tool for exploring strongly interacting matter at high temperature and/or density, inaccessible to LQCD due to the infamous fermion sign problem. Among these, the NJL model and its Polyakov-extended variant (PNJL) are particularly popular.

In this chapter, we first present the NJL Lagrangian including both scalar and vector fermion interactions, and develop its mean-field approximation. We then introduce the Polyakov loop and construct the corresponding effective potential, thereby obtaining the PNJL model. The role of centre symmetry and its spontaneous breaking is interpret through the behaviour of the Polyakov loop, and we discuss how this leads to a statistical (though not dynamical) realisation of confinement in the PNJL model.

5.1 NJL Model

The **Nambu–Jona-Lasinio model** was introduced by Yoichiro Nambu and Giovanni Jona-Lasinio in 1961 [288], inspired by the BCS theory of superconductivity. The NJL model is an effective field theory realising chiral symmetry breaking, and paralleling the generation of the mass gap in the Dirac operator spectrum with the energy gap of a superconductor. Originally, proposed to described the dynamics of nucleons interacting through a local effective four-body interaction, with the development of QCD, the model was abandoned, but later recovered as an effective theory of QCD with quark degrees of freedom as they share identical symmetries.

5.1.1 Lagrangian Density

The $(2+1)-$flavour NJL model with vector and isovector interactions can be expressed as

$$\begin{aligned}\mathcal{L}_{\mathrm{NJL}} &= \bar{\psi}\left(i\gamma^{\mu}\partial_{\mu} - m + \mu\gamma^{0}\right)\psi \\ &+ G_S\sum_{a=0}^{8}\left[(\bar{\psi}\lambda^{a}\psi)^2 + (\bar{\psi}i\gamma_5\lambda^{a}\psi)^2\right] \\ &+ G_D\left[\det_f \bar{\psi}(1+\gamma_5)\psi + \det_f \bar{\psi}(1-\gamma_5)\psi\right] \\ &- G_V\sum_{a=0}^{8}\left[(\bar{\psi}\gamma^{\mu}\lambda^{a}\psi)^2 + (\bar{\psi}\gamma^{\mu}\gamma_5\lambda^{a}\psi)^2\right].\end{aligned} \tag{5.1}$$

Here $\psi = (u\ d\ s)^T$ and $m = \mathrm{diag}_f(m_u\ m_d\ m_s)$ are the quark fields and the current quark mass matrix in flavour space, respectively. The first term includes finite-density effects by considering a chemical potential matrix $\mu = \mathrm{diag}_f(\mu_u\ \mu_d\ \mu_s)$, associated with a conserved current $j^0 = \bar{\psi}\gamma^0\psi$.

The G_S scalar–pseudo-scalar coupling constant reproduces the contributions from gluon exchange in quark interactions. The many possible diagrams corresponding to the exchange of gluons in the four-leg fermion interaction are replaced by a local effective four-point vertex diagram. This term is responsible to spontaneously break the chiral symmetry in the vacuum by generating a quark-antiquark condensate, and, consequently, a constituent quark mass.

The third term in the NJL Lagrangian corresponds to the so-called **Kobayashi–Maskawa–'t Hooft interaction** (KMT) [289, 290], responsible for the generation of the six-fermion interaction which explicitly breaks the $U(1)_A$ symmetry — as is the case in QCD — reproducing the correct hadron spectra. The determinant is taken over the flavour space, and leads to a six-quark interaction in the $N_f = 2+1$ case.

As long as one preserves the symmetries of QCD, additional quark interaction can be added. The last term in $\mathcal{L}_{\mathrm{NJL}}$ corresponds to a four-quark vector interaction containing both a vector-isoscalar interaction,

$$G_{V-IS}\left[(\bar{\psi}\gamma^{\mu}\lambda^{0}\psi)^2 - (\bar{\psi}\gamma^{\mu}\gamma_5\lambda^{0}\psi)^2\right], \tag{5.2}$$

and a vector-isovector interaction,

$$G_{V-IV}\sum_{a=1}^{8}\left[(\bar{\psi}\gamma^{\mu}\lambda^{a}\psi)^2 + (\bar{\psi}\gamma^{\mu}\gamma_5\lambda^{a}\psi)^2\right], \tag{5.3}$$

in which we will assume $G_V = G_{V-IS} = G_{V-IV}$. As mentioned before, the vector interaction are known to couple to density degrees of freedom, meaning that a in-medium dependence cannot be discarded. However, there is still no restriction when setting the value, or even the sign, of the vector coupling. Nevertheless, vector interactions are useful to describe in-medium behaviour, such as repulsive or attractive interaction, which could weaken or enhance the first-order phase transition and determine the existence of the CEP (see Ch. 2).

5.1.2 Mean-Field NJL Model

As mentioned in the previous chapter, describing the NJL model in the MFA provides good results in comparison to the 1-loop approximation, while simplifying many calculations and reducing the computational cost.

To apply this approximation, we split an operator $\mathcal{O}_1$ into its vacuum expectation ($\langle\mathcal{O}_1\rangle$) value and a perturbation (η_1) — similar to the background-field method introduced in Subsection 4.2.2. Hence,

$$\mathcal{O}_1 = \langle\mathcal{O}_1\rangle + \eta_1. \tag{5.4}$$

The product of two operator $\mathcal{O}_1$ and $\mathcal{O}_2$ becomes

$$\mathcal{O}_1\mathcal{O}_2 = \langle\mathcal{O}_1\rangle\langle\mathcal{O}_2\rangle + \eta_1\langle\mathcal{O}_2\rangle + \eta_2\langle\mathcal{O}_1\rangle + \eta_1\eta_2. \tag{5.5}$$

In the MFA only linear terms in the perturbation are taken into account, i.e., neglecting second-order infinitesimals, $\eta_1\eta_2$. Writing the perturbation in terms of the operators and their expectation values, we obtain

$$\begin{aligned}\mathcal{O}_1\mathcal{O}_2 &\approx \langle\mathcal{O}_1\rangle\langle\mathcal{O}_2\rangle + (\mathcal{O}_1 - \langle\mathcal{O}_1\rangle)\langle\mathcal{O}_2\rangle + (\mathcal{O}_2 - \langle\mathcal{O}_2\rangle)\langle\mathcal{O}_1\rangle \\ &\approx \langle\mathcal{O}_1\rangle\mathcal{O}_2 + \mathcal{O}_1\langle\mathcal{O}_2\rangle - \langle\mathcal{O}_1\rangle\langle\mathcal{O}_2\rangle .\end{aligned} \tag{5.6}$$

The linearisation of a three operator product can be obtain following the same steps as before: splinting each operator in the expectation value and a perturbation term, and keeping only linear terms in perturbation one obtains

$$\mathcal{O}_1\mathcal{O}_2\mathcal{O}_3 \approx \mathcal{O}_1\langle\mathcal{O}_2\rangle\langle\mathcal{O}_3\rangle + \langle\mathcal{O}_1\rangle\mathcal{O}_2\langle\mathcal{O}_3\rangle + \langle\mathcal{O}_1\rangle\langle\mathcal{O}_2\rangle\mathcal{O}_3 - 2\langle\mathcal{O}_1\rangle\langle\mathcal{O}_2\rangle\langle\mathcal{O}_3\rangle . \tag{5.7}$$

Therefore, from (5.1) we obtain the linearised products:

$$(\bar\psi\lambda^a\psi)^2 \approx 2\left\langle\bar\psi\lambda^a\psi\right\rangle(\bar\psi\lambda^a\psi) - \left\langle\bar\psi\lambda^a\psi\right\rangle^2, \tag{5.8a}$$

$$(\bar\psi i\gamma_5\lambda^a\psi)^2 \approx 2\left\langle\bar\psi i\gamma_5\lambda^a\psi\right\rangle(\bar\psi i\gamma_5\lambda^a\psi) - \left\langle\bar\psi i\gamma_5\lambda^a\psi\right\rangle^2, \tag{5.8b}$$

$$(\bar\psi\gamma^\mu\lambda^a\psi)^2 \approx 2\left\langle\bar\psi\gamma^\mu\lambda^a\psi\right\rangle(\bar\psi\gamma^\mu\lambda^a\psi) - \left\langle\bar\psi\gamma^\mu\lambda^a\psi\right\rangle^2, \tag{5.8c}$$

$$(\bar\psi\gamma^\mu\gamma_5\lambda^a\psi)^2 \approx 2\left\langle\bar\psi\gamma^\mu\gamma_5\lambda^a\psi\right\rangle(\bar\psi\gamma^\mu\gamma_5\lambda^a\psi) - \left\langle\bar\psi\gamma^\mu\gamma_5\lambda^a\psi\right\rangle^2. \tag{5.8d}$$

The vacuum state has definite charge, spin and parity. Any off-diagonal terms in the flavour space — i.e., terms proportional to λ^a for $a = 1, 2, 4, 5, 6, 7, 8$ — would alter these properties. Physically, such terms correspond to condensates of charged-mesons condensates (e.g. $\pi^\pm$ or $K^\pm$ condensates), which can only form if the isospin chemical potential exceeds the corresponding meson mass. In this work, we assume that these conditions are not met.

Moreover, within the mean-field approximation at thermal equilibrium, a spatial vector condensate $\left\langle\bar\psi\gamma^i\lambda^a\psi\right\rangle$ $(i = 1, 2, 3)$ would select a preferred direction in space and thus break

rotational invariance; consequently, only the temporal component $\left\langle \bar{\psi}\gamma^0\lambda^a\psi \right\rangle$ may be non-zero.

Finally, any pseudo-vector condensate of the form $\left\langle \bar{\psi}\gamma^\mu\gamma_5 \right\rangle$, would violate parity. Since we assume the vacuum (or medium) to be parity-even, such condensates are excluded.

Therefore, the non-vanishing condensates can be expressed as:

$$\left\langle \bar{\psi}\lambda^0\bar{\psi} \right\rangle = \sqrt{\frac{2}{3}}(\sigma_u + \sigma_d + \sigma_s), \tag{5.9a}$$

$$\left\langle \bar{\psi}\lambda^3\psi \right\rangle = \sigma_u - \sigma_d, \tag{5.9b}$$

$$\left\langle \bar{\psi}\lambda^8\psi \right\rangle = \frac{1}{\sqrt{3}}(\sigma_u + \sigma_d - 2\sigma_s), \tag{5.9c}$$

$$\left\langle \bar{\psi}\gamma^0\lambda^0\psi \right\rangle = \sqrt{\frac{2}{3}}(\rho_u + \rho_d + \rho_s), \tag{5.9d}$$

$$\left\langle \bar{\psi}\gamma^0\lambda^3\psi \right\rangle = \rho_u - \rho_d, \tag{5.9e}$$

$$\left\langle \bar{\psi}\gamma^0\lambda^8\psi \right\rangle = \frac{1}{\sqrt{3}}(\rho_u + \rho_d - 2\rho_s), \tag{5.9f}$$

where

$$\sigma_f = \left\langle \bar{\psi}_f\psi_f \right\rangle \quad \text{and} \quad \rho_f = \left\langle \bar{\psi}_f^\dagger\psi_f \right\rangle \tag{5.10}$$

are the quark condensate and density of flavour f, respectively.

The KMT interaction in (5.1) can be analysed through

$$\det_f \bar{\psi}\mathcal{O}\psi = \epsilon_{ijk}(\bar{\psi}_u\mathcal{O}\psi_i)(\bar{\psi}_d\mathcal{O}\psi_j)(\bar{\psi}_s\mathcal{O}\psi_k). \tag{5.11}$$

Applying (5.7) and following the same steps as before (see Appendix B.1), the KMT term in the MFA can be written as

$$\begin{aligned}\tilde{\mathcal{L}}_{\text{KMT}} &= 2G_D\Big[(\bar{\psi}_u\psi_u)\left\langle \bar{\psi}_d\psi_d \right\rangle\left\langle \bar{\psi}_s\psi_s \right\rangle + (\bar{\psi}_d\psi_d)\left\langle \bar{\psi}_d\psi_d \right\rangle\left\langle \bar{\psi}_s\psi_s \right\rangle \\ &\qquad + (\bar{\psi}_s\psi_s)\left\langle \bar{\psi}_u\psi_u \right\rangle\left\langle \bar{\psi}_d\psi_d \right\rangle - 2\left\langle \bar{\psi}_u\mathcal{O}\psi_u \right\rangle\left\langle \bar{\psi}_d\mathcal{O}\psi_d \right\rangle\left\langle \bar{\psi}_s\mathcal{O}\psi_s \right\rangle\Big] \\ &= 2G_D\left(\bar{\psi}\boldsymbol{\sigma}\psi - 2\sigma_u\sigma_d\sigma_s\right),\end{aligned} \tag{5.12}$$

where $\boldsymbol{\sigma} = \text{diag}_f(\sigma_d\sigma_s\ \sigma_u\sigma_s\ \sigma_u\sigma_d)$.

Gathering all the above results, the $(2+1)-$flavour NJL Lagrangian in the MFA reads

$$\begin{aligned}\tilde{\mathcal{L}}_{\rm NJL} &= \bar{\psi}\left(i\gamma^\mu\partial_\mu - m + \mu\gamma^0\right)\psi \\ &+ 2G_S\left[\sqrt{\frac{2}{3}}(\bar{\psi}\lambda^0\psi)(\sigma_u+\sigma_d+\sigma_s) - \frac{1}{3}(\sigma_u+\sigma_d+\sigma_s)^2\right. \\ &\quad + (\bar{\psi}\lambda^3\psi)(\sigma_u-\sigma_d) - \frac{1}{2}(\sigma_u-\sigma_d)^2 \\ &\quad \left. + \frac{1}{\sqrt{3}}(\bar{\psi}\lambda^8\psi)(\sigma_u+\sigma_d-2\sigma_s) - \frac{1}{6}(\sigma_u+\sigma_d-2\sigma_s)^2\right] \\ &+ 2G_D\left(\bar{\psi}\boldsymbol{\sigma}\psi - 2\sigma_u\sigma_d\sigma_s\right) \\ &- 2G_V\left[\sqrt{\frac{2}{3}}(\bar{\psi}\gamma^0\lambda^0\psi)(\rho_u+\rho_d+\rho_s) - \frac{1}{3}(\rho_u+\rho_d+\rho_s)^2\right. \\ &\quad + (\bar{\psi}\gamma^0\lambda^3\psi)(\rho_u-\rho_d) - \frac{1}{2}(\rho_u-\rho_d)^2 \\ &\quad \left. + \frac{1}{\sqrt{3}}(\bar{\psi}\gamma^0\lambda^8\psi)(\rho_u+\rho_d-2\rho_s) - \frac{1}{6}(\rho_u+\rho_d-2\rho_s)^2\right],\end{aligned} \tag{5.13}$$

which can be written in the form given by (4.69) as

$$\tilde{\mathcal{L}}_{\rm NJL} = \bar{\psi}\left[i\gamma^\mu\left(\partial_\mu + iV_0\delta^0_\mu\right) + \mu\gamma^0 - (m+S)\right]\psi + U_{\rm cond}, \tag{5.14}$$

with

$$V_0 = G_V\left[\sqrt{\frac{8}{3}}\lambda^0(\rho_u+\rho_d+\rho_s) + 2\lambda^3(\rho_u-\rho_d) + \frac{2}{\sqrt{3}}\lambda^8(\rho_u+\rho_d-2\rho_s)\right], \tag{5.15}$$

$$S = -G_S\left[\sqrt{\frac{8}{3}}\lambda^0(\sigma_u+\sigma_d+\sigma_s) - 2\lambda^3(\sigma_u-\sigma_d) - \frac{2}{3}\lambda^8(\sigma_u+\sigma_d-2\sigma_s)\right] - 2G_D\boldsymbol{\sigma}, \tag{5.16}$$

and the mean-field (condensate) potential

$$U_{\rm cond} = -2G_S\left(\sigma_u^2+\sigma_d^2+\sigma_s^2\right) + 2G_V\left(\rho_u^2+\rho_d^2+\rho_s^2\right) - 4G_D\sigma_u\sigma_d\sigma_s. \tag{5.17}$$

5.2 PNJL Model

Although the NJL model successfully describes spontaneous chiral-symmetry breaking, it does not account for the confinement-deconfinement transition. To incorporate this mechanism, one extends the NJL model by coupling it to an effective potential for the Polyakov loop, which encodes the spontaneous breaking of centre symmetry and thereby provides a statistical description of confinement in the resulting PNJL model.

5.2.1 Centre Symmetry

Phase transitions are usually associated with a breakdown of a global symmetry. This is also the case in the pure $SU(3)_c$ gauge theory[1]. In the limit of infinitely heavy quarks, a particular important part of the gauge symmetry at finite temperature is the so-called **centre symmetry**[2] which characterises the deconfinement of quark degrees of freedom in a gluonic medium. In the pure $SU(3)_c$ Yang-Mills theory, the gauge symmetry is not $SU(3)_c$ (see Sec. 3.2) but $SU(3)_c/Z_3$. One can understand this from the gluonic transformation law (3.18) by choosing $U = z_3 = z\mathbb{1}$, where

$$z = \exp\left(i\frac{2\pi n}{3}\right), \quad n \in \{0, 1, 2\}, \tag{5.18}$$

is an element of Z_3. Clearly, z_3 is also an element of $SU(3)_c$ that commutes with all other elements of the group. By definition this means that z_3 is an element of the centre subgroup of $SU(3)_c$ that is nothing but Z_3.

In Ch. 4 we have shown that bosonic fields must have periodic boundary condition, while fermionic fields have anti-periodic boundary conditions. Thus, gluon and quark fields must transform according to

$$A_\mu(0, \mathbf{x}) = A_\mu(\beta, \mathbf{x}) \tag{5.19}$$

and

$$\psi(0, \mathbf{x}) = -\psi(\beta, \mathbf{x}), \tag{5.20}$$

respectively. Let $U(\tau, \mathbf{x}) \in SU(3)_c$, be a (Euclidean-time dependent) gauge transformation. The gluon (gauge) field A_μ then transforms as

$$U^\dagger(0, \mathbf{x})A_\mu(0, \mathbf{x})U(0, \mathbf{x}) = U^\dagger(\beta, \mathbf{x})A_\mu(\beta, \mathbf{x})U(\beta, \mathbf{x}), \tag{5.21}$$

in order to maintain periodic boundary conditions in the temporal direction. Hence, the two gauge transformations at $\tau = 0$ and $\tau = \beta$ must differ by an element $z \in Z_3$, i.e.

$$U(\beta, \mathbf{x}) = zU(0, \mathbf{x}). \tag{5.22}$$

Substituting this into Eq. (5.21), we recover condition (5.19).

On the other hand, by including quark fields the Z_3 symmetry at the boundary is explicitly broken. To show this, consider the transformation law for fermionic fields given by (3.11) and the anti-periodic boundary condition (5.20). One has,

$$U(0, \mathbf{x})\psi(0, \mathbf{x}) = -U(\beta, \mathbf{x})\psi(\beta, \mathbf{x}), \tag{5.23}$$

which indicates that

$$U(0, \mathbf{x}) = U(\beta, \mathbf{x}). \tag{5.24}$$

[1] We shall focus on the $N_c = 3$ case, but our discussion also applies for a different number of colours.

[2] The centre Z of a group G is defined by $Z(G) = \left\{z \in G \mid \forall g \in G, zgz^{-1} = g\right\}$.

Thus, only the trivial centre element $z = 1$ is compatible with anti-periodic boundary conditions; consequently the Z_3 symmetry is explicitly broken by dynamical quarks and is recovered only in the limit of infinitely heavy quarks.

There are two important remarks to be made:

- First, one must not associate the global Z_3 symmetry of the QCD Lagrangian with the centre symmetry acting on the gluon fields at the Euclidean-time boundary. The former is an internal symmetry of the action, whereas the latter arises only when enforcing periodic boundary conditions in the imaginary-time direction.

- Second, this global centre symmetry is defined in Euclidean space-time and should not be regarded as a subgroup of the local gauge group $SU(3)_c$, which is itself a symmetry of the Minkowski space-time Lagrangian. Although the Lagrangian remains invariant under the local gauge transformations given in (3.18), the topology and boundary conditions of the Euclidean manifold do not need to respect the full centre symmetry.

It is precisely the spontaneous breaking of this Euclidean-time centre symmetry that underlies the confinement-deconfinement phase transition, as we shall explore in the following.

5.2.2 Polyakov Loop and Deconfinement

In Sec. 3.3 we have shown that the Wilson loop could be used as an order parameter for confinement at $T = 0$ and to study the inter-quark potential. At finite temperatures, however, due to the compactification of the imaginary-time component, the Wilson loop no longer plays this role but it is replaced by a very similar object — the **Polyakov loop** [291]. Because the imaginary-time component is periodic, we can consider a path integral identical to (3.47) but taking the integration between $\tau = 0$ and $\tau = \beta$ over the Euclidean temporal component of the gluon field, $A_4(\tau, \mathbf{x})$. The Polyakov loop is then defined by

$$\Phi(\mathbf{x}) \equiv \frac{1}{N_c}\mathrm{Tr}_c \left\{ \mathcal{P} \exp\left(ig \int_0^\beta \mathrm{d}\tau \; A_4(\tau, \mathbf{x}) \right) \right\}, \tag{5.25}$$

where $\mathcal{P}$ is the path-ordering operator and the trace is taken over colour degrees of freedom. Also, $A_4 = iA^0$ is the temporal component of the Euclidean gauge field $(A_4, \mathbf{A})$.

The connection between the Polyakov loop to the deconfinement-transition can better be understood from its relation to the free energy of the system. Again, we consider the limit of heavy quark fields coupled to a static gluonic background field. From the (static) Dirac equation,

$$\left(i\gamma^0(\partial_\tau + iA_4) + m \right) \psi(\tau, \mathbf{x}) = 0, \tag{5.26}$$

which yields the solution

$$\psi(\tau, \mathbf{x}) = e^{-m\tau} \mathcal{T} \exp\left(ig \int_0^\tau \mathrm{d}\tau' \; A_4(\tau', \mathbf{x}) \right) \psi(0, \mathbf{x}). \tag{5.27}$$

The free energy can be obtained through the partition function,

$$\mathcal{Z} = \sum_s \langle s| \, e^{-\beta H} \, |s\rangle \, . \tag{5.28}$$

Here the sum is taken over all gluonic states $|s\rangle$ with heavy quarks. Introducing the quark fields

$$\mathcal{Z} = N \sum_{s',i} \langle s'| \, \psi_i(0,\mathbf{x}) e^{-\beta H} \psi_i^\dagger(0,\mathbf{x}) \, |s'\rangle \, , \tag{5.29}$$

where N is a normalisation of the quark state, and $\psi_i^\dagger(0,\mathbf{x})$ ($\psi_i(0,\mathbf{x})$) creates (annihilates) a heavy quark of colour i located at $\mathbf{x}$ at time $\tau = 0$ when acting on the states $|s'\rangle$ with no heavy quarks. Since $\exp(-\beta H)$ generates Euclidean time-translations, i.e.,

$$e^{\beta H} \psi_i(0,\mathbf{x}) e^{-\beta H} = \psi_i(\beta,\mathbf{x}), \tag{5.30}$$

Eq. (5.29) becomes

$$\mathcal{Z} = N \sum_{s'} \langle s'| \, e^{-\beta H} \psi_i(\beta,\mathbf{x}) \psi_i^\dagger(0,\mathbf{x}) \, |s'\rangle \, . \tag{5.31}$$

Replacing (5.27) into the above:

$$\begin{aligned}
\mathcal{Z} &= N e^{-m\beta} \sum_{s',i} \langle s'| \, e^{-\beta H} \mathcal{T} \exp\left(ig \int_0^\beta \mathrm{d}\tau' \, A_4(\tau',\mathbf{x}) \right) \underbrace{\psi_i(0,\mathbf{x}) \psi_j^\dagger(0,\mathbf{x})}_{\delta_{ij}} \, |s'\rangle \\
&= N e^{-m\beta} \sum_{s',i} \langle s'| \, e^{-\beta H} \, |s'\rangle \, \langle s'| \, \mathcal{T} \exp\left(ig \int_0^\beta \mathrm{d}\tau' \, A_4(\tau',\mathbf{x}) \right) |s'\rangle \\
&= e^{-m\beta} \sum_{s'} e^{-\beta E} \, \langle s'| \, \frac{1}{N_c} \mathrm{Tr}_i \left[\mathcal{T} \exp\left(ig \int_0^\beta \mathrm{d}\tau' \, A_4(\tau',\mathbf{x}) \right) \right] |s'\rangle \, ,
\end{aligned} \tag{5.32}$$

where we have set $N = 1/N_c$. In this case, $\mathcal{T}$ is equivalent to the path-ordering operator $\mathcal{P}$. Thus, from definition (5.25)

$$\begin{aligned}
\mathcal{Z} &= e^{-m\beta} \sum_{s'} e^{-\beta E} \, \langle s'| \, \Phi(\mathbf{x}) \, |s'\rangle \\
&= e^{-m\beta} \mathrm{Tr} \left(e^{-\beta H} \Phi(x) \right) ,
\end{aligned} \tag{5.33}$$

where the trace is taken over the states of the pure gauge theory. From the relation between the partition function and the free energy for a single quark, F_q,

$$\beta F_q = -\ln \mathcal{Z}, \tag{5.34}$$

one obtains

$$\beta F_q = \beta F_0 + m\beta - \ln \langle \Phi \rangle_{\mu=0} \, , \tag{5.35}$$

where F_0 is the gluonic free energy and $\langle\Phi\rangle_{\mu=0}$ is the thermal expectation value of the Polyakov loop at zero chemical potential. From (5.35) two regimes emerge:

- If $\langle\Phi\rangle_{\mu=0} = 0$, then $\ln\langle\Phi\rangle_{\mu=0} \to -\infty$ and hence $F_q \to +\infty$. Physically, this implies that an infinite amount of energy is required to introduce an isolated quark into the gluonic medium, so single-quark states cannot exist.
- If $\langle\Phi\rangle_{\mu=0} \neq 0$, then $\ln\langle\Phi\rangle_{\mu=0}$ and F_q are finite, indicating that it is energetically possible to create a single quark in the gluonic background.

The similarity between Φ and the world line of a static quark in a Wilson loop, suggests that free energy of a static quark-antiquark pair separated by $\mathbf{x}_1$ and $\mathbf{x}_2$ can be extracted from the correlation function of two such loops with opposite orientations,

$$\Big\langle \Phi(\mathbf{x}_1)\Phi^\dagger(\mathbf{x}_2)\Big\rangle_{\mu=0} \propto \exp(-\beta F_{\bar{q}q}(|\mathbf{x}_1 - \mathbf{x}_2|)). \tag{5.36}$$

As in the $T = 0$ Wilson loop case, the static quark-antiquark potential $F_{\bar{q}q}(r)$ is an important quantity to characterise whether the system is in a confined or deconfined phase. The confined phase should be described by a linearly rising potential characterised by a string tension σ, as discussed in Sec. 3.3. On the other hand, in the deconfined phase, the inter-quark potential is thermally screened and $F_{\bar{q}q}$ converges to a constant. Thus,

$$F_{\bar{q}q}(r) = \begin{cases} \sigma\, r\,, & \text{(confined phase, string tension } \sigma\text{)}, \\ \text{const.}\,, & \text{(deconfined phase, screened potential)}. \end{cases} \tag{5.37}$$

Accordingly, the Polyakov loop correlator decays exponentially with the separation in the confined phase, while it approaches a constant in the deconfined phase.

Moreover we may view $\langle\Phi\rangle_{\mu=0}$ as an order parameter for the spontaneous breaking of centre symmetry. If a physical state is invariant under the gauge transformation (5.22), the expectation value Polyakov loop changes as

$$\langle\Phi\rangle_{\mu=0} \longrightarrow z\,\langle\Phi\rangle_{\mu=0}\,, \quad z \in Z_{N_c}. \tag{5.38}$$

If $z \neq 1$, then $\langle\Phi\rangle_{\mu=0}$ is gauge-dependent, and by the Elitzur's theorem must vanish in the confined phase in order to preserve the centre symmetry,

$$\langle\Phi\rangle_{\mu=0} = 0. \tag{5.39}$$

Intuitively, confinement implies no preferred colour direction: all Z_{N_c} sectors contribute equally, so the thermal weight for quark excitations involves a sum of phase factors, $\sum_n e^{i2\pi n/N_c} = 0$, and the Polyakov-loop expectation value vanishes, screening single-quark states.

In the deconfined phase, $\langle\Phi\rangle_{\mu=0} \neq 0$ and the centre symmetry is spontaneously broken.

There are then N_c distinct possible values of $\langle\Phi\rangle_{\mu=0}$, with

$$\langle\Phi\rangle_{\mu=0} = e^{i2\pi n/N_c} |\langle\Phi\rangle_{\mu=0}|. \tag{5.40}$$

In summary, in the pure Yang-Mills theory and assuming that $\left\langle\Phi(\mathbf{x}_1)\Phi^\dagger(\mathbf{x}_2)\right\rangle_{\mu=0}$ satisfies clustering,

$$\left\langle\Phi(\mathbf{x}_1)\Phi^\dagger(\mathbf{x}_2)\right\rangle_{\mu=0} \xrightarrow[|\mathbf{x}_1-\mathbf{x}_2|\to\infty]{} |\langle\Phi\rangle_{\mu=0}|^2, \tag{5.41}$$

we have:

- **Confined (Symmetric) Phase:**

$$\left\langle\Phi(\infty)\Phi^\dagger(0)\right\rangle_{\mu=0} = 0 \implies \langle\Phi\rangle_{\mu=0} = 0 \implies F_q \longrightarrow \infty, \tag{5.42}$$

- **Deconfined (Broken) Phase:**

$$\left\langle\Phi(\infty)\Phi^\dagger(0)\right\rangle_{\mu=0} \neq 0 \implies \langle\Phi\rangle_{\mu=0} \neq 0 \implies F_q \geq 0, \tag{5.43}$$

meaning that the Polyakov loop can be used as an exact order parameter for deconfinement in a pure gluonic medium and the breaking of the centre symmetry. A centre-symmetric state corresponds to the confined phase, while the deconfined phase is accompanied by the spontaneous breaking of centre symmetry. Physically, the Polyakov loop represents the screening factor of colour charge in a gluonic medium.

When dynamical quarks are included the centre symmetry is explicitly broken, as we have shown in the previous subsection, meaning that the Polyakov loop is only an approximate symmetry order parameter. Furthermore, when considering a finite chemical potential, $\mu \neq 0$, the free energy is not purely real, and the argument given above is not completely valid. Nevertheless, as already mentioned before, in much situations it remains a good indicator for confinement.

5.2.3 Effective PNJL Potential

As already mentioned, to explore the deconfinement transition and the spontaneous breaking of centre symmetry within the NJL model, we couple the Polyakov loop to the quark sector. Concretely, one introduces an effective PNJL potential U_{PNJL}, constructed via a Ginzburg–Landau ansatz so that the Z_3 symmetry is preserved at low temperatures and spontaneously broken above the critical temperature. A widely used choice is the logarithmic form proposed in Refs. [292–294] that reads

$$\begin{aligned}\frac{U_{\text{PNJL}}(\Phi,\bar{\Phi},T)}{T^4} = &-\frac{a(T)}{2}\langle\bar{\Phi}\rangle\langle\Phi\rangle \\ &+ b(T)\ln\left[1 - 6\langle\bar{\Phi}\rangle\langle\Phi\rangle + 4\left(\langle\bar{\Phi}\rangle^3 + \langle\Phi\rangle^3\right) - 3\left(\langle\bar{\Phi}\rangle\langle\Phi\rangle\right)^2\right],\end{aligned} \tag{5.44}$$

with the temperature-dependent coefficients

$$a(T) = a_0 + a_1\left(\frac{T_0}{T}\right) + a_2\left(\frac{T_0}{T}\right)^2, \quad b(T) = b_3\left(\frac{T_0}{T}\right)^3, \tag{5.45}$$

where a_0, a_1, a_2, b_3, T_0 are fixed by fits to LQCD calculations. Here, the Polyakov loop field is set to be equal to its expectation value, i.e., $\langle\Phi(\mathbf{x})\rangle = \langle\Phi\rangle$ and $\langle\bar{\Phi}(\mathbf{x})\rangle = \langle\bar{\Phi}\rangle$, which minimises (5.44). At vanishing chemical potential ($\mu = 0$), or in the absence of quarks, the Polyakov loop and its conjugate coincide, i.e., $\langle\Phi\rangle = \langle\bar{\Phi}\rangle$. In contrast, at finite chemical potential ($\mu \neq 0$), it is common to treat $\langle\Phi\rangle$ and $\langle\bar{\Phi}\rangle$ as two independent real fields. This prescription is motivated by the so-called sign problem within the PNJL model. In the case of the gauge group $SU(3)_c$, the Polyakov loop variables Φ and $\bar{\Phi}$ are generally complex. While the effective potential remains real and positive at $\mu = 0$, a non-zero chemical potential introduces an imaginary part into the thermodynamic potential, arising from quark-antiquark contributions (see Eq. (5.53)). By promoting Φ and $\bar{\Phi}$ to independent variables, one can avoid this issue and ensure a real-valued effective potential, thus maintaining a consistent mean-field treatment at finite density.

The logarithmic term arises from the Haar measure[3] of $SU(3)_c$, with the cubic contributions reflecting the centre symmetry structure. Alternative forms of the Polyakov loop potential, such as the polynomial parametrization [296], are possible, but the logarithmic form (5.44) has the advantage of restricting $\langle\Phi\rangle, \langle\bar{\Phi}\rangle \leq 1$, with equality reached in the deconfined phase.

5.2.4 Mean-Field PNJL Model

Introducing the PNJL potential U_{PNJL} in the NJL Lagrangian (5.1), we obtain the $(2+1)-$ flavour PNJL model:

$$\begin{aligned}
\mathcal{L}_{\text{PNJL}} &= \bar{\psi}\left(i\gamma^\mu D_\mu - m + \mu\gamma^0\right)\psi \\
&+ G_D\left[\det_f \bar{\psi}(1+\gamma_5)\psi + \det_f \bar{\psi}(1-\gamma_5)\psi\right] \\
&+ G_S\sum_{a=0}^{8}\left[(\bar{\psi}\lambda^a\psi)^2 + (\bar{\psi}i\gamma_5\lambda^a\psi)^2\right] \\
&- G_V\sum_{a=0}^{8}\left[(\bar{\psi}\gamma^\mu\lambda^a\psi)^2 + (\bar{\psi}\gamma^\mu\gamma_5\lambda^a\psi)^2\right] \\
&- U_{\text{PNJL}}(\Phi, \bar{\Phi}, T).
\end{aligned} \tag{5.46}$$

The Lagrangian is identical to the NJL model aside from two differences: the additional Polyakov loop potential U_{PNJL} that describes the breaking of the Z_3 symmetry, and a minimal coupling of quark fields to a background gluonic in the temporal direction A_4^0, through the covariant derivative

$$D_\mu = \partial_\mu - A_4^0\delta_\mu^0, \tag{5.47}$$

[3] See, e.g., [295] for an introduction to Haar measures on compact groups.

which is a simple way to take into account back-reaction of the quark sector to the gluonic sector.

The mean-field approach to the PNJL Lagrangian follows the same steps as for the NJL model. Thus,

$$\begin{aligned}
\tilde{\mathcal{L}}_{\rm PNJL} &= \bar{\psi}\left(i\gamma^\mu D_\mu - m + \mu\gamma^0\right)\psi \\
&+ 2G_D\left(\bar{\psi}\boldsymbol{\sigma}\psi - 2\sigma_u\sigma_d\sigma_s\right) \\
&+ 2G_S\left[\sqrt{\frac{2}{3}}(\bar{\psi}\lambda^0\psi)(\sigma_u+\sigma_d+\sigma_s) - \frac{1}{3}(\sigma_u+\sigma_d+\sigma_s)^2\right. \\
&\quad + (\bar{\psi}\lambda^3\psi)(\sigma_u-\sigma_d) - \frac{1}{2}(\sigma_u-\sigma_d)^2 \\
&\quad \left. + \frac{1}{\sqrt{3}}(\bar{\psi}\lambda^8\psi)(\sigma_u+\sigma_d-2\sigma_s) - \frac{1}{6}(\sigma_u+\sigma_d-2\sigma_s)^2\right] \\
&- 2G_V\left[\sqrt{\frac{2}{3}}(\bar{\psi}\gamma^0\lambda^0\psi)(\rho_u+\rho_d+\rho_s) - \frac{1}{3}(\rho_u+\rho_d+\rho_s)^2\right. \\
&\quad + (\bar{\psi}\gamma^0\lambda^3\psi)(\rho_u-\rho_d) - \frac{1}{2}(\rho_u-\rho_d)^2 \\
&\quad \left. + \frac{1}{\sqrt{3}}(\bar{\psi}\gamma^0\lambda^8\psi)(\rho_u+\rho_d-2\rho_s) - \frac{1}{6}(\rho_u+\rho_d-2\rho_s)^2\right] \\
&- U_{\rm PNJL}(\Phi,\bar{\Phi},T).
\end{aligned} \tag{5.48}$$

The above can be written in the more compact form given by Eq. (4.69):

$$\tilde{\mathcal{L}}_{\rm PNJL} = \bar{\psi}\left[i\gamma^\mu\left(D_\mu + iV_0\delta^0_\mu\right) + \mu\gamma^0 - (m+S)\right]\psi + U_{\rm cond} - U_{\rm PNJL}(\Phi,\bar{\Phi},T), \tag{5.49}$$

where the auxiliary field V_0 and S, and the condensate (mean-field) potential $U_{\rm cond}$ are as the same as in the NJL model, given by Eqs. (5.15), (5.16) and (5.17), respectively.

Gap Equations

Let m^* be the effective (dynamical) mass defined by

$$m^* \equiv m + S, \tag{5.50}$$

and the effective chemical potential μ^*

$$\mu^* \equiv \mu - V_0. \tag{5.51}$$

From (4.90) the grand-canonical potential in the MFA is

$$\begin{aligned}
\tilde{\Omega}_{\rm PNJL} &= \Omega_0 + U_{\rm PNJL} - U_{\rm cond} \\
&- 2T\ {\rm Tr}_{f,c}\int\frac{{\rm d}^3p}{(2\pi)^3}\left[\beta E(\mathbf{p}) + \ln\left(1+e^{-\beta(E+\mu^*-iA_4^0)}\right) + \ln\left(1+e^{-\beta(E-\mu^*+iA_4^0)}\right)\right],
\end{aligned} \tag{5.52}$$

with the Hartree single quasi-particle energy $E(\mathbf{p}) = \sqrt{\mathbf{p}^2 + m^{*2}}$. Applying the identity $\mathrm{Tr}\ln A = \ln\det A$ over the colour indices, we obtain

$$\begin{aligned}\tilde{\Omega}_{\mathrm{PNJL}} &= \Omega_0 + U_{\mathrm{PNJL}} - U_{\mathrm{cond}} \\ &\quad - 2T \sum_{f=u,d,s} \int \frac{\mathrm{d}^3p}{(2\pi)^3} \left[N_c \beta E(\mathbf{p}) + \ln \det_c \left(1 + L e^{-\beta(E_f + \mu_f^*)}\right) + \ln \det_c \left(1 + L^\dagger e^{-\beta(E_f - \mu_f^*)}\right)\right],\end{aligned} \tag{5.53}$$

where we have defined

$$L = \exp(i\beta A_4) \quad \text{and} \quad L^\dagger = \exp(-i\beta A_4). \tag{5.54}$$

To evaluate the determinant over colour space, we can use, without loss of generality, the gauge condition proposed in [297], in which A_4 is diagonal in colour space, i.e., $A_4 = \mathrm{diag}_c(A_{11}\ A_{22}\ A_{33})$. Thus, after some algebra, we obtain

$$\begin{aligned}\det_c \left(1 + L e^{-\beta(E_f + \mu_f^*)}\right) &= 1 + N_c \Phi e^{-\beta(E_f+\mu_f^*)} + N_c \bar{\Phi} e^{-2\beta(E_f+\mu_f^*)} + e^{-3\beta(E_f+\mu_f^*)}, \\ \det_c \left(1 + L^\dagger e^{-\beta(E_f - \mu_f^*)}\right) &= 1 + N_c \bar{\Phi} e^{-\beta(E_f-\mu_f^*)} + N_c \Phi e^{-2\beta(E_f-\mu_f^*)} + e^{-3\beta(E_f-\mu_f^*)},\end{aligned} \tag{5.55}$$

where we have associated the Polyakov loop and its complex conjugate with L and $L^\dagger$ through

$$\Phi = \frac{1}{N_c}\mathrm{Tr}_c L, \quad \text{and} \quad \bar{\Phi} = \frac{1}{N_c}\mathrm{Tr}_c L^\dagger. \tag{5.56}$$

The grand canonical potential $\tilde{\Omega}_{\mathrm{PNJL}}$ now reads

$$\begin{aligned}\tilde{\Omega}_{\mathrm{PNJL}} &= \Omega_0 + U_{\mathrm{PNJL}} - U_{\mathrm{cond}} \\ &\quad - 2T \sum_{f=u,d,s} \int \frac{\mathrm{d}^3p}{(2\pi)^3} \left[N_c \beta E(\mathbf{p}) + z^+(\Phi, \bar{\Phi}, E_f, \mu_f^*) + z^-(\Phi, \bar{\Phi}, E_f, \mu_f^*)\right],\end{aligned} \tag{5.57}$$

where we have defined for simplicity,

$$\begin{aligned}z^-(\Phi, \bar{\Phi}, E_f, \mu_f^*) &\equiv \ln\left(1 + N_c \Phi e^{-\beta(E_f+\mu_f^*)} + N_c \bar{\Phi} e^{-2\beta(E_f+\mu_f^*)} + e^{-3\beta(E_f+\mu_f^*)}\right), \\ z^+(\Phi, \bar{\Phi}, E_f, \mu_f^*) &\equiv \ln\left(1 + N_c \bar{\Phi} e^{-\beta(E_f-\mu_f^*)} + N_c \Phi e^{-2\beta(E_f-\mu_f^*)} + e^{-3\beta(E_f-\mu_f^*)}\right).\end{aligned} \tag{5.58}$$

The fields Φ, $\bar{\Phi}$, and the quantities m_f^*, σ_f can be obtained by solving

$$\frac{\partial \tilde{\Omega}_{\mathrm{PNJL}}}{\partial \Phi} = \frac{\partial \tilde{\Omega}_{\mathrm{PNJL}}}{\partial \bar{\Phi}} = 0, \tag{5.59}$$

$$\frac{\partial \tilde{\Omega}_{\mathrm{PNJL}}}{\partial m_u^*} = \frac{\partial \tilde{\Omega}_{\mathrm{PNJL}}}{\partial m_d^*} = \frac{\partial \tilde{\Omega}_{\mathrm{PNJL}}}{\partial m_s^*} = 0, \tag{5.60}$$

i.e., by finding the fields and parameters that minimise the mean-field grand canonical potential. Each condition above will lead to a system self-consistent equations that are required to be solved in order to find each quantity. These will constitute the **gap equations** of the theory.

The gap equations for the Polyakov loop fields Φ and $\bar{\Phi}$ yield (see App. B.2)

$$-\frac{a(T)}{2}\bar{\Phi} = \frac{6b(T)(\bar{\Phi} - 2\Phi^2 + \bar{\Phi}^2\Phi)}{1 - 6\bar{\Phi}\Phi + 4(\bar{\Phi}^3 + \Phi) - 3(\bar{\Phi}\Phi)^2} + \frac{2N_c}{T^3}\sum_{f=u,d,s}\int\frac{\mathrm{d}^3p}{(2\pi)^3}\left(e^{-\beta(E_f+\mu_f^*)-z^-} + e^{-2\beta(E_f-\mu_f^*)-z^+}\right), \tag{5.61a}$$

$$-\frac{a(T)}{2}\Phi = \frac{6b(T)(\Phi - 2\bar{\Phi}^2 + \bar{\Phi}\Phi^2)}{1 - 6\bar{\Phi}\Phi + 4(\bar{\Phi}^3 + \Phi) - 3(\bar{\Phi}\Phi)^2} + \frac{2N_c}{T^3}\sum_{f=u,d,s}\int\frac{\mathrm{d}^3p}{(2\pi)^3}\left(e^{-\beta(E_f-\mu_f^*)-z^+} + e^{-2\beta(E_f+\mu_f^*)-z^-}\right). \tag{5.61b}$$

The mass gap equations read[4]

$$m_i^* = m_i - 4G_S\sigma_i - 2G_D\sigma_j\sigma_k, \quad i \neq j \neq k \in \{u, d, s\}, \tag{5.62}$$

where m_i is the current mass, and σ_i is the quark condensate for flavour i, obtained by solving

$$\frac{\partial\tilde{\Omega}_{\mathrm{PNJL}}}{\partial\sigma_u} = \frac{\partial\tilde{\Omega}_{\mathrm{PNJL}}}{\partial\sigma_d} = \frac{\partial\tilde{\Omega}_{\mathrm{PNJL}}}{\partial\sigma_s} = 0, \tag{5.63}$$

that yields (see App. B.2)

$$\sigma_f = -2N_c\int\frac{\mathrm{d}^3p}{(2\pi)^3}\frac{m_f^{*2}}{E_f}(1 - \mathcal{F}_f^+ - \mathcal{F}_f^-), \tag{5.64}$$

where $\mathcal{F}_f^+$ and $\mathcal{F}_f^-$ are the particle and antiparticle modified Fermi-Dirac distribution functions defined by

$$\mathcal{F}_f^+ = \frac{\frac{3}{N_c}e^{-3\beta(E_f-\mu_f^*)} + \bar{\Phi}e^{-\beta(E_f-\mu_f^*)} + 2\Phi e^{-2\beta(E_f-\mu_f^*)}}{1 + e^{-3\beta(E_f-\mu_f^*)} + N_c\bar{\Phi}e^{-\beta(E_f-\mu_f^*)} + N_c\Phi e^{-2\beta(E_f-\mu_f^*)}}, \tag{5.65a}$$

$$\mathcal{F}_f^- = \frac{\frac{3}{N_c}e^{-3\beta(E_f+\mu_f^*)} + \Phi e^{-\beta(E_f+\mu_f^*)} + 2\bar{\Phi}e^{-2\beta(E_f+\mu_f^*)}}{1 + e^{-3\beta(E_f+\mu_f^*)} + N_c\Phi e^{-\beta(E_f+\mu_f^*)} + N_c\bar{\Phi}e^{-2\beta(E_f+\mu_f^*)}}. \tag{5.65b}$$

Bulk properties of the system can be obtained from derivatives of $\tilde{\Omega}_{\mathrm{PNJL}}$ with respect to various thermodynamical quantities as expressed by Eqs. (4.27)

5.2.5 Statistical Confinement

We close this chapter by emphasizing an important point: the deconfinement transition induced by coupling the Polyakov loop to the NJL model is of a statistical nature only — it does not represent true confinement. In the PNJL framework, gluons remain a static background field rather than dynamical degrees of freedom, and the underlying Lagrangian still permits

[4] The same result could also be obtained by simplifying each matrix element of (5.50) in flavour space.

asymptotically free quark states.

The role of the Polyakov loop fields Φ and $\bar{\Phi}$ becomes clear in last term of the mean-field potential (5.53). Through the relation (5.56), the matrices L and $L^\dagger$ suppress the thermal weights $\exp(-\beta(E_f \pm \mu_f^*))$ whenever Φ, $\bar{\Phi}$ are small. This mechanism reduces unphysical quark excitations below T_c, mimicking confinement effects in the thermodynamics. However, these contributions never vanish entirely, and the Fock space still contains asymptotically free quark states; only their occupation number distributions are modified.

Nonetheless, extending the NJL to the PNJL model offers several advantages besides describing confinement: it yields thermodynamic observables in better agreement with LQCD, predicts lower baryon densities at fixed T and μ than the NJL model alone [293], and sharpens the chiral transition into a narrower temperature interval [298].

Chapter 6

Hadronic Models

If I could remember the names of all these particles I'd be a botanist.

– Enrico Fermi[1]

Under ordinary conditions of temperature and density, quarks and gluons are confined within colour-singlet hadrons (for example, protons and neutrons) by the strong force. Analogous to quark matter, nuclear matter is characterised by its **equation of state** (EoS). As discussed in Ch. 2, a first-order transition to deconfined/chiral restored matter is conjectured to occur at sufficiently high density or temperature, giving rise to a mixed phase of hadrons and deconfined quarks. To model this intermediate regime accurately, a reliable hadronic EoS is required.

In this chapter, we begin by defining nuclear matter and summarising its key empirical properties. We then discuss the shortcomings of early non-relativistic approaches and introduce the early Walecka model as the basis of relativistic mean-field theory. Building on this, we analyse modern covariant field-theoretical models that incorporate non-linear meson couplings and density-dependent interactions. Finally, we present arguments for the possible appearance of hyperons in dense baryonic systems and the implications for the high-density EoS.

6.1 Nuclear Matter

With the exception of the deuteron and other few-nucleon systems, most nuclear-structure calculations are phenomenological rather than derived from first principles. Even in a non-relativistic formulation, solving the many-body Schrödinger equation for multiple interacting nucleons is a formidable task. An analogous situation arises in atomic physics: the hydrogen atom admits an exact solution, whereas atoms with several electrons generally require approximation methods despite the Coulombic nature of the inter-particle forces.

[1] As quoted in [299].

The corresponding problem in nuclear physics, of several nucleons interacting quantum mechanically with each other, is even more difficult than the one involving several electrons in atoms. There are two reasons for this:

1. **Identical-mass dynamics.** Electrons move in the static field of a heavy nucleus; nucleons all have comparable mass and interact dynamically, so no fixed-centre approximation is possible

2. **Nuclear force complexity.** The complexity of the force between two nucleons (the residual strong force) is much higher than the electromagnetic force at the atomic level. A complete theory of nuclear interactions at arbitrarily large values of density, temperature and isospin asymmetry, should in principle be derived from QCD. This is, however, a very difficult task which has not been realized.

Although describing a n-body dynamics is exceedingly difficult for any finite value of $n > 2$, in the limit $n \to \infty$ we can, in most situations, exploit the translational invariance of the system, making its description more tractable. For this reason, one hypothesises what is known by (infinite) **nuclear matter**: an ideal infinite system of strongly-interacting nucleons in the absence of electromagnetic interactions.

6.1.1 General Properties

Before we introduce a many-body description of nuclear matter, it is useful to first characterise the two-nucleon potential. Since an exact derivation from QCD remains out of reach, theoretical models are constructed to reproduce accurately empirical features of the nuclear force:

- **Short-ranged attraction.** The attractive component of the nuclear interaction is much stronger than the Coulomb repulsion at short range; nevertheless, nuclei remain finite in size. This observation indicates that the attractive force is short ranged, decaying rapidly for separations larger than of order $1 - 2$ fm.

- **Hard repulsive core.** Even though the short-range of the nuclear attraction prevents nuclei from growing arbitrary, one might question why cannot many more nucleons, especially neutrons, squeeze within this range? As more nucleons into the same volume, the system should become increasingly stable since each nucleon would now be held in by the combined attraction of all the others. Therefore, nucleons of very high atomic weight should exist. That such heavy nuclei are not observed in nature is due to a steep repulsive component at short distances, which prevent nucleons to be packed too close to each other. This short range repulsion extends up to about $0.5 - 0.7$ fm depending on details of our model.

- **Saturation.** The addition of a nucleon to the bulk only increases the volume, not the binding energy per nucleon, which implies an intermediate attraction.

- **Homogeneity and isotropy.** The nuclear medium is homogeneous, isotropic and composed of independent particles.

These properties led to a qualitative illustration of the nucleon-nucleon potential as shown in Fig. 6.1. Moreover, they were the basis for early successful phenomenological models, namely the **liquid-drop model** [300] and the **Bethe-Weizsäcker semi-empirical mass formula** [151,301], where the nucleus is treated as an incompressible quantum liquid drop with a constant (saturation) density ρ_0 at first approximation.

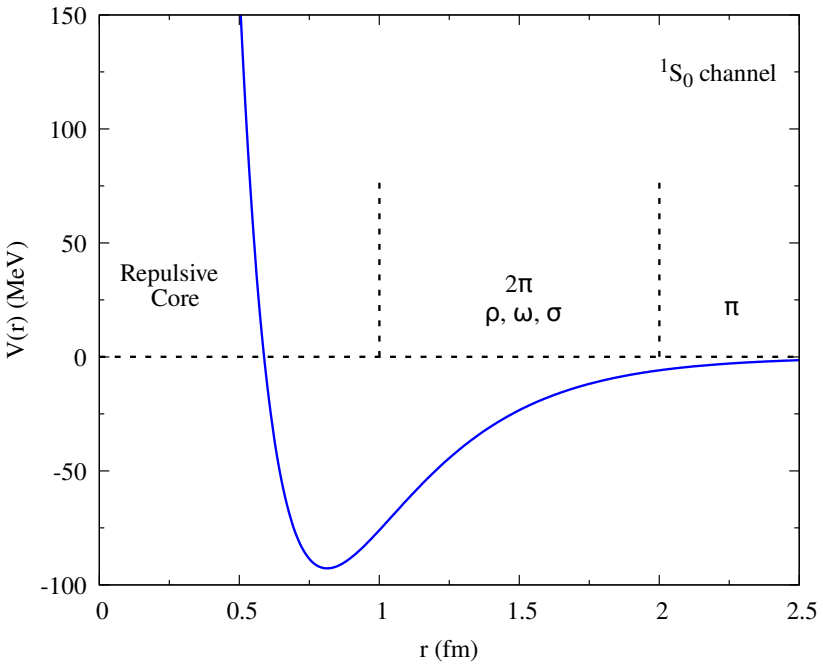

Figure 6.1: Model of the nucleon-nucleon potential. At large separations, the longest-range attraction is mediated by the lightest meson (π). At intermediate distances, heavier mesons (ρ, ω, σ) provide additional attractive and repulsive contributions. Below $r \approx 1$ fm, the interaction becomes strongly repulsive ("hard core"), preventing nucleons merging and signalling the onset of quark–gluon dynamics that must be treated within QCD. (The figure is purely illustrative.)

6.1.2 Limitations of Non-Relativistic Models

Among various quantities in nuclear matter, the saturation density and the binding energy are the most basic physical observables. For symmetric nuclear matter the empirical value for the binding energy per nucleon is $\epsilon_B \approx 16.3$ MeV, realized at the saturation density $\rho_0 \approx 0.153$ fm^{-3}. Up until the mid 1970's microscopic non-relativistic approaches to describe the nucleon-nucleon interaction could not predict both of these basic nuclear properties. Part of the discrepancies were assigned to a poor description of many-body interactions, but also relativistic effects play an important role, especially, in high-density media. Its importance can better be understood by comparing the Fermi momentum to the nucleon mass. The baryon density for a free Fermi

gas reads

$$\rho = \frac{g}{V}\int_{|\mathbf{p}|\leq k_f}\frac{\mathrm{d}^3p}{(2\pi)^3} = \frac{2k_F^3}{3\pi^2}, \tag{6.1}$$

where $g = 4$ is the degeneracy due to spin and isospin degrees of freedom. The Fermi momentum corresponding to ρ_0 is $k_F \approx 260$ MeV, which is less than one third of $m_N \approx 939$ MeV, meaning that $k_F/m_N < 1$ and an expansion in terms of $v_F \approx k_F/m_N$ is possible. Therefore, the Fermi kinetic energy reads

$$K_F = m_N\left(\frac{1}{\sqrt{1-v_F^2}} - 1\right) \approx \frac{1}{2}m_N v_F^2 + \frac{3}{8}m_N v_F^4 + \ldots, \tag{6.2}$$

At ρ_0, the second term gives relativistic corrections of about 2 MeV, which is small but not insignificant, compared the binding energy. For higher baryon densities, these corrections cannot be neglected, meaning that in order to achieve an accurate description of nuclear matter, relativity must be taken into consideration. A relativistic field-theory approach to nuclear matter was pioneered by Johnson and Teller [302], Duer [303] and Walecka [123].

6.2 Relativistic Hadron Field Theory

In the relativistic field theory of hadronic matter, baryons are treated as Dirac particles that interact through the exchange of mesons, providing a covariant description of the EoS and nuclear system [124]. This formalism has been in wide use over the last four decades for describing the properties of the nuclear EoS and of finite nuclei in a relativistic quantum framework.

In this section we start by reviewing the early Walecka model and its limitations. We follow by introducing some modern extensions, namely, the NL3$\omega\rho$ model and the hyperonic FSU2R model.

6.2.1 The Walecka Model

In the **Walecka model** or the $\boldsymbol{\sigma - \omega}$ **model** [123], nuclear matter is approximated by a Fermi gas of in-medium nucleons that act as sources for mean-fields in the scalar channel (represented by the σ meson) and the vector channel (represented by the ω meson). In other words, baryons are the constituents of the nuclear medium, whereas the mesons are the carriers of the interaction between baryons.

The nucleon-nucleon potential has an origin in the pion exchange for the long-range part of the nuclear force and also heavier mesons for short distances. At low temperature, in the mean-field approximations, pion degrees of freedom can be dropped as it is assumed that interaction effects due to pion exchanges can be renormalised in a one-body potential represented by the mean-fields. However, at high enough temperatures pions are thermally excited and should be considered in our model. In [304] it has been shown that the influence of pions on the hadron-quark phase transition becomes important at $T \approx m_\pi$. Here the presence of pions results in

a change of the CEP. In most situations this correspond in small shift of the CEP to higher temperatures, but in one case the CEP was completely removed from the transition curve. Pion degrees of freedom will not be considered in this work, but the effects due to their presence will be reserved for future investigation.

The Lagrangian of the Walecka model is defined by[2]

$$\begin{aligned}\mathcal{L}_{\mathrm{W}} = \sum_{b=n,p} \bar{\psi}_b \left[i\gamma^\mu(\partial_\mu + ig_{\omega N}\omega_\mu - i\mu_b\delta^0_\mu) - (m_b - g_{\sigma N}\sigma) \right] \psi_b \\ + \frac{1}{2}\left[\partial_\mu\sigma\partial^\mu\sigma - m_\sigma^2\sigma^2\right] - \frac{1}{4}\omega_{\mu\nu}\omega^{\mu\nu} + \frac{1}{2}m_\omega^2\omega_\mu\omega^\mu,\end{aligned} \tag{6.3}$$

where m_σ and m_ω are the masses, and g_σ, g_ω, $g_{\sigma N}$ and $g_{\omega N}$ are coupling constants. The term $\omega_{\mu\nu} = \partial_\mu\omega_\nu - \partial_\nu\omega_\mu$ is the strength tensor of the vector meson, and ψ_b represents the nucleonic Dirac fields. Apart from the free terms, an interaction term has been included,

$$\mathcal{L}^{\mathrm{int}}_{\mathrm{W}} = g_{\sigma N}\sigma\bar{\psi}_b\psi_b - g_{\omega N}\bar{\psi}_b\gamma_\mu\omega^\mu\psi_b, \tag{6.4}$$

where the σ mesons is coupled to the scalar density $\bar{\psi}_b\psi_b$ and the ω meson is coupled to the baryon four-current $\bar{\psi}_b\gamma^\mu\psi_b$.

The simple Walecka model is able to predict the expected energy per nucleon minimum at ρ_0 for symmetric nuclear matter, and provides a reasonable value for the critical-point temperature of the liquid-gas phase transition. However, it fails to predict other quantities such as the compression modulus at saturation, $K \approx 553$ MeV, which is two times larger than it should be, or the in-medium nucleon mass ratio, $m^*_N/m_N \approx 0.55$, where $m^*_N \equiv m_N - g_{\sigma N}\sigma$, which is in poor agreement with the empirical range. Both features lead to an extremely stiff equation of state at high density. Consequently, this model's extrapolation to densities beyond nuclear saturation — whether in symmetric or asymmetric matter — is unreliable. To correct this, a potential term $U(\sigma,\omega)$ should be added in the Lagrangian (6.3).

6.2.2 Non-Linear Walecka-type Model

In the present work we are also interested to study the effects due to the inclusion of hyperons[3] in the baryon octet. Three modern hadronic models will be used: the nucleonic **NL3$\omega\rho$ model** and the hyperonic **FSU2R** and **FSU2H models** .

The three models for the EoS are based on a **non-linear Waleka** (NLW) Lagrangian [124, 305–307]:

[2] Note that $g_{\sigma p} = g_{\sigma n} \equiv g_{\sigma N}$ and $g_{\omega p} = g_{\omega n} \equiv g_{\omega N}$.

[3] Hyperons are baryons containing one or more strange quarks, but no charm, top, or bottom quarks.

$$
\begin{aligned}
\mathcal{L}_{\rm NLW} = &\sum_b \bar{\psi}_b \left[i\gamma^\mu \left(\partial_\mu + i g_{\omega b}\omega_\mu + \frac{i}{2} g_{\rho b}\boldsymbol{\tau}_b \boldsymbol{\rho}_\mu + i g_{\phi b}\phi_\mu - i\mu_b \delta^0_\mu \right) - (m_b - g_{\sigma b}\sigma) \right] \psi_b \\
&+ \frac{1}{2}\partial_\mu\sigma\partial^\mu\sigma - \frac{1}{2}m_\sigma^2\sigma^2 - \frac{\kappa}{3!}(g_{\sigma N}\sigma)^3 - \frac{\lambda}{4!}(g_{\sigma N}\sigma)^4 \\
&- \frac{1}{4}\omega_{\mu\nu}\omega^{\mu\nu} + \frac{1}{2}m_\omega^2\omega_\mu\omega^\mu + \frac{\xi}{4!}g_{\omega N}^4(\omega_\mu\omega^\mu)^2 \\
&- \frac{1}{4}\boldsymbol{\rho}_{\mu\nu}\boldsymbol{\rho}^{\mu\nu} + \frac{1}{2}m_\rho^2\boldsymbol{\rho}_\mu\boldsymbol{\rho}^\mu + \Lambda_\omega g_{\rho N}^2 g_{\omega N}^2 \boldsymbol{\rho}_\mu\boldsymbol{\rho}^\mu\omega_\mu\omega^\mu \\
&- \frac{1}{4}\phi_{\mu\nu}\phi^{\mu\nu} + \frac{1}{2}m_\phi^2\phi_\mu\phi^\mu .
\end{aligned}
\tag{6.5}
$$

Here b runs over the spin-1/2 baryons in the baryon octet which consists of n, p, Λ^0, Σ^+, Σ^0, Σ^-, Ξ^0, Ξ^-. The strong interaction coupling of a meson to a certain baryon is denoted by g (with N indicating nucleon). All models mentioned above correspond to the exclusion or inclusion of some of the terms in (6.5).

The addition of σ meson self-interactions to (6.3) were introduced in [308], and they allowed for a better quantitatively descriptions of nuclear matter and finite nuclei within the relativistic framework. This corresponds to adding a potential composed of three- and four-body interactions:

$$
\mathcal{L}_{\sigma\sigma} = -\frac{\kappa}{3!}\left(g_{\sigma N}\sigma\right)^3 - \frac{\lambda}{4!}(g_{\sigma N}\sigma)^4 . \tag{6.6}
$$

Their presence leads to a softening of the EoS at moderate densities and allow one to obtain a realistic compressibility of nuclear matter [308, 309].

A quartic self-coupling of the ω meson was proposed in [310],

$$
\mathcal{L}_{\omega\omega} = \frac{\xi}{4!}\left(g_{\omega N}\,\omega_\mu\omega^\mu\right)^4 , \tag{6.7}
$$

where the coupling ξ must be non-negative to avoid abnormal solutions of the ω-field equation of motion [310, 311]. This term increases the effective vector repulsion at high density, thereby softening the equation of state and allowing improved fits to nuclear ground-state properties and to Dirac-Brueckner-Hartree-Fock calculations at large densities [310].

Furthermore, since we are interested in study the effects due to isospin asymmetry the isovector ρ meson must be included in our model,

$$
\mathcal{L}_\rho = -\frac{1}{4}\boldsymbol{\rho}_{\mu\nu}\boldsymbol{\rho}^{\mu\nu} + \frac{1}{2}m_\rho^2\boldsymbol{\rho}_\mu\boldsymbol{\rho}^\mu , \tag{6.8}
$$

with $\boldsymbol{\rho}_{\mu\nu} = \partial_\mu\boldsymbol{\rho}_\nu - \partial_\nu\boldsymbol{\rho}_\mu$, that couples to the isospin current of the baryons as

$$
\mathcal{L}_{\rho b} = -\frac{1}{2}g_{\rho b}\bar{\psi}_b\gamma^\mu\boldsymbol{\tau}_b\boldsymbol{\rho}_\mu\psi_b , \tag{6.9}
$$

as it is key for the nuclear symmetry energy, which measures the energy cost involved in changing all the protons into neutrons in nuclear matter [312].

A non-linear interaction between the ω and ρ mesons can be allowed,

$$\mathcal{L}_{\omega\rho} = \Lambda_\omega g_{\rho N}^2 g_{\omega N}^2 \boldsymbol{\rho}_\mu \boldsymbol{\rho}^\mu \omega_\mu \omega^\mu. \tag{6.10}$$

This term modulates the density dependence of the nuclear symmetry energy, allowing one to obtain a good slope of the symmetry energy at saturation density [305, 313].

Finally, when including hyperons, one can also includes the vector meson ϕ, since it couples to the hyperons and represents vector repulsions among them. This correspond to adding the free term

$$\frac{1}{2} m_\phi^2 \phi_\mu \phi^\mu - \frac{1}{4} \phi_{\mu\nu} \phi^{\mu\nu}, \tag{6.11}$$

and the interaction terms

$$\mathcal{L}_{\phi b} = -g_{\phi b} \bar{\psi}_b \gamma^\mu \phi_\mu \psi_b. \tag{6.12}$$

The various couplings in Lagrangian (6.5) are determined in order to fit more of the empirically known properties of nuclear matter such as the saturation density, binding energy, compressibility, etc. obtained from HICs, neutron star observations, or scattering experiments. In the present work, the constrains used for the value of each coupling will be discussed in Ch. 7.

6.2.3 Mean-Field NLW Model

Similar to the NJL and PNJL models, we will work in the mean-field approximation. Here, the σ, ω_μ, $\boldsymbol{\rho}_\mu$ and ϕ_μ fields can take finite expectation values induced by the non-zero chiral condensate and the baryon density. We recall that in the MFA, one neglects fluctuations in the meson fields, meaning that baryons are taken to move independently in the (classical) mean-fields, which themselves are generated self-consistently by the baryons. This approach is known as the **relativistic mean-field theory** [124]. Once more, we replace each field by their respective vacuum expectation value:

$$\langle \sigma \rangle = \sigma, \tag{6.13a}$$
$$\langle \omega_0 \rangle = \omega_0, \tag{6.13b}$$
$$\left\langle \rho_0^3 \right\rangle = \rho_0^3, \tag{6.13c}$$
$$\langle \phi_0 \rangle = \phi_0, \tag{6.13d}$$
$$\langle \omega_i \rangle = \langle \phi_i \rangle = \langle \boldsymbol{\rho}_i \rangle = \left\langle \rho_0^1 \right\rangle = \left\langle \rho_0^2 \right\rangle = 0. \tag{6.13e}$$

where in the last expression $\langle \omega_i \rangle = \langle \phi_i \rangle = 0$ on account of rotational symmetry and $\langle \rho_0^1 \rangle = \langle \rho_0^2 \rangle = 0$ due to charge conservation. Thus, the non-linear Walecka Lagrangian (6.5) in the MFA reads,

$$
\begin{aligned}
\tilde{\mathcal{L}}_{\rm NLW} = & \sum_b \bar{\psi}_b \left[i\gamma^\mu \left(\partial_\mu + i g_{\omega b}\omega_0 \delta^0_\mu + \frac{i}{2} g_{\rho b}\tau^3 \rho^3_0 \delta^0_\mu + i g_{\phi b}\phi_0 \delta^0_\mu - i\mu_b \delta^0_\mu \right) - (m_b - g_{\sigma b}\sigma) \right] \psi_b \\
& - \frac{1}{2} m_\sigma^2 \sigma^2 - \frac{\kappa}{3!}(g_{\sigma N}\sigma)^3 - \frac{\lambda}{4!}(g_{\sigma N}\sigma)^4 \\
& + \frac{1}{2} m_\omega^2 \omega_0^2 + \frac{\xi}{4!}(g_{\omega N}\omega_0)^4 \\
& + \frac{1}{2} m_\rho^2 (\rho_0^3)^2 + \Lambda_\omega g_{\rho N}^2 g_{\omega N}^2 (\rho_0^3)^2 (\omega_0)^2 \\
& + \frac{1}{2} m_\phi^2 \phi_0^2,
\end{aligned}
\tag{6.14}
$$

This expression can be written in the more compact form given by Eq. (4.69):

$$
\tilde{\mathcal{L}}_{\rm NLW} \approx \sum_b \bar{\psi}_b \left[i\gamma^\mu \left(\partial_\mu - i(\mu_b - V_{0,b})\delta^0_\mu \right) - (m_b + S_b) \right] \psi_b + U_{\rm meson}, \tag{6.15}
$$

where

$$
S_b = -g_{\sigma b}\sigma, \tag{6.16}
$$

$$
V_{0,b} = g_{\omega b}\omega_0 + \frac{1}{2} g_{\rho b}\tau_b^3 \rho_0^3 + g_{\phi b}\phi_0, \tag{6.17}
$$

and the mean-field (meson) potential is given by

$$
\begin{aligned}
U_{\rm meson} = & - \frac{1}{2} m_\sigma^2 \sigma^2 - \frac{\kappa}{3!}(g_{\sigma N}\sigma)^3 - \frac{\lambda}{4!}(g_{\sigma N}\sigma)^4 \\
& + \frac{1}{2} m_\omega^2 \omega_0^2 + \frac{\xi}{4!}(g_{\omega N}\omega_0)^4 \\
& + \frac{1}{2} m_\rho^2 (\rho_0^3)^2 + \Lambda_\omega g_{\rho N}^2 g_{\omega N}^2 (\rho_0^3)^2 (\omega_0)^2 \\
& + \frac{1}{2} m_\phi^2 \phi_0^2.
\end{aligned}
\tag{6.18}
$$

From this one can identify the in-medium baryon masses as

$$
m_b^* = m_b - g_{\sigma b}\sigma, \tag{6.19}
$$

and the effective chemical potentials as

$$
\mu_b^* = \mu_b - g_{\omega b}\omega_0 - g_{\rho b} I_{3b} \rho_0^3 - g_{\phi b}\phi_0, \tag{6.20}
$$

where $I_{3b} = \tau_b^3/2$ is the third component of the isospin of a given baryon, and we use the convention that for protons $I_{3p} = +1/2$.

The correspondent grand canonical potential of this model can be obtain from (4.90), where the only additional internal symmetry is the isospin, $I = \{b\}$:

$$
\begin{aligned}
\tilde{\Omega}_{\mathrm{NLW}} = \Omega_0 &+ \frac{1}{2}m_\sigma^2\sigma^2 + \frac{\kappa}{3!}(g_{\sigma N}\sigma)^3 + \frac{\lambda}{4!}(g_{\sigma N}\sigma)^4 \\
&- \frac{1}{2}m_\omega^2\omega_0^2 - \frac{\xi}{4!}(g_{\omega N}\omega_0)^4 \\
&- \frac{1}{2}m_\rho^2(\rho_0^3)^2 - \Lambda_\omega g_{\rho N}^2 g_{\omega N}^2(\rho_0^3)^2(\omega_0)^2 \\
&- \frac{1}{2}m_\phi^2\phi_0^2 \\
&- 2T\sum_b \int \frac{\mathrm{d}^3p}{(2\pi)^3}\left[-\beta E(\mathbf{p}) + \ln\left(1+e^{-\beta\left(E_b+\mu_b^*\right)}\right) + \ln\left(1+e^{-\beta\left(E_b-\mu_b^*\right)}\right)\right],
\end{aligned}
\tag{6.21}
$$

where Ω_0 is chosen in such a way that pressure and energy density are zero in vacuum.

Gap Equations

The mesonic equations of motion in the MFA for the uniform medium can be obtained from the stationary conditions

$$
\frac{\partial\tilde{\Omega}_{\mathrm{NLW}}}{\partial\sigma} = \frac{\partial\tilde{\Omega}_{\mathrm{NLW}}}{\partial\omega_0} = \frac{\partial\tilde{\Omega}_{\mathrm{NLW}}}{\partial\rho_0^3} = \frac{\partial\tilde{\Omega}_{\mathrm{NLW}}}{\partial\phi_0} = 0, \tag{6.22}
$$

which leads to a set of coupled non-linear field equations that involve strong couplings:

$$
m_\sigma^2\sigma + \frac{\kappa}{2}g_{\sigma N}^3\sigma^2 + \frac{\lambda}{3!}g_{\sigma N}^4\sigma^3 = 2\sum_b g_{\sigma b}\int\frac{\mathrm{d}^3p}{(2\pi)^3}\frac{m_b^*}{E_b}(n_b^+ + n_b^-), \tag{6.23a}
$$

$$
m_\omega^2\omega_0 + \frac{\xi}{3!}g_{\omega N}^4\omega_0^3 + 2\Lambda_\omega g_{\rho N}^2 g_{\omega N}^2(\rho_0^3)^2\omega_0 = 2\sum_b g_{\omega b}\int\frac{\mathrm{d}^3p}{(2\pi)^3}(n_b^+ - n_b^-), \tag{6.23b}
$$

$$
m_\rho^2\rho_0^3 + 2\Lambda_\omega g_{\rho N}^2 g_{\omega N}^2\rho_0^3(\omega_0)^2 = -4\sum_b g_{\rho b}\int\frac{\mathrm{d}^3p}{(2\pi)^3}I_{3,b}(n_b^+ - n_b^-), \tag{6.23c}
$$

$$
m_\phi^2\phi_0 = 2\sum_b g_{\phi b}\int\frac{\mathrm{d}^3p}{(2\pi)^3}(n_b^+ - n_b^-), \tag{6.23d}
$$

where n_b^+ and n_b^- are the particle and anti-particle occupation numbers, defined as

$$
n_b^+ = \frac{1}{e^{\beta(E_b-\mu_b^*)}+1} \quad \text{and} \quad n_b^- = \frac{1}{e^{\beta(E_b+\mu_b^*)}+1}, \tag{6.24}
$$

respectively. We note that the zero-point oscillation energy was dropped, i.e., the term βE in Eq. (6.21) was not considered. This is called the **no-sea approximation**, and it is usually applied in nuclear hadrodynamics [314]. With this approximation, we assume that the parameters of the theory already include its effects. Of course, one could include the βE term, but the coupling parameters values would be different.

Thermodynamical quantities such as pressure, particle density, entropy and energy density can be derived from (6.21) using relations (4.27).

The difference between the NL3$\omega\rho$ model, the FSU2R model, and the FSU2H model lies

only on the number of baryons, mesons and couplings constant values considered:

- **NL3$\omega\rho$ model.** Only protons and neutrons are considered, i.e., b only runs over n and p in all the expressions above. Interactions are carried through the σ, ω and ρ mesons (the ϕ meson is excluded), meaning that the only equations of motion to be solve are Eqs. (6.23a)-(6.23c).

- **FSU2R model.** All the baryons in the baryon octet are considered. Interactions are carried through the σ, ω, ρ and ϕ mesons, meaning that one needs to solve the equations of motion (6.23a)-(6.23d). This provides a more general model as one includes a larger range of baryons and allows us to study the effects due to hyperons. However, this parametrisation set is unable predict neutron star masses above $2M_\odot$, which have been empirically observed in the pulsars PSR J1614–2230 [315] and PSR J0348+0432 [316].

- **FSU2H model.** Similar to the FSU2R model, but with adjusted parameters to produce stiffer EoSs such that $2M_\odot$ are reached.

6.2.4 The Hyperon Puzzle

It has been well-known that the transition from nuclear matter to hyperonic matter is energetically favoured as the density increases [317]. The emergence of hyperon degrees of freedom leads to a considerable reduction in pressure [318] and the EoS is said to be softened, on account of the energy having been put into the hyperons masses rather than into the kinetic energy of nucleons.

A particular consequence of this is in the modelling of neutron stars, as the maximum masses obtained are usually smaller than the $2M_\odot$ observations [315, 316]. This is the so-called "**hyperon puzzle**". One requires an increase of repulsive interaction to make the EoS stiffer. Possible mechanics have been proposed: stiffer hyperon-nucleon and/or hyperon-hyperon interactions [319,320], presence of strong magnetic field inside neutron stars [321,322], inclusion of three-body forces with one or more hyperons [323, 324], etc. For a detailed review see [325]. Despite most nuclear models for the EoS are able to satisfy the $2M_\odot$ constraint, predicting the existence of stellar radii below 13 km, suggested by recent astrophysical analyses [326–335], poses as a difficult challenge.

The FSU2H model developed in [307, 336], reconciles both the $2M_\odot$ mass and radii constraints, and therefore satisfies the upper limit of about $13.4-13.8$ km for the radius of a $1.4M_\odot$ neutron star, deduced [337–340] from the gravitational-wave signal of a neutron star binary merger detected by the LIGO and Virgo collaborations [341]. It reproduces the properties of nuclear matter and of finite nuclei [306] together with the constraints on the EoS extracted from nuclear collective flow [342] and kaon production [343,344] in HICs. Furthermore, neutron stars described by this model exhibits more reasonable cooling patterns than those using the FSU2R parametrisation set [345]. For these reasons, this will be our main choice when studying the effects due to hyperons in our system.

Chapter 7

Hadron-Quark Mixed Phase

It's a dangerous business, Frodo, going out of your door. [...] You step into the road, and if you don't keep your feet, there's no knowing where you might be swept off to.

– J.R.R. Tolkien, *The Fellowship of the Ring*

If a first-order phase transition from hadronic to quark matter exists, it should be characterized by a mixed-phase regime in which different regions of the system are at distinct stages of the transition. The presence of such a regime is expected to be manifested in measurable quantities from HIC experiments and astrophysical observations, such as net-baryon number fluctuations and the behaviour of the sound velocity.

In this chapter, we investigate the hadron-quark mixed phase within a two-phase model and compute key properties associated with its phase diagram. In Sec. 7.1, we define the thermodynamical framework and specify the parameter sets employed for the hadronic models and the PNJL model. In Sec. 7.2, we present results for the NL3$\omega\rho$-PNJL model, considering only nucleons in the hadronic EoS; an analysis is performed along isentropic trajectories, from which we extract various physical properties. Finally, in Sec. 7.3, we extend the analysis to a more general scenario incorporating the full baryon octet, where we assess the impact of hyperons on the phase diagram and on the derived thermodynamic properties.

7.1 Equilibrium Conditions and Parametrisations

In this section, we define the Maxwell and Gibbs construction for the hadron-quark phase, as well as important thermodynamical constraints on density and chemical potential in each phase for our setup. The parametrisations used for each model are explained in detail.

7.1.1 Chemical Potentials from Conserved Charges

When there are more particle species that conserved charges, conditions for chemical equilibrium are necessary. In many cases, there exist some conserved charges, but the single particle numbers are not conserved. Then it will be more convenient to use these (total) conserved charges as the independent degrees of freedom for the description of the state of the system, instead of specifying all the single particle numbers. The chemical potential of a particle i in phase I can be related to the chemical potential of the total charges by the linear combination

$$\mu_i^{\mathrm{I}} = B_i\mu_B + I_{3i}\mu_3 + S_i\mu_S, \tag{7.1}$$

where B_i, I_{3i} and S_i are the baryon number, the third component of isospin, and the strangeness of particle i, respectively, and μ_B, μ_3 and μ_S are the corresponding chemical potentials.

Maxwell vs. Gibbs Constructions

As mentioned before, the hadron-mixed phase may exist in the region between hadronic and quark matter based on the conjecture that a first-order phase transition takes place. Inside the co-existence region, one has to consider equilibrium conditions between the two phase. There are two typical choices for the treatment of this region which depend on the constraints of our system (H = hadron phase; Q = quark phase):

- **Maxwell construction.** The co-existing hadronic and quark phases have identical temperature, pressure and baryonic chemical potential,

$$T = T^H = T^Q, \tag{7.2a}$$
$$P = P^H = P^Q, \tag{7.2b}$$
$$\mu_B = \mu_B^H = \mu_B^Q, \tag{7.2c}$$

  but the chemical potential of any other charge can be different in each phase and constrained locally.

- **Gibbs construction.** The co-existing hadronic and quark phases have identical temperature, pressure, baryonic chemical potential, but also, electric or isospin charge is constrained globally,

$$T = T^H = T^Q, \tag{7.3a}$$
$$P = P^H = P^Q, \tag{7.3b}$$
$$\mu_B = \mu_B^H = \mu_B^Q, \tag{7.3c}$$
$$\mu_3 = \mu_3^H = \mu_3^Q. \tag{7.3d}$$

  These equilibrium conditions for the chemical potentials express that particles are allowed to be exchanged between the two phase, as long as the conversion of baryons to quarks

and quarks to baryons maintains an identical baryonic and isospin chemical potential in both phases. The Gibbs construction is more generally adopted for the description of hadron-quark mixed phase, where the coexisting hadronic and quark phases are allowed to be charged separately.

In HICs there are more than one conserved charge, namely, net the baryon number, net isospin, etc. Therefore, the Gibbs construction is be adopted in all our results.

Phase and Chemical Equilibrium Conditions

The density of a total conserved charge $\mathcal{Q}$ in phase I can be obtained from

$$\rho_{\mathcal{Q}}^{\mathrm{I}} = \sum_b \mathcal{Q}_b \rho_b, \tag{7.4}$$

where $\mathcal{Q}_b$ is the corresponding quantum number.

In the quark phase, the baryon and isospin densities and the respective chemical potentials can be obtained from (7.4) and by consulting Table 7.1:

$$\rho_B^Q = \frac{1}{3}(\rho_u + \rho_d + \rho_s), \quad \rho_3^Q = \frac{1}{2}(\rho_u - \rho_d), \quad \rho_S^Q = -\rho_s; \tag{7.5}$$

$$\mu_B^Q = \frac{3}{2}(\mu_u + \mu_d), \quad \mu_3^Q = (\mu_u - \mu_d), \quad \mu_S^Q = \frac{1}{2}(\mu_u + \mu_d - 2\mu_s). \tag{7.6}$$

Quark	Current Mass (MeV) [35]	B	I_3	S	Q
u	2.16	+1/3	+1/2	0	+2/3
d	4.70	+1/3	-1/2	0	-1/3
s	93.5	+1/3	0	-1	-1/3

Table 7.1: Current mass, baryon (B), third component of isospin (I_3), strangeness (S) and electric charge (Q) quantum numbers for $N_f = 2 + 1$ quarks.

Analogous definitions hold for hadronic matter, but using Table 7.2:

$$\rho_B^H = \sum_b B_b \rho_b, \quad \rho_3^H = \sum_b I_{3b} \rho_b, \quad \rho_S^H = -\rho_{\Lambda^0}; \tag{7.7}$$

$$\mu_B^H = \frac{1}{2}(\mu_p + \mu_n), \quad \mu_3^H = (\mu_p - \mu_n), \quad \mu_S^H = \frac{1}{2}(\mu_p + \mu_n - 2\mu_{\Lambda^0}), \tag{7.8}$$

where $b \in \{n,\ p,\ \Lambda^0,\ \Sigma^+,\ \Sigma^0,\ \Sigma^-,\ \Xi^0,\ \Xi^-\}$. The chemical potentials of other baryons in the baryon octet can be written in terms of μ_n, μ_p and μ_{Λ^0}. For each baryon, applying (7.8) in (7.1)

leads to[1]:

$$\mu_{\Sigma^+} = \mu_p - \mu_n + \mu_{\Lambda^0}, \tag{7.9a}$$

$$\mu_{\Sigma^0} = \mu_{\Lambda^0}, \tag{7.9b}$$

$$\mu_{\Sigma^-} = \mu_n - \mu_p + \mu_{\Lambda^0}, \tag{7.9c}$$

$$\mu_{\Xi^0} = 2\mu_{\Lambda^0} - \mu_n, \tag{7.9d}$$

$$\mu_{\Xi^+} = 2\mu_{\Lambda^0} - \mu_p. \tag{7.9e}$$

Although μ_p, μ_n and μ_{Λ^0} were used as a basis for chemical potentials, other ones could be constructed using different combinations of baryons.

Baryon	**Mass (MeV)** [35]	$\boldsymbol{B}$	$\boldsymbol{I_3}$	$\boldsymbol{S}$	$\boldsymbol{Q}$
n	939.6	1	+1/2	0	0
p	938.3	1	-1/2	0	+1
Λ^0	1116.0	1	0	-1	0
Σ^+	1189.0	1	1	-1	+1
Σ^0	1193.0	1	0	-1	0
Σ^-	1197.0	1	-1	-1	-1
Ξ^0	1315.0	1	+1/2	-2	0
Ξ^-	1321.0	1	-1/2	-2	-1

Table 7.2: Mass and quantum numbers of baryons in the spin-1/2 baryon octet.

In the mixed regime, the total baryon density is defined as

$$\rho_B = (1-\lambda)\rho_B^H + \lambda\rho_B^Q, \tag{7.10}$$

the energy density by

$$\epsilon = (1-\lambda)\epsilon^H + \lambda\epsilon^Q, \tag{7.11}$$

and the total isospin density as

$$\rho_3 = (1-\lambda)\rho_3^H + \lambda\rho_3^Q, \tag{7.12}$$

where λ is the quark fraction. The asymmetry parameter, α (isospin ratio) of the nuclei is defined as

$$\alpha \equiv \frac{N-Z}{N+Z} = 1 - 2Y_Q, \tag{7.13}$$

where N is the number of neutrons, Z the number of protons and $Y_Q \equiv Z/(N+Z)$. Here, α runs from 0 (symmetric matter) to 1 (pure neutron matter), $0 \leq \alpha \leq 1$. In the co-existence

[1] In HICs, the typical time scales are on the order of 10^{-23}s, which is much less than weak interaction time scales. However, when studying neutron stars, one usually considers that matter is in β-equilibrium: $n \rightleftharpoons p + e^- + \bar{\nu}_e \iff d \rightleftharpoons u + e^- \bar{\nu}_e$ and $d \rightleftharpoons s$. These relations act as additional constrains on the chemical potentials: $\mu_d = \mu_u + \mu_{e^-} + \mu_{\bar{\nu}_e} = \mu_s$.

phase, α can be re-written using (7.10) and (7.12):

$$\alpha = -2\frac{\rho_3}{\rho_B} = -2\frac{(1-\lambda)\rho_3^H + \lambda\rho_3^Q}{(1-\lambda)\rho_B^H + \lambda\rho_B^Q}. \tag{7.14}$$

In HICs, for a given isospin asymmetry prepared in experiment, α should be constant according to the isospin charge conservation in strong interaction, but the local asymmetry parameters α^Q and α_H, given by

$$\alpha^Q = -2\frac{\rho_3^Q}{\rho_B^Q} = 3\frac{\rho_d - \rho_u}{\rho_u + \rho_d + \rho_s}, \quad \alpha^H = -2\frac{\rho_3^H}{\rho_B^H} = -2\frac{\sum_b I_{3b}\rho_b}{\sum_b B_b\rho_b}, \tag{7.15}$$

can vary with λ. Systems with isospin ratios $0 \leq \alpha \leq 0.23$ are up to now experimentally accessible in HICs [25]. Therefore, we will fix $\alpha = 0.2$ when studying asymmetric matter. This choice is particularly relevant for Au-Au and Pb-Pb collisions [25].

Furthermore, the total net strangeness is set to zero in each phase, $S^H = S^Q = 0$, because there is no strangeness in the two colliding nuclei during a HIC[2]. Thus, we fix the strangeness density fraction to zero in each phase:

$$Y_S^H = Y_S^Q = 0, \tag{7.16}$$

where $Y_S = \rho_S/\rho_B$. Hence, the local net strangeness vanishes — the total number of strange quarks (whether free or bound in baryons) exactly balances (locally) that of anti-strange quarks. Moreover, the strange chemical potential remains finite and differs between the two phases, i.e., $\mu_S^H \neq \mu_S^Q \neq 0$.

Finite-Size Effects

Both of the Maxwell and Gibbs constructions involve only bulk contributions, but we neglect finite-size effects like Coulomb and surface contributions, meaning that the two-phase mixtures at equilibrium within the two-phase regions are always described as the co-existence of two macroscopic phases. This approximation is to some extent reasonable for the description of HICs, since Coulomb energies are small compared to typical collision energies, and the long-range nature of Coulomb force could be ignored in comparison to the small size of the ensemble of HICs products. However, in neutron stars and nuclear clusters appearing in the liquid-gas phase transition of low-energy HICs, finite-size effects can lead to stiffer EoSs for the quark-hadron mixed phase (in the latter case increasing the maximum mass of hybrid stars [347]). Surface tension effects have also been studied in [348] within a nucleon-meson model, where the parameter regime where there is a direct transition between the vacuum and quark matter, i.e. where nuclear matter is metastable, has been identified. The vacuum-quark surface tension, Σ_{VQ}, in this regime has been computed to be $\Sigma_{VQ} \approx (8-15)$ MeV/fm^2 [348]. A smaller value for

[2] In principle, there is still the possibility that one has a non-zero strangeness in the each phase with $S^{\mathrm{I}} = -S^{\mathrm{II}}$, which is known as **strangeness distillation** [346].

$m_{u,d}$ (MeV)	m_s (MeV)	Λ (MeV)	$G_S\Lambda^2$	$G_D\Lambda^5$	T_0 (MeV)	a_0	a_1	a_2	b_3
5.5	135.7	630	1.781	9.29	210	3.51	-2.47	15.2	-1.75

Table 7.3: Parametrisation for the PNJL model proposed in [4].

the nuclear-quark surface tension, Σ_{NQ} has also been obtained [348], $\Sigma_{NQ} \approx (2-10)$ MeV/fm^2, which seems to favour the formation of quark matter in the core of neutron stars via nucleation during their formation in a supernova explosion [349, 350].

Nevertheless, values of the surface tension are associated with large uncertainties. The Gibbs construction corresponds to the extreme case of a vanishing surface tension, whereas the Maxwell construction is associated with the limit of infinitely high surface tension.

7.1.2 Model Parametrisations

The PNJL model is composed of ten free parameters that can be fixed to reproduce empirical and LQCD results: the light quarks current mass $m_u = m_d$, the strange quark mass m_s; the model cut-off Λ, because the PNJL model is non-renormalisable and a regularisation scheme has to be introduced to deal with the divergent ultraviolet sea-quark integrals; the coupling constant G_S and the coupling constant G_D, necessary to give the right degeneracy between the η and η' mesons; a_0, a_1, a_2, b_3 and T_0 define the PNJL potential $U_{\rm PNJL}$, where T_0 defines the critical temperature for $\mu_B = 0$, and here we will rescale it from $T_0 = 270$ MeV, in the pure gauge sector, to $T_0 = 210$ MeV due to the presence of quarks, and to better reproduce LQCD calculations. In this work we will use the $SU(3)_f - {\rm I}$ parametrisation proposed in [4] (see Table 7.3). This parameter set is defined in a way that the constituent quark mass in the vacuum, is approximately one third of the baryonic mass of the nucleon. Moreover, the vacuum nucleon mass is reproduced, and the vacuum properties of the π, K, η and η' are well reproduce within a certain range.

The hadronic phase is described using the relativistic mean-field Lagrangian (6.14). Three different parameter sets are used: NL3$\omega\rho$ [351, 352], FSU2R [336] and FSU2H [336] parameter sets. As already mentioned, the coupling of all three models are obtained from performing a multi-parameter fit to finite-nuclei properties and astrophysical observations. The coupling constants and saturation properties of both models are reported in Table 7.4. The NL3$\omega\rho$ parameter set was obtained from fitting the charge radii, binding energies and neutron radii of various spherical nuclei [351]. This corrected systematic deviations from empirical value of earlier models. In [305, 352], g_ρ was adjusted to fit the symmetry energy of nuclear matter at $k_F = 226.9$ MeV, while at the same time Λ_ω is chosen to describe measurements of the radii of neutron stars and obtain a better value of $L(\rho_0)$, but simultaneous making very small changes to the proton density which is well constrained by the measured charge density in ^{208}Pb [353].

The FSU2H and FSU2R parameter sets were based on the earlier FSU2 model [306]. The various couplings were optimised to reproduce ground-state properties of several nuclei such as binding energies and charge radii obtained from recent empirical data [354, 355]. Measurements

Models	NL3$\omega\rho$ [351,352]	FSU2R [336]	FSU2H [336]
m_σ (MeV)	497.479	497.479	497.479
m_ω (MeV)	782.500	782.500	782.500
m_ρ (MeV)	763.000	763.000	763.000
$g^2_{\sigma N}$	104.387	107.5751	102.7200
$g^2_{\omega N}$	165.585	182.3949	169.5315
$g^2_{\rho N}$	127.000	206.4260	197.2692
κ	3.860	3.0911	4.0014
λ	-0.016	-0.001680	-0.013298
ξ	0.000	0.024	0.008
Λ_ω	0.030	0.045	0.045
ρ_0 (fm^{-3})	0.148	0.1505	0.1505
ϵ_B (MeV)	-16.3	-16.28	-16.28
K (MeV)	271.6	238.0	238.0
m^*_N/m_N	0.60	0.593	0.593
$E_{\rm sym}(\rho_0)$ (MeV)	31.7	30.7	30.5
L (MeV)	55.5	46.9	45.5

Table 7.4: Parameters of the NL3$\omega\rho$, FSU2R and FSU2H models. Also reported are the values in nuclear matter at the saturation density (ρ_0) for the energy per particle (ϵ_B), compressibility (K), effective nucleon mass (m^*_N/m_N) in symmetric nuclear matter, symmetry energy ($E_{\rm sym}$), and slope parameter of the symmetry energy (L).

of giant monopole resonances[3] energies for ^{90}Zr, ^{116}Sn, ^{144}Sm, and ^{208}Pb [356–360] were also incorporated to constrain the couplings. Additionally, the parameter set was optimised to both sustain neutron stars of $\approx 2M_\odot$ [315,316] and stellar radii below 13 km [326–335], as we have already mentioned above. The essential difference between the two models is that the FSU2H EoS is stiffer at densities larger than twice the saturation density (when hyperons start to appear) [307].

The coupling of hyperons to vector mesons can be related to the nucleon coupling $g_{\omega N}$ and $g_{\rho N}$ by assuming $SU(3)$-flavour symmetry and ideal mixing for the ω and ϕ mesons. This leads to the following relative coupling strengths (see Ref. [361] and references therein):

$$\begin{aligned} g_{\omega\Lambda} : g_{\omega\Sigma} : g_{\omega\Xi} : g_{\omega N} &= \frac{2}{3} : \frac{2}{3} : \frac{1}{3} : 1 \\ g_{\rho\Lambda} : g_{\rho\Sigma} : g_{\rho\Xi} : g_{\rho N} &= 0 : 1 : 1 : 1 \\ g_{\phi\Lambda} : g_{\phi\Sigma} : g_{\phi\Xi} : g_{\omega N} &= -\frac{\sqrt{2}}{3} : -\frac{\sqrt{2}}{3} : -\frac{2\sqrt{2}}{3} : 1. \end{aligned} \tag{7.17}$$

Also, $g_{\phi N} = 0$ on the basis that nucleons contain no strange valence quarks while the ϕ meson is composed of $s\bar{s}$. The couplings $g_{\sigma b}$ are adjusted to reproduce the hyperon potential in symmetric nuclear matter derived from hypernuclear observables [362,363]. This leads us to fix the ratios

[3] Giant monopole resonances are high-frequency, small-amplitude and collective excitation of atomic nuclei. This is a property of many-body systems, characterised by the excitation energy of the system. One can use these vibrations to extract the compressibility at saturation.

Models	**FSU2R** [336]	**FSU2H** [336]
$g_{\sigma\Lambda}/g_{\sigma N}$	0.618	0.620
$g_{\sigma\Sigma}/g_{\sigma N}$	0.454	0.461
$g_{\sigma\Xi}/g_{\sigma N}$	0.316	0.310

Table 7.5: Coupling constants ratios of the hyperon-σ meson interaction in the FSU2R and FSU2H models.

reported in Table 7.5.

7.2 Numerical Results: Quarks and Nucleons

In this section we analyse the phase diagram and thermodynamic properties of the hadron–quark transition at finite temperature and baryon density using the NL3$\omega\rho$-PNJL two-phase model framework. We consider both isospin-symmetric and isospin-asymmetric matter and two values of the vector couplings in the quark sector, $G_V/G_S = 0$ and 0.5. The mean-field equations for the quark phase (Eqs. (5.61) and (5.62)) and for the hadron phase (Eqs. (6.23)) are solved self-consistently together with the Gibbs construction (7.3). In the hadronic phase we include only neutrons and protons, while the quark phase contains up, down and strange quark flavours.

We further compute net-baryon-number susceptibilities along isentropic trajectories with $s/\rho_B = 2$, 5, and evaluate the squared sound velocity v_s^2 along these isentropes in the hadronic, mixed, and quark phases.

7.2.1 Phase Diagram of the NL3$\omega\rho$-PNJL Model

We first present in Fig. 7.1 the dependence of pressure as a function of the baryon density to exemplify the hadron-quark phase transition for the absence (left panels) and presence (right panels) of vector interactions in symmetric (top panels) and asymmetric (bottom panels) matter, and at high (blue) and low (red) temperatures. This phase transition is obtained by fixing T and α, and using the NL3$\omega\rho$ model for the hadron phase and the PNJL model for the quark phase. The dots in Fig. 7.1 represent the range of the hadron-quark mixed phase.

Clearly the pressure is a constant in the mixed phase of symmetric matter (top panels) just the same as with the Maxwell construction. This fact is not new, and has already been argued in Ref. [147] that the Gibbs and Maxwell constructions are equivalent in the isospin-symmetric case. Our symmetric matter case is a binary system with baryon number and isospin charge as two globally conserved charges. Therefore, it would be expected that more complicated Gibbs construction had to be applied during the phase transition. However, since $\mu_3 = 0$ ($\mu_u = \mu_d$ and $\mu_p = \mu_n$), independently of temperature and density, the relation of chemical equilibrium with respect to changes of Y_3 ($= \rho_3/\rho_B$), in (7.3d), is automatically fulfilled, and only Eq. (7.3c) is relevant. In other words, no isospin distillation occurs, i.e., there is no transfer of isospin per baryon between the two phases. Consequently, the isospin-symmetric case behaves as a one-fluid

(or unary) system and the phase co-existence line in the $T - \mu_B$ phase can be obtained using Maxwell construction, despite more than one globally charge charge is conserved. This is called **azeotropic** behaviour [147].

On the other hand, in the asymmetric case (bottom panels of Fig. 7.1), the mixed region exhibits a monotonic increase of the pressure with the baryon density ρ_B. This curvature becomes increasingly pronounced as the asymmetry factor is raised. It can be seen that the inclusion of vectors more than doubles the transition pressure for both temperatures in comparison to system where these are absent. This result is expected since the addition of repulsive vector interactions is known to make the EoSs stiffer at smaller densities. Moreover, when these are present, the onset of the phase transition moves to higher densities since the transition pressure is also increasing under the Gibbs construction. At $T = 10$ MeV, the phase transition becomes stronger when vector interactions are included with $G_V/G_S = 0.5$, as evidenced by an increase of approximately 25% in the density jump $\Delta\rho_B$ (cf. Table 7.6). At $T = 100$ MeV, however, the transition is weakened: $\Delta\rho_B$ decreases by about $5 - 9\%$ compared to the case without vector interactions. This behaviour reflects the non-monotonic structure of the phase diagram and the role of the CEP, which modifies the size of the coexistence region, as illustrated in Fig. 7.2.

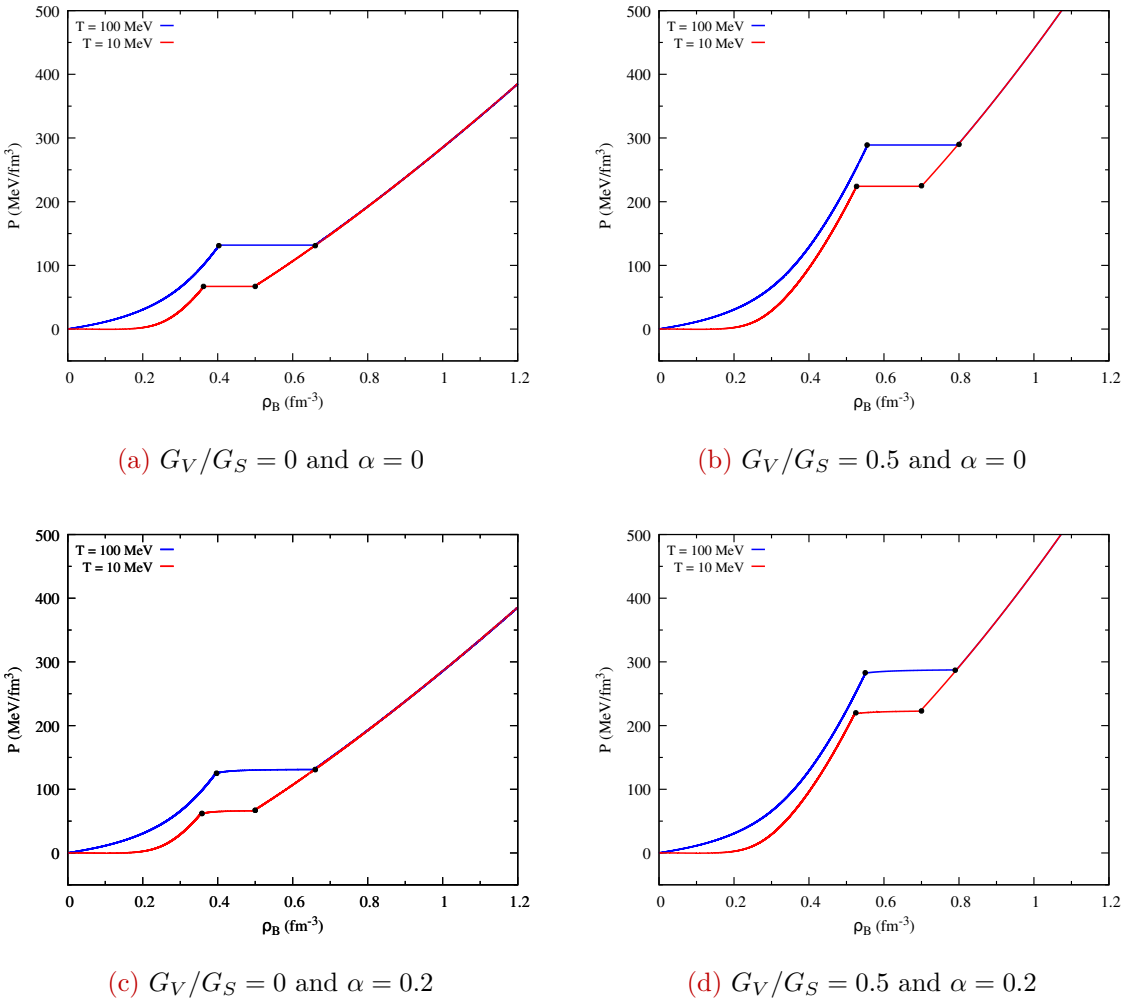

(a) $G_V/G_S = 0$ and $\alpha = 0$

(b) $G_V/G_S = 0.5$ and $\alpha = 0$

(c) $G_V/G_S = 0$ and $\alpha = 0.2$

(d) $G_V/G_S = 0.5$ and $\alpha = 0.2$

Figure 7.1: Phase transition in the $P - \rho_B$ plane for symmetric (top) and asymmetric (bottom) matter at $T = 10$ MeV (red) and $T = 100$ MeV (blue) for $G_V/G_S = 0$ (left) and $G_V/G_S = 0.5$ (right) within the NL3$\omega\rho$-PNJL two-model approach. The range between the dots corresponds to the mixed phase. (See text for more details.)

		$T = 10$ MeV			
G_V/G_S	α	ρ_B^i (fm^{-3})	ρ_B^f (fm^{-3})	P^i (MeV/fm^3)	P^f (MeV/fm^3)
0	0	0.362	0.5	67	67
0.5	0	0.527	0.7	224	224
0	0.2	0.358	0.5	62	67
0.5	0.2	0.525	0.7	220	223
		$T = 100$ MeV			
0	0	0.403	0.66	131	131
0.5	0	0.555	0.8	290	290
0	0.2	0.397	0.66	125	131
0.5	0.2	0.55	0.79	283	287

Table 7.6: Initial and final position of the mixed phase in the $P - \rho_B$ plane for the isotherms $T = 10$, 100 MeV of each scenario within the NL3$\omega\rho$-PNJL two-phase model.

In Figs. 7.2 and 7.3 we show the boundaries of the hadron-quark transition in the $T-\rho_B$ and $T-\mu_B$ planes for symmetric and asymmetric matter, in the presence and absence of vector quark interactions. The parameter λ denotes the quark fraction: $\lambda = 0$ (at low densities) corresponds to pure-hadron phase and $\lambda = 1$ (at high density) of pure-quark phase. The region in between is the hadron-quark co-existing phase.

At low temperatures a slight early onset of the transition occurs for isospin asymmetric matter, $\alpha = 0.2$, in comparison with the symmetric case, $\alpha = 0$. The effects due to vector interactions are more striking, moving the onset of the transition to higher values of density/-chemical potential by a factor of about 1.5 and enlarging the mixed phase, due to the repulsive contributions from the isoscalar-vector channel. This translation has also been reported in previous studies, e.g, see Refs. [28, 364]. On the other hand, coexisting region shrinks greatly at high temperature. The NL3$\omega\rho$-PNJL scheme predicts a CEP at temperature about $T^{\rm CEP} = 158$ MeV, which agrees with the value obtained in [153]. Comparing the different cases in Figs- 7.2 and 7.3 we notice that while $T^{\rm CEP}$ remains almost unaffected, there is a translation of the CEP to larger values of density and chemical potential when vectors quark interactions are included and $\alpha = 0.2$. The CEP is then found within the range $\mu_B^{\rm CEP} = (500 - 630)$ MeV, which agrees with the values found in [106], but also with lower limit imposed by LQCD for the crossover transition [43, 44] and experimental hadron yields [40, 41].

Additionally, we notice that for symmetric matter there is only one phase transition line in the $T - \mu_B$ plane, independent of the quark fraction λ; see top panels in Fig. 7.3. In contrast, for asymmetric matter, the phase transition curve splits and varies for the different values of λ forming a phase co-existence region; see both bottom panels in Fig. 7.3. This feature is due to the nature of the phase transition and the number of relevant globally conserved charges.

Remark 1. Comparing the results of Refs. [28, 106] with ours, we find a significant discrepancy in the onset of the mixed phase. In those works, the onset occurs at much higher densities and chemical potentials (around $5.5\,\rho_0$ at low T). These differences derive from the distinct parametrisations adopted: while our analysis employs the NL3$\omega\rho$ model, Refs. [28, 106] use the NLρ model. As discussed in Ref. [25], the NL3$\omega\rho$ parametrisation is characterised by a relatively high compressibility at large densities. This high compressibility partly mitigates the influence of the asymmetry parameter. In contrast, the NLρ parametrisation yields a softer EoS and symmetry energy, causing the corresponding curves at fixed asymmetry to span a broader range of densities.

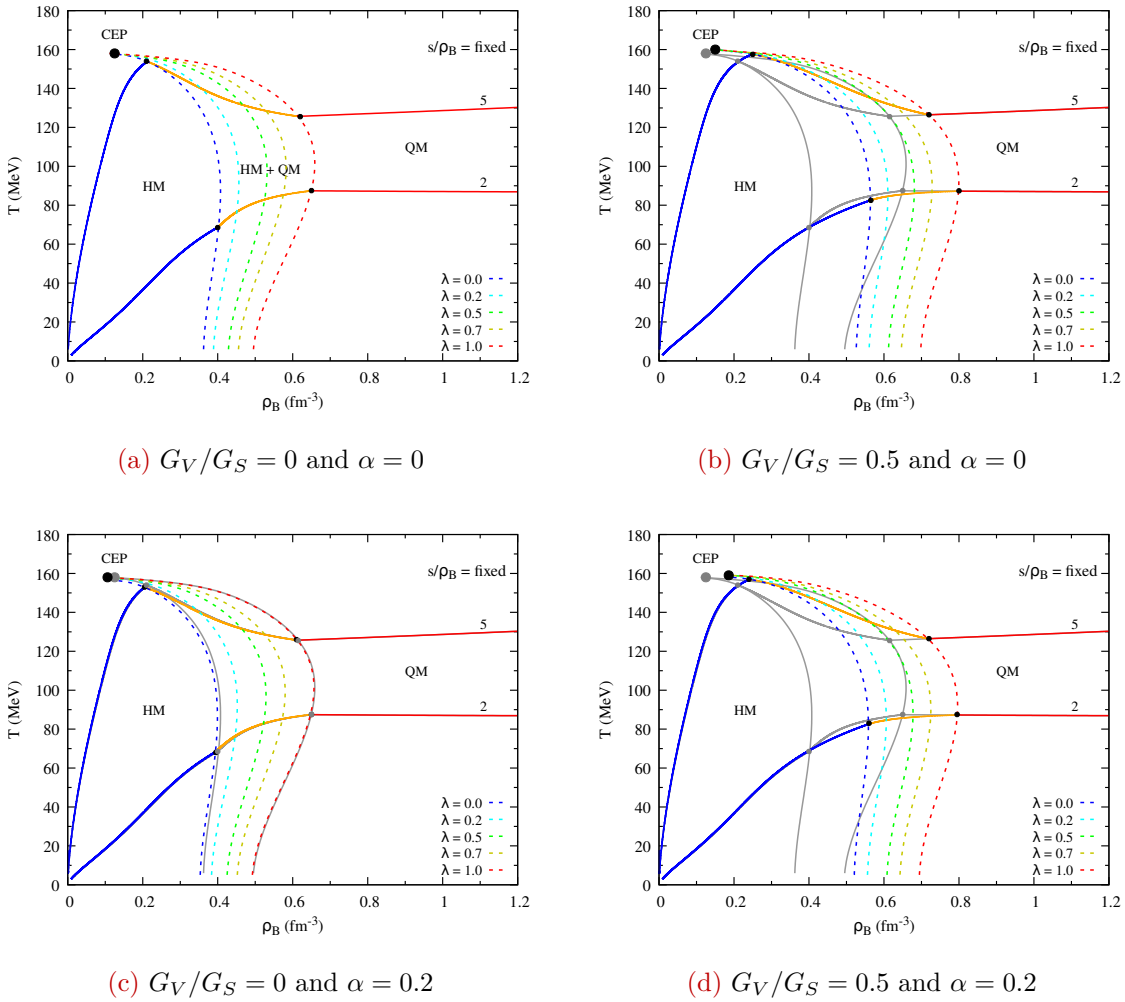

(a) $G_V/G_S = 0$ and $\alpha = 0$

(b) $G_V/G_S = 0.5$ and $\alpha = 0$

(c) $G_V/G_S = 0$ and $\alpha = 0.2$

(d) $G_V/G_S = 0.5$ and $\alpha = 0.2$

Figure 7.2: Phase diagram of the NL3$\omega\rho$-PNJL two-model approach in the $T - \rho_B$ plane for $\alpha = 0$ (top) and $\alpha = 0.2$ (bottom), and for $G_V/G_S = 0$ (left) and $G_V/G_S = 0.5$ (right). The big black dot is the CEP and the dashed lines identify the mixed phase where 0% (pure-hadron), 20%, 50%, 70%, and 100% (pure-quark) of the matter is in the quark phase, respectively. The solid lines are isentropes for fixed $s/\rho_B = 2$, 5 in hadron matter (HM, blue), in a co-existence phase (HM + QM, orange), and in quark matter (QM, red). For clarity, the pure-hadron and pure-quark boundaries, together with the isentropes from panel (a), are displayed in grey to highlight the differences.

Remark 2. At chemical potentials below the CEP value ($\mu_B < \mu_B^{\text{CEP}}$) in the T–μ_B plane (see Fig. 7.3), one would physically expect a crossover transition, i.e., a smooth interpolation between the two phases, as observed in lattice QCD calculations and in effective quark models. However, within the two-phase model framework, such a smooth behaviour cannot be realized, since a discontinuity in the thermodynamic variables is always present. This limitation provides a strong motivation for the development of more advanced effective quark Lagrangians that consistently incorporate hadronic degrees of freedom.

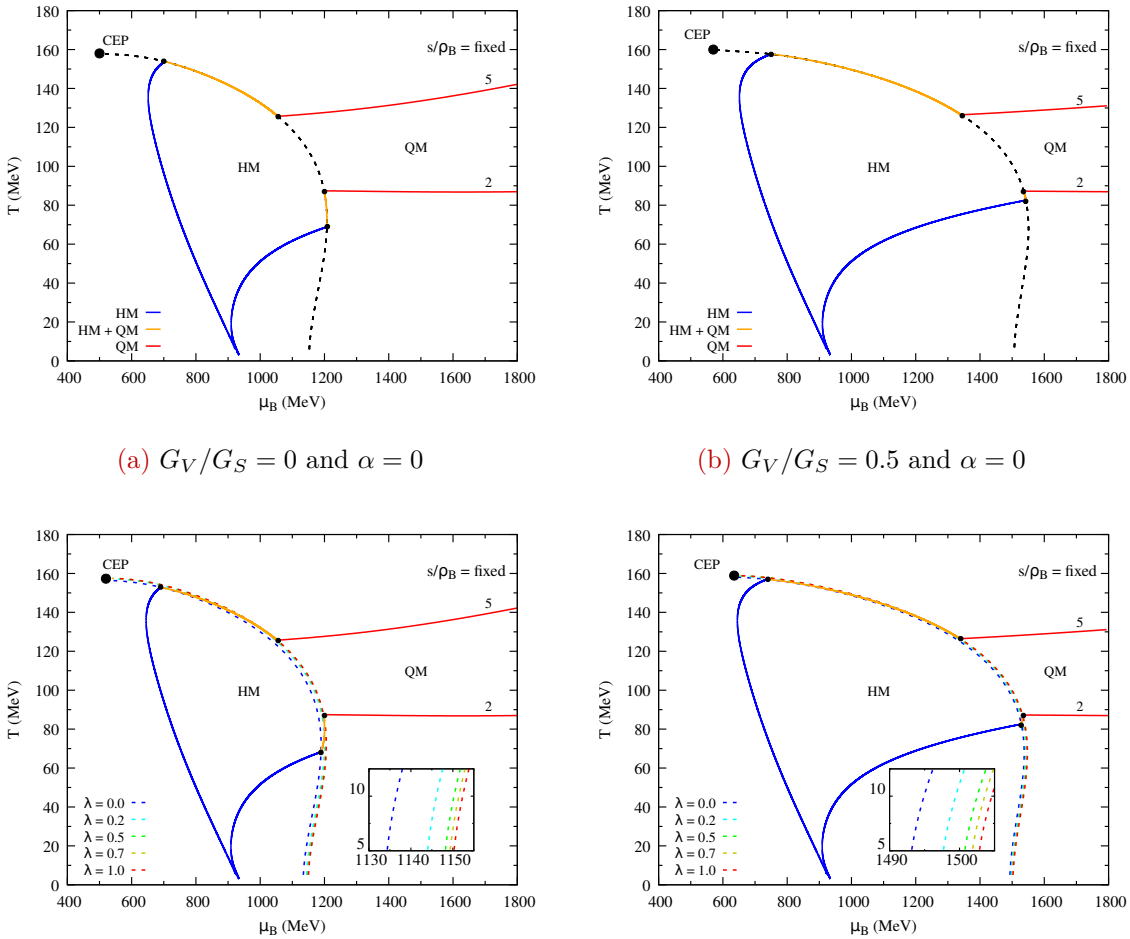

(a) $G_V/G_S = 0$ and $\alpha = 0$

(b) $G_V/G_S = 0.5$ and $\alpha = 0$

(c) $G_V/G_S = 0$ and $\alpha = 0.2$

(d) $G_V/G_S = 0.5$ and $\alpha = 0.2$

Figure 7.3: The same of Fig. 7.2 but for the $T - \mu_B$ plane.

7.2.2 Isentropic Trajectories

We also include various isentropic trajectories in Figs. 7.2 and 7.3. As already mentioned in Sec. 2.3, HICs produce a system which undergoes an approximate isentropic expansion moved by pressure gradients along trajectories of fixed s/ρ_B; the higher the centre-of-mass energy of the collision the higher the s/ρ_B ratio. We must remark that, considering this kind of evolution, one is implicitly assuming that the nucleation rate of bubbles of the hadron phase is larger than the expansion rate of the fireball so it can be treated as evolving close to local equilibrium. Ensuring whether this is a realistic assumption or whether one would need to account for non-equilibrium dynamics like supercooling/superheating, spinodal decomposition, etc., would require an analysis of the rate of bubble nucleation and the computation of the surface tension of the interface between the two phases. This could be the subject of future investigation.

In a two-phase system one has

$$\frac{s}{\rho_B} = \frac{(1-\lambda)s^H + \lambda s^Q}{(1-\lambda)\rho_B^H + \lambda \rho_B^Q}, \tag{7.18}$$

where s^H and s^Q are the entropy density of the hadron and quark phase, respectively. At a given value of T and μ_B (or ρ_B), λ is not automatically fixed, but one has to specify the isentrope followed by the system. We have chosen the trajectories for $s/\rho_B = 2,\ 5$. The first value allows us to discuss the phase diagram at low T and high μ_B (or ρ_B), where the (approximate) chiral restoration of the strange quark occurs and where T grows with μ_B (or ρ_B) inside the co-existence region. The second value has been chosen to be as close as possible of the CEP before numerical errors, due to divergences associated with this point, take place and in order to observe a decreasing in temperature with μ_B (or ρ_B) inside the mixed phase.

From Figs. 7.2 and 7.3 we can see the evolution of the isentropes across the phase diagram. In the hadron phase, the isentrope starts in the vacuum with $\mu_B = m_N$, and propagates, as temperature increases, until it intersects the pure-hadron co-existence line ($\lambda = 0$). As μ_B (or ρ_B) increases, quark matter emerges leading to an increase or decrease in temperature, depending on the fixed s/ρ_B value, until the isentrope crosses the pure-quark co-existence line ($\lambda = 1$), where quark degrees of freedom become dominant. Additionally, in Fig. 7.3, while in the symmetric case the isentrope follows the co-existence line in the mixed regime (orange), for asymmetric matter, it crosses the co-existence plane defined between $\lambda = 0$ (blue, dashed) and $\lambda = 1$ (red, dashed). Furthermore, one can clearly see that by adding vector interactions in the quark phase, the intersection of the isentrope with the co-existence line at low density occurs at a point of higher density and temperature, and the isentrope $s/\rho_B = 5$ becomes closer to the CEP. The variation of T, for the isentrope in the mixed phase, also decreases significantly. This behaviour can be better understood by looking at the entropy density per baryon number in each phase, as shown in Fig. 7.4. Here, we present the ratios $s^{(Q/H)}/\rho_B^{(Q/H)}$ as a function of λ for each isentrope with and without quark vector interactions in the symmetric case[4]. The key point is that the entropy per baryon of each phase is generally different,

$$\frac{s^Q}{\rho_B^Q} \neq \frac{s^H}{\rho_B^H}. \tag{7.19}$$

As can be seen in Fig. 7.4, depending on which phase has the larger entropy per baryon, the system will adjust T and μ_B as the fraction of quarks λ increases in order to keep the mixture ratio s/ρ_B fixed:

- At a lower ratio, $s/\rho_B = 2$, the quark phase has a lower entropy per baryon than the hadron phase, then increasing λ tends to lower s/ρ_B. To compensate and keep the ratio fixed, the system increases its temperature.

- At a higher ratio, $s/\rho_B = 5$, the quark phase has a higher entropy per baryon, and the opposite effect occurs: increasing its fraction tends to increase s/ρ_B, so the system compensates by decreasing its temperature.

Finally, we observe that a enhancement on s^Q/ρ_B^H occurs as vector interaction are added to the quark phase. Consequently, this decreases the ratio s^H/ρ_B^H for a given λ, leading to an increase

[4]The asymmetric case would be identical.

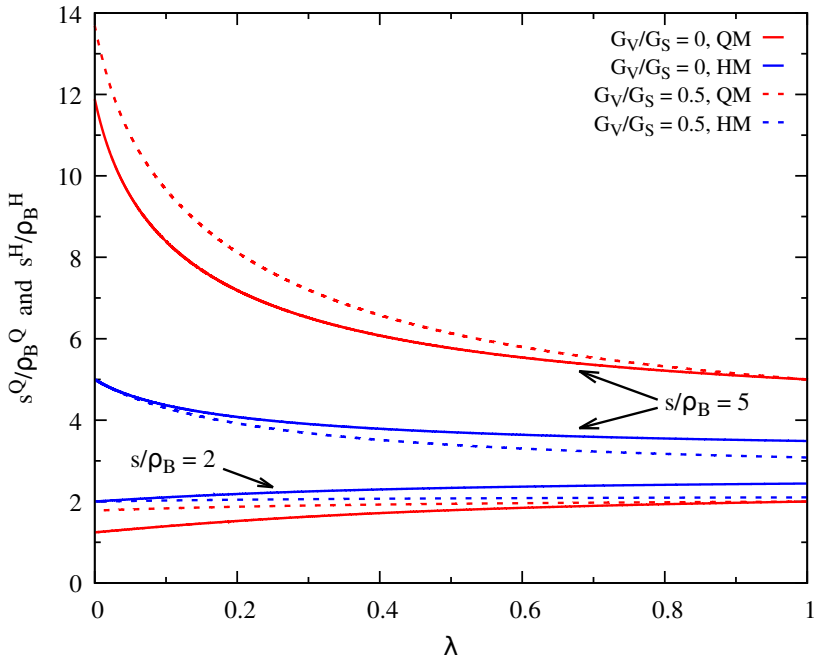

Figure 7.4: Local entropy per baryon number density of quark (red) and hadronic (blue) matter as a function of the quark concentration in isospin-symmetric matter for $G_V/G_S = 0$ (solid) and $G_V/G_S = 0.5$ (dashed).

in the separation between the hadron and quark entropy per baryon ratios for the isentrope $s/\rho_B = 5$, but a decrease for $s/\rho_B = 2$; respectively explaining the increase and decrease of the temperature variation shown on the right panels in Fig. 7.3.

Results for the pressure $P(\rho_B)$ on the two isentropes are given in App. C.1.

Strange Chiral Restoration

The restoration of chiral symmetry in the strange quark sector is expected at large μ_B either as a first-order transition with a an associated CEP [365] or as a smooth crossover [98]. This feature appears in the isentropes as a kink: the isentropic temperature initially decreases during the system's expansion but then rises rapidly after the trajectory crosses the strange chiral restoration region. We observe a similar behaviour at large μ_B in our results; for clarity, these features are shown in greater detail in a dedicated figure separate from Figs. 7.2 and 7.3. In Fig. 7.5a we display the temperature dependence on μ_B for isentropes within the quark phase across all studied cases, highlighting the kink associated with strange chiral restoration. While the $s/\rho_B = 5$ isentropes increase monotonically, the $s/\rho_B = 2$ isentropes first decrease and then rise after the onset of strange chiral restoration (labelled "sχT"). For $G_V/G_S = 0.5$ the kink is less pronounced and occurs at larger μ_B, consistent with the findings of Ref. [98]. In Fig. 7.5b we plot the $s/\rho_B = 2$ isentropes in the $T - \mu_B$ plane and mark the restoration points sχT and sχT$'$ (located at sχT(1630 MeV, 86.8 MeV) and sχT$'$(2120 MeV, 86.8 MeV)). The positions of sχT and sχT$'$ are shifted to higher values of μ_B relative to the ones in Refs. [98, 365]; this shift can be attributed to the different strangeness constraint used in those studies, which fixed

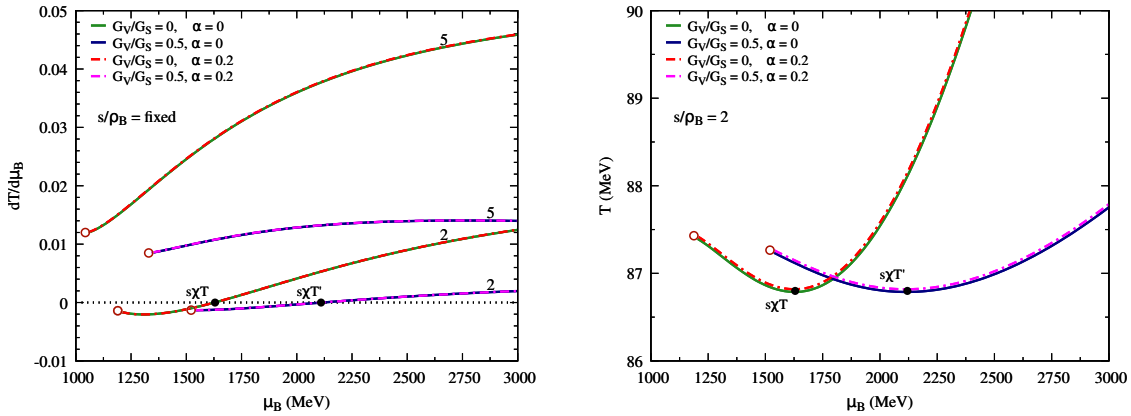

(a) (b)

Figure 7.5: Isentropic trajectories in the quark phase at large baryon chemical potential for asymmetry parameters $\alpha = 0$, 0.2, and vector couplings $G_V/G_S = 0$, 0.5. **Left:** $dT/d\mu_B$ as a function of μ_B. Only the $s/\rho_B = 2$ isentropes exhibit a non-monotonic temperature evolution with μ_B. **Right:** $s/\rho_B = 2$ isentropes in the $T - \mu_B$ plane. Along the $s/\rho_B = 2$ trajectory the temperature first decreases with μ_B until a minimum is reached, then develops a kink associated with the strange chiral-restoration transition (denoted "sχT"), after which T increases with μ_B. The marked transition points have coordinates sχT(1630 MeV, 86.8 MeV) and sχT$'$(2120 MeV, 86.8 MeV). Open circles denote intersections with the $\lambda = 1$ boundary. (See text for further details.)

$\mu_u = \mu_d = \mu_s$, whereas in the present work the strange sector is only constrained by Eq. (7.16).

Net-Baryon Susceptibilities

Here, we study the net-baryon number fluctuations, given its importance for HICs in locating the CEP and the hadron-quark phase boundary; see Sec. 2.3. Therefore, we focus on analysing two interesting ratios of cumulants — χ_B^3/χ_B^1 and χ_B^4/χ_B^2 — directly related to the skewness and the kurtosis of the baryon-number by Eq. (2.23). The generalised nth-order susceptibilities χ_B^n are obtained from the nth-derivative of P/T^4 with respect to μ_B/T (see Eq. (2.17)). Thus, it is important to observe the behaviour of each isentrope in the $P/T^4 - \mu/T$ plane before we compute the ratios above. This is shown in Fig. 7.6.

In Fig. 7.6 the isentropes should be read from right to left to follow increasing baryon chemical potential (or density); accordingly, during expansion within the hadronic phase the quantity P/T^4 decreases as μ_B/T decreases along the isentrope. However, close to the phase boundary, i.e., just before entering the mixed phase (orange), the isentropes bend and both μ_B/T and P/T^4 increase. This produces a point where the nth-derivatives $\partial^n(P/T^4)/\partial(\mu_B/T)^n$ diverge, which leads to very large values of the susceptibilities χ_B^n in the hadron phase (see Fig. 7.7). In contrast, for $G_V/G_S = 0$ the asymmetric $s/\rho_B = 2$ isentropes display a monotonic decrease of μ_B/T during their evolution. Within the mixed phase the $s/\rho_B = 5$ isentropes move towards larger values of μ_B/T and P/T^4 until they cross the pure-quark boundary ($\lambda = 1$), where a kink is observed. By contrast, the $s/\rho_B = 2$ isentropes decrease towards lower μ_B/T

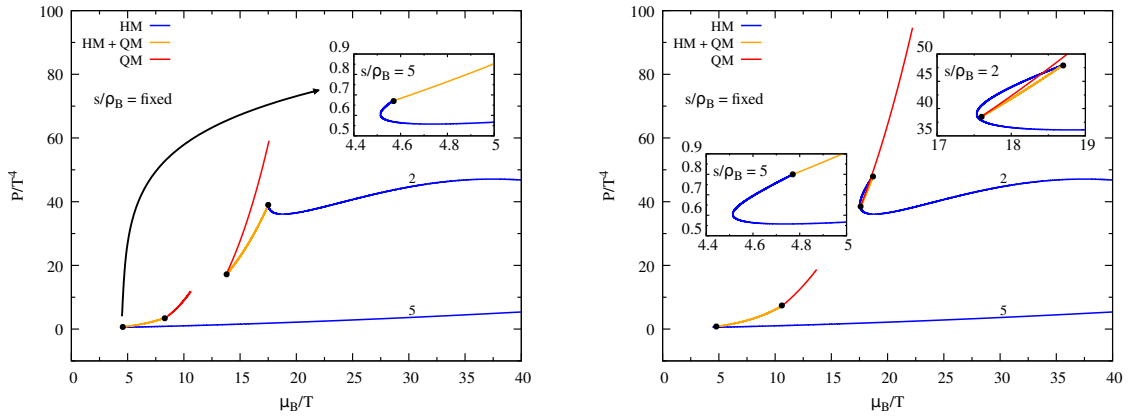

(a) $G_V/G_S = 0$ and $\alpha = 0$ (b) $G_V/G_S = 0.5$ and $\alpha = 0$

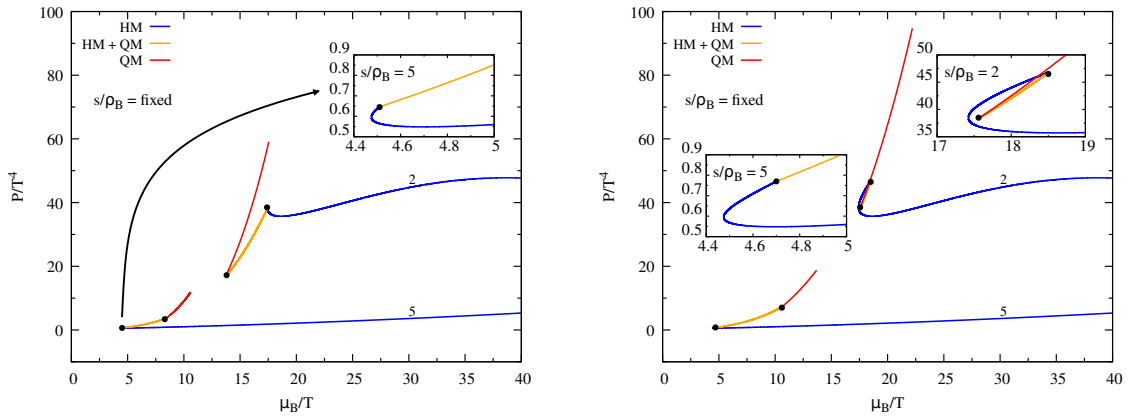

(c) $G_V/G_S = 0$ and $\alpha = 0.2$ (d) $G_V/G_S = 0.5$ and $\alpha = 0.2$

Figure 7.6: P/T^4 versus the ratio μ_B/T along the isentropes $s/\rho_B = 2$ and $s/\rho_B = 5$ for $G_V/G_S = 0$ (left), $G_V/G_S = 0.5$ (right), and $\alpha = 0$ (top), $\alpha = 0.2$ (bottom) within the NL3$\omega\rho$-PNJL two-phase approach. The graphics should be read from right to left to follow increasing ρ_B.

and P/T^4 and then enter the quark phase with a more abrupt change, after which they evolve to larger μ_B/T and P/T^4. Quark vector interactions (right panels) amplify these effects and shift them to higher values of P/T^4 and μ_B/T: the quark onset appears with a sharper kink and at larger P/T^4 and μ_B/T, the asymmetric $s/\rho_B = 2$ isentropes become non-monotonous close to the pure-hadron boundary, and the extent of the mixed phase is modified as discussed above. The discontinuities of the isentropes at the pure-hadron and pure-quark boundaries (black dots) are a direct consequence of the first-order transition and our two-model approach.

As noted above, the bending of the isentropes in the pure-hadron phase leads to divergences of the susceptibility ratios $\chi_B^{(n)}/\chi_B^{(n-2)}$ at a temperature T. This behaviour affects the form of the susceptibility ratios and hence our subsequent analysis of net-baryon fluctuations. As illustrated in Fig. 7.7, a non-monotonic (bending) isentrope splits into two branches; when mapped into the $\chi_B^{(n)}/\chi_B^{(n-2)} - T$ plane these branches appear as two curves that become singular at the turning point — i.e. at the temperature and the corresponding μ_B (or ρ_B) where the isentrope reverses direction.

If the hadronic isentrope follows only the green branch in the left panel, then the susceptibility ratios trace the green curve in the right panel (Fig. 7.7) and increase monotonically with T. If instead the isentrope also traverses the purple branch (the typical case), the relevant fluctuations are associated with the purple branch and the susceptibility ratios follow the purple curve in the right panel (Fig. 7.7), decreasing monotonically with T. In many cases the purple branch spans a very narrow temperature interval and therefore appears nearly vertical in the $\chi_B^{(n)}/\chi_B^{(n-2)} - T$ plane.

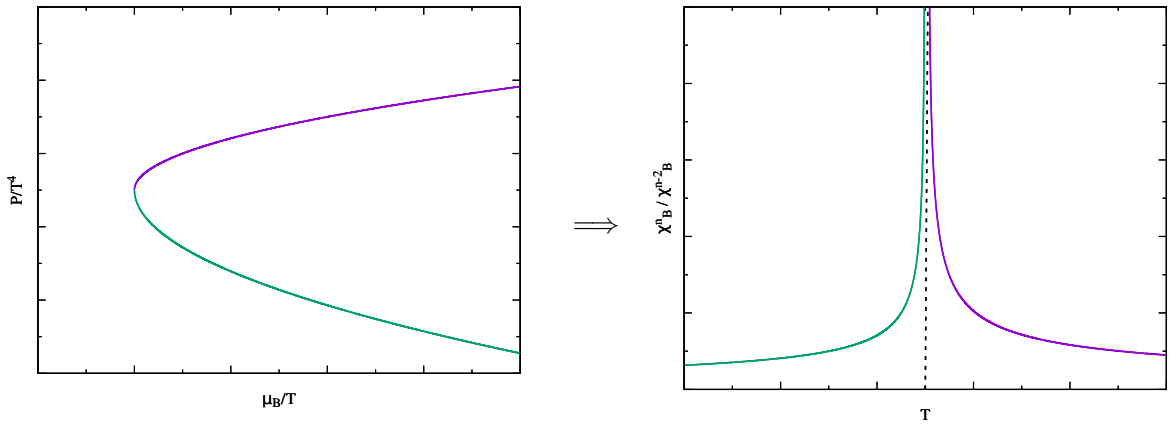

Figure 7.7: Schematic mapping between a bending isentrope in the $P/T^4 - \mu_B/T$ plane (left) and the resulting susceptibility ratio behaviour $\chi^{(n)}/\chi^{n-2}$ as a function of T (right). The green and purple branches on the left map to the correspondingly coloured curves on the right; the vertical dotted line marks the turning point where $\partial(P/T^4)/\partial(\mu_B/T) \to \infty$.

In Figs. 7.8 and 7.9 we present the susceptibility ratios $\chi_B^{(3)}/\chi_B^{(1)}$ and $\chi_B^{(4)}/\chi_B^{(2)}$, evaluated along isentropes with fixed $s/\rho_B \in \{2, 5\}$ for each scenario considered. Instead of continuous oscillatory curves, we observe discontinuities (indicated by dashed lines) at the pure-hadron and pure-quark boundaries. These arise from the two-phase construction and the presence of a first-order phase transition.

As discussed above, when the hadronic isentrope is monotonic in the $P/T^4 - \mu_B/T$ plane the susceptibility ratios $\chi_B^{(n)}/\chi_B^{(n-2)}$ increase monotonically with T; this behaviour is observed for the $s/\rho_B = 2$ isentrope in the case $G_V/G_S = 0$ with asymmetry parameter $\alpha = 2$ (Figs. 7.8c and 7.8g). By contrast, when the isentrope bends and follows the purple branch in Fig. 7.7, the mapping into the $\chi_B^{(n)}/\chi_B^{(n-2)} - T$ plane decreases with T, as seen in the remaining scenarios in Figs. 7.8 and 7.9. If the purple branch extends only over a narrow temperature interval, the corresponding isentropes appear almost vertical; examples are Figs. 7.8a and 7.8e for $s/\rho_B = 2$, and the panels in Fig. 7.9 for $s/\rho_B = 5$.

At the onset of the mixed phase, the low-isentrope ($s/\rho_B = 2$) continues to evolve toward higher T as the baryon density increases (Fig. 7.8), whereas for the high-isentrope ($s/\rho_B = 5$) the hadron–quark transition induces a bending of the $\chi_B^{(n)}/\chi_B^{(n-2)}$ curve toward lower T with increasing density (Fig. 7.9). These features reflect the behaviour of the corresponding isentropes described above. Finally, at the pure-quark boundary the $\chi_B^{(n)}/\chi_B^{(n-2)}$ branch reverses direction

upon entering the quark phase; for the $s/\rho_B = 2$ isentropes a second inversion occurs due to the kink associated with strange-quark chiral restoration (not shown).

The discontinuity at the hadron–mixed boundary is substantially larger than that at the mixed–quark boundary. Quark vector interactions reduce the magnitude of the discontinuities at both boundaries — most markedly at the pure-hadron boundary — and shift the transition to higher temperatures, consistent with Ref. [98]. In isospin-asymmetric matter the hadron–mixed discontinuity is reduced for $s/\rho_B = 2$ but increased for $s/\rho_B = 5$. Higher-order susceptibility ratios are more sensitive to the hadron–quark transition and therefore display larger fluctuations, as expected.

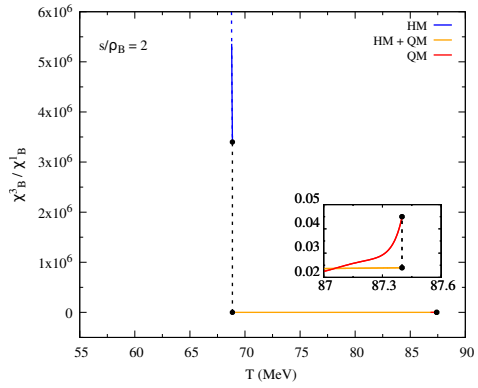

(a) $G_V/G_S = 0$ and $\alpha = 0$

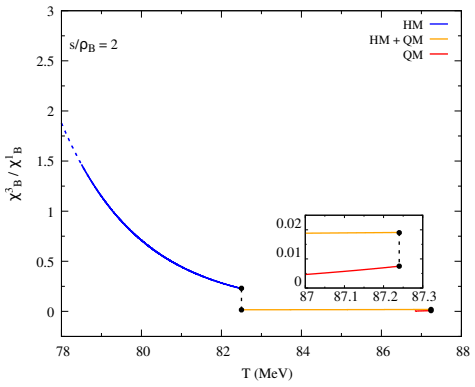

(b) $G_V/G_S = 0.5$ and $\alpha = 0$

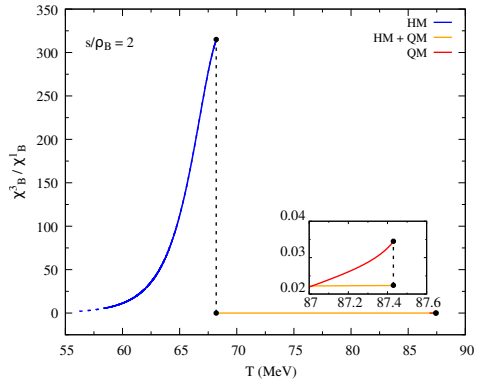

(c) $G_V/G_S = 0$ and $\alpha = 0.2$

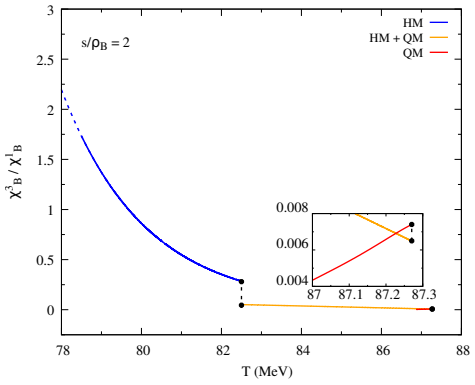

(d) $G_V/G_S = 0.5$ and $\alpha = 0.2$

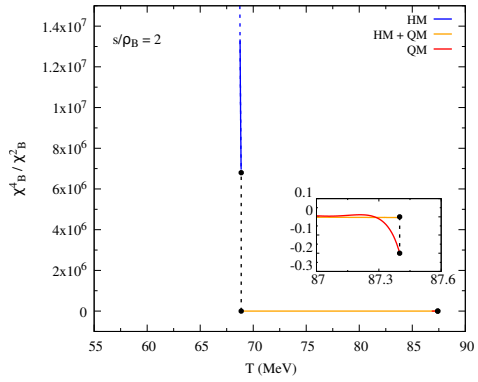

(e) $G_V/G_S = 0$ and $\alpha = 0$

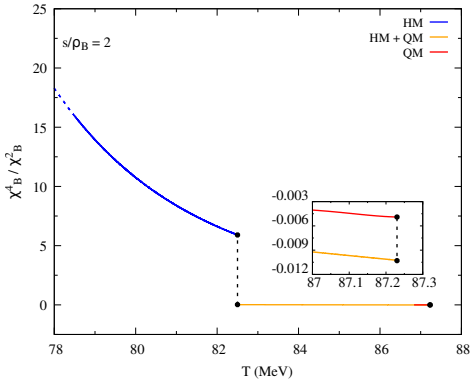

(f) $G_V/G_S = 0.5$ and $\alpha = 0$

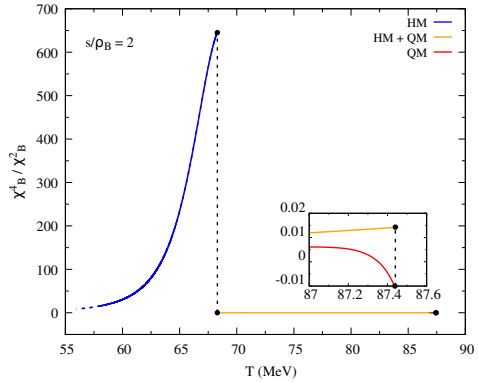

(g) $G_V/G_S = 0$ and $\alpha = 0.2$

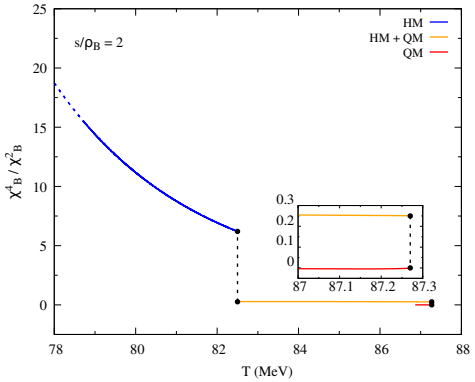

(h) $G_V/G_S = 0.5$ and $\alpha = 0.2$

Figure 7.8: Susceptibility ratios χ_B^3/χ_B^1 (a - d) and χ_B^4/χ_B^2 (e - h) as functions of temperature along the isentrope $s/\rho_B = 2$ for $G_V/G_S = 0$, 0.5 and $\alpha = 0$, 0.2 (see legend).

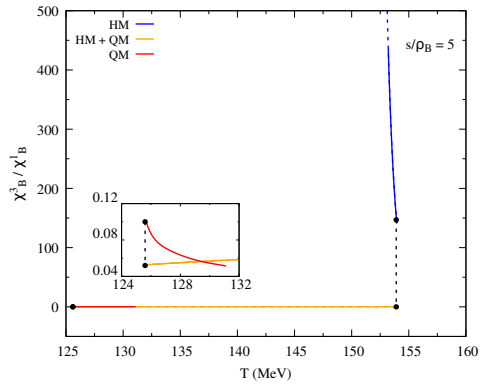

(a) $G_V/G_S = 0$ and $\alpha = 0$

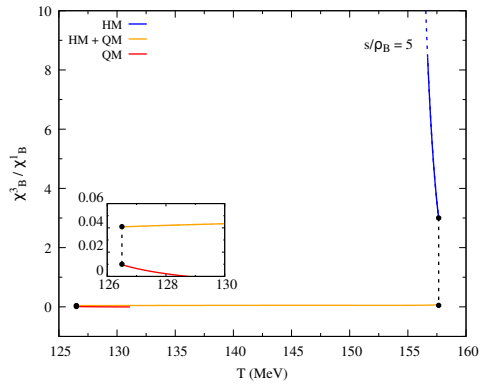

(b) $G_V/G_S = 0.5$ and $\alpha = 0$

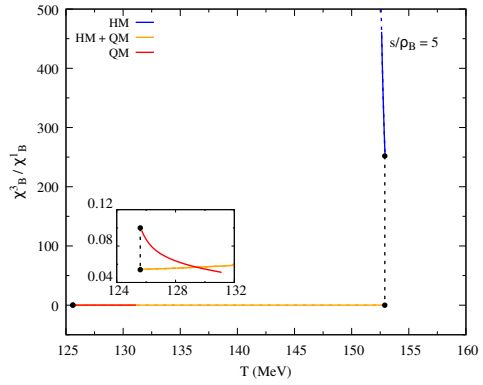

(c) $G_V/G_S = 0$ and $\alpha = 0.2$

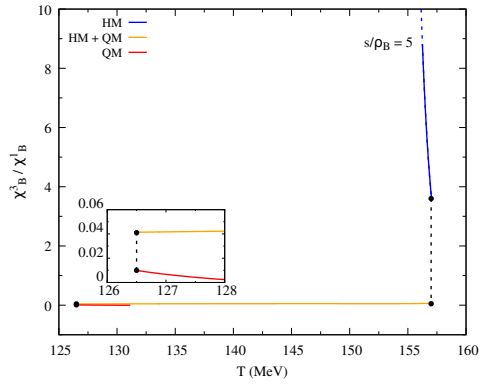

(d) $G_V/G_S = 0.5$ and $\alpha = 0.2$

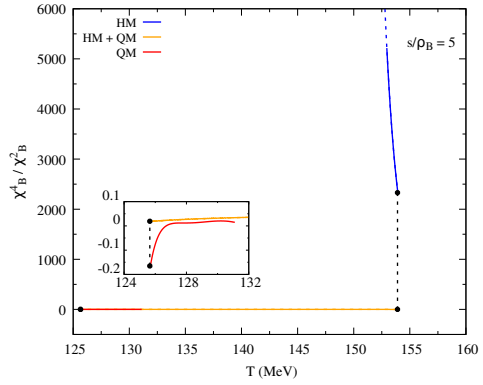

(e) $G_V/G_S = 0$ and $\alpha = 0$

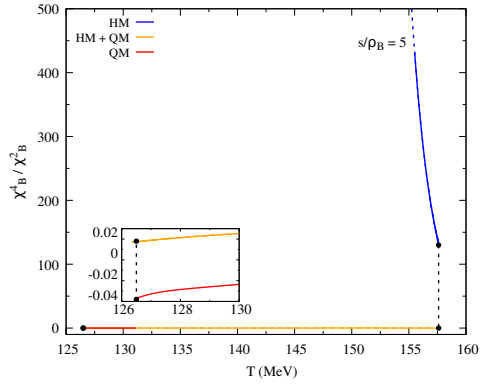

(f) $G_V/G_S = 0.5$ and $\alpha = 0$

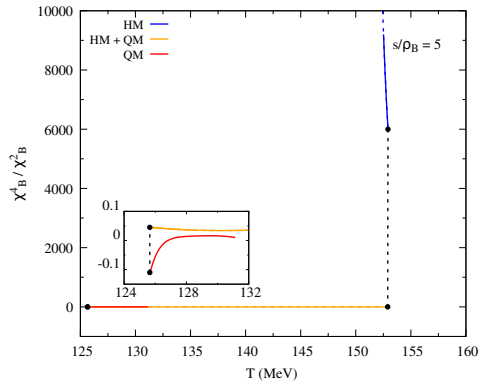

(g) $G_V/G_S = 0$ and $\alpha = 0.2$

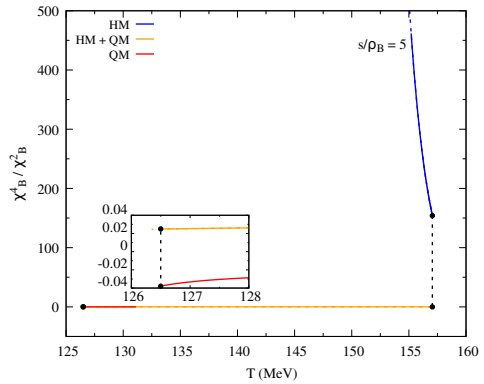

(h) $G_V/G_S = 0.5$ and $\alpha = 0.2$

Figure 7.9: Susceptibility ratios χ_B^3/χ_B^1 (a - d) and χ_B^4/χ_B^2 (e - h) as functions of temperature along the isentrope $s/\rho_B = 5$ for $G_V/G_S = 0$, 0.5 and $\alpha = 0$, 0.2 (see legend).

Speed of Sound

In Ref. [98], it was shown that the existence of a critical end point (CEP) cannot be established solely on the basis of non-monotonic behaviour in net-baryon number susceptibilities, since such behaviour may also occur in the absence of a CEP. This motivates the study of additional observables whose quantitative and qualitative features may serve as additional indicators of the hadron-quark phase transition. Two particularly relevant quantities in this context are the speed of sound and the polytropic index, $\gamma = \mathrm{d}(\ln P)/\,\mathrm{d}(\ln \epsilon)$. In the present work, we restrict our analysis to the former, while noting that the latter can be directly obtained from our results and will be the subject of a future analysis.

We have determined the square of the sound velocity v_s^2,

$$v_s^2 = \left(\frac{\partial P}{\partial \epsilon}\right)_{s/\rho_B}, \tag{7.20}$$

along two isentropic trajectories. The speed of sound plays a central role in the hydrodynamical evolution of the matter produced in heavy-ion collisions (HICs): it controls the system's response to initial energy-density gradients and thereby influences the collective acceleration of the fireball [170]. The sound velocity changes significantly during the different stages of the expansion and, in particular, upon entering a mixed or a quark phase. Such changes should leave an imprint on the transverse-momentum distributions of hadrons measured at freeze-out [366]. Values of the squared sound velocity can be extracted from the widths of rapidity (or pseudo-rapidity) distributions [366–368].

Results for v_s^2 corresponding to the values of s/ρ_B considered in this work are shown in Fig. 7.10, plotted as a function of baryon density for each case studied. The dotted horizontal line at $v_s^2 = 1/3$ denotes the conformal limit for free massless fermions. For the $s/\rho_B = 2$ isentrope, in all scenarios, however, the sound velocity in the hadronic phase exceeds this conformal limit at $\rho_B \approx 0.21$ fm^{-3}. This behaviour is found in many hadronic approaches, including chiral effective field theory: while $v_s^2 \ll 1/3$ below nuclear saturation density, it has been predicted to reach values above 0.5 at higher densities [369, 370].

At the hadron–quark transition we also observe a pronounced change in v_s^2: the onset of quark degrees of freedom softens the equation of state, producing a marked drop in the sound velocity, which is later recovered as the system evolves into a high-density quark phase dominated by quark degrees of freedom. This softening of the EoS reduces the acceleration of the fluid during the transition, leaving imprints on the final transverse-momentum spectra of hadrons emitted from the fireball.

The isospin-asymmetric matter case ($\alpha = 0.2$) is similar to the symmetric one, except that the step at the hadron-mixed phase boundary for $s/\rho_B = 2$ becomes less pronounced.

We find that a vector coupling of $G_V/G_S = 0.5$ in the quark sector causes v_s^2 to exceed the conformal limit already at the mixed-quark boundary at high baryon densities. Because vector interactions tend to stiffen the quark equation of state and thereby increase v_s^2, this behaviour

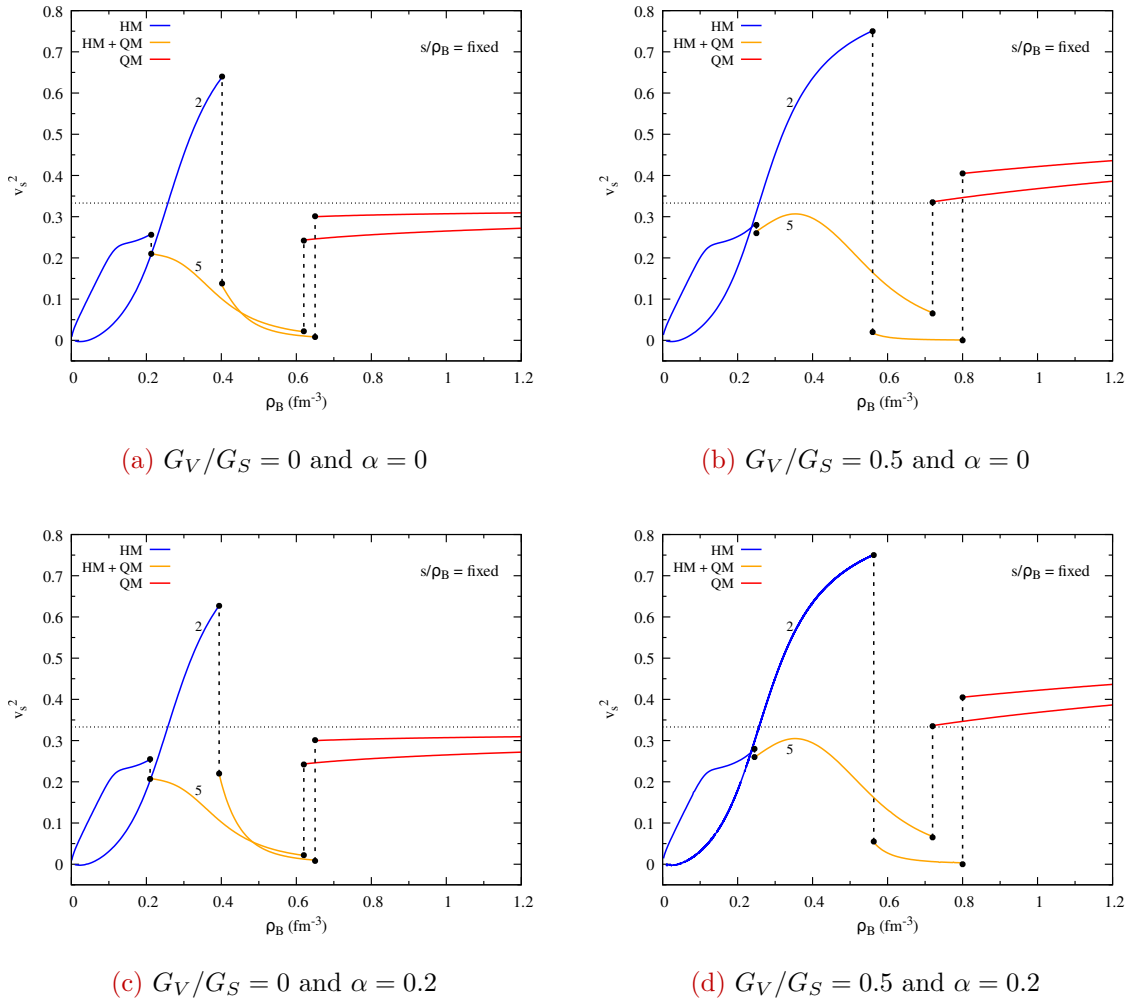

(a) $G_V/G_S = 0$ and $\alpha = 0$

(b) $G_V/G_S = 0.5$ and $\alpha = 0$

(c) $G_V/G_S = 0$ and $\alpha = 0.2$

(d) $G_V/G_S = 0.5$ and $\alpha = 0.2$

Figure 7.10: Sound velocity squared v_s^2 as a function of the baryon density along the isentropes $s/\rho_B = 2$, 5 for $G_V/G_S = 0$ (left) and $G_V/G_S = 0.5$ (right), and for $\alpha = 0$ (top) and $\alpha = 0.2$ (bottom) within the NL3$\omega\rho$-PNJL two-model approach. The horizontal dotted line $v_s^2 = 1/3$ indicates the conformal limit.

indicates that the vector coupling should be restricted to smaller values in the region of interest. Accordingly, when analysing the influence of hyperons on the phase diagram (see Sec. 7.3) we adopt $G_V/G_S = 0.1$.

Nevertheless, it should be noted that the vales of v_s^2 in the hadron-quark mixed phase is always less than 1/3, which may also be used as a new evidence for the existence of the hadron-quark mixed phase.

7.3 Numerical Results: Quarks, Nucleons and Hyperons

We extend the nucleonic two-phase construction by including the full baryon octet and by studying the impact of hyperons at finite temperature and baryon density. Calculations are performed using two hadronic parametrizations, FSU2H and FSU2R; the FSU2H EoS is adopted as the reference model for comparison (see the discussion at the end of the previous chapter). Results obtained with the FSU2R parametrization are reported in App. C.3. In the quark sector

the vector coupling has been reduced to $G_V/G_S = 0.1$ to improve agreement with the conformal limit at high densities.

In what follows we compute isentropic trajectories (notably $s/\rho_B = 2$ and $s/\rho_B = 5$), phase diagrams in the $T\rho_B$ and $T - \mu_B$ planes, hyperon fractions along the isentropes, and the speed of sound evaluated along these trajectories. Results are presented for symmetric and isospin-asymmetric matter ($\alpha = 0$ and $\alpha = 0.2$) and for different values of the quark vector interaction, with particular emphasis on how the inclusion of hyperons modifies the onset and extent of the mixed phase as well as the thermodynamic response of the system.

Results for the pressure $P(\rho_B)$ in the FSU2H-PNJL model along the two isentropes are given in App. C.2.

7.3.1 Phase Diagram of the FSU2H-PNJL Model

The hadron-quark phase transition in the FSU2H-PNJL two-phase model is presented in Fig. 7.11. Qualitatively, Figs. 7.1 and 7.11 display the same overall features. The main effect of including the full baryon octet is a systematic shift of the transition to higher pressures and baryon densities: at fixed T the onset of the mixed phase moves to larger ρ_B (by $\approx 25\% - 35\%$) and to larger P (by $\approx 35\% - 50\%$) (cf. Tables 7.6 and 7.7). In the isospin-asymmetric case ($\alpha = 0.2$), the pressure increases more rapidly over the same density interval.

		$T = 10$ MeV			
G_V/G_S	α	ρ_B^i (fm^{-3})	ρ_B^f (fm^{-3})	P^i (MeV/fm^3)	P^f (MeV/fm^3)
0	0	0.47	0.6	105	105
0.1	0	0.55	0.68	155	155
0	0.2	0.455	0.595	95	105
0.1	0.2	0.525	0.68	140	155
		$T = 100$ MeV			
0	0	0.545	0.784	184	184
0.1	0	0.62	0.845	235	235
0	0.2	0.526	0.784	171	184
0.1	0.2	0.60	0.845	220	235

Table 7.7: Initial (i) and final (f) position of the mixed phase in the $P - \rho_B$ plane for the isotherms $T = \{10, 100\}$ MeV of each scenario within the FSU2H-PNJL two-phase model.

These changes are even more pronounced in the FSU2R-PNJL model (cf. Fig. C.4 and Table C.1): both the transition pressure and density increase by more than a factor of two, and the pressure rises more steeply throughout the mixed phase. A distinguishing qualitative feature for $\alpha = 0.2$ is that the isothermal curves enter the mixed regime more smoothly, i.e., the discontinuity at the onset of the mixed phase is substantially reduced. Furthermore, when quark vector interactions are included the low-temperature pressure exceeds the high-temperature pressure within the mixed phase at large ρ_B.

We attribute the upward shifts in pressure and density to the softening of the hadronic

equation of state induced by the additional degrees of freedom (hyperons), which are expected to appear at $\gtrsim 2\rho_0$ [345]. This softening reduces the hadronic pressure at a given density and therefore requires a larger density (or chemical potential) for the quark phase to become thermodynamically favourable. Because the FSU2R model yields a softer hyperonic EoS than FSU2H (see previous chapter), the densities and pressures required for the transition are correspondingly higher (cf. App. C.3).

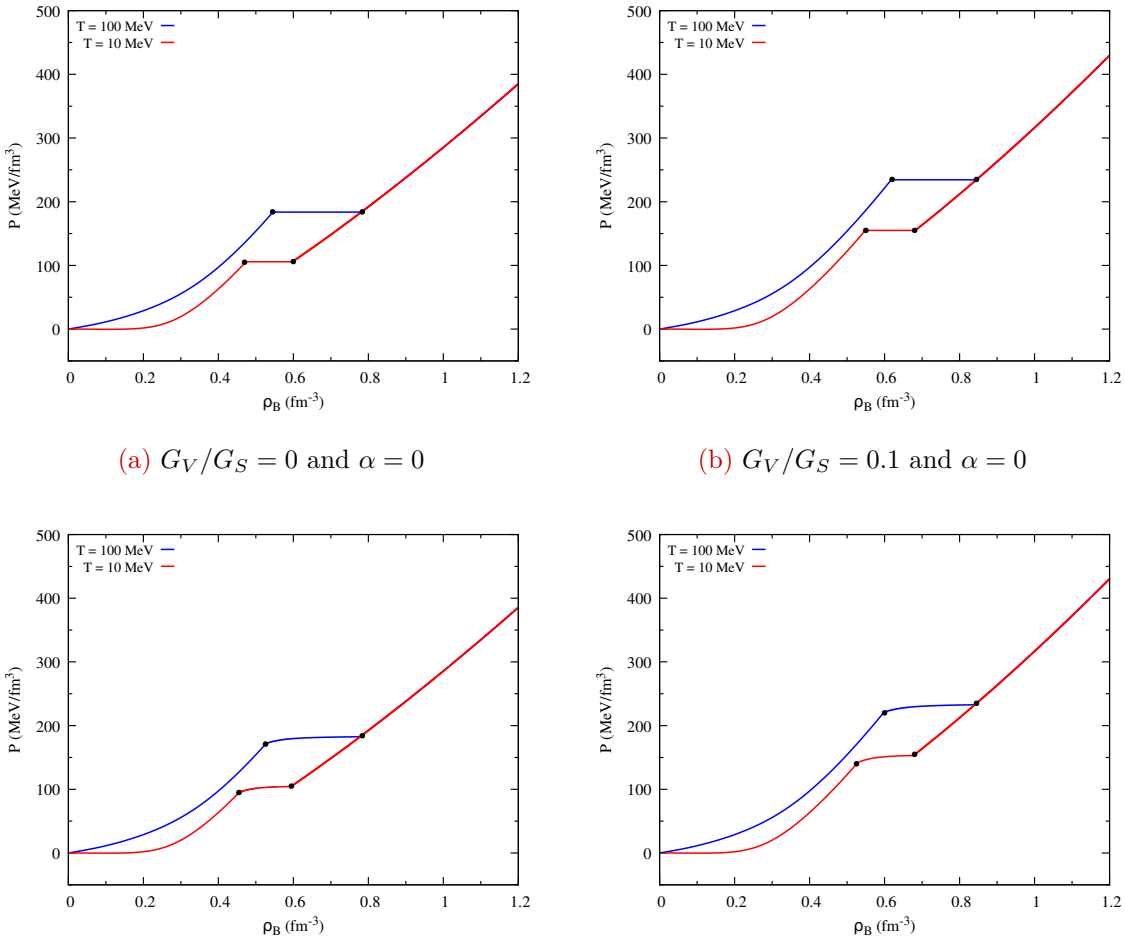

(a) $G_V/G_S = 0$ and $\alpha = 0$

(b) $G_V/G_S = 0.1$ and $\alpha = 0$

(c) $G_V/G_S = 0$ and $\alpha = 0.2$

(d) $G_V/G_S = 0.1$ and $\alpha = 0.2$

Figure 7.11: Phase transition in the $P-\rho_B$ plane for symmetric (top) and asymmetric (bottom) matter at $T = 10$ MeV (red) and $T = 100$ MeV (blue) for $G_V/G_S = 0$ (left) and $G_V/G_S = 0.1$ (right) within the FSU2H-PNJL two-model approach. The range between the dots corresponds to the mixed phase.

The phase diagram of the FSU2H-PNJL model in the $T-\rho_B$ and $T-\mu_B$ planes is shown in Figs. 7.12 and 7.13. The influences of isospin asymmetry and quark vector interactions are small, and the CEP is located at $T^{\mathrm{CEP}} \approx 160$ MeV and $\mu_B^{\mathrm{CEP}} \approx 500$ MeV. These coordinates are close to those obtained with the NL3$\omega\rho$-PNJL model under the same conditions, the latter favouring a slightly lower μ_B and a somewhat higher T. This proximity is consistent with the expectation that hyperonic effects become significant only at higher densities.

At low temperature, hyperons noticeably shift the onset of the mixed phase: for $G_V/G_S = 0$

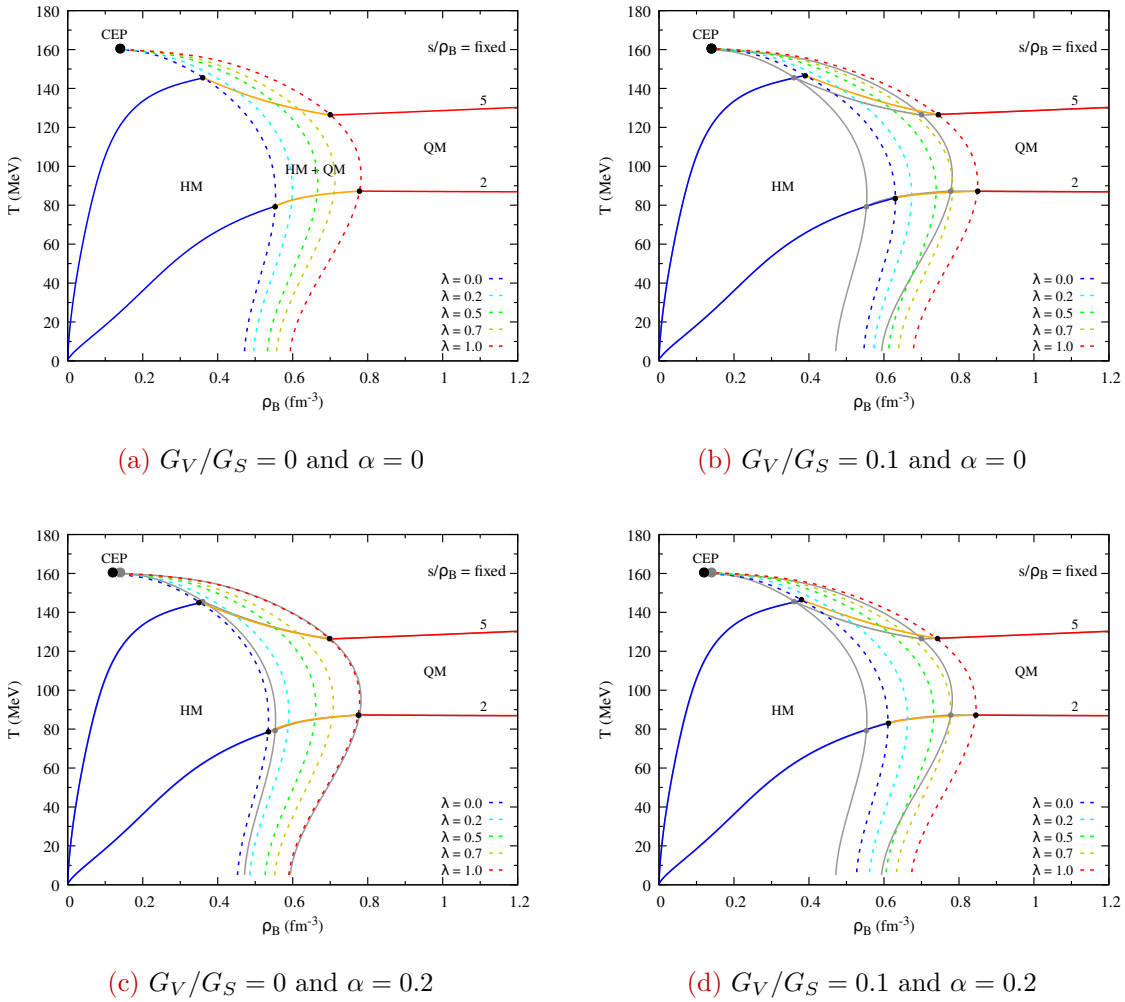

(a) $G_V/G_S = 0$ and $\alpha = 0$

(b) $G_V/G_S = 0.1$ and $\alpha = 0$

(c) $G_V/G_S = 0$ and $\alpha = 0.2$

(d) $G_V/G_S = 0.1$ and $\alpha = 0.2$

Figure 7.12: Phase diagram and isentropes $s/\rho_B = 2, 5$ of the FSU2H-PNJL two-model approach in the $T - \rho_B$ plane for $\alpha = 0$ (top) and $\alpha = 0.2$ (bottom), and for $G_V/G_S = 0$ (left) and $G_V/G_S = 0.1$ (right). For clarity, the pure-hadron and pure-quark boundaries, together with the isentropes from panel (a), are displayed in grey to highlight the differences.

and $\alpha = 0$ the onset occurs at $\approx 3\rho_0$, while for $G_V/G_S = 0$ and $\alpha = 0.2$ it moves slightly lower, to $\approx 2.8\rho_0$. This behaviour follows directly from the softening of the hadronic equation of state discussed above. For the softer FSU2R EoS the onset is delayed further, to $\approx 5\rho_0$.

The delayed onset in the FSU2R case produces a markedly sharper bending of the co-existence lines when vector interactions are included (see Figs. C.5c and C.5d), whereas the FSU2H co-existence lines (Figs. 7.12c and 7.12d) bend more smoothly, resembling the NL3$\omega\rho$–PNJL behaviour. Finally, for both the FSU2R and FSU2H EoSs the mixed-phase region is more noticeably enlarged by a finite isospin asymmetry than when using the NL3$\omega\rho$ EoS.

7.3.2 Isentropic Trajectories

We compute isentropic trajectories for $s/\rho_B = 2$ and $s/\rho_B = 5$, shown in Figs. 7.12 and 7.13. Qualitatively, the behaviour is similar to that obtained with the NL3$\omega\rho$ EoS (cf. Subsec. 7.2.2). Quantitatively, however, the two isentropes display distinct intersections with the phase bound-

ary: the higher-entropy isentrope ($s/\rho_B = 5$) meets the boundary at a lower temperature but at larger μ_B (and correspondingly larger ρ_B), whereas the lower-entropy isentrope ($s/\rho_B = 2$) intersects the boundary at a higher temperature.

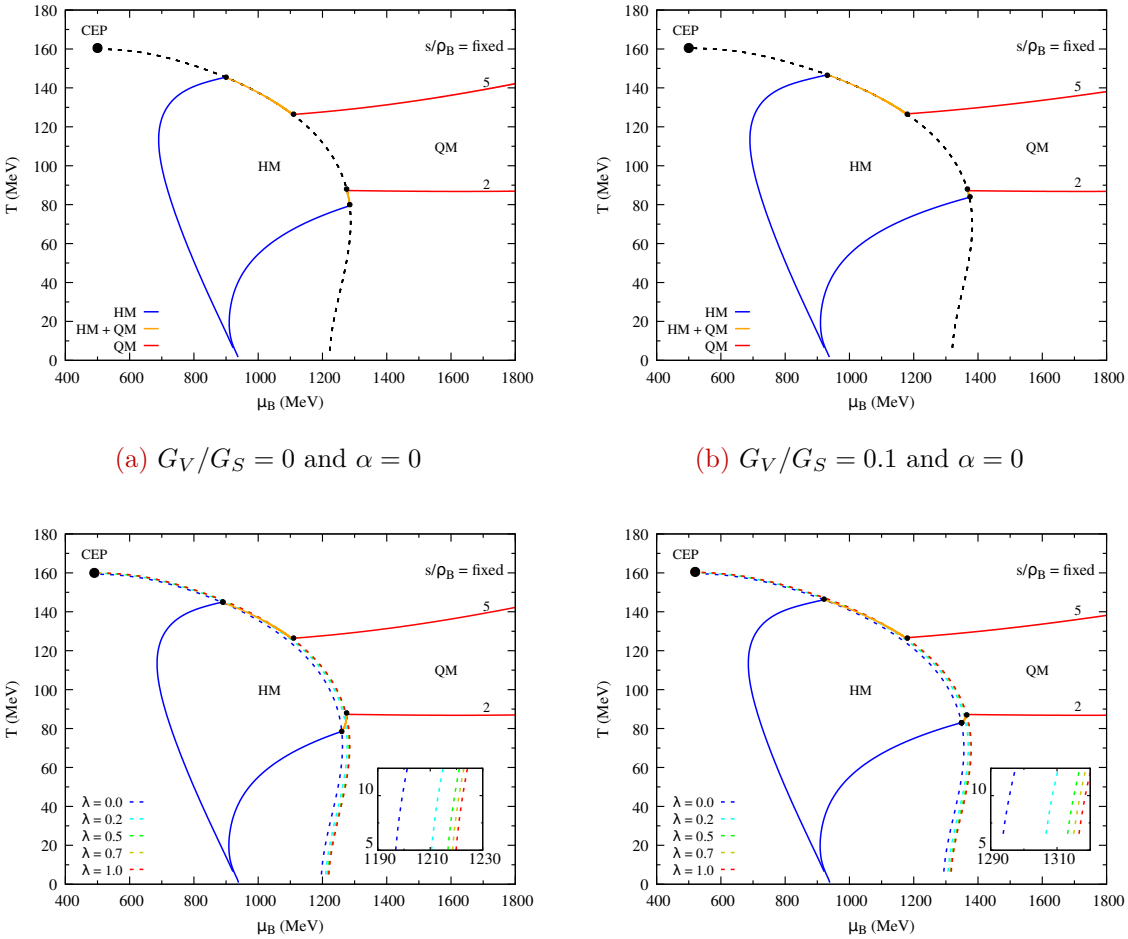

(a) $G_V/G_S = 0$ and $\alpha = 0$

(b) $G_V/G_S = 0.1$ and $\alpha = 0$

(c) $G_V/G_S = 0$ and $\alpha = 0.2$

(d) $G_V/G_S = 0.1$ and $\alpha = 0.2$

Figure 7.13: The same of Fig. 7.12 but for the $T - \mu_B$ plane.

In both cases the extent of the mixed phase in the $T - \mu_B$ plane is reduced, so the change in temperature that accompanies entry into the mixed regime during the first-order transition is less pronounced than in the nucleonic case. The different behaviour of the two isentropes can be traced to the hyperon content along each trajectory: the evolution of the hyperon fractions with ρ_B modifies the thermal and compositional response of the hadronic phase and thus alters where, and at which temperature, the isentropes intersect the co-existence region (see Fig. 7.14).

Hyperon Fractions Along Isentropes

Fig. 7.14 shows the hyperon fractions along the isentropic trajectories. The left panel corresponds to the isospin-symmetric case, while the right panel displays the isospin-asymmetric case with $\alpha = 0.2$. The isospin asymmetry modifies the relative populations within the isospin doublet (n, p) and the isospin triplet $(\Sigma^-, \Sigma^0, \Sigma^+)$, producing noticeable changes in their abundances.

Solid lines denote the low-entropy isentrope $s/\rho_B = 2$ and dashed lines denote the high-entropy isentrope $s/\rho_B = 5$. The Ξ^0 and Ξ^- fractions are negligible in all cases[5].

The splitting of the Σ-baryon abundances is governed by their coupling to the ρ-meson. In isospin-symmetric matter ($\alpha = 0$) the ρ-meson field vanishes, $\rho_\mu = 0$. For $\alpha \neq 0$, however, the field becomes finite and the term $g_{\rho b} I_{3b} \rho_0^3$ in Eq. (6.20) contributes to the effective chemical potential. For the $\Sigma^\pm$, with $I_{3b} = \pm 1$, this causes the effective chemical potential μ^*_Σ to decrease for Σ^+ and to increase for Σ^-. Consequently, the number-density fraction of Σ^+ is reduced, while that of Σ^- is enhanced.[6] The same argument explains the relative-abundance splitting of the isospin doublet (n, p).

In both panels hyperons appear at lower densities for the $s/\rho_B = 5$ isentrope because thermal excitation is stronger (the temperature increases rapidly along that trajectory). Consequently, by the time the $s/\rho_B = 5$ isentrope reaches the mixed phase the hyperon fractions are substantially larger (roughly an order of magnitude) than along the $s/\rho_B = 2$ isentrope. The earlier and more abundant appearance of hyperons produces an earlier softening of the hadronic EoS, which leads to a reduction of the temperature along the high-entropy isentrope as it approaches the phase boundary.

By contrast, the $s/\rho_B = 2$ isentrope experiences a milder temperature rise and smaller thermal contributions. Hyperons for this trajectory become relevant only above $\rho_B \gtrsim 0.3$ fm^{-3}, providing a larger density window over which the isentrope can increase its temperature before new degrees of freedom set in. Because the onset of the mixed phase occurs at a higher ρ_B in the FSU2H model, the $s/\rho_B = 2$ isentrope therefore intersects the coexistence region at a higher temperature than in the NL3$\omega\rho$ case.

Overall, the contrasting behaviour of the two isentropes is directly linked to the different population of hyperons along their evolution.

Strange Chiral Restoration

As in the previous model (cf. Subsec. 7.2.2), we examine in detail the effect of strange chiral restoration in Fig. 7.15. Because this region of the phase diagram corresponds to pure quark matter, the behaviour of the isentropes is governed entirely by the PNJL model; consequently, for identical values of G_V/G_S and α the chiral restoration of the strange sector occurs at the same (μ_B, T) coordinates in both two-phase constructions. Indeed, the point denoted by sχT in Fig. 7.15 coincides with the same marker in Fig. 7.5, as it should be.

[5] This is not surprising: the corresponding chemical potential is below $m_\Xi \approx 1320$ MeV, and thermal effects are insufficient to yield a significant Ξ abundance.

[6] For simplicity, consider the zero-temperature limit. The relation between the effective chemical potential μ^*_b and the density ρ_b of a baryon species b is

$$k_{F,b} = \sqrt{\mu^{*2}_b - m^{*2}_b} \propto \rho_b^{1/3},$$

so that an increase in μ^*_b implies an increase in ρ_b.

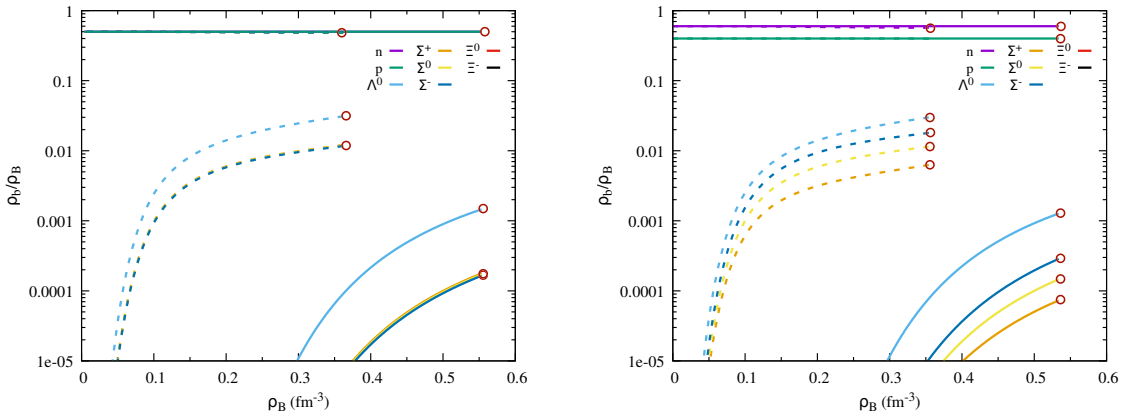

(a) (b)

Figure 7.14: Particle fractions as functions of the baryonic density for $\alpha = 0$ (left) and $\alpha = 0.2$ (right) in the FSU2H model with $G_V/G_S = 0$. Full lines denote $s/\rho_B = 2$ isentropes, while dashed lines denote $s/\rho_B = 5$ isentropes. Open circles denote intersections with the $\lambda = 0$ boundary. The fraction of Ξ^0, Ξ^- baryons is negligible and cannot be see in the plots. A log scale is used on the y axis

For a smaller vector coupling we find that strange chiral restoration is located at sχT$''$ (1732 MeV, 86.9 MeV) in the $T-\mu_B$ plane. By contrast, in the FSU2R case the $s/\rho_B = 2$ isentrope in the quark phase intersects the phase-boundary at $\mu_B \approx 1900$ MeV (cf. Figs. C.6b and C.6d), so that the low-entropy isentropes remain monotonic within the quark phase.

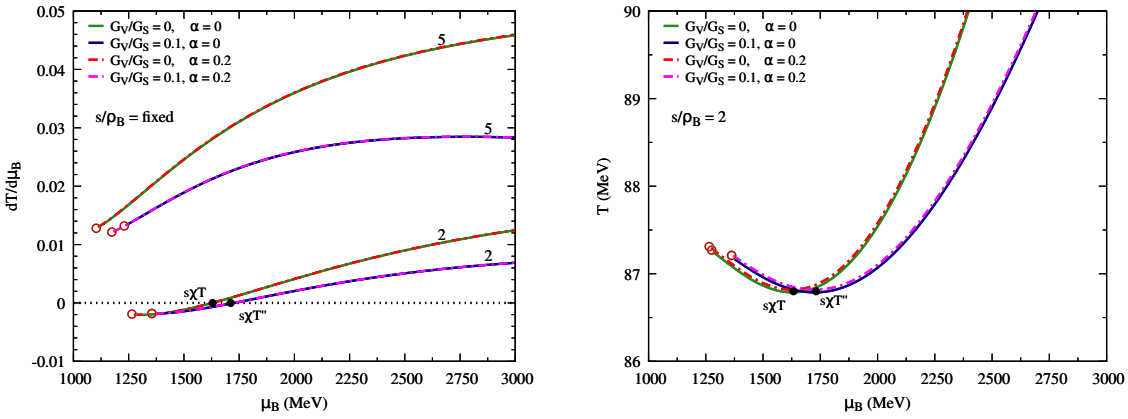

(a) (b)

Figure 7.15: Isentropic trajectories in the quark phase at large baryon chemical potential for asymmetry parameters $\alpha = 0$, 0.2, and vector couplings $G_V/G_S = 0$, 0.1. **Left:** $dT/d\mu_B$ as a function of μ_B. Only the $s/\rho_B = 2$ isentropes exhibit a non-monotonic temperature evolution with μ_B. **Right:** $s/\rho_B = 2$ isentropes in the $T-\mu_B$ plane. Along the $s/\rho_B = 2$ trajectory the temperature first decreases with μ_B until a minimum is reached, then develops a kink associated with the strange chiral-restoration transition (denoted "sχT"), after which T increases with μ_B. The marked transition points have coordinates sχT(1630 MeV, 86.8 MeV) and sχT$''$(1732 MeV, 86.9 MeV). Open circles denote intersections with the $\lambda = 1$ boundary.

Speed of Sound

The behaviour of the isentropes in the P/T^4–μ_B/T plane is qualitatively similar to that obtained with the NL3$\omega\rho$ model (cf. Figs. C.2 and C.8); consequently, the net-baryon number fluctuation patterns are expected to be comparable. For this reason we concentrate here on the speed of sound computed along each isentropic trajectory.

Comparing Figs. 7.10 and 7.16, the $s/\rho_B = 2$ isentrope attains a smaller maximum value of v_s^2 in the FSU2H model, while the $s/\rho_B = 5$ isentrope attains a larger maximum but at a higher baryon density. This behaviour is a direct consequence of the hyperon-induced softening of the hadronic EoS: at the same ρ_B the FSU2H model yields a lower v_s^2 than the nucleonic EoS, and therefore the fireball acceleration during the mixed phase is reduced relative to the hyperon-free case. The effect of isospin asymmetry is also consistent with previous findings: finite α smooths the isentropic curves at the onset of the mixed phase and reduces the discontinuity there, an effect that is most pronounced for the $s/\rho_B = 2$ trajectory.

As noted above, the quark vector coupling has been reduced to prevent quark-phase isentropes from exceeding the conformal limit $v_s^2 = 1/3$. With the chosen coupling this limit is respected by the $s/\rho_B = 5$ isentrope, while a mild violation remains for the $s/\rho_B = 2$ isentrope at $\rho_B \gtrsim 1$ fm^{-3} (see Figs. 7.16b and 7.16d). The magnitude of this violation is small, suggesting that a slight further reduction of the vector coupling would restore agreement with the conformal bound. Lower isentropes (for example $s/\rho_B = 1$) would likely breach the conformal limit at smaller ρ_B and with greater magnitude. If one wishes to constrain systematically the quark-vector coupling, a natural procedure is to map the speed of sound $v_s^2(\rho_B)$ for different values of G_V/G_S along the $T = 0$ trajectory and require $v_s^2(\rho_B) < 1/3$ for all relevant baryon densities. This yields an upper bound on G_V/G_S given by the largest coupling for which the $T = 0$ isentrope remains below the conformal limit in the $v_s^2 - \rho_B$ plane. Although an implementation of this procedure is beyond the scope of the present work, our results indicate that a focused exploration should concentrate on values $G_V/G_S < 0.1$ using the FSU2H model.

In contrast, the softer FSU2R equation of state attains an even smaller maximum v_s^2 (see Fig. C.9); nonetheless, for that model both isentropes exceed the conformal limit at very large baryon densities, which implies that G_V/G_S must be taken to substantially lower values (i.e. weaker vector interactions) to avoid violation.

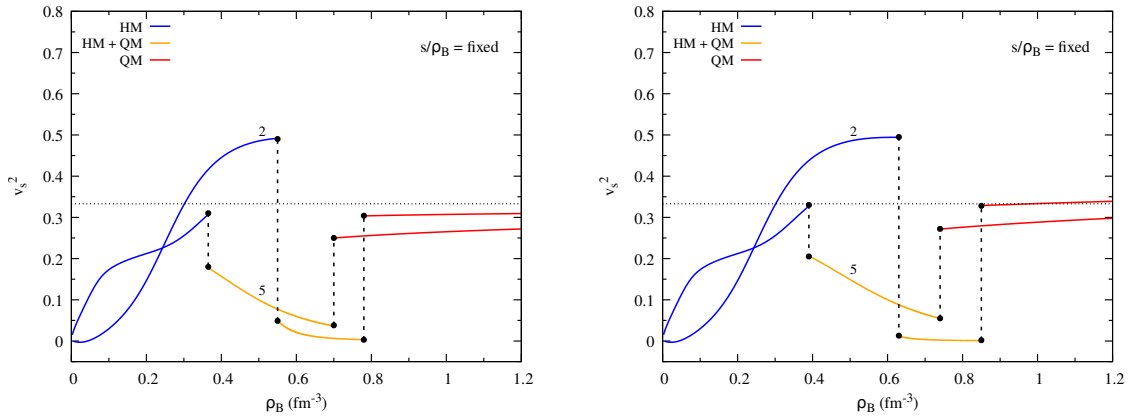

(a) $G_V/G_S = 0$ and $\alpha = 0$

(b) $G_V/G_S = 0.1$ and $\alpha = 0$

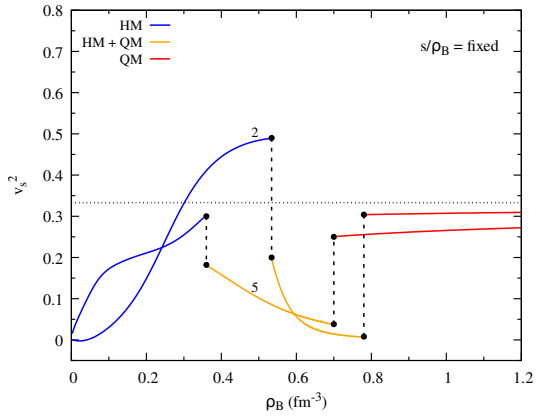

(c) $G_V/G_S = 0$ and $\alpha = 0.2$

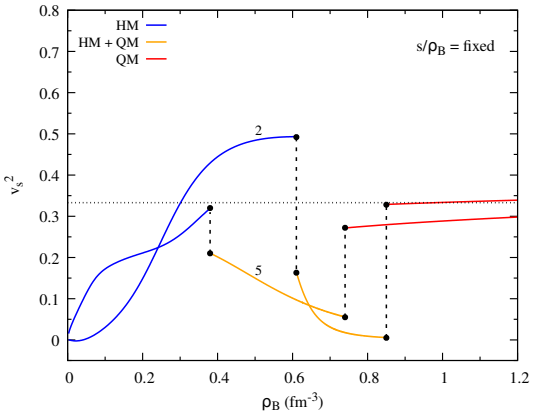

(d) $G_V/G_S = 0.1$ and $\alpha = 0.2$

Figure 7.16: Sound velocity squared v_s^2 as a function of the baryon density along the isentropes $s/\rho_B = 2$, 5 for $G_V/G_S = 0$ (left) and $G_V/G_S = 0.1$ (right), and for $\alpha = 0$ (top) and $\alpha = 0.2$ (bottom) within the FSU2H-PNJL two-model approach. The horizontal dotted line $v_s^2 = 1/3$ indicates the conformal limit.

Chapter 8

Conclusions and Outlook

Don't adventures ever have an end? I suppose not. Someone else always has to carry on the story.

– J.R.R. Tolkien, *The Fellowship of the Ring*

8.1 Conclusions

Throughout this work, we have studied the hadron-quark phase transition within a two-phase model for different scenarios of isospin asymmetry and for various strengths of vector interactions in the quark sector. The quark phase was described using a three-flavour PNJL model, while the hadronic phase was modelled with three parameter sets: NL3$\omega\rho$ for purely nucleonic matter, and FSU2R and FSU2H for matter including hyperons.

Phase boundaries and the CEP. We analysed the phase transition boundaries for different quark matter fractions. Our two-EoS approach suggests the presence of a CEP at a quark chemical potential in agreement with previous studies [28, 29].

A non-zero isospin-asymmetry parameter was found to split the phase boundary in the $T-\mu_B$ plane and to enlarge the mixed-phase region in the $T-\rho_B$ plane by lowering the onset chemical potential and density. Vector interactions further modify the transition: the vector channels shifts the phase diagram to higher baryon densities and chemical potentials while leaving the CEP temperature nearly unchanged. The CEP density and chemical potential, however, increase markedly when vector interactions are included. In Fig. 7.2d, for instance, ρ_B^{CEP} nearly doubles. These findings are consistent with Refs. [28, 106], although our model yields a much earlier onset of the mixed phase. This discrepancy originates from the hadronic sector: while our study employs the stiffer NL3$\omega\rho$ parametrisation, those works used the softer NLρ model [371], characterised by a less stiff EOS and symmetry energy [25].

The inclusion of hyperons shifts the phase boundary to higher densities and chemical potentials, as new degrees of freedom open. This effect is stronger for the softer FSU2R parametrisation (see Figs. C.5 and C.6). Nevertheless, the position of the CEP remains largely unaffected by hyperons.

Isentropic trajectories. We examined isentropic trajectories with $s/\rho_B = 2, 5$ in all scenarios. In most cases, the low-isentrope ($s/\rho_B = 2$) increases its temperature inside the mixed phase, while the high-isentrope cools sharply as the quark fraction λ increases, with this cooling becoming more pronounced near the CEP. For both the NL3$\omega\rho$- and FSU2H-PNJL two-phase models, we observed a kink at high temperature along the low-isentrope, producing a non-monotonic dependence on ρ_B (or μ_B) (see Figs. 7.5 and 7.15). This behaviour reflects the restoration of chiral symmetry in the strange sector. In contrast, no such effect is found for the FSU2R-PNJL model.

Vector interactions also impact the isentropes: they extend the mixed-phase region (increasing the μ_B range) but reduce the extension for low-isentropes. This behaviour can be traced to the entropy per baryon in each phase (see Fig. 7.4): while the ratio s^Q/ρ_B^Q in the quark phase always increases with vector interactions, the hadronic ratio s^H/ρ_B^H decreases so that the global entropy per baryon remains fixed.

The inclusion of hyperons modifies the intersection of isentropes with the pure-hadron boundary ($\lambda = 0$): for high-isentropes the intersection shifts to lower temperatures, while for low-isentropes it shifts to higher temperatures, in both cases moving to larger ρ_B and μ_B. These differences arise from the emergence and relative fraction of hyperons along the isentropes. As shown in Fig. 7.14, hyperons appear much earlier for high-isentropes due to thermal excitations, therefore playing a stronger role in softening the EOS and lowering the transition temperature.

Fluctuations and sound velocity. To connect our results with experimentally accessible quantities, we studied the baryon-number susceptibility ratios $\chi_B^{(3)}/\chi_B^{(1)}$ and $\chi_B^{(4)}/\chi_B^{(2)}$, as well as the speed of sound. The susceptibilities, computed along isentropic trajectories, display strong oscillations and rapid sign changes in the transition region. Vector interactions and isospin asymmetry reduce the step at the onset of the mixed phase, weakening the signal of the transition. However, extremely large values of the susceptibilities were often found in the hadronic phase. This behaviour is linked to the non-monotonic dependence of isentropes in the $P/T^4 - \mu_B/T$ plane, which leads to divergences and complicates the analysis. Such non-monotonic behaviour was observed in all two-EoS parametrisations considered.

By contrast, the squared speed of sound v_s^2 exhibits a much clearer pattern. At the hadron-quark transition, v_s^2 shows a distinct step, which is restored as hadronic degrees of freedom are reduced in the high-density quark phase. In isospin-asymmetric matter this step is milder, particularly for low-isentropes. Vector interactions enhance the step height at the transition boundary, producing an approximate plateau where v_s^2 nearly vanishes at lower densities, while reducing the step near the CEP. The inclusion of hyperons significantly reduces the step size for

fixed s/ρ_B. Since v_s^2 maps energy-density gradients into pressure gradients, responsible for the fluid acceleration, this softening of the EOS at low s/ρ_B (or $\sqrt{s_{\rm NN}}$) should strongly affect the flow of the medium, leaving imprints on the momentum distribution of hadrons in HICs.

Finally, even when the coupling constant of the quark vector interaction is reduced from $G_V/G_S = 0.5$ to $G_V/G_S = 0.1$, the conformal limit remains broken for low-isentropes. Although our analysis does not allow us to constrain a precise interval for this coupling, our results suggest that future constraints should be explored for $G_V/G_S < 0.1$, as we will discuss in the next section.

8.2 Future Work

As occasionally highlighted throughout this text, our study could benefit from several additional explorations that would further enhance our understanding of the mixed phase. Some immediate future directions include:

- **Isospin distillation.** Following Refs. [28,106], it would be interesting to study the effects of isospin distillation in our two-EoS models and examine how the enhancement of the local quark asymmetry parameter depends on temperature. As discussed in Ref. [28], these features of local asymmetry may lead to observable effects during the hadronisation stage of heavy-ion collisions, such as an inversion in the emission trend of neutron-rich clusters, an enhancement of π^-/π^+ and K^0/K^+ yield ratios in high-density regions, as well as an increased production of isospin-rich resonances and their subsequent decays.

- **Polytropic index.** The polytropic index has been proposed as an approximate criterion for identifying the hadron-quark phase transition. This quantity can be directly obtained from our present analysis and would serve as an additional diagnostic tool.

- **Fluctuations along isotherms.** Our analysis showed that net-baryon number fluctuations along isentropic trajectories are challenging to interpret. As an alternative, we propose computing susceptibility ratios along isothermal trajectories, which are expected to display simpler behaviour in the $P/T^4 - \mu_B/T$ plane. This would provide a more transparent picture of fluctuations in the mixed phase and improve the physical interpretation of our results.

- **Constraining G_V/G_S.** We observed that isentropes with $s/\rho_B \leq 2$ still break the conformal limit $v_s^2 = 1/3$. To constrain the range of physically consistent values for the coupling ratio, it will be important to study the zero-temperature limit and determine the largest values of G_V/G_S for which the conformal bound is respected.

- **Neutron stars.** Although our discussion has mainly focused on heavy-ion collisions, our framework could be straightforwardly extended to neutron-star matter. This would require imposing β-equilibrium, which constrains both hadronic and quark chemical potentials, reducing the number of independent variables and equations to be solved self-consistently.

It would also be interesting to study the impact of additional degrees of freedom on the mixed phase. For instance, pion condensates are expected to play a role at low densities, large isospin asymmetries, and high temperatures [25].

Another promising direction is to investigate the role of rotation. Rapid rotation is relevant both for neutron stars [372] and heavy-ion collisions, where the most vortical strongly interacting fluid created to date reached a vorticity of about 10^{22} s^{-1} [373]. Rotation can induce novel transport phenomena [374, 375] that may leave measurable experimental signatures. Beyond transport properties, rotation also affects the phase structure itself. For example, Ref. [376] showed within a two-flavour NJL model at $\mu_B = 0$ that both rotation and finite-size effects catalyse the transition from the hadron to the quark phase at lower temperature and reduce the effective quark mass at finite temperature. Extending such studies to our more complete setup with three flavours and finite baryon density could reveal important modifications of the phase diagram and its properties.

Appendix A

Conventions

In this appendix, we will introduced the used conventions. We will begin general remarks before we continue with the Dirac space, the $SU(N)$ group, and the Euclidean space, where we shown how it is related to the Minkowski space.

In general, we use natural (Planck) units:

$$\hbar = c = k_B = 1, \tag{A.1}$$

where c is the speed of light, $\hbar$ is the reduced Planck's constant and k_B is the Boltzmann constant. In this units

$$[\text{energy}] = [\text{mass}] = [\text{temperature}] = [\text{lenght}]^{-1} = [\text{time}]^{-1}. \tag{A.2}$$

We also employ the Einstein sum convention

$$a \cdot b = a_\mu b^\mu = \sum_\mu a_\mu b^\mu, \tag{A.3}$$

unless the sum is specified.

A.1 Dirac Space

The most important basis elements of the Dirac space are the so-called Dirac (gamma) matrices $\gamma^m u$. They are defined by the Clifford algebra which is inherited from the Pauli matrices (see App. A.3). They defined by

$$\gamma^\mu = (\gamma^0, \boldsymbol{\gamma}), \tag{A.4}$$

and in Minkowski space they are given by the anti-commutation relations

$$\{\gamma^\mu, \gamma^\nu\} = \gamma^\mu\gamma^\nu + \gamma^\nu\gamma^\mu = 2\eta^{\mu\nu}, \tag{A.5}$$

where $\eta_{\mu\nu}$ is the Minkowski metric, defined in this thesis with the signature $(+,-,-,-)$, i.e.

$$\eta_{\mu\nu} = \begin{pmatrix} 1 & 0 & 0 & 0 \\ 0 & -1 & 0 & 0 \\ 0 & 0 & -1 & 0 \\ 0 & 0 & 0 & -1 \end{pmatrix}. \tag{A.6}$$

On the other hand, the covariant gamma matrices are defined by

$$\gamma_\mu = \eta_{\mu\nu}\gamma^\nu = (\gamma^0, -\boldsymbol{\gamma}). \tag{A.7}$$

Moreover, γ^μ have the following properties:

$$\begin{aligned} \left(\gamma^0\right)^\dagger &= \gamma^0, & \left(\gamma^i\right)^\dagger &= -\gamma^i, \\ \left(\gamma^0\right)^2 &= \mathbb{1}_{4\times4}, & \left(\gamma^i\right)^2 &= -\mathbb{1}_{4\times4}. \end{aligned} \tag{A.8}$$

The γ_5 matrix is defined as the product

$$\gamma^5 \equiv i\gamma^0\gamma^1\gamma^2\gamma^3, \tag{A.9}$$

and satisfy the following properties:

$$\{\gamma^5, \gamma^\mu\} = 0, \quad \left(\gamma^5\right)^\dagger = \gamma^5, \quad \left(\gamma^5\right)^2 = \mathbb{1}_{4\times4}. \tag{A.10}$$

The standard representation for the gamma matrices reads:

$$\gamma^0 = \begin{pmatrix} \mathbb{1}_{2\times2} & 0 \\ 0 & -\mathbb{1}_{2\times2} \end{pmatrix}, \quad \gamma^i = \begin{pmatrix} 0 & \sigma^i \\ -\sigma^i & 0 \end{pmatrix}, \quad \gamma^5 = \begin{pmatrix} 0 & \mathbb{1}_{2\times2} \\ \mathbb{1}_{2\times2} & 0 \end{pmatrix}, \tag{A.11}$$

where σ^i are the Pauli matrices of the $SU(2)$ group (see App. A.3). Other representations are possible but have to be unitary transformations $\gamma'_\mu = U\gamma_\mu U^\dagger$ of the Dirac representation. One of these other representations is the Weyl (or chiral) representation obtained by the unitary transformation

$$U = \frac{1}{\sqrt{2}} \begin{pmatrix} \mathbb{1}_{2\times2} & -\mathbb{1}_{2\times2} \\ \mathbb{1}_{2\times2} & \mathbb{1}_{2\times2} \end{pmatrix} \tag{A.12}$$

This representation is important, since in this notation the $\text{Weyl}(\gamma^5) = -\text{Dirac}(\gamma^0)$ matrix is diagonal and used to project onto left- and right-handed particles. This is relevant in the chiral or ultra-relativistic limit where the quark masses are neglectable.

We also denote

$$a \cdot b = a_0 b_0 - a_i b^i, \quad \partial_\mu \equiv \frac{\partial}{\partial x^\mu} = (\partial_t, \nabla), \quad \partial^\mu \equiv \frac{\partial}{\partial x_\mu} = (\partial_t, -\nabla), \tag{A.13}$$

and the d'Alembert operator

$$\Box \equiv \partial^\mu \partial_\mu. \tag{A.14}$$

A.2 Euclidean Space

All calculations in this work are performed in Euclidean space. In this section, we introduce Euclidean space as the counterpart of Minkowski space and clarify the correspondence between the two formulations. Throughout, quantities carrying the subscript "E" are defined in Euclidean space, whereas those without a subscript refer to Minkowski space. A key feature of Euclidean space is that the distinction between covariant and contravariant vectors disappears, i.e.,

$$a^\mu = a_\mu, \tag{A.15}$$

and the Minkowski metric is replaced by the Euclidean metric,

$$\eta_{\mu\nu} \to \delta_{\mu\nu}. \tag{A.16}$$

Consequently, the scalar products and the Clifford algebra are now given by

$$a^E_\mu a^E_\mu = a^E_0 b^E_0 + a^E_i a^E_i, \tag{A.17}$$

for $\mu = 0, 1, 2, 3$ and $i = 1, 2, 3$. We achieve this property via Wick rotation,

$$x_0 = t \to i\tau, \quad \tau = x^E_0, \tag{A.18}$$

and the resulting redefinition of the Lorentz vectors, tensors and gamma matrices. The Euclidean counterparts are defined via

$$\gamma^0_E = \gamma^0, \quad \gamma^i_E = -i\gamma^i, \tag{A.19}$$

and obey the relations

$$\{\gamma^\mu_E, \gamma^\nu_E\} = 2\delta^{\mu\nu}, \qquad (\gamma^\mu_E)^\dagger = \gamma^\mu_E, \tag{A.20}$$

where $\eta_{\mu\nu}$ is the Euclidean metric, $\delta_{\mu\nu} = \mathbb{1}_{4\times4}$.

The γ^5_E matrix is defined as the product

$$\gamma^5_E \equiv -\gamma^0_E \gamma^1_E \gamma^2_E \gamma^3_E, \tag{A.21}$$

and satisfy the same properties as in Minkowski space (see Eq. (A.10)).

The standard representation for the gamma matrices reads:

$$\gamma^0_E = \begin{pmatrix} \mathbb{1}_{2\times2} & 0 \\ 0 & -\mathbb{1}_{2\times2} \end{pmatrix}, \quad \gamma^i_E = \begin{pmatrix} 0 & -i\sigma^i \\ i\sigma^i & 0 \end{pmatrix}, \quad \gamma^5_E = \begin{pmatrix} 0 & \mathbb{1}_{2\times2} \\ \mathbb{1}_{2\times2} & 0 \end{pmatrix}, \tag{A.22}$$

where σ^i are the Pauli matrices of the $SU(2)$ group (see App. A.3).

A.3 $SU(N)$ Matrices

We denote the N^2-1 generators that form the algebra of the $SU(N)$ group by Γ_a. This fulfil the Lie algebra

$$[\Gamma_a, \Gamma_b] = i f_{abc} \Gamma_c, \tag{A.23}$$

where f_{abc} are the totally anti-symmetric structure constants. One also defines the anti-commutation relation

$$\{\Gamma_a, \Gamma_b\} = \frac{1}{N}\delta_{ab}\mathbb{1}_{N\times N} + \frac{1}{2} d_{abc}\Gamma_c, \tag{A.24}$$

where d_{abc} are the totally symmetric structure constants. In addition, the generators also fulfil the relations

$$\mathrm{Tr}(\Gamma_a\Gamma_b) = T(R)\delta_{ab} \quad \text{and} \quad \left(\sum_a^{N^2-1} \Gamma_a^2\right)_{ij} = C(R)\delta_{ij}, \tag{A.25}$$

with $T(R)$ and $C(R)$ representing the Dynkin index and Casimir factor in the representation R, respectively.

For $N=2$, we have the three Pauli matrices of $SU(2)$:

$$\sigma_1 = \begin{pmatrix} 0 & 1 \\ 1 & 0 \end{pmatrix}, \quad \sigma_2 = \begin{pmatrix} 0 & -i \\ i & 0 \end{pmatrix}, \quad \sigma_3 = \begin{pmatrix} 1 & 0 \\ 0 & -1 \end{pmatrix}, \tag{A.26}$$

characterised by

$$\Gamma_a = \frac{1}{2}\sigma_a, \quad f_{abc} = \varepsilon_{abc}, \quad d_{abc} = 0, . \tag{A.27}$$

with $a = 1, 2, 3$. Here ε_{abc} is the Levi-Civita symbol.

For $N=3$, we have the eight Gell-Mann matrices of $SU(3)$:

$$\lambda_1 = \begin{pmatrix} 0 & 1 & 0 \\ 1 & 0 & 0 \\ 0 & 0 & 0 \end{pmatrix}, \quad \lambda_2 = \begin{pmatrix} 0 & -i & 0 \\ i & 0 & 0 \\ 0 & 0 & 0 \end{pmatrix}, \quad \lambda_3 = \begin{pmatrix} 1 & 0 & 0 \\ 0 & -1 & 0 \\ 0 & 0 & 0 \end{pmatrix}, \quad \lambda_4 = \begin{pmatrix} 0 & 0 & 1 \\ 0 & 0 & 0 \\ 1 & 0 & 0 \end{pmatrix},$$

$$\lambda_5 = \begin{pmatrix} 0 & 0 & -i \\ 0 & 0 & 0 \\ i & 0 & 0 \end{pmatrix}, \quad \lambda_6 = \begin{pmatrix} 0 & 0 & 0 \\ 0 & 0 & 1 \\ 0 & 1 & 0 \end{pmatrix}, \quad \lambda_7 = \begin{pmatrix} 0 & 0 & 0 \\ 0 & 0 & -i \\ 0 & i & 0 \end{pmatrix}, \quad \lambda_8 = \frac{1}{\sqrt{3}}\begin{pmatrix} 1 & 0 & 0 \\ 0 & 1 & 0 \\ 0 & 0 & -2 \end{pmatrix}. \tag{A.28}$$

The generators are thus $\Gamma_a = \lambda_a/2$. The anti-symmetric structure constants f_{abc} are:

$$\begin{aligned} f_{123} &= 1, \\ f_{147} &= f246 = f_{257} = f_{345} = -f_{156} = -f_{367} = \frac{1}{2}, \\ f_{458} &= f_{678} = \frac{\sqrt{3}}{2}, \end{aligned} \tag{A.29}$$

while all other not related to these by permutation are zero. The symmetric structure constants d_{abc} are:

$$\begin{aligned} d_{118} &= d_{228} = d_{338} = -d_{888} = \frac{1}{\sqrt{3}}, \\ d_{448} &= d_{558} = d_{668} = d_{778} = -\frac{1}{2\sqrt{3}}, \\ d_{146} &= d_{157} = d_{256} = d_{344} = d_{355} = d_{247} = -d_{366} = -d_{377} = \frac{1}{2}. \end{aligned} \tag{A.30}$$

There are two main representations R: the fundamental and the adjoint representation. In colour space, the fundamental representation is used for quarks fields while the adjoint representation is used for the gluons as gauge bosons that mediate the strong interaction. The Dynkin index and the Casimir factor values are given in Table A.1 for each representation together with the representation of the matrices and their dimension.

Representation R	$(\Gamma_a)_{ij}$	$\dim(\Gamma_a)$	$T(R)$	$C(R)$
Fundamental	$(\lambda_a/2)_{ij}$	N	$1/2$	$\frac{N^2-1}{2N}$
Adjoint	$-if_{aij}$	N^2-1	N	N

Table A.1: Fundamental and adjoint representation of the $SU(N)$ group generators and corresponding properties.

Appendix B

Auxiliary Calculations

B.1 The 't Hooft Determinant in the MFA for $N_f = 2 + 1$

For $(2+1)$-flavour NJL Lagrangian density, the 't Hooft determinant in (5.1) can be computed thorough

$$\det_f \bar{\psi}\mathcal{O}\psi = \varepsilon_{ijk}(\bar{\psi}_u\mathcal{O}\psi_i)(\bar{\psi}_d\mathcal{O}\psi_j)(\bar{\psi}_s\mathcal{O}\psi_k), \tag{B.1}$$

where summation over repeated indices is understood, and ε_{ijk} is the Levi-Civita symbol in three dimensions defined by

$$\varepsilon_{ijk} = \begin{cases} +1, & \text{if } (i,j,k) \text{ is an even permutation of (1,2,3),} \\ -1, & \text{if } (i,j,k) \text{ is an odd permutation of (1,2,3),} \\ 0, & \text{if } i=j, \text{ or } j=k, \text{ or } k=i. \end{cases} \tag{B.2}$$

Applying the linearisation of the product between three operator given by Equation (5.7), the determinant reads

$$\begin{aligned} \det_f \bar{\psi}\mathcal{O}\psi \approx \varepsilon_{ijk}\Big[&(\bar{\psi}_u\mathcal{O}\psi_i)\left\langle\bar{\psi}_d\mathcal{O}\psi_j\right\rangle\left\langle\bar{\psi}_s\mathcal{O}\psi_k\right\rangle + \left\langle\bar{\psi}_u\mathcal{O}\psi_i\right\rangle(\bar{\psi}_d\mathcal{O}\psi_j)\left\langle\bar{\psi}_s\mathcal{O}\psi_k\right\rangle \\ &+ \left\langle\bar{\psi}_u\mathcal{O}\psi_i\right\rangle\left\langle\bar{\psi}_d\mathcal{O}\psi_j\right\rangle(\bar{\psi}_s\mathcal{O}\psi_k) - 2\left\langle\bar{\psi}_u\mathcal{O}\psi_i\right\rangle\left\langle\bar{\psi}_d\mathcal{O}\psi_j\right\rangle\left\langle\bar{\psi}_s\mathcal{O}\psi_k\right\rangle\Big]. \end{aligned} \tag{B.3}$$

We assign the flavour indices $u = 1$, $d = 2$, and $s = 3$, and defining the projection operator

$$\mathcal{O} = 1 \pm \gamma^5 \tag{B.4}$$

so as to recover the 't Hooft determinant In the presence of a non-zero constituent quark mass — generated by the formation of a quark condensate — and under the assumption that the energy scale is below the threshold for pion condensation, the only non-vanishing quark bilinear is

$$\left\langle\bar{\psi}_i\psi_j\right\rangle = \delta_{ij}\left\langle\bar{\psi}_i\psi_j\right\rangle. \tag{B.5}$$

Therefore, the only non-zero terms in (B.3) are:

$$\begin{aligned}\det_f \bar{\psi}\mathcal{O}\psi \approx\ & (\bar{\psi}_u\mathcal{O}\psi_u)\left[\left\langle\bar{\psi}_d\mathcal{O}\psi_d\right\rangle\left\langle\bar{\psi}_s\mathcal{O}\psi_s\right\rangle-\left\langle\bar{\psi}_d\mathcal{O}\psi_s\right\rangle\left\langle\bar{\psi}_s\mathcal{O}\psi_d\right\rangle\right]\\ &+(\bar{\psi}_d\mathcal{O}\psi_d)\left[\left\langle\bar{\psi}_u\mathcal{O}\psi_u\right\rangle\left\langle\bar{\psi}_s\mathcal{O}\psi_s\right\rangle-\left\langle\bar{\psi}_u\mathcal{O}\psi_s\right\rangle\left\langle\bar{\psi}_s\mathcal{O}\psi_u\right\rangle\right]\\ &+(\bar{\psi}_s\mathcal{O}\psi_s)\left[\left\langle\bar{\psi}_u\mathcal{O}\psi_u\right\rangle\left\langle\bar{\psi}_d\mathcal{O}\psi_d\right\rangle-\left\langle\bar{\psi}_u\mathcal{O}\psi_u\right\rangle\left\langle\bar{\psi}_d\mathcal{O}\psi_u\right\rangle\right]\\ &-2\left\langle\bar{\psi}_u\mathcal{O}\psi_u\right\rangle\left[\left\langle\bar{\psi}_d\mathcal{O}\psi_d\right\rangle\left\langle\bar{\psi}_s\mathcal{O}\psi_s\right\rangle-\left\langle\bar{\psi}_d\mathcal{O}\psi_s\right\rangle\left\langle\bar{\psi}_s\mathcal{O}\psi_d\right\rangle\right]\\ &+\ldots,\end{aligned} \tag{B.6}$$

where the ellipsis are other terms that will vanish due to rule (B.5). By the same argument, in Eq. (B.6) only the first term within the brackets survives. Thus, in the mean-field approximation the KMT interaction in Lagrangian (5.1) reads

$$\begin{aligned}G_D\left[\det_f\bar{\psi}(1+\gamma_5)\psi+\det_f\bar{\psi}(1-\gamma_5)\psi\right]\approx 2G_D\Big[&(\bar{\psi}_u\psi_u)\left\langle\bar{\psi}_d\psi_d\right\rangle\left\langle\bar{\psi}_s\psi_s\right\rangle\\ &+(\bar{\psi}_d\psi_d)\left\langle\bar{\psi}_d\psi_d\right\rangle\left\langle\bar{\psi}_s\psi_s\right\rangle\\ &+(\bar{\psi}_s\psi_s)\left\langle\bar{\psi}_u\psi_u\right\rangle\left\langle\bar{\psi}_d\psi_d\right\rangle\\ &-2\left\langle\bar{\psi}_u\mathcal{O}\psi_u\right\rangle\left\langle\bar{\psi}_d\mathcal{O}\psi_d\right\rangle\left\langle\bar{\psi}_s\mathcal{O}\psi_s\right\rangle\Big]\end{aligned}. \tag{B.7}$$

B.2 Gap Equations of the (2+1)-flavour PNJL model

The gap equations of the three-flavour PNJL model can be found by solving the systems:

$$\frac{\partial\tilde{\Omega}_{\rm PNJL}}{\partial\sigma_u}=\frac{\partial\tilde{\Omega}_{\rm PNJL}}{\partial\sigma_d}=\frac{\partial\tilde{\Omega}_{\rm PNJL}}{\partial\sigma_s}=0, \tag{B.8}$$

$$\frac{\partial\tilde{\Omega}_{\rm PNJL}}{\partial\Phi}=\frac{\partial\tilde{\Omega}_{\rm PNJL}}{\partial\bar{\Phi}}=0, \tag{B.9}$$

which defines the values of the quark condensates σ_u, σ_d and σ_s, and the Polyakov loop fields Φ and $\bar{\Phi}$. The grand canonical potential of the PNJL mode in the MFA, $\tilde{\Omega}_{\rm PNJL}$ is given by Eq. (5.57):

$$\begin{aligned}\tilde{\Omega}_{\rm PNJL}=&\,\Omega_0+U_{\rm PNJL}-U_{\rm cond}\\ &-2T\sum_{f=u,d,s}\int\frac{{\rm d}^3p}{(2\pi)^3}\Big[N_c\beta E(\mathbf{p})+z^+(\Phi,\bar{\Phi},E_f,\mu_f^*)++z^-(\Phi,\bar{\Phi},E_f,\mu_f^*)\Big],\end{aligned} \tag{B.10}$$

where we have defined (Eqs. (5.58)),

$$\begin{aligned}z^-(\Phi,\bar{\Phi},E_f,\mu_f^*)&\equiv\ln\left(1+N_c\Phi e^{-\beta(E_f+\mu_f^*)}+N_c\bar{\Phi}e^{-2\beta(E_f+\mu_f^*)}+e^{-3\beta(E_f+\mu_f^*)}\right),\\ z^+(\Phi,\bar{\Phi},E_f,\mu_f^*)&\equiv\ln\left(1+N_c\bar{\Phi}e^{-\beta(E_f-\mu_f^*)}+N_c\Phi e^{-2\beta(E_f-\mu_f^*)}+e^{-3\beta(E_f-\mu_f^*)}\right).\end{aligned} \tag{B.11}$$

For the quark condensates, tt will be useful to consider the following decomposition:

$$\frac{\partial\tilde{\Omega}_{\rm PNJL}}{\partial\sigma_i}=\frac{\partial\tilde{\Omega}_{\rm PNJL}}{\partial\sigma_i}+\frac{\partial\tilde{\Omega}_{\rm PNJL}}{\partial m_i^*}\frac{\partial m_i^*}{\partial\sigma_i}+\frac{\partial\tilde{\Omega}_{\rm PNJL}}{\partial m_j^*}\frac{\partial m_j^*}{\partial\sigma_i}+\frac{\partial\tilde{\Omega}_{\rm PNJL}}{\partial m_k^*}\frac{\partial m_k^*}{\partial\sigma_i}=0, \tag{B.12}$$

where $i\neq j\neq k\in(u,d,s)$. Each term yields:

$$\frac{\partial\tilde{\Omega}_{\rm PNJL}}{\partial\sigma_i}=4G_S\sigma_i+4G_D\sigma_j\sigma_k, \tag{B.13}$$

$$\frac{\partial m_i^*}{\partial\sigma_i}=-4G_S,\qquad \frac{\partial m_j^*}{\partial\sigma_i}=-2G_D\sigma_k, \tag{B.14}$$

and for the quark flavour f

$$\frac{\partial\tilde{\Omega}_{\rm PNJL}}{\partial m_f^*}=-2T\int\frac{\mathrm{d}^3p}{(2\pi)^3}\left[N_c\beta\frac{\partial E(\mathbf{p})}{\partial m_f^*}+\frac{\partial z^+}{\partial m_f^*}+\frac{\partial z^-}{\partial m_f^*}\right]. \tag{B.15}$$

The derivatives in Eq. (B.15) are given by

$$\frac{\partial E(\mathbf{p})}{\partial m_f^*}=\frac{m_f^*}{E_f} \tag{B.16a}$$

$$\frac{\partial z^+}{\partial m_f^*}=-\frac{N_c}{T}\frac{m_f^*}{E_f}\mathcal{F}_f^+, \tag{B.16b}$$

$$\frac{\partial z^-}{\partial m_f^*}=-\frac{N_c}{T}\frac{m_f^*}{E_f}\mathcal{F}_f^-, \tag{B.16c}$$

where $\mathcal{F}_f^+$ and $\mathcal{F}_f^-$ are the particle and antiparticle occupation numbers in the PNJL model (Eqs. (5.65)),

$$\mathcal{F}_f^+=\frac{\frac{3}{N_c}e^{-3\beta(E_f-\mu_f^*)}+\bar{\Phi}e^{-\beta(E_f-\mu_f^*)}+2\Phi e^{-2\beta(E_f-\mu_f^*)}}{1+e^{-3\beta(E_f-\mu_f^*)}+N_c\bar{\Phi}e^{-\beta(E_f-\mu_f^*)}+N_c\Phi e^{-2\beta(E_f-\mu_f^*)}}, \tag{B.17a}$$

$$\mathcal{F}_f^-=\frac{\frac{3}{N_c}e^{-3\beta(E_f+\mu_f^*)}+\Phi e^{-\beta(E_f+\mu_f^*)}+2\bar{\Phi}e^{-2\beta(E_f+\mu_f^*)}}{1+e^{-3\beta(E_f+\mu_f^*)}+N_c\Phi e^{-\beta(E_f+\mu_f^*)}+N_c\bar{\Phi}e^{-2\beta(E_f+\mu_f^*)}}. \tag{B.17b}$$

Thus, Eq. (B.15) reads,

$$\frac{\partial\tilde{\Omega}_{\rm PNJL}}{\partial m_f^*}=-2N_c\int\frac{\mathrm{d}^3p}{(2\pi)^3}\frac{m_f^*}{E_f}\left(1-\mathcal{F}_f^+-F_f^-\right)\equiv I_f. \tag{B.18}$$

Substituting the above expressions in Eq. (B.12), we obtain,

$$4G_S(\sigma_i-I_i)-2G_D(\sigma_kI_j+\sigma_jI_k-2\sigma_j\sigma_k)=0, \tag{B.19}$$

with $i\neq j\neq k\in(u,d,s)$, which corresponds to a system of three equations:

$$4G_S(\sigma_u-I_u)=2G_D(\sigma_sI_d+\sigma_dI_s-2\sigma_d\sigma_s), \tag{B.20a}$$

$$4G_S(\sigma_d - I_d) = 2G_D(\sigma_u I_s + \sigma_s I_u - 2\sigma_u\sigma_s), \tag{B.20b}$$

$$4G_S(\sigma_s - I_s) = 2G_D(\sigma_d I_u + \sigma_u I_d - 2\sigma_u\sigma_d). \tag{B.20c}$$

If G_S and G_D are non-zero, the above equalities are satisfied if and only if

$$\sigma_u = I_u = -2N_c \int \frac{\mathrm{d}^3p}{(2\pi)^3}\frac{m_u^*}{E_u}\left(1 - \mathcal{F}_u^+ - \mathcal{F}_u^-\right), \tag{B.21a}$$

$$\sigma_d = I_d = -2N_c \int \frac{\mathrm{d}^3p}{(2\pi)^3}\frac{m_d^*}{E_d}\left(1 - \mathcal{F}_d^+ - \mathcal{F}_d^-\right), \tag{B.21b}$$

$$\sigma_s = I_s = -2N_c \int \frac{\mathrm{d}^3p}{(2\pi)^3}\frac{m_s^*}{E_s}\left(1 - \mathcal{F}_s^+ - \mathcal{F}_s^-\right), \tag{B.21c}$$

defining the quark condensates for each flavour in the PNJL model.

The gap equations of the Polyakov loops (Eqs. (5.61)) are obtained by solving Eqs. (B.9) . We promote Φ and $\bar{\Phi}$ to independent real variables, even though they are complex by definition. This is made to avoid problems arising from minimizing a complex potential [287, 377]. Thus, we have:

$$\frac{\partial\tilde{\Omega}_{\mathrm{PNJL}}}{\partial\Phi} = \frac{\partial U_{\mathrm{PNJL}}}{\partial\Phi} - 2T\sum_{f=u,d,s}\int\frac{\mathrm{d}^3p}{(2\pi)^3}\left[\frac{\partial z^+}{\partial\Phi} + \frac{\partial z^-}{\partial\Phi}\right] = 0, \tag{B.22a}$$

$$\frac{\partial\tilde{\Omega}_{\mathrm{PNJL}}}{\partial\bar{\Phi}} = \frac{\partial U_{\mathrm{PNJL}}}{\partial\bar{\Phi}} - 2T\sum_{f=u,d,s}\int\frac{\mathrm{d}^3p}{(2\pi)^3}\left[\frac{\partial z^+}{\partial\bar{\Phi}} + \frac{\partial z^-}{\partial\bar{\Phi}}\right] = 0. \tag{B.22b}$$

For the first term, the U_{PNJL} potential is defined in Eq. (5.44) as

$$\begin{aligned}\frac{U_{\mathrm{PNJL}}(\Phi,\bar{\Phi},T)}{T^4} = &-\frac{a(T)}{2}\langle\bar{\Phi}\rangle\langle\Phi\rangle \\ &+ b(T)\ln\left[1 - 6\langle\bar{\Phi}\rangle\langle\Phi\rangle + 4\left(\langle\bar{\Phi}\rangle^3 + \langle\Phi\rangle^3\right) - 3\left(\langle\bar{\Phi}\rangle\langle\Phi\rangle\right)^2\right].\end{aligned} \tag{B.23}$$

In mean-field we define $\Phi = \langle\Phi\rangle$ ($\bar{\Phi} = \langle\bar{\Phi}\rangle$). Hence, we obtain:

$$\frac{\partial U_{\mathrm{PNJL}}}{\partial\Phi} = T^4\left[-\frac{a(T)}{2}\bar{\Phi} - \frac{6b(T)\left(\bar{\Phi} - 2\Phi^2 + \bar{\Phi}^2\Phi\right)}{1 - 6\bar{\Phi}\Phi + 4\left(\bar{\Phi}^3 + \Phi^3\right) - 3\left(\bar{\Phi}\Phi\right)^2}\right], \tag{B.24a}$$

$$\frac{\partial U_{\mathrm{PNJL}}}{\partial\bar{\Phi}} = T^4\left[-\frac{a(T)}{2}\Phi - \frac{6b(T)\left(\Phi - 2\bar{\Phi}^2 + \bar{\Phi}\Phi^2\right)}{1 - 6\bar{\Phi}\Phi + 4\left(\bar{\Phi}^3 + \Phi^3\right) - 3\left(\bar{\Phi}\Phi\right)^2}\right]. \tag{B.24b}$$

The derivatives of the thermal functions are given by:

$$\frac{\partial z^+}{\partial\Phi} = N_c e^{-2\beta(E_f - \mu_f^*) - z^+}, \qquad \frac{\partial z^+}{\partial\bar{\Phi}} = N_c e^{-\beta(E_f - \mu_f^*) - z^+}, \tag{B.25a}$$

$$\frac{\partial z^-}{\partial\Phi} = N_c e^{-\beta(E_f + \mu_f^*) - z^-}, \qquad \frac{\partial z^-}{\partial\bar{\Phi}} = N_c e^{-2\beta(E_f + \mu_f^*) - z^-}. \tag{B.25b}$$

Gathering all the results yields the gap equations for the Polyakov loop:

$$-\frac{a(T)}{2}\bar{\Phi} = \frac{6b(T)(\bar{\Phi} - 2\Phi^2 + \bar{\Phi}^2\Phi)}{1 - 6\bar{\Phi}\Phi + 4(\bar{\Phi}^3 + \Phi) - 3(\bar{\Phi}\Phi)^2} + \frac{2N_c}{T^3}\sum_{f=u,d,s}\int\frac{\mathrm{d}^3p}{(2\pi)^3}\left(e^{-\beta(E_f+\mu_f^*)-z^-} + e^{-2\beta(E_f-\mu_f^*)-z^+}\right), \tag{B.26a}$$

$$-\frac{a(T)}{2}\Phi = \frac{6b(T)(\Phi - 2\bar{\Phi}^2 + \bar{\Phi}\Phi^2)}{1 - 6\bar{\Phi}\Phi + 4(\bar{\Phi}^3 + \Phi) - 3(\bar{\Phi}\Phi)^2} + \frac{2N_c}{T^3}\sum_{f=u,d,s}\int\frac{\mathrm{d}^3p}{(2\pi)^3}\left(e^{-\beta(E_f-\mu_f^*)-z^+} + e^{-2\beta(E_f+\mu_f^*)-z^-}\right). \tag{B.26b}$$

Appendix C

Supplementary Results

This appendix collects supplementary numerical results for the NL3$\omega\rho$-PNJL and FSU2H-PNJL models, together with the complete set of results for the FSU2R-PNJL family introduced in the main text. The material includes additional phase diagrams, isentropic trajectories, and tabulated thermodynamic quantities that support and extend the discussion presented in Ch. 7.

C.1 NL3$\omega\rho$-PNJL Model

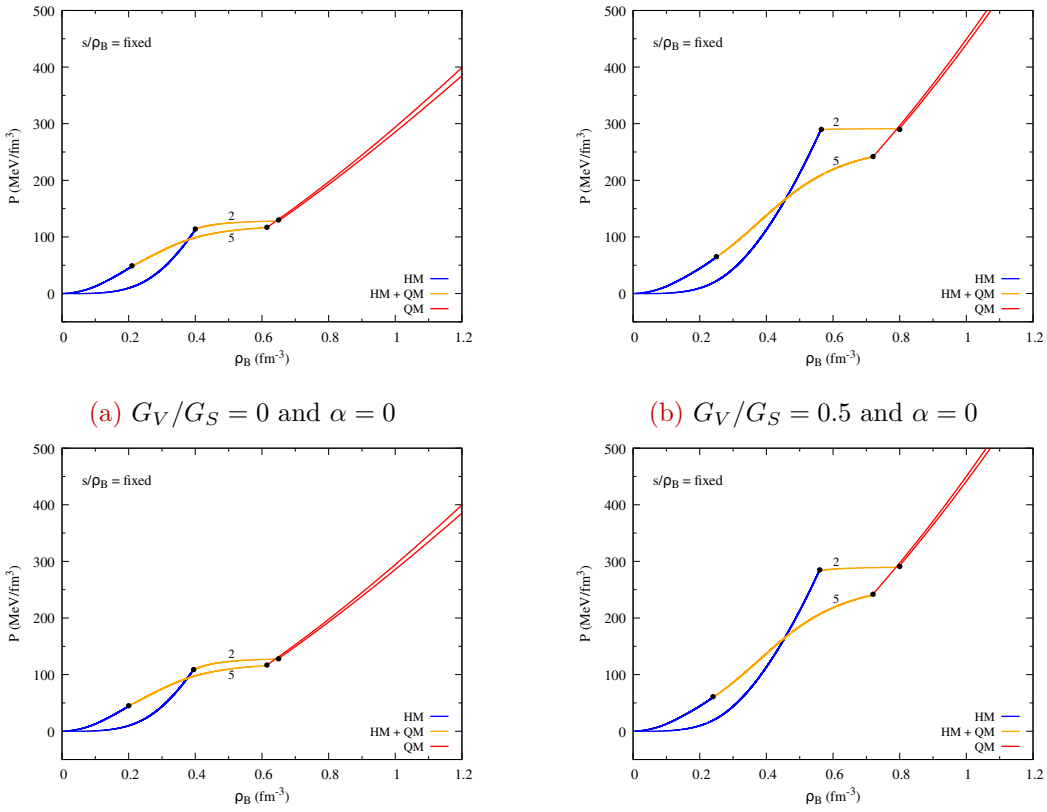

(a) $G_V/G_S = 0$ and $\alpha = 0$

(b) $G_V/G_S = 0.5$ and $\alpha = 0$

(c) $G_V/G_S = 0$ and $\alpha = 0.2$

(d) $G_V/G_S = 0.5$ and $\alpha = 0.2$

Figure C.1: Pressure as a function number density for the isentropes s/ρ_B =2, 5 for the NL3$\omega\rho$-PNJL two-phase model. The range between the dots denote the mixed-phase regime (in orange).

C.2 FSU2H-PNJL Model

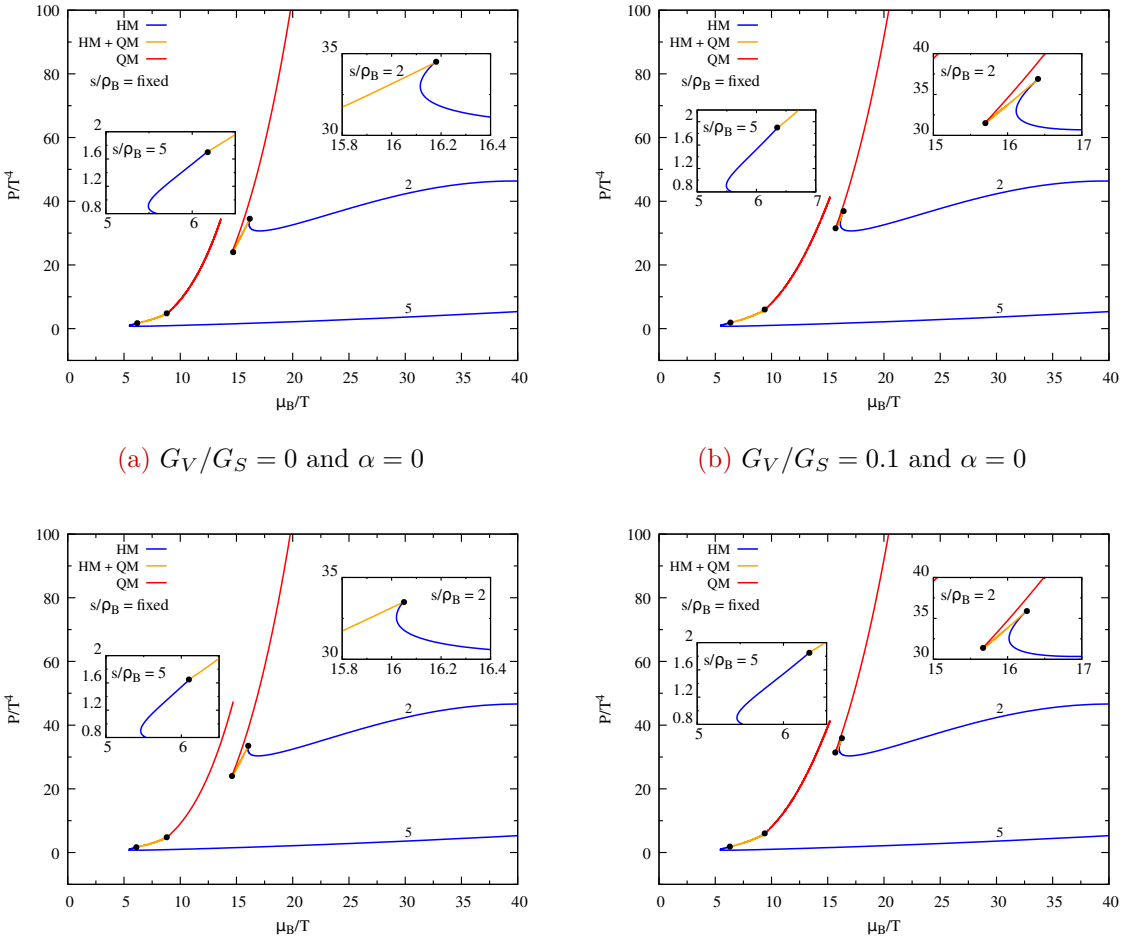

(a) $G_V/G_S = 0$ and $\alpha = 0$

(b) $G_V/G_S = 0.1$ and $\alpha = 0$

(c) $G_V/G_S = 0$ and $\alpha = 0.2$

(d) $G_V/G_S = 0.1$ and $\alpha = 0.2$

Figure C.2: P/T^4 versus the ratio μ_B/T along the isentropes $s/\rho_B = 2$ and $s/\rho_B = 5$ for $G_V/G_S = 0$ (left), $G_V/G_S = 0.1$ (right), and $\alpha = 0$ (top), $\alpha = 0.2$ (bottom) for the FSU2H-PNJL two-phase model. The graphics should be read from right to left to follow increasing ρ_B.

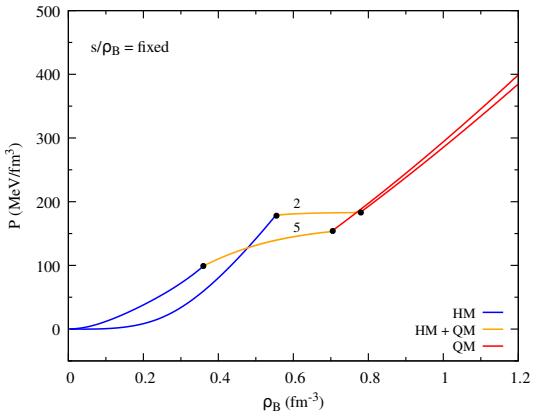

(a) $G_V/G_S = 0$ and $\alpha = 0$

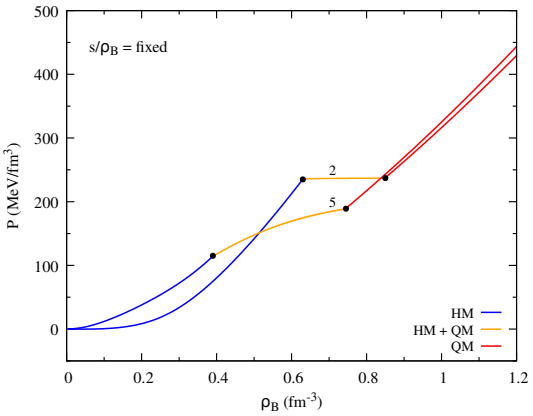

(b) $G_V/G_S = 0.1$ and $\alpha = 0$

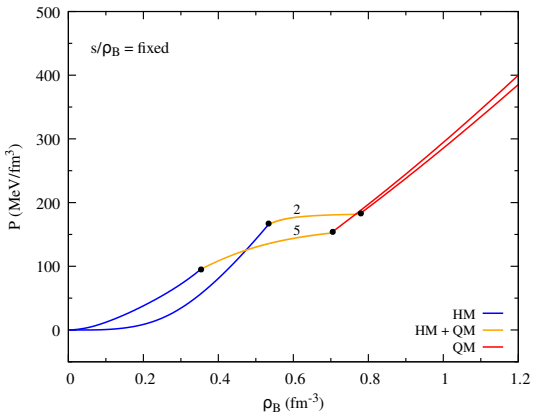

(c) $G_V/G_S = 0$ and $\alpha = 0.2$

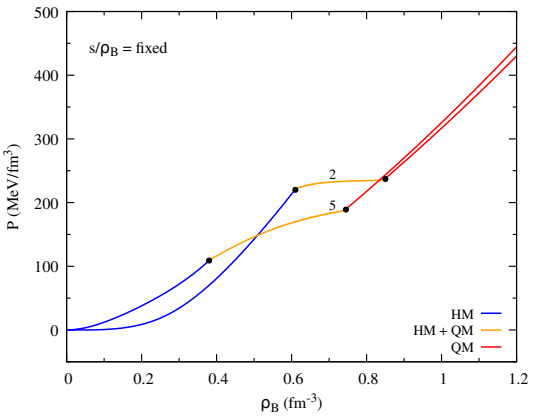

(d) $G_V/G_S = 0.1$ and $\alpha = 0.2$

Figure C.3: Pressure as a function number density for the isentropes s/ρ_B =2, 5 for the FSU2H-PNJL two-phase model. The range between the dots denotes the mixed-phase regime (in orange).

C.3 FSU2R-PNJL Model

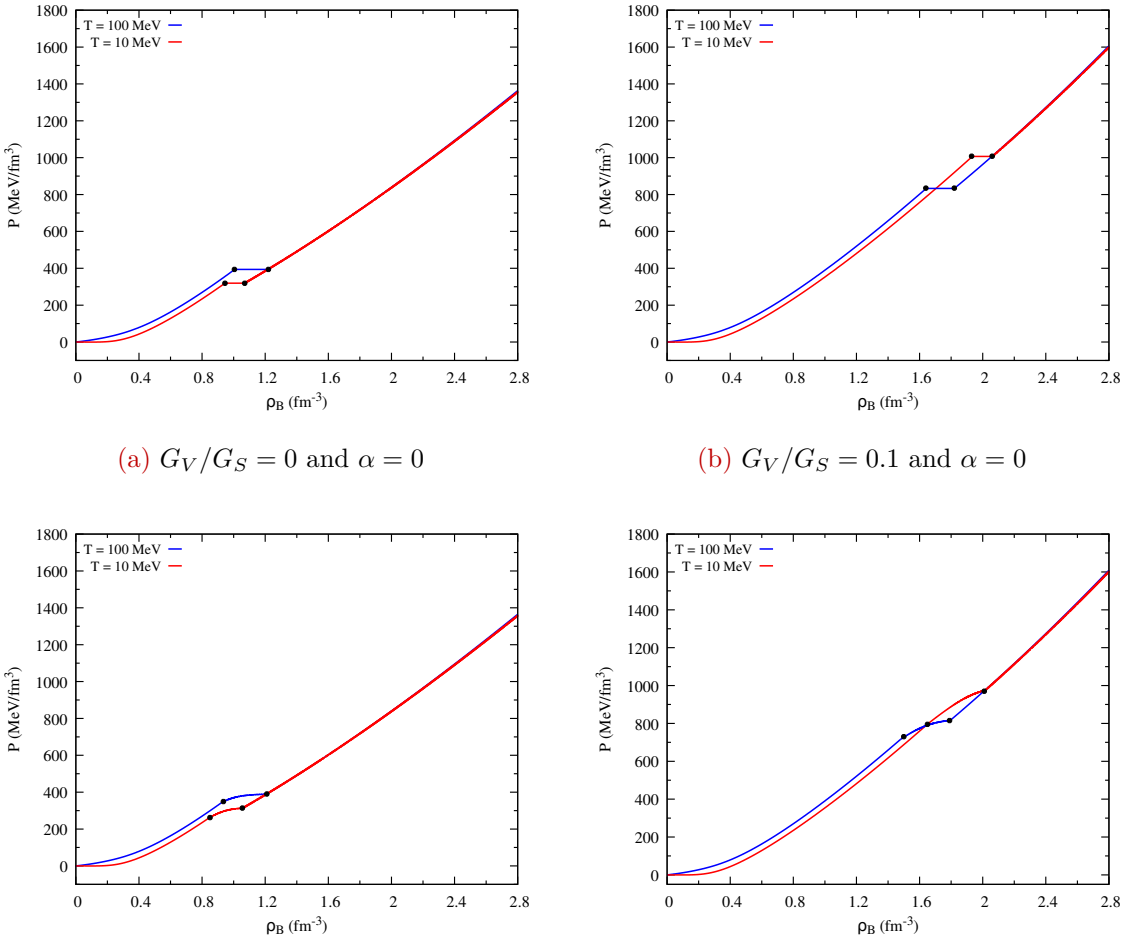

(a) $G_V/G_S = 0$ and $\alpha = 0$

(b) $G_V/G_S = 0.1$ and $\alpha = 0$

(c) $G_V/G_S = 0$ and $\alpha = 0.2$

(d) $G_V/G_S = 0.1$ and $\alpha = 0.2$

Figure C.4: Phase transition in the $P - \rho_B$ plane for symmetric (top) and asymmetric (bottom) matter at $T = 10$ MeV (red) and $T = 100$ MeV (blue) for $G_V/G_S = 0$ (left) and $G_V/G_S = 0.1$ (right) within the FSU2R-PNJL two-model approach. The range between the dots corresponds to the mixed phase.

		$T = 10$ MeV			
G_V/G_S	α	ρ_B^i (fm^{-3})	ρ_B^f (fm^{-3})	P^i (MeV/fm^3)	P^f (MeV/fm^3)
0	0	0.945	1.07	319	319
0.1	0	1.93	2.06	1008	1008
0	0.2	0.85	1.06	262	314
0.1	0.2	1.65	2.01	795	970
		$T = 100$ MeV			
0	0	1.01	1.22	394	394
0.1	0	1.64	1.82	835	835
0	0.2	0.935	1.21	349	390
0.1	0.2	1.5	1.79	730	815

Table C.1: Initial and final position of the mixed phase in the $P - \rho_B$ plane for the isotherms $T = 10$, 100 MeV of each scenario for the FSU2R-PNJL two-phase model.

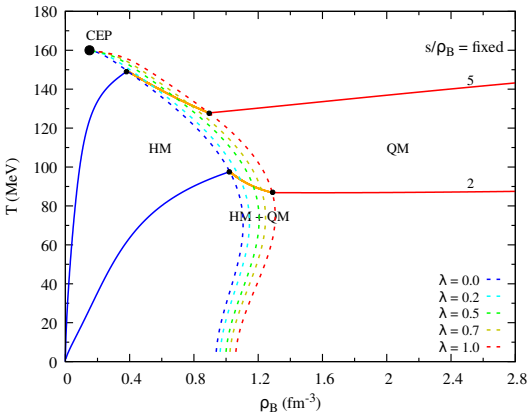

(a) $G_V/G_S = 0.0$ and $\alpha = 0$

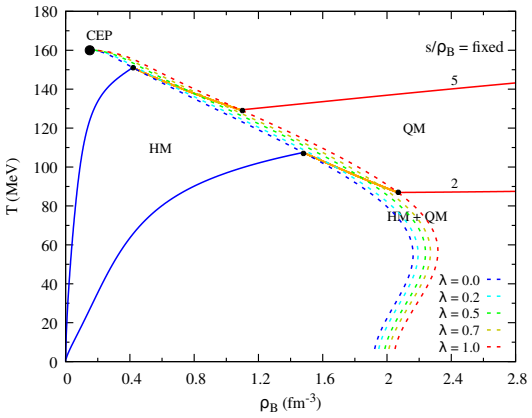

(b) $G_V/G_S = 0.1$ and $\alpha = 0$

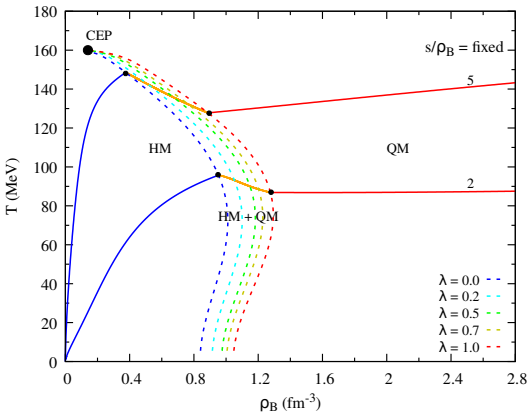

(c) $G_V/G_S = 0.0$ and $\alpha = 0.2$

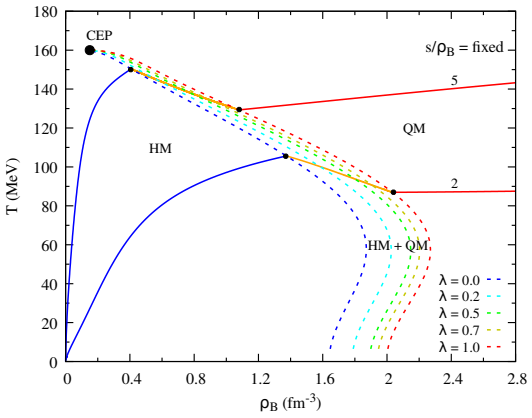

(d) $G_V/G_S = 0.1$ and $\alpha = 0.2$

Figure C.5: Phase diagram and isentropes $s/\rho_B = 2$, 5 for the FSU2R-PNJL two-model approach in the $T - \rho_B$ plane for $\alpha = 0$ (top) and $\alpha = 0.2$ (bottom), and for $G_V/G_S = 0$ (left) and $G_V/G_S = 0.1$ (right).

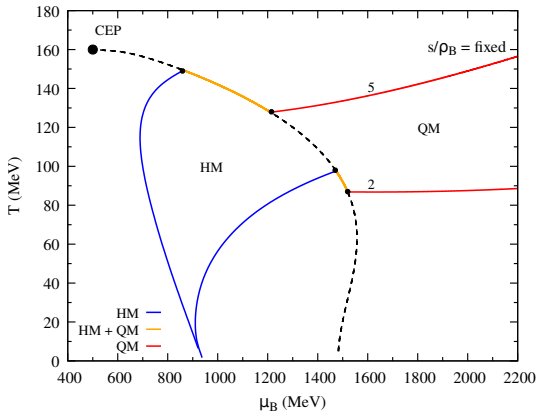

(a) $G_V/G_S = 0.0$ and $\alpha = 0$

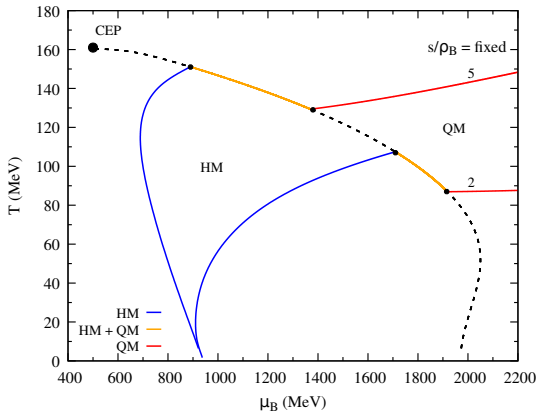

(b) $G_V/G_S = 0.1$ and $\alpha = 0$

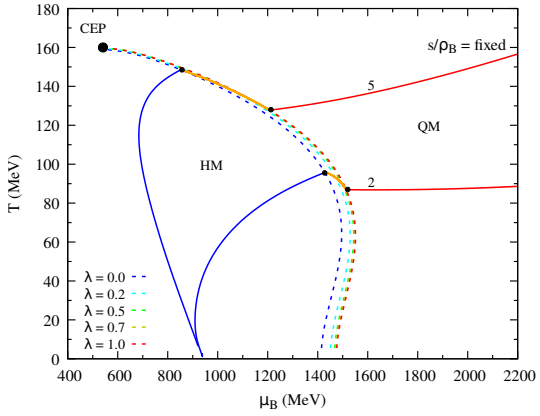

(c) $G_V/G_S = 0.0$ and $\alpha = 0.2$

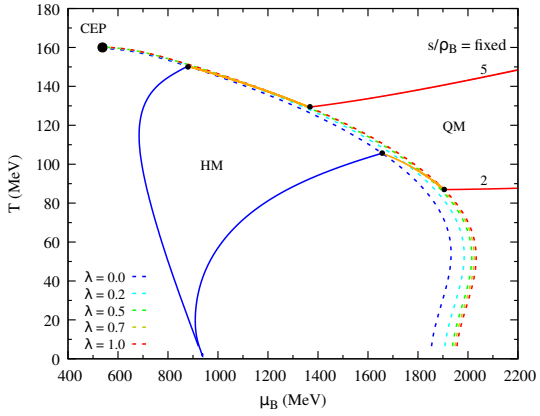

(d) $G_V/G_S = 0.1$ and $\alpha = 0.2$

Figure C.6: The same as Fig. C.5 but for $T - \mu_B$ plane.

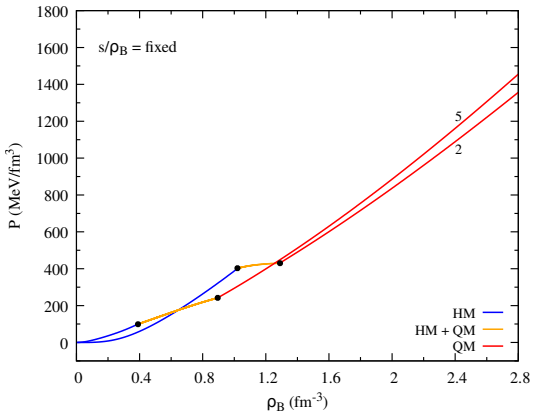

(a) $G_V/G_S = 0$ and $\alpha = 0$

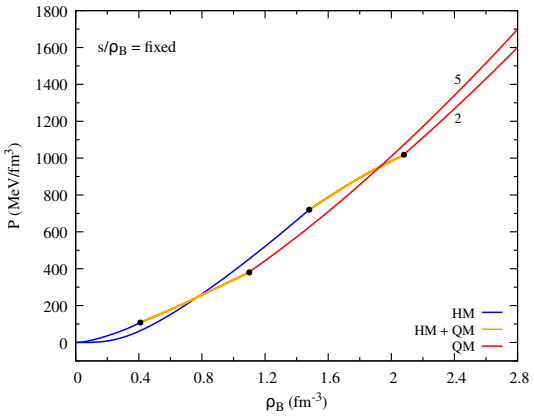

(b) $G_V/G_S = 0.1$ and $\alpha = 0$

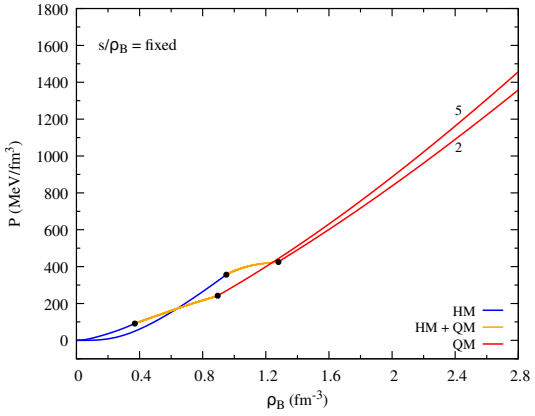

(c) $G_V/G_S = 0$ and $\alpha = 0.2$

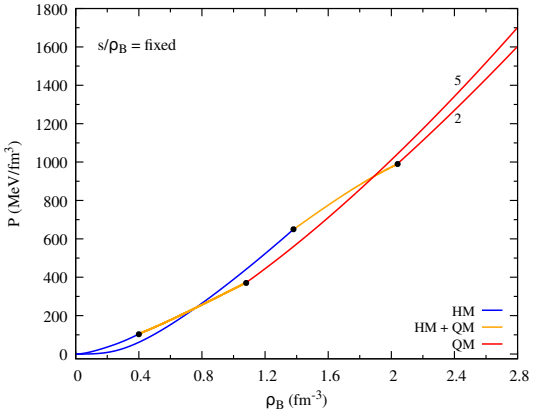

(d) $G_V/G_S = 0.1$ and $\alpha = 0.2$

Figure C.7: Pressure as a function number density for the isentropes s/ρ_B =2, 5 for the FSU2R-PNJL two-phase model. The range between the dots denotes the mixed-phase regime (in orange).

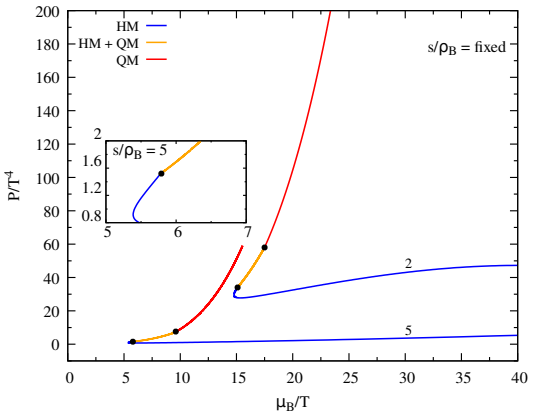

(a) $G_V/G_S = 0$ and $\alpha = 0$

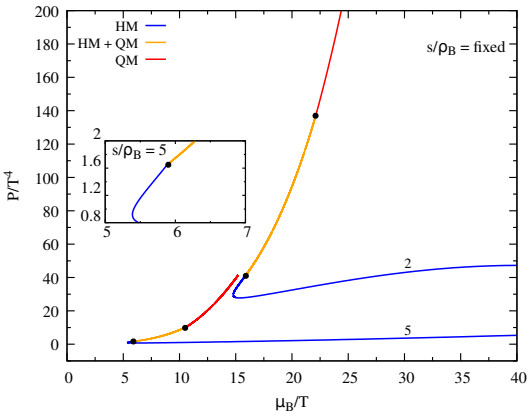

(b) $G_V/G_S = 0.1$ and $\alpha = 0$

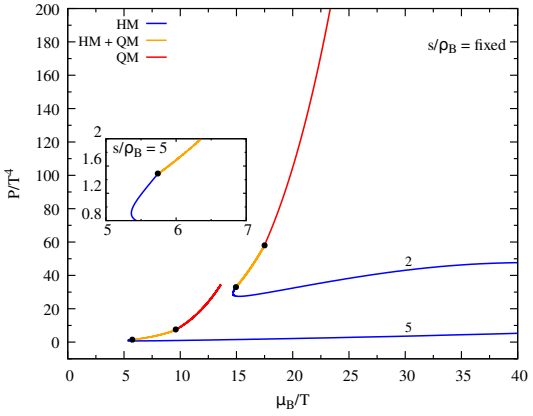

(c) $G_V/G_S = 0$ and $\alpha = 0.2$

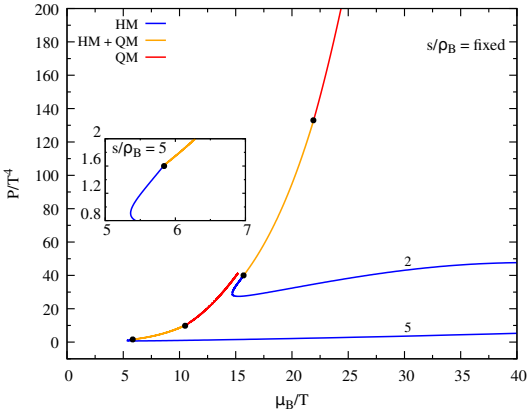

(d) $G_V/G_S = 0.1$ and $\alpha = 0.2$

Figure C.8: P/T^4 versus the ratio μ_B/T along the isentropes $s/\rho_B = 2$, 5 for $G_V/G_S = 0$ (left), $G_V/G_S = 0.1$ (right), and $\alpha = 0$ (top), $\alpha = 0.2$ (bottom) within the FSU2R-PNJL two-model approach. The graphics should be read from right to left to follow increasing ρ_B.

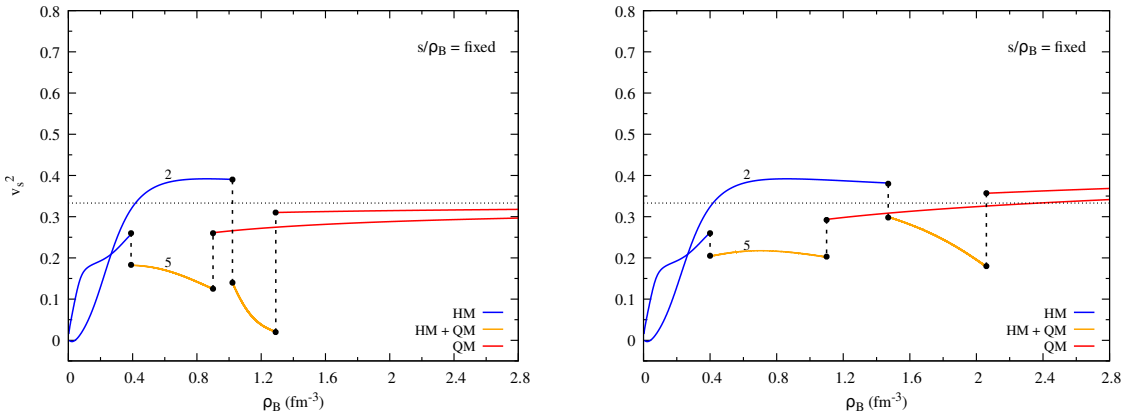

(a) $G_V/G_S = 0$ and $\alpha = 0$ (b) $G_V/G_S = 0.1$ and $\alpha = 0$

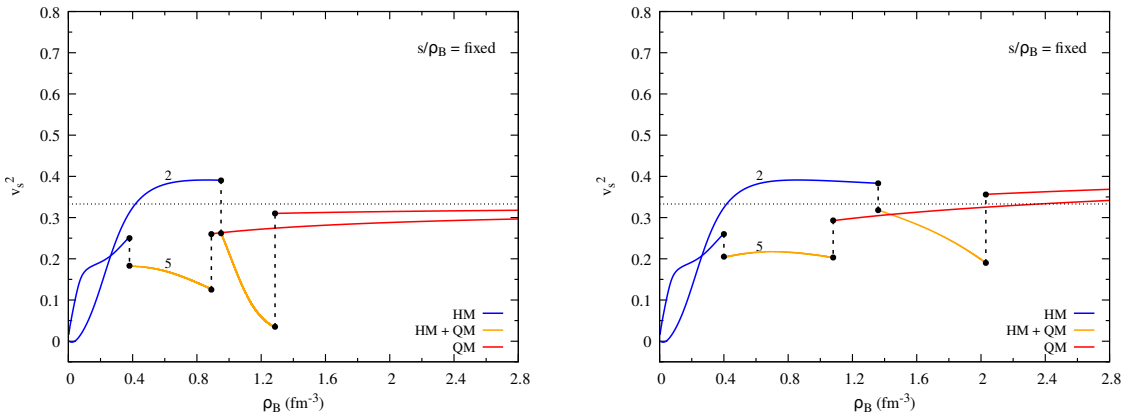

(c) $G_V/G_S = 0$ and $\alpha = 0.2$ (d) $G_V/G_S = 0.1$ and $\alpha = 0.2$

Figure C.9: Sound velocity squared v_s^2 as a function of the baryon density along the isentropes $s/\rho_B = 2$, 5 for $G_V/G_S = 0$ (left) and $G_V/G_S = 0.1$ (right), and for $\alpha = 0$ (top) and $\alpha = 0.2$ (bottom) within the FSU2R-PNJL two-model approach. The horizontal dotted line $v_s^2 = 1/3$ indicates the conformal limit.

Bibliography

[1] K. Fukushima and C. Sasaki, "The phase diagram of nuclear and quark matter at high baryon density," *Progress in Particle and Nuclear Physics*, vol. 72, pp. 99–154, 2013.

[2] D. Binosi, J. Collins, C. Kaufhold, and L. Theussl, "JaxoDraw: A Graphical user interface for drawing Feynman diagrams. Version 2.0 release notes," *Comput. Phys. Commun.*, vol. 180, pp. 1709–1715, 2009.

[3] S. Borsányi, Z. Fodor, C. Hoelbling, S. D. Katz, S. Krieg, and K. K. Szabo, "Full result for the qcd equation of state with 2+ 1 flavors," *Physics Letters B*, vol. 730, pp. 99–104, 2014.

[4] R. C. Pereira, "Chiral transition and deconfinement in hybrid stars," Master's thesis, Universidade de Coimbra (Portugal), 2016.

[5] Y. Aoki, G. Endrődi, Z. Fodor, S. D. Katz, and K. K. Szabó, "The order of the quantum chromodynamics transition predicted by the standard model of particle physics," *Nature*, vol. 443, no. 7112, pp. 675–678, 2006.

[6] S. Borsanyi, Z. Fodor, C. Hoelbling, S. D. Katz, S. Krieg, C. Ratti, and K. K. Szabo, "Is there still any t c mystery in lattice qcd? results with physical masses in the continuum limit iii," *Journal of High Energy Physics*, vol. 2010, no. 9, pp. 1–26, 2010.

[7] H.-T. Ding, P. Hegde, O. Kaczmarek, F. Karsch, A. Lahiri, S.-T. Li, S. Mukherjee, H. Ohno, P. Petreczky, C. Schmidt, and P. Steinbrecher, "Chiral phase transition temperature in $(2+1)$-flavor qcd," *Phys. Rev. Lett.*, vol. 123, p. 062002, Aug 2019.

[8] A. Bazavov, T. Bhattacharya, M. Cheng, C. DeTar, H.-T. Ding, S. Gottlieb, R. Gupta, P. Hegde, U. M. Heller, F. Karsch, E. Laermann, L. Levkova, S. Mukherjee, P. Petreczky, C. Schmidt, R. A. Soltz, W. Soeldner, R. Sugar, D. Toussaint, W. Unger, and P. Vranas, "Chiral and deconfinement aspects of the qcd transition," *Phys. Rev. D*, vol. 85, p. 054503, Mar 2012.

[9] A. Y. Kotov, M. P. Lombardo, and A. Trunin, "Qcd transition at the physical point, and its scaling window from twisted mass wilson fermions," *Physics Letters B*, vol. 823, p. 136749, 2021.

[10] F. Cuteri, O. Philipsen, and A. Sciarra, "On the order of the qcd chiral phase transition for different numbers of quark flavours," *Journal of high energy physics*, vol. 2021, no. 11, pp. 1–32, 2021.

[11] C. S. Fischer, "Qcd at finite temperature and chemical potential from dyson–schwinger equations," *Progress in Particle and Nuclear Physics*, vol. 105, pp. 1–60, 2019.

[12] A. Bzdak, S. Esumi, V. Koch, J. Liao, M. Stephanov, and N. Xu, "Mapping the phases of quantum chromodynamics with beam energy scan," *Physics Reports*, vol. 853, pp. 1–87, 2020.

[13] L. Du, A. Sorensen, and M. Stephanov, "The qcd phase diagram and beam energy scan physics: A theory overview," *International Journal of Modern Physics E*, vol. 33, no. 07, p. 2430008, 2024.

[14] G. Eichmann, C. S. Fischer, and C. A. Welzbacher, "Baryon effects on the location of QCD's critical end point," *Phys. Rev. D*, vol. 93, no. 3, p. 034013, 2016.

[15] W.-j. Fu, J. M. Pawlowski, and F. Rennecke, "Qcd phase structure at finite temperature and density," *Physical Review D*, vol. 101, no. 5, p. 054032, 2020.

[16] P. Salabura and J. Stroth, "Dilepton radiation from strongly interacting systems," *Progress in Particle and Nuclear Physics*, vol. 120, p. 103869, 2021.

[17] B. Friman, C. Höhne, J. Knoll, S. Leupold, J. Randrup, R. Rapp, and P. Senger, *The CBM physics book: Compressed baryonic matter in laboratory experiments*, vol. 814. Springer, 2011.

[18] N. K. Glendenning, "First-order phase transitions with more than one conserved charge: Consequences for neutron stars," *Physical Review D*, vol. 46, no. 4, p. 1274, 1992.

[19] N. K. Glendenning and J. Schaffner-Bielich, "First order kaon condensate," *Physical Review C*, vol. 60, no. 2, p. 025803, 1999.

[20] V. Dexheimer and S. Schramm, "Novel approach to modeling hybrid stars," *Physical Review C—Nuclear Physics*, vol. 81, no. 4, p. 045201, 2010.

[21] G.-y. Shao, "Evolution of proto-neutron stars with the hadron–quark phase transition," *Physics Letters B*, vol. 704, no. 4, pp. 343–346, 2011.

[22] M. Di Toro, A. Drago, T. Gaitanos, V. Greco, and A. Lavagno, "Testing deconfinement at high isospin density," *Nuclear Physics A*, vol. 775, no. 1-2, pp. 102–126, 2006.

[23] M. Di Toro, V. Baran, M. Colonna, G. Ferini, T. Gaitanos, V. Giordano, V. Greco, L. Bo, M. Zielinska-Pfabe, S. Plumari, *et al.*, "Isospin dynamics in heavy ion collisions: From coulomb barrier to quark gluon plasma," *Progress in Particle and Nuclear Physics*, vol. 62, no. 2, pp. 389–401, 2009.

[24] M. Di Toro, B. Liu, V. Greco, V. Baran, M. Colonna, and S. Plumari, "Symmetry energy effects on the mixed hadron-quark phase at high baryon density," *Physical Review C—Nuclear Physics*, vol. 83, no. 1, p. 014911, 2011.

[25] R. Cavagnoli, C. Providência, and D. P. Menezes, "Hadron-quark phase transition in asymmetric matter with boson condensation," *Physical Review C—Nuclear Physics*, vol. 83, no. 4, p. 045201, 2011.

[26] G. Shao, M. Di Toro, B. Liu, M. Colonna, V. Greco, Y. Liu, and S. Plumari, "Hadron-quark phase transition in asymmetric matter with dynamical quark masses," *Physical Review D—Particles, Fields, Gravitation, and Cosmology*, vol. 83, no. 9, p. 094033, 2011.

[27] G. Shao, M. Di Toro, V. Greco, M. Colonna, S. Plumari, B. Liu, and Y. Liu, "Phase diagrams in the hadron–polyakov–nambu–jona-lasinio model," *Physical Review D—Particles, Fields, Gravitation, and Cosmology*, vol. 84, no. 3, p. 034028, 2011.

[28] G. Shao, M. Colonna, M. Di Toro, B. Liu, and F. Matera, "Influence of vector interactions on the hadron-quark/gluon phase transition," *Physical Review D—Particles, Fields, Gravitation, and Cosmology*, vol. 85, no. 11, p. 114017, 2012.

[29] G.-y. Shao, Z.-d. Tang, M. Di Toro, M. Colonna, X.-y. Gao, and N. Gao, "Phase transition of strongly interacting matter with a chemical potential dependent polyakov loop potential," *Physical Review D*, vol. 94, no. 1, p. 014008, 2016.

[30] A. Russell, "Lord rutherford: Manchester, 1907-19: A partial portrait," *Proceedings of the Physical Society. Section A*, vol. 64, no. 3, p. 217, 1951.

[31] J. C. Collins and M. J. Perry, "Superdense matter: Neutrons or asymptotically free quarks?," *Phys. Rev. Lett.*, vol. 34, pp. 1353–1356, May 1975.

[32] N. Cabibbo and G. Parisi, "Exponential hadronic spectrum and quark liberation," *Physics Letters B*, vol. 59, no. 1, pp. 67–69, 1975.

[33] R. Hagedorn, "Statistical thermodynamics of strong interactions at high-energies," *Nuovo Cim. Suppl.*, vol. 3, pp. 147–186, 1965.

[34] G. Baym, "Rhic: From dreams to beams in two decades," *Nuclear Physics A*, vol. 698, p. xxiii–xxxii, Feb. 2002.

[35] S. Navas *et al.*, "Review of particle physics," *Phys. Rev. D*, vol. 110, no. 3, p. 030001, 2024.

[36] A. Andronic *et al.*, "Hadron Production in Ultra-relativistic Nuclear Collisions: Quarkyonic Matter and a Triple Point in the Phase Diagram of QCD," *Nucl. Phys. A*, vol. 837, pp. 65–86, 2010.

[37] P. Alba, W. Alberico, R. Bellwied, M. Bluhm, V. Mantovani Sarti, M. Nahrgang, and C. Ratti, "Freeze-out conditions from net-proton and net-charge fluctuations at rhic," *Physics Letters B*, vol. 738, pp. 305–310, 2014.

[38] V. Vovchenko, V. V. Begun, and M. I. Gorenstein, "Hadron multiplicities and chemical freeze-out conditions in proton-proton and nucleus-nucleus collisions," *Phys. Rev. C*, vol. 93, p. 064906, Jun 2016.

[39] F. Becattini, J. Steinheimer, R. Stock, and M. Bleicher, "Hadronization conditions in relativistic nuclear collisions and the qcd pseudo-critical line," *Physics Letters B*, vol. 764, pp. 241–246, 2017.

[40] L. Adamczyk *et al.*, "Bulk Properties of the Medium Produced in Relativistic Heavy-Ion Collisions from the Beam Energy Scan Program," *Phys. Rev. C*, vol. 96, no. 4, p. 044904, 2017.

[41] A. Andronic, P. Braun-Munzinger, K. Redlich, and J. Stachel, "Decoding the phase structure of qcd via particle production at high energy," *Nature*, vol. 561, p. 321–330, Sept. 2018.

[42] V. Sagun, K. Bugaev, A. Ivanytskyi, I. Yakimenko, E. Nikonov, A. Taranenko, C. Greiner, D. Blaschke, and G. Zinovjev, "Hadron resonance gas model with induced surface tension," *The European Physical Journal A*, vol. 54, pp. 1–16, 2018.

[43] A. Bazavov, H.-T. Ding, P. Hegde, O. Kaczmarek, F. Karsch, N. Karthik, E. Laermann, A. Lahiri, R. Larsen, S.-T. Li, S. Mukherjee, H. Ohno, P. Petreczky, H. Sandmeyer, C. Schmidt, S. Sharma, and P. Steinbrecher, "Chiral crossover in qcd at zero and non-zero chemical potentials," *Physics Letters B*, vol. 795, pp. 15–21, 2019.

[44] S. Borsanyi, Z. Fodor, J. N. Guenther, R. Kara, S. D. Katz, P. Parotto, A. Pasztor, C. Ratti, and K. K. Szabó, "Qcd crossover at finite chemical potential from lattice simulations," *Phys. Rev. Lett.*, vol. 125, p. 052001, Jul 2020.

[45] S. Borsányi, Z. Fodor, J. N. Guenther, P. Parotto, A. Pásztor, L. Pirelli, K. K. Szabó, and C. H. Wong, "Qcd deconfinement transition line up to $\mu_B = 400$ MeV from finite volume lattice simulations," *Phys. Rev. D*, vol. 110, p. 114507, Dec 2024.

[46] G. Baym, "Confinement of quarks in nuclear matter," *Physica A: Statistical Mechanics and its Applications*, vol. 96, no. 1, pp. 131–135, 1979.

[47] H. Satz, "Deconfinement and percolation," *Nuclear Physics A*, vol. 642, no. 1, pp. c130–c142, 1998. QCD at Finite Baryon Density.

[48] L. D. McLerran and B. Svetitsky, "Quark liberation at high temperature: A monte carlo study of su(2) gauge theory," *Phys. Rev. D*, vol. 24, pp. 450–460, Jul 1981.

[49] S. Elitzur, "Impossibility of spontaneously breaking local symmetries," *Phys. Rev. D*, vol. 12, pp. 3978–3982, Dec 1975.

[50] F. Cuteri, O. Philipsen, A. Schön, and A. Sciarra, "Deconfinement critical point of lattice qcd with $N_{\mathrm{f}} = 2$ wilson fermions," *Phys. Rev. D*, vol. 103, p. 014513, Jan 2021.

[51] Y. Aoki, Z. Fodor, S. Katz, and K. Szabó, "The qcd transition temperature: Results with physical masses in the continuum limit," *Physics Letters B*, vol. 643, no. 1, pp. 46–54, 2006.

[52] A. Bazavov *et al.*, "Equation of state and QCD transition at finite temperature," *Phys. Rev. D*, vol. 80, p. 014504, 2009.

[53] A. Bazavov and P. Petreczky, "Polyakov loop in 2+1 flavor qcd," *Phys. Rev. D*, vol. 87, p. 094505, May 2013.

[54] S. Borsányi, Z. Fodor, S. D. Katz, A. Pásztor, K. K. Szabó, and C. Torok, "Static qq pair free energy and screening masses from correlators of polyakov loops: continuum extrapolated lattice results at the qcd physical point," 2015.

[55] D. A. Clarke, O. Kaczmarek, F. Karsch, A. Lahiri, and M. Sarkar, "Sensitivity of the polyakov loop and related observables to chiral symmetry restoration," *Phys. Rev. D*, vol. 103, p. L011501, Jan 2021.

[56] P. J. Silva and O. Oliveira, "Gluon dynamics, center symmetry, and the deconfinement phase transition in su(3) pure yang-mills theory," *Phys. Rev. D*, vol. 93, p. 114509, Jun 2016.

[57] V. Paiva, P. J. Silva, and O. Oliveira, "Deconfinement, center symmetry and the ghost propagator in Landau gauge pure SU(3) Yang-Mills theory," *JHEP*, vol. 05, p. 164, 2024.

[58] C. DeTar and L. McLerran, "Order parameters for the confinement-deconfinement phase transition in su (n) gauge theories with quarks," *Physics Letters B*, vol. 119, no. 1-3, pp. 171–173, 1982.

[59] H. Meyer-Ortmanns, "Unexpected behavior of an order parameter for lattice gauge theories with matter fields," *Nuclear Physics B*, vol. 230, no. 1, pp. 31–48, 1984.

[60] C. Bonati, M. D'Elia, F. Negro, F. Sanfilippo, and K. Zambello, "Curvature of the pseudocritical line in qcd: Taylor expansion matches analytic continuation," *Phys. Rev. D*, vol. 98, p. 054510, Sep 2018.

[61] A. Pásztor, Z. Szép, and G. Markó, "Apparent convergence of padé approximants for the crossover line in finite density qcd," *Phys. Rev. D*, vol. 103, p. 034511, Feb 2021.

[62] S. Pratt, E. Sangaline, P. Sorensen, and H. Wang, "Constraining the equation of state of superhadronic matter from heavy-ion collisions," *Phys. Rev. Lett.*, vol. 114, p. 202301, May 2015.

[63] L.-G. Pang, K. Zhou, N. Su, H. Petersen, H. Stöcker, and X.-N. Wang, "An equation-of-state-meter of quantum chromodynamics transition from deep learning," *Nature communications*, vol. 9, no. 1, p. 210, 2018.

[64] V. Vovchenko, J. Steinheimer, O. Philipsen, and H. Stoecker, "Cluster expansion model for qcd baryon number fluctuations: No phase transition at $\mu_B/t < \pi$," *Phys. Rev. D*, vol. 97, p. 114030, Jun 2018.

[65] D. Bollweg, J. Goswami, O. Kaczmarek, F. Karsch, S. Mukherjee, P. Petreczky, C. Schmidt, and P. Scior, "Taylor expansions and padé approximants for cumulants of conserved charge fluctuations at nonvanishing chemical potentials," *Phys. Rev. D*, vol. 105, p. 074511, Apr 2022.

[66] S. Borsányi, R. Kara, Z. Fodor, D. A. Godzieba, P. Parotto, and D. Sexty, "Precision study of the continuum su(3) yang-mills theory: How to use parallel tempering to improve on supercritical slowing down for first-order phase transitions," *Phys. Rev. D*, vol. 105, p. 074513, Apr 2022.

[67] R. D. Pisarski and F. Wilczek, "Remarks on the chiral phase transition in chromodynamics," *Phys. Rev. D*, vol. 29, pp. 338–341, Jan 1984.

[68] G. Fejős and T. Hatsuda, "Order of the $su(N_f)\times su(N_f)$ chiral transition via the functional renormalization group," *Phys. Rev. D*, vol. 110, p. 016021, Jul 2024.

[69] A. Y. Kotov, M. P. Lombardo, and A. Trunin, "Qcd transition at the physical point, and its scaling window from twisted mass wilson fermions," *Physics Letters B*, vol. 823, p. 136749, 2021.

[70] J. Braun, Y.-r. Chen, W.-j. Fu, F. Gao, C. Huang, F. Ihssen, J. M. Pawlowski, F. Rennecke, F. R. Sattler, Y.-y. Tan, *et al.*, "Soft modes in hot qcd matter," *arXiv preprint arXiv:2310.19853*, 2023.

[71] M. A. Halasz, A. D. Jackson, R. E. Shrock, M. A. Stephanov, and J. J. M. Verbaarschot, "Phase diagram of qcd," *Phys. Rev. D*, vol. 58, p. 096007, Sep 1998.

[72] Y. Hatta and T. Ikeda, "Universality, the qcd critical and tricritical point, and the quark number susceptibility," *Phys. Rev. D*, vol. 67, p. 014028, Jan 2003.

[73] T. SCHÄFER, "Color superconductivity," *International Journal of Modern Physics B*, vol. 15, no. 10n11, pp. 1474–1490, 2001.

[74] M. A. Stephanov, "Qcd critical point and complex chemical potential singularities," *Phys. Rev. D*, vol. 73, p. 094508, May 2006.

[75] M. Buballa and S. Carignano, "Inhomogeneous chiral phases away from the chiral limit," *Physics Letters B*, vol. 791, pp. 361–366, 2019.

[76] A. Butti, A. Pelissetto, and E. Vicari, "On the nature of the finite-temperature transition in qcd," *Journal of High Energy Physics*, vol. 2003, no. 08, p. 029, 2003.

[77] A. Pelissetto and E. Vicari, "Relevance of the axial anomaly at the finite-temperature chiral transition in qcd," *Phys. Rev. D*, vol. 88, p. 105018, Nov 2013.

[78] M. I. Buchoff, M. Cheng, N. H. Christ, H.-T. Ding, C. Jung, F. Karsch, Z. Lin, R. D. Mawhinney, S. Mukherjee, P. Petreczky, D. Renfrew, C. Schroeder, P. M. Vranas, and H. Yin, "Qcd chiral transition, $u(1)_A$ symmetry and the dirac spectrum using domain wall fermions," *Phys. Rev. D*, vol. 89, p. 054514, Mar 2014.

[79] S. Resch, F. Rennecke, and B.-J. Schaefer, "Mass sensitivity of the three-flavor chiral phase transition," *Phys. Rev. D*, vol. 99, p. 076005, Apr 2019.

[80] S. Aoki, Y. Aoki, G. Cossu, H. Fukaya, S. Hashimoto, T. Kaneko, C. Rohrhofer, and K. Suzuki, "Study of the axial $u(1)$ anomaly at high temperature with lattice chiral fermions," *Phys. Rev. D*, vol. 103, p. 074506, Apr 2021.

[81] H.-T. Ding, S.-T. Li, S. Mukherjee, A. Tomiya, X.-D. Wang, and Y. Zhang, "Correlated dirac eigenvalues and axial anomaly in chiral symmetric qcd," *Phys. Rev. Lett.*, vol. 126, p. 082001, Feb 2021.

[82] H.-T. Ding, W.-P. Huang, S. Mukherjee, and P. Petreczky, "Microscopic encoding of macroscopic universality: Scaling properties of dirac eigenspectra near qcd chiral phase transition," *Phys. Rev. Lett.*, vol. 131, p. 161903, Oct 2023.

[83] T. G. Kovács, "Fate of chiral symmetries in the quark-gluon plasma from an instanton-based random matrix model of qcd," *Phys. Rev. Lett.*, vol. 132, p. 131902, Mar 2024.

[84] F. Gao and J. M. Pawlowski, "Qcd phase structure from functional methods," *Physical Review D*, vol. 102, no. 3, p. 034027, 2020.

[85] F. Gao and J. M. Pawlowski, "Chiral phase structure and critical end point in qcd," *Physics Letters B*, vol. 820, p. 136584, 2021.

[86] P. J. Gunkel and C. S. Fischer, "Locating the critical endpoint of qcd: Mesonic backcoupling effects," *Physical Review D*, vol. 104, no. 5, p. 054022, 2021.

[87] Y. Lu, F. Gao, Y.-x. Liu, and J. M. Pawlowski, "Qcd equation of state and thermodynamic observables from computationally minimal dyson-schwinger equations," *Physical Review D*, vol. 110, no. 1, p. 014036, 2024.

[88] P. Dimopoulos, L. Dini, F. Di Renzo, J. Goswami, G. Nicotra, C. Schmidt, S. Singh, K. Zambello, and F. Ziesché, "Contribution to understanding the phase structure of strong interaction matter: Lee-yang edge singularities from lattice qcd," *Phys. Rev. D*, vol. 105, p. 034513, Feb 2022.

[89] G. Başar, "Qcd critical point, lee-yang edge singularities, and padé resummations," *Physical Review C*, vol. 110, no. 1, p. 015203, 2024.

[90] D. A. Clarke, P. Dimopoulos, F. Di Renzo, J. Goswami, C. Schmidt, S. Singh, and K. Zambello, "Searching for the qcd critical endpoint using multi-point pad\'e approximations," *arXiv preprint arXiv:2405.10196*, 2024.

[91] K. Fukushima, "Phase diagrams in the three-flavor nambu–jona-lasinio model with the polyakov loop," *Phys. Rev. D*, vol. 77, p. 114028, Jun 2008.

[92] P. Costa, "Influence of the vector interaction and an external magnetic field on the isentropes near the chiral critical end point," *Phys. Rev. D*, vol. 93, p. 114035, Jun 2016.

[93] P. Costa, M. Ferreira, D. P. Menezes, J. a. Moreira, and C. m. c. Providência, "Influence of the inverse magnetic catalysis and the vector interaction in the location of the critical end point," *Phys. Rev. D*, vol. 92, p. 036012, Aug 2015.

[94] R. C. Pereira, P. Costa, and C. m. c. Providência, "Two-solar-mass hybrid stars: A two model description using the nambu–jona-lasinio quark model," *Phys. Rev. D*, vol. 94, p. 094001, Nov 2016.

[95] P. Costa, R. C. Pereira, and C. m. c. Providência, "Role of the conserved charges in the chiral symmetry restoration phase transition," *Phys. Rev. D*, vol. 102, p. 054010, Sep 2020.

[96] A. Zacchi, R. Stiele, and J. Schaffner-Bielich, "Compact stars in a su(3) quark-meson model," *Phys. Rev. D*, vol. 92, p. 045022, Aug 2015.

[97] G. Baym, "Rhic: From dreams to beams in two decades," *arXiv preprint hep-ph/0104138*, 2001.

[98] M. Ferreira, P. Costa, and C. m. c. Providência, "Presence of a critical endpoint in the qcd phase diagram from the net-baryon number fluctuations," *Phys. Rev. D*, vol. 98, p. 034006, Aug 2018.

[99] P. Costa, M. C. Ruivo, C. A. De Sousa, and H. Hansen, "Phase diagram and critical properties within an effective model of qcd: the nambu–jona-lasinio model coupled to the polyakov loop," *Symmetry*, vol. 2, no. 3, pp. 1338–1374, 2010.

[100] J. Bardeen, L. N. Cooper, and J. R. Schrieffer, "Theory of superconductivity," *Phys. Rev.*, vol. 108, pp. 1175–1204, Dec 1957.

[101] B.-A. Li, C. M. Ko, and W. Bauer, "Isospin physics in heavy-ion collisions at intermediate energies," *International Journal of Modern Physics E*, vol. 7, no. 02, pp. 147–229, 1998.

[102] A. B. Migdal, E. Saperstein, M. Troitsky, and D. N. Voskresensky, "Pion degrees of freedom in nuclear matter," *Physics Reports*, vol. 192, no. 4-6, pp. 179–437, 1990.

[103] A. W. Steiner, M. Prakash, J. M. Lattimer, and P. J. Ellis, "Isospin asymmetry in nuclei and neutron stars," *Physics reports*, vol. 411, no. 6, pp. 325–375, 2005.

[104] D. J. Schwarz and M. Stuke, "Lepton asymmetry and the cosmic QCD transition," *JCAP*, vol. 11, p. 025, 2009. [Erratum: JCAP 10, E01 (2010)].

[105] Z.-Y. Lu, C.-J. Xia, and M. Ruggieri, "Thermodynamics and susceptibilities of isospin imbalanced qcd matter," *The European Physical Journal C*, vol. 80, no. 1, p. 46, 2020.

[106] G.-y. Shao, Z.-d. Tang, M. Di Toro, M. Colonna, X.-y. Gao, and N. Gao, "Phase transition of strongly interacting matter with a chemical potential dependent polyakov loop potential," *Phys. Rev. D*, vol. 94, p. 014008, Jul 2016.

[107] D. T. Son and M. A. Stephanov, "Qcd at finite isospin density," *Phys. Rev. Lett.*, vol. 86, pp. 592–595, Jan 2001.

[108] P. Adhikari, J. O. Andersen, and P. Kneschke, "Two-flavor chiral perturbation theory at nonzero isospin: Pion condensation at zero temperature," *The European Physical Journal C*, vol. 79, no. 10, pp. 1–13, 2019.

[109] P. Adhikari and J. O. Andersen, "Qcd at finite isospin density: chiral perturbation theory confronts lattice data," *Physics Letters B*, vol. 804, p. 135352, 2020.

[110] W.-b. He, G.-y. Shao, and C.-l. Xie, "Speed of sound and liquid-gas phase transition in nuclear matter," *Phys. Rev. C*, vol. 107, p. 014903, Jan 2023.

[111] B. B. Brandt, G. Endrődi, and S. Schmalzbauer, "Qcd phase diagram for nonzero isospin-asymmetry," *Phys. Rev. D*, vol. 97, p. 054514, Mar 2018.

[112] B. B. Brandt, F. Cuteri, and G. Endrődi, "Equation of state and speed of sound of isospin-asymmetric qcd on the lattice," *Journal of High Energy Physics*, vol. 2023, no. 7, pp. 1–32, 2023.

[113] B. B. Brandt, G. Endrodi, and G. Markó, "Equation of state of isospin asymmetric qcd with small baryon chemical potentials," *arXiv preprint arXiv:2411.12918*, 2024.

[114] C. Ratti and W. Weise, "Thermodynamics of two-color qcd and the nambu jona-lasinio model," *Phys. Rev. D*, vol. 70, p. 054013, Sep 2004.

[115] B. B. Brandt and G. Endrodi, "Qcd phase diagram with isospin chemical potential," *arXiv preprint arXiv:1611.06758*, 2016.

[116] B. B. Brandt, G. Endrodi, and S. Schmalzbauer, "QCD at finite isospin chemical potential," *EPJ Web Conf.*, vol. 175, p. 07020, 2018.

[117] J. E. Finn, S. Agarwal, A. Bujak, J. Chuang, L. J. Gutay, A. S. Hirsch, R. W. Minich, N. T. Porile, R. P. Scharenberg, B. C. Stringfellow, and F. Turkot, "Nuclear fragment mass yields from high-energy proton-nucleus interactions," *Phys. Rev. Lett.*, vol. 49, pp. 1321–1325, Nov 1982.

[118] A. D. Panagiotou, M. W. Curtin, H. Toki, D. K. Scott, and P. J. Siemens, "Experimental evidence for a liquid-gas phase transition in nuclear systems," *Phys. Rev. Lett.*, vol. 52, pp. 496–499, Feb 1984.

[119] J. B. Natowitz, K. Hagel, Y. Ma, M. Murray, L. Qin, R. Wada, and J. Wang, "Limiting temperatures and the equation of state of nuclear matter," *Phys. Rev. Lett.*, vol. 89, p. 212701, Nov 2002.

[120] C. Sfienti *et al.*, "Isotopic Dependence of the Nuclear Caloric Curve," *Phys. Rev. Lett.*, vol. 102, p. 152701, 2009.

[121] J. B. Elliott, P. T. Lake, L. G. Moretto, and L. Phair, "Determination of the coexistence curve, critical temperature, density, and pressure of bulk nuclear matter from fragment emission data," *Phys. Rev. C*, vol. 87, p. 054622, May 2013.

[122] B. Borderie and J. Frankland, "Liquid–gas phase transition in nuclei," *Progress in Particle and Nuclear Physics*, vol. 105, pp. 82–138, 2019.

[123] J. D. Walecka, "A theory of highly condensed matter," *Annals of Physics*, vol. 83, no. 2, pp. 491–529, 1974.

[124] B. D. Serot and J. D. Walecka, "The Relativistic Nuclear Many Body Problem," *Adv. Nucl. Phys.*, vol. 16, pp. 1–327, 1986.

[125] B. D. Serot and J. D. Walecka, "Recent progress in quantum hadrodynamics," *International Journal of Modern Physics E*, vol. 6, no. 04, pp. 515–631, 1997.

[126] S. Typel, G. Röpke, T. Klähn, D. Blaschke, and H. H. Wolter, "Composition and thermodynamics of nuclear matter with light clusters," *Phys. Rev. C*, vol. 81, p. 015803, Jan 2010.

[127] O. Savchuk, V. Vovchenko, R. V. Poberezhnyuk, M. I. Gorenstein, and H. Stoecker, "Traces of the nuclear liquid-gas phase transition in the analytic properties of hot qcd," *Phys. Rev. C*, vol. 101, p. 035205, Mar 2020.

[128] M. I. Haftel and F. Tabakin, "Nuclear saturation and the smoothness of nucleon-nucleon potentials," *Nuclear Physics A*, vol. 158, no. 1, pp. 1–42, 1970.

[129] M. Baldo and L. S. Ferreira, "Nuclear liquid-gas phase transition," *Phys. Rev. C*, vol. 59, pp. 682–703, Feb 1999.

[130] A. Carbone, A. Polls, and A. Rios, "Microscopic predictions of the nuclear matter liquid-gas phase transition," *Phys. Rev. C*, vol. 98, p. 025804, Aug 2018.

[131] N. Ishii, S. Aoki, and T. Hatsuda, "Nuclear force from lattice qcd," *Phys. Rev. Lett.*, vol. 99, p. 022001, Jul 2007.

[132] P. de Forcrand and M. Fromm, "Nuclear physics from lattice qcd at strong coupling," *Phys. Rev. Lett.*, vol. 104, p. 112005, Mar 2010.

[133] M. Fromm, J. Langelage, S. Lottini, M. Neuman, and O. Philipsen, "Onset transition to cold nuclear matter from lattice qcd with heavy quarks," *Phys. Rev. Lett.*, vol. 110, p. 122001, Mar 2013.

[134] J. Kim, P. Pattanaik, and W. Unger, "Nuclear liquid-gas transition in the strong coupling regime of lattice qcd," *Phys. Rev. D*, vol. 107, p. 094514, May 2023.

[135] K. Fukushima, J. Horak, J. M. Pawlowski, N. Wink, and C. P. Zelle, "Nuclear liquid-gas transition in qcd," *Phys. Rev. D*, vol. 110, p. 076022, Oct 2024.

[136] F. Gao, Y. Lu, S.-x. Qin, Z. Bai, L. Chang, and Y.-x. Liu, "Illustrating the liquid gas transition of nuclear matter in qcd," *arXiv preprint arXiv:2504.00539*, 2025.

[137] A. Le Fevre, G. Auger, M. Begemann-Blaich, N. Bellaize, R. Bittiger, F. Bocage, B. Borderie, R. Bougault, B. Bouriquet, J. Charvet, *et al.*, "Isotopic scaling and the symmetry energy in spectator fragmentation," *Physical review letters*, vol. 94, no. 16, p. 162701, 2005.

[138] A. B. McIntosh, A. Bonasera, P. Cammarata, K. Hagel, L. Heilborn, Z. Kohley, J. Mabiala, L. W. May, P. Marini, A. Raphelt, *et al.*, "Asymmetry dependence of the nuclear caloric curve," in *Journal of Physics: Conference Series*, vol. 420, p. 012085, IOP Publishing, 2013.

[139] A. B. McIntosh, A. Bonasera, Z. Kohley, P. J. Cammarata, K. Hagel, L. Heilborn, J. Mabiala, L. W. May, P. Marini, A. Raphelt, G. A. Souliotis, S. Wuenschel, A. Zarrella, and S. J. Yennello, "Using light charged particles to probe the asymmetry dependence of the nuclear caloric curve," *Phys. Rev. C*, vol. 87, p. 034617, Mar 2013.

[140] T. Miyatsu, M.-K. Cheoun, K. Kim, and K. Saito, "Novel features of asymmetric nuclear matter from terrestrial experiments and astrophysical observations of neutron stars," *Front. in Phys.*, vol. 12, p. 1531475, 2024.

[141] C. Horowitz, E. Brown, Y. Kim, W. Lynch, R. Michaels, A. Ono, J. Piekarewicz, M. Tsang, and H. Wolter, "A way forward in the study of the symmetry energy: experiment, theory,

and observation," *Journal of Physics G: Nuclear and Particle Physics*, vol. 41, no. 9, p. 093001, 2014.

[142] F. Sammarruca, "Recent advances in microscopic approaches to nuclear matter and symmetry energy," *Symmetry*, vol. 6, no. 4, pp. 851–879, 2014.

[143] H. Müller and B. D. Serot, "Phase transitions in warm, asymmetric nuclear matter," *Phys. Rev. C*, vol. 52, pp. 2072–2091, Oct 1995.

[144] V. Baran, M. Colonna, M. Di Toro, and A. Larionov, "Spinodal decomposition of low-density asymmetric nuclear matter," *Nuclear Physics A*, vol. 632, no. 2, pp. 287–303, 1998.

[145] M. Dutra, O. Lourenço, A. Delfino, J. S. Sá Martins, C. Providência, S. S. Avancini, and D. P. Menezes, "Skyrme forces versus relativistic models: Reexamining instabilities," *Phys. Rev. C*, vol. 77, p. 035201, Mar 2008.

[146] B. K. Sharma and S. Pal, "Nuclear symmetry energy effects on liquid-gas phase transition in hot asymmetric nuclear matter," *Phys. Rev. C*, vol. 81, p. 064304, Jun 2010.

[147] M. Hempel, V. Dexheimer, S. Schramm, and I. Iosilevskiy, "Noncongruence of the nuclear liquid-gas and deconfinement phase transitions," *Phys. Rev. C*, vol. 88, p. 014906, Jul 2013.

[148] A. Fedoseew and H. Lenske, "Thermal properties of asymmetric nuclear matter," *Phys. Rev. C*, vol. 91, p. 034307, Mar 2015.

[149] S. Yang, B. N. Zhang, and B. Y. Sun, "Critical parameters of the liquid-gas phase transition in thermal symmetric and asymmetric nuclear matter," *Phys. Rev. C*, vol. 100, p. 054314, Nov 2019.

[150] H. A. Bethe and R. F. Bacher, "Nuclear physics a. stationary states of nuclei," *Reviews of Modern Physics*, vol. 8, no. 2, p. 82, 1936.

[151] C. v. Weizsäcker, "Zur theorie der kernmassen," *Zeitschrift für Physik*, vol. 96, no. 7, pp. 431–458, 1935.

[152] V. Baran and J. Margueron, "Instabilities in nuclear matter and finite nuclei," in *Dynamics and Thermodynamics with Nuclear Degrees of Freedom*, pp. 141–151, Springer, 2006.

[153] M. Di Toro, M. Colonna, V. Greco, and G.-Y. Shao, "Probing the hadron-quark mixed phase at high isospin and baryon density: Sensitive observables," *The European Physical Journal A*, vol. 52, pp. 1–6, 2016.

[154] Y. Leifels, "Status and physics perspectives of FAIR," *Nuovo Cim. C*, vol. 48, no. 2, p. 59, 2025.

[155] K. Ozawa, K. Aoki, S.-i. Esumi, T. Gunji, T. Hachiya, H. Harada, Y. Ichikawa, M. Kitazawa, Y. Miake, Y. Morino, *et al.*, "The j-parc heavy ion project," in *EPJ Web of Conferences*, vol. 271, p. 11004, EDP Sciences, 2022.

[156] F. Gelis, E. Iancu, J. Jalilian-Marian, and R. Venugopalan, "The color glass condensate," *Annual Review of Nuclear and Particle Science*, vol. 60, no. 1, pp. 463–489, 2010.

[157] F. Gelis, "Color glass condensate and glasma," *International Journal of Modern Physics A*, vol. 28, no. 01, p. 1330001, 2013.

[158] E. V. Shuryak, "Theory of Hadronic Plasma," *Sov. Phys. JETP*, vol. 47, pp. 212–219, 1978.

[159] J. Parkkila, A. Onnerstad, S. Taghavi, C. Mordasini, A. Bilandzic, M. Virta, and D. Kim, "New constraints for qcd matter from improved bayesian parameter estimation in heavy-ion collisions at lhc," *Physics Letters B*, vol. 835, p. 137485, 2022.

[160] P. Braun-Munzinger, V. Koch, T. Schäfer, and J. Stachel, "Properties of hot and dense matter from relativistic heavy ion collisions," *Phys. Rept.*, vol. 621, pp. 76–126, 2016.

[161] W. Busza, K. Rajagopal, and W. Van Der Schee, "Heavy ion collisions: the big picture and the big questions," *Annual Review of Nuclear and Particle Science*, vol. 68, no. 1, pp. 339–376, 2018.

[162] P. Romatschke and U. Romatschke, *Relativistic Fluid Dynamics In and Out of Equilibrium*. Cambridge Monographs on Mathematical Physics, Cambridge University Press, 5 2019.

[163] L. Du, A. Sorensen, and M. Stephanov, "The qcd phase diagram and beam energy scan physics: a theory overview," *International Journal of Modern Physics E*, vol. 33, no. 07, p. 2430008, 2024.

[164] M. Asakawa and M. Kitazawa, "Fluctuations of conserved charges in relativistic heavy ion collisions: An introduction," *Progress in Particle and Nuclear Physics*, vol. 90, pp. 299–342, 2016.

[165] M. Stephanov, K. Rajagopal, and E. Shuryak, "Signatures of the tricritical point in qcd," *Phys. Rev. Lett.*, vol. 81, pp. 4816–4819, Nov 1998.

[166] M. Stephanov, K. Rajagopal, and E. Shuryak, "Event-by-event fluctuations in heavy ion collisions and the qcd critical point," *Phys. Rev. D*, vol. 60, p. 114028, Nov 1999.

[167] M. A. Stephanov, "Non-gaussian fluctuations near the qcd critical point," *Phys. Rev. Lett.*, vol. 102, p. 032301, Jan 2009.

[168] F. Karsch, "Determination of Freeze-out Conditions from Lattice QCD Calculations," *Central Eur. J. Phys.*, vol. 10, pp. 1234–1237, 2012.

[169] S. Borsanyi, Z. Fodor, S. D. Katz, S. Krieg, C. Ratti, and K. K. Szabo, "Freeze-out parameters from electric charge and baryon number fluctuations: Is there consistency?," *Phys. Rev. Lett.*, vol. 113, p. 052301, Jul 2014.

[170] M. Motta, R. Stiele, W. M. Alberico, and A. Beraudo, "Isentropic evolution of the matter in heavy-ion collisions and the search for the critical endpoint," *The European Physical Journal C*, vol. 80, pp. 1–16, 2020.

[171] S. Collaboration *et al.*, "Precision measurement of (net-) proton number fluctuations in au+ au collisions at rhic," *arXiv preprint arXiv:2504.00817*, 2025.

[172] V. Vovchenko and V. Koch, "Proton cumulants from hydrodynamics in light of new star data," *Journal of Subatomic Particles and Cosmology*, p. 100053, 2025.

[173] V. Vovchenko, V. Koch, and C. Shen, "Proton number cumulants and correlation functions in au-au collisions at $\sqrt{s_{NN}} = 7.7$–200 gev from hydrodynamics," *Phys. Rev. C*, vol. 105, p. 014904, Jan 2022.

[174] M. A. Stephanov, "Sign of kurtosis near the qcd critical point," *Phys. Rev. Lett.*, vol. 107, p. 052301, Jul 2011.

[175] E. Shuryak, "Four-nucleon clustering near the QCD critical point: theory versus experiment," 5 2024.

[176] F. Gross *et al.*, "50 Years of Quantum Chromodynamics," *Eur. Phys. J. C*, vol. 83, p. 1125, 2023.

[177] J. Chadwick, "The Existence of a Neutron," *Proc. Roy. Soc. Lond. A*, vol. 136, no. 830, pp. 692–708, 1932.

[178] H. Yukawa, "On the Interaction of Elementary Particles I," *Proc. Phys. Math. Soc. Jap.*, vol. 17, pp. 48–57, 1935.

[179] R. D. Woods and D. S. Saxon, "Diffuse surface optical model for nucleon-nuclei scattering," *Phys. Rev.*, vol. 95, pp. 577–578, Jul 1954.

[180] R. Vinh Mau, J. Richard, B. Loiseau, M. Lacombe, and W. Cottingham, "Nucleon-nucleon interaction from pion-nucleon phase shift analysis: The nn peripheral partial waves," *Physics Letters B*, vol. 44, no. 1, pp. 1–4, 1973.

[181] R. Machleidt, K. Holinde, and C. Elster, "The bonn meson-exchange model for the nucleon—nucleon interaction," *Physics Reports*, vol. 149, no. 1, pp. 1–89, 1987.

[182] D. J. Gross, "Nobel lecture: The discovery of asymptotic freedom and the emergence of qcd," *Rev. Mod. Phys.*, vol. 77, pp. 837–849, Sep 2005.

[183] R. P. Feynman, "The present status of quantum electrodynamics," *The Quantum Theory of Fields*, p. 61, 1961.

[184] L. D. Landau and I. Y. Pomeranchuk, "On point interactions in quantum electrodynamics," *Dokl. Akad. Nauk SSSR*, vol. 102, no. 3, pp. 489–492, 1955.

[185] "100 - fundamental problems," in *Collected Papers of L.D. Landau* (D. TER HAAR, ed.), pp. 800–802, Pergamon, 1965.

[186] G. F. Chew, "S-matrix theory of strong interactions without elementary particles," *Reviews of Modern Physics*, vol. 34, no. 3, p. 394, 1962.

[187] G. Chew, "Tha analytic s-matrix: A basis for nuclear democracy," 1966.

[188] E. Fermi and C. N. Yang, "Are mesons elementary particles?," *Phys. Rev.*, vol. 76, pp. 1739–1743, Dec 1949.

[189] S. Sakata, "On a composite model for the new particles*," *Progress of Theoretical Physics*, vol. 16, pp. 686–688, 12 1956.

[190] M. Ikeda, S. Ogawa, and Y. Ohnuki, "A possibile symmetry in sakata's model for bosons-baryons system," *Progress of Theoretical Physics*, vol. 22, pp. 715–724, 11 1959.

[191] T. Nakano and K. Nishijima, "Charge independence for v-particles*," *Progress of Theoretical Physics*, vol. 10, pp. 581–582, 11 1953.

[192] M. Gell-Mann, "The interpretation of the new particles as displaced charge multiplets," *Nuovo Cim.*, vol. 4, no. S2, pp. 848–866, 1956.

[193] M. Gell-Mann, "Symmetries of baryons and mesons," *Phys. Rev.*, vol. 125, pp. 1067–1084, Feb 1962.

[194] Y. Ne'eman, "Derivation of strong interactions from a gauge invariance," *Nucl. Phys.*, vol. 26, pp. 222–229, 1961.

[195] M. Gell-Mann, "A Schematic Model of Baryons and Mesons," *Phys. Lett.*, vol. 8, pp. 214–215, 1964.

[196] G. Zweig, *An SU(3) model for strong interaction symmetry and its breaking. Version 2*, pp. 22–101. 2 1964.

[197] V. E. Barnes *et al.*, "Observation of a Hyperon with Strangeness Minus Three," *Phys. Rev. Lett.*, vol. 12, pp. 204–206, 1964.

[198] J. D. Bjorken, "Asymptotic sum rules at infinite momentum," *Phys. Rev.*, vol. 179, pp. 1547–1553, Mar 1969.

[199] E. D. Bloom, D. H. Coward, H. DeStaebler, J. Drees, G. Miller, L. W. Mo, R. E. Taylor, M. Breidenbach, J. I. Friedman, G. C. Hartmann, and H. W. Kendall, "High-energy inelastic $e - p$ scattering at 6° and 10°," *Phys. Rev. Lett.*, vol. 23, pp. 930–934, Oct 1969.

[200] H. Deden *et al.*, "Experimental Study of Structure Functions and Sum Rules in Charge Changing Interactions of Neutrinos and anti-neutrinos on Nucleons," *Nucl. Phys. B*, vol. 85, pp. 269–288, 1975.

[201] O. W. Green'sberg, "Spin and unitary-spin independence in a paraquark model of baryons and mesons," *Phys. Rev. Lett.*, vol. 13, pp. 598–602, Nov 1964.

[202] N. N. Bogolubov, B. V. Struminsky, and A. N. Tavkhelidze, "On composite models in the theory of elementary particles," 1 1965.

[203] M. Y. Han and Y. Nambu, "Three-triplet model with double SU(3) symmetry," *Phys. Rev.*, vol. 139, pp. B1006–B1010, Aug 1965.

[204] Y. Miyamoto, "Three kinds of triplet model," *Progress of Theoretical Physics Supplement*, vol. E65, pp. 187–192, 01 1965.

[205] W. A. Bardeen, H. Fritzsch, and M. Gell-Mann, "Light cone current algebra, π^0 decay, and e^+e^- annihilation," in *Topical Meeting on the Outlook for Broken Conformal Symmetry in Elementary Particle Physics*, 7 1972.

[206] H. Fritzsch, M. Gell-Mann, and H. Leutwyler, "Advantages of the Color Octet Gluon Picture," *Phys. Lett. B*, vol. 47, pp. 365–368, 1973.

[207] G. 't Hooft, "renormalisable Lagrangians for Massive Yang-Mills Fields," *Nucl. Phys. B*, vol. 35, pp. 167–188, 1971.

[208] K. G. Wilson and J. B. Kogut, "The Renormalization group and the epsilon expansion," *Phys. Rept.*, vol. 12, pp. 75–199, 1974.

[209] E. S. von Breidenbach and A. Petermann, "La normalisation des constantes dans la theorie des quanta," *Helvetica Physica Acta*, vol. 26, p. 499, 1953.

[210] S. L. Glashow, "Partial-symmetries of weak interactions," *Nuclear Physics*, vol. 22, no. 4, pp. 579–588, 1961.

[211] A. Salam and J. Ward, "Electromagnetic and weak interactions," *Physics Letters*, vol. 13, no. 2, pp. 168–171, 1964.

[212] S. Weinberg, "A model of leptons," *Phys. Rev. Lett.*, vol. 19, pp. 1264–1266, Nov 1967.

[213] V. S. Vanyashin and M. V. Terentev, "The Vacuum Polarization of a Charged Vector Field," *Zh. Eksp. Teor. Fiz.*, vol. 48, no. 2, pp. 565–573, 1965.

[214] I. B. Khriplovich, "Green's's functions in theories with non-abelian gauge group.," *Sov. J. Nucl. Phys.*, vol. 10, pp. 235–242, 1969.

[215] D. J. Gross and F. Wilczek, "Ultraviolet behavior of non-abelian gauge theories," *Phys. Rev. Lett.*, vol. 30, pp. 1343–1346, Jun 1973.

[216] H. D. Politzer, "Reliable perturbative results for strong interactions?," *Phys. Rev. Lett.*, vol. 30, pp. 1346–1349, Jun 1973.

[217] H. J. Rothe, *Lattice gauge theories: an introduction*. World Scientific Publishing Company, 2012.

[218] J. Greensite, *An introduction to the confinement problem*, vol. 821. 2011.

[219] J. H. Christenson, J. W. Cronin, V. L. Fitch, and R. Turlay, "Evidence for the 2π decay of the k_2^0 meson," *Phys. Rev. Lett.*, vol. 13, pp. 138–140, Jul 1964.

[220] C. Abel *et al.*, "Measurement of the Permanent Electric Dipole Moment of the Neutron," *Phys. Rev. Lett.*, vol. 124, no. 8, p. 081803, 2020.

[221] D. E. Kharzeev, L. D. McLerran, and H. J. Warringa, "The effects of topological charge change in heavy ion collisions: "event by event p and cp violation"," *Nuclear Physics A*, vol. 803, no. 3, pp. 227–253, 2008.

[222] K. Fukushima, D. E. Kharzeev, and H. J. Warringa, "Chiral magnetic effect," *Phys. Rev. D*, vol. 78, p. 074033, Oct 2008.

[223] M. D. Schwartz, *Quantum Field Theory and the Standard Model*. Cambridge University Press, 2013.

[224] E. Witten, "Current algebra theorems for the u(1) "goldstone boson"," *Nuclear Physics B*, vol. 156, no. 2, pp. 269–283, 1979.

[225] G. Veneziano, "U(1) without instantons," *Nuclear Physics B*, vol. 159, no. 1, pp. 213–224, 1979.

[226] Y. Nambu, "Axial vector current conservation in weak interactions," *Phys. Rev. Lett.*, vol. 4, pp. 380–382, Apr 1960.

[227] L. Ryder, *Quantum Field Theory*. Cambridge University Press, 1996.

[228] E. Fabri and L. E. Picasso, "Quantum field theory and approximate symmetries," *Phys. Rev. Lett.*, vol. 16, pp. 408–410, Mar 1966.

[229] J. Goldstone, A. Salam, and S. Weinberg, "Broken symmetries," *Phys. Rev.*, vol. 127, pp. 965–970, Aug 1962.

[230] I. A. Shovkovy, "Two lectures on color superconductivity," *Foundations of Physics*, vol. 35, no. 8, pp. 1309–1358, 2005.

[231] S. Weinberg, "The u(1) problem," *Phys. Rev. D*, vol. 11, pp. 3583–3593, Jun 1975.

[232] A. Belavin, A. Polyakov, A. Schwartz, and Y. Tyupkin, "Pseudoparticle solutions of the yang-mills equations," *Physics Letters B*, vol. 59, no. 1, pp. 85–87, 1975.

[233] G. 't Hooft, "Computation of the quantum effects due to a four-dimensional pseudoparticle," *Phys. Rev. D*, vol. 14, pp. 3432–3450, Dec 1976.

[234] G. 't Hooft, "How instantons solve the u(1) problem," *Physics Reports*, vol. 142, no. 6, pp. 357–387, 1986.

[235] K. Osterwalder and E. Seiler, "Gauge Field Theories on the Lattice," *Annals Phys.*, vol. 110, p. 440, 1978.

[236] E. Fradkin and S. H. Shenker, "Phase diagrams of lattice gauge theories with higgs fields," *Phys. Rev. D*, vol. 19, pp. 3682–3697, Jun 1979.

[237] F. J. Dyson, "The s matrix in quantum electrodynamics," *Phys. Rev.*, vol. 75, pp. 1736–1755, Jun 1949.

[238] J. S. Schwinger, "On the Green's functions of quantized fields. 1.," *Proc. Nat. Acad. Sci.*, vol. 37, pp. 452–455, 1951.

[239] J. Schwinger, "On the green's functions of quantized fields. 2," *Proceedings of the National Academy of Sciences*, vol. 37, no. 7, pp. 455–459, 1951.

[240] C. Itzykson and J.-B. Zuber, *Quantum field theory*. Courier Corporation, 2006.

[241] C. D. Roberts and A. G. Williams, "Dyson-schwinger equations and their application to hadronic physics," *Progress in Particle and Nuclear Physics*, vol. 33, pp. 477–575, 1994.

[242] J. M. Pawlowski, "Aspects of the functional renormalisation group," *Annals Phys.*, vol. 322, pp. 2831–2915, 2007.

[243] K. G. Wilson, "Confinement of quarks," *Phys. Rev. D*, vol. 10, pp. 2445–2459, Oct 1974.

[244] C. Morningstar, "The Monte Carlo method in quantum field theory," in *21st Annual Hampton University Graduate Studies Program*, 2 2007.

[245] L. S. Brown and W. I. Weisberger, "Remarks on the static potential in quantum chromodynamics," *Phys. Rev. D*, vol. 20, pp. 3239–3245, Dec 1979.

[246] E. Eichten and F. Feinberg, "Spin-dependent forces in quantum chromodynamics," *Phys. Rev. D*, vol. 23, pp. 2724–2744, Jun 1981.

[247] M. E. Peskin, "Aspects of the dynamics of heavy-quark systems," tech. rep., Stanford Linear Accelerator Center, CA (USA), 1983.

[248] D. Gromes, "Relativistic corrections to the long-range quark antiquark potential electric flux tubes, and area law," *Zeitschrift für Physik C Particles and Fields*, vol. 22, pp. 265–270, 1984.

[249] A. Barchielli, E. Montaldi, and G. Prosperi, "On a systematic derivation of the quark-antiquark potential," *Nuclear Physics B*, vol. 296, no. 3, pp. 625–656, 1988.

[250] A. Barchielli, N. Brambilla, and G. M. Prosperi, "Relativistic corrections to the quark-antiquark potential and the quarkonium spectrum," *Il Nuovo Cimento A (1965-1970)*, vol. 103, no. 1, pp. 59–83, 1990.

[251] W. Lucha, F. F. Schoberl, and D. Gromes, "Bound states of quarks," *Phys. Rept.*, vol. 200, pp. 127–240, 1991.

[252] K. Sakai and S. Sasaki, "Glueball spectroscopy in lattice qcd using gradient flow," *Phys. Rev. D*, vol. 107, p. 034510, Feb 2023.

[253] P. Goddard, J. Goldstone, C. Rebbi, and C. B. Thorn, "Quantum dynamics of a massless relativistic string," *Nuclear Physics B*, vol. 56, no. 1, pp. 109–135, 1973.

[254] M. Baker, P. Cea, V. Chelnokov, L. Cosmai, and A. Papa, "Unveiling the flux tube structure in full QCD," *Eur. Phys. J. C*, vol. 85, no. 1, p. 29, 2025.

[255] V. Koch, J. Bulava, B. Hörz, F. Knechtli, G. Moir, C. Morningstar, and M. Peardon, "String breaking with 2+1 dynamical fermions using the stochastic LapH method," *PoS*, vol. LATTICE2018, p. 053, 2018.

[256] G. 't Hooft, "On the Phase Transition Towards Permanent Quark Confinement," *Nucl. Phys. B*, vol. 138, pp. 1–25, 1978.

[257] G. 't Hooft, "A Property of Electric and Magnetic Flux in Nonabelian Gauge Theories," *Nucl. Phys. B*, vol. 153, pp. 141–160, 1979.

[258] J. C. Biddle, W. Kamleh, and D. B. Leinweber, "Static quark potential from center vortices in the presence of dynamical fermions," *Physical Review D*, vol. 106, no. 5, p. 054505, 2022.

[259] J. C. Biddle, W. Kamleh, and D. B. Leinweber, "Impact of dynamical fermions on the center vortex gluon propagator," *Physical Review D*, vol. 106, no. 1, p. 014506, 2022.

[260] J. C. Biddle, W. Kamleh, and D. B. Leinweber, "Center vortex structure in the presence of dynamical fermions," *Physical Review D*, vol. 107, no. 9, p. 094507, 2023.

[261] J. A. Mickley, W. Kamleh, and D. B. Leinweber, "Center vortex geometry at finite temperature," *Physical Review D*, vol. 110, no. 3, p. 034516, 2024.

[262] P. O. Bowman, K. Langfeld, D. B. Leinweber, A. Sternbeck, L. von Smekal, and A. G. Williams, "Role of center vortices in chiral symmetry breaking in SU(3) gauge theory," *Phys. Rev. D*, vol. 84, p. 034501, 2011.

[263] K. Langfeld, H. Reinhardt, and J. Gattnar, "Gluon propagators and quark confinement," *Nucl. Phys. B*, vol. 621, pp. 131–156, 2002.

[264] M. Quandt, H. Reinhardt, and G. Burgio, "The role of center vortices in Gribov's confinement scenario," *Phys. Rev. D*, vol. 81, p. 065016, 2010.

[265] A. Trewartha, W. Kamleh, and D. Leinweber, "Centre vortex removal restores chiral symmetry," *J. Phys. G*, vol. 44, no. 12, p. 125002, 2017.

[266] S. Datta and S. Gupta, "Continuum thermodynamics of the su (n c) gluon plasma," *Physical Review D—Particles, Fields, Gravitation, and Cosmology*, vol. 82, no. 11, p. 114505, 2010.

[267] C. R. Allton, S. Ejiri, S. J. Hands, O. Kaczmarek, F. Karsch, E. Laermann, and C. Schmidt, "Equation of state for two flavor qcd at nonzero chemical potential," *Phys. Rev. D*, vol. 68, p. 014507, Jul 2003.

[268] C. R. Allton, M. Döring, S. Ejiri, S. J. Hands, O. Kaczmarek, F. Karsch, E. Laermann, and K. Redlich, "Thermodynamics of two flavor qcd to sixth order in quark chemical potential," *Phys. Rev. D*, vol. 71, p. 054508, Mar 2005.

[269] S. Borsanyi, G. Endrodi, Z. Fodor, S. D. Katz, S. Krieg, C. Ratti, and K. K. Szabo, "QCD equation of state at nonzero chemical potential: continuum results with physical quark masses at order mu^2," *JHEP*, vol. 08, p. 053, 2012.

[270] A. Bazavov, H.-T. Ding, P. Hegde, O. Kaczmarek, F. Karsch, E. Laermann, Y. Maezawa, S. Mukherjee, H. Ohno, P. Petreczky, H. Sandmeyer, P. Steinbrecher, C. Schmidt, S. Sharma, W. Soeldner, and M. Wagner, "Qcd equation of state to $\mathcal{O}(\mu_B^6)$ from lattice qcd," *Phys. Rev. D*, vol. 95, p. 054504, Mar 2017.

[271] D. Bollweg, D. A. Clarke, J. Goswami, O. Kaczmarek, F. Karsch, S. Mukherjee, P. Petreczky, C. Schmidt, and S. Sharma, "Equation of state and speed of sound of (2+1)-flavor qcd in strangeness-neutral matter at nonvanishing net baryon-number density," *Phys. Rev. D*, vol. 108, p. 014510, Jul 2023.

[272] J. N. Guenther, "Overview of the qcd phase diagram: Recent progress from the lattice," *The European Physical Journal A*, vol. 57, no. 4, p. 136, 2021.

[273] C. P. Burgess, *Introduction to Effective Field Theory: Thinking Effectively about Hierarchies of Scale*. Cambridge University Press, 2020.

[274] T. Appelquist and J. Carazzone, "Infrared singularities and massive fields," *Phys. Rev. D*, vol. 11, pp. 2856–2861, May 1975.

[275] K. G. Wilson, "The renormalization group and critical phenomena," *Rev. Mod. Phys.*, vol. 55, pp. 583–600, Jul 1983.

[276] J. F. Donoghue, E. Golowich, and B. R. Holstein, *Dynamics of the standard model*, vol. 2. CUP, 2014.

[277] T. Matsubara, "A New approach to quantum statistical mechanics," *Prog. Theor. Phys.*, vol. 14, pp. 351–378, 1955.

[278] E. S. Fradkin, "Method of Green's functions in quantum field theory and quantum statistics," *Trud. Fiz. Inst. Akad. Nauk SSSR (Fiz. Inst. Lebedev)*, vol. 29, pp. 7–138, 1965.

[279] C. W. Bernard, "Feynman rules for gauge theories at finite temperature," *Phys. Rev. D*, vol. 9, pp. 3312–3320, Jun 1974.

[280] S. Weinberg, "Gauge and global symmetries at high temperature," *Phys. Rev. D*, vol. 9, pp. 3357–3378, Jun 1974.

[281] L. Dolan and R. Jackiw, "Symmetry behavior at finite temperature," *Phys. Rev. D*, vol. 9, pp. 3320–3341, Jun 1974.

[282] J. Ghiglieri, A. Kurkela, M. Strickland, and A. Vuorinen, "Perturbative Thermal QCD: Formalism and Applications," *Phys. Rept.*, vol. 880, pp. 1–73, 2020.

[283] J. I. Kapusta and C. Gale, *Finite-temperature field theory: Principles and applications*. Cambridge university press, 2007.

[284] Y. Nakawaki, A. Tanaka, and K. Ozaki, "On quasi-particles at finite temperature," *Progress of theoretical physics*, vol. 81, no. 2, pp. 498–511, 1989.

[285] R. Pathria and P. Beale, "Statistical mechanics—third edition," 2011.

[286] R. C. Pereira and P. Costa, "One-meson-loop njl model: Effect of collective and noncollective excitations on the quark condensate at finite temperature," *Phys. Rev. D*, vol. 101, p. 054025, Mar 2020.

[287] T. Kähärä, "Thermodynamics of two-flavor qcd from chiral models with polyakov loop," *Research report/Department of Physics, University of Jyväskylä*, no. 12/2010, 2010.

[288] Y. Nambu and G. Jona-Lasinio, "Dynamical model of elementary particles based on an analogy with superconductivity. i," *Phys. Rev.*, vol. 122, pp. 345–358, Apr 1961.

[289] S. P. Klevansky, "The nambu—jona-lasinio model of quantum chromodynamics," *Rev. Mod. Phys.*, vol. 64, pp. 649–708, Jul 1992.

[290] T. Hatsuda and T. Kunihiro, "Qcd phenomenology based on a chiral effective lagrangian," *Physics Reports*, vol. 247, no. 5-6, pp. 221–367, 1994.

[291] A. M. Polyakov, "Thermal properties of gauge fields and quark liberation," *Phys. Lett., B;(Netherlands)*, vol. 72, no. 4, 1978.

[292] K. Fukushima, "Chiral effective model with the polyakov loop," *Physics Letters B*, vol. 591, no. 3-4, pp. 277–284, 2004.

[293] C. Ratti, M. A. Thaler, and W. Weise, "Phases of qcd: Lattice thermodynamics and a field theoretical model," *Phys. Rev. D*, vol. 73, p. 014019, Jan 2006.

[294] S. Rößner, C. Ratti, and W. Weise, "Polyakov loop, diquarks, and the two-flavor phase diagram," *Phys. Rev. D*, vol. 75, p. 034007, Feb 2007.

[295] J. Faraut, *Haar measure*, p. 74–94. Cambridge Studies in Advanced Mathematics, Cambridge University Press, 2008.

[296] R. D. Pisarski, "Quark-gluon plasma as a condensate of $z(3)$ wilson lines," *Phys. Rev. D*, vol. 62, p. 111501, Nov 2000.

[297] G. t Hooft, "Topology of the gauge condition and new confinement phases in non-abelian gauge theories," *Nuclear Physics B*, vol. 190, no. 3, pp. 455–478, 1981.

[298] P. Costa, M. C. Ruivo, C. A. de Sousa, and H. Hansen, "Phase diagram and critical properties within an effective model of QCD: the Nambu-Jona-Lasinio model coupled to the Polyakov loop," *Symmetry*, vol. 2, pp. 1338–1374, 2010.

[299] R. Weber, "More random walks in science," 1983.

[300] G. Gamow, "Mass defect curve and nuclear constitution," *Proceedings of the Royal Society of London. Series A, Containing Papers of a Mathematical and Physical Character*, vol. 126, no. 803, pp. 632–644, 1930.

[301] H. A. Bethe and R. F. Bacher, "Nuclear physics a. stationary states of nuclei," *Rev. Mod. Phys.*, vol. 8, pp. 82–229, Apr 1936.

[302] M. H. Johnson and E. Teller, "Classical field theory of nuclear forces," *Phys. Rev.*, vol. 98, pp. 783–787, May 1955.

[303] H.-P. Duerr, "Relativistic effects in nuclear forces," *Phys. Rev.*, vol. 103, pp. 469–480, Jul 1956.

[304] O. Lourenço, M. Dutra, T. Frederico, A. Delfino, and M. Malheiro, "Influence of pions on the hadron-quark phase transition," in *AIP Conference Proceedings*, vol. 1529, pp. 241–243, American Institute of Physics, 2013.

[305] C. J. Horowitz and J. Piekarewicz, "Neutron star structure and the neutron radius of ^{208}pb," *Phys. Rev. Lett.*, vol. 86, pp. 5647–5650, Jun 2001.

[306] W.-C. Chen and J. Piekarewicz, "Building relativistic mean field models for finite nuclei and neutron stars," *Phys. Rev. C*, vol. 90, p. 044305, Oct 2014.

[307] L. Tolos, M. Centelles, and A. Ramos, "Equation of State for Nucleonic and Hyperonic Neutron Stars with Mass and Radius Constraints," *Astrophys. J.*, vol. 834, no. 1, p. 3, 2017.

[308] J. Boguta and A. Bodmer, "Relativistic calculation of nuclear matter and the nuclear surface," *Nuclear Physics A*, vol. 292, no. 3, pp. 413–428, 1977.

[309] J. Boguta and H. Stocker, "Systematics of nuclear matter properties in a non-linear relativistic field theory," *Physics Letters B*, vol. 120, no. 4-6, pp. 289–293, 1983.

[310] A. Bodmer, "Relativistic mean field theory of nuclei with a vector meson self-interaction," *Nuclear Physics A*, vol. 526, no. 3-4, pp. 703–721, 1991.

[311] H. Mueller and B. D. Serot, "Relativistic mean-field theory and the high-density nuclear equation of state," *Nuclear Physics A*, vol. 606, no. 3-4, pp. 508–537, 1996.

[312] B.-A. Li, À. Ramos, G. Verde, and I. Vidaña, "Topical issue on nuclear symmetry energy," *The European Physical Journal A*, vol. 50, no. 2, p. 9, 2014.

[313] C. J. Horowitz and J. Piekarewicz, "Neutron radii of ^{208}Pb and neutron stars," *Phys. Rev. C*, vol. 64, p. 062802, Nov 2001.

[314] M. Buballa, "The Problem of matter stability in the Nambu-Jona-Lasinio model," *Nucl. Phys. A*, vol. 611, pp. 393–408, 1996.

[315] P. B. Demorest, T. Pennucci, S. Ransom, M. Roberts, and J. Hessels, "A two-solar-mass neutron star measured using shapiro delay," *nature*, vol. 467, no. 7319, pp. 1081–1083, 2010.

[316] J. Antoniadis, P. C. Freire, N. Wex, T. M. Tauris, R. S. Lynch, M. H. Van Kerkwijk, M. Kramer, C. Bassa, V. S. Dhillon, T. Driebe, *et al.*, "A massive pulsar in a compact relativistic binary," *Science*, vol. 340, no. 6131, p. 1233232, 2013.

[317] V. Ambartsumyan and G. Saakyan, "The degenerate superdense gas of elementary particles," *Soviet Astronomy, Vol. 4, p. 187*, vol. 4, p. 187, 1960.

[318] N. K. Glendenning, *Compact stars: Nuclear physics, particle physics and general relativity.* Springer Science & Business Media, 2012.

[319] M. Oertel, F. Gulminelli, C. Providência, and A. R. Raduta, "Hyperons in neutron stars and supernova cores," *The European Physical Journal A*, vol. 52, no. 3, p. 50, 2016.

[320] K. A. Maslov, E. E. Kolomeitsev, and D. N. Voskresensky, "Solution of the Hyperon Puzzle within a Relativistic Mean-Field Model," *Phys. Lett. B*, vol. 748, pp. 369–375, 2015.

[321] A. Rabhi and C. Providencia, "Dense stellar matter with trapped neutrinos under strong magnetic fields," *J. Phys. G*, vol. 37, p. 075102, 2010.

[322] R. O. Gomes, V. Dexheimer, and C. A. Z. Vasconcellos, "Effects of strong magnetic fields on the population of hyperon stars," *Astron. Nachr.*, vol. 335, p. 666, 2014.

[323] Y. Yamamoto, T. Furumoto, N. Yasutake, and T. A. Rijken, "Hyperon mixing and universal many-body repulsion in neutron stars," *Physical Review C*, vol. 90, no. 4, p. 045805, 2014.

[324] D. Lonardoni, A. Lovato, S. Gandolfi, and F. Pederiva, "Hyperon puzzle: hints from quantum monte carlo calculations," *Physical review letters*, vol. 114, no. 9, p. 092301, 2015.

[325] D. Chatterjee and I. Vidana, "Do hyperons exist in the interior of neutron stars?," *The European Physical Journal A*, vol. 52, no. 2, p. 29, 2016.

[326] S. Guillot, M. Servillat, N. A. Webb, and R. E. Rutledge, "Measurement of the Radius of Neutron Stars with High S/N Quiescent Low-mass X-ray Binaries in Globular Clusters," *Astrophys. J.*, vol. 772, p. 7, 2013.

[327] T. Güver and F. Özel, "The mass and the radius of the neutron star in the transient low-mass x-ray binary sax j1748. 9- 2021," *The Astrophysical Journal Letters*, vol. 765, no. 1, p. L1, 2013.

[328] S. Guillot and R. E. Rutledge, "Rejecting proposed dense matter equations of state with quiescent low-mass x-ray binaries," *The Astrophysical Journal Letters*, vol. 796, no. 1, p. L3, 2014.

[329] C. O. Heinke *et al.*, "Improved mass and radius constraints for quiescent neutron stars in ω Cen and NGC 6397," *Mon. Not. Roy. Astron. Soc.*, vol. 444, no. 1, pp. 443–456, 2014.

[330] J. M. Lattimer and A. W. Steiner, "Constraints on the symmetry energy using the mass-radius relation of neutron stars," *The European Physical Journal A*, vol. 50, no. 2, p. 40, 2014.

[331] J. M. Lattimer and A. W. Steiner, "Neutron star masses and radii from quiescent low-mass x-ray binaries," *The Astrophysical Journal*, vol. 784, no. 2, p. 123, 2014.

[332] J. Nättilä, M. Miller, A. Steiner, J. Kajava, V. Suleimanov, and J. Poutanen, "Neutron star mass and radius measurements from atmospheric model fits to x-ray burst cooling tail spectra," *Astronomy & Astrophysics*, vol. 608, p. A31, 2017.

[333] F. Özel, D. Psaltis, T. Güver, G. Baym, C. Heinke, and S. Guillot, "The dense matter equation of state from neutron star radius and mass measurements," *The Astrophysical Journal*, vol. 820, no. 1, p. 28, 2016.

[334] F. Özel and P. Freire, "Masses, Radii, and the Equation of State of Neutron Stars," *Ann. Rev. Astron. Astrophys.*, vol. 54, pp. 401–440, 2016.

[335] J. M. Lattimer and M. Prakash, "Neutron Star Observations: Prognosis for Equation of State Constraints," *Phys. Rept.*, vol. 442, pp. 109–165, 2007.

[336] L. Tolos, M. Centelles, and A. Ramos, "The equation of state for the nucleonic and hyperonic core of neutron stars," *Publications of the Astronomical Society of Australia*, vol. 34, p. e065, 2017.

[337] F. J. Fattoyev, J. Piekarewicz, and C. J. Horowitz, "Neutron skins and neutron stars in the multimessenger era," *Phys. Rev. Lett.*, vol. 120, p. 172702, Apr 2018.

[338] E. Annala, T. Gorda, A. Kurkela, and A. Vuorinen, "Gravitational-wave constraints on the neutron-star-matter equation of state," *Phys. Rev. Lett.*, vol. 120, p. 172703, Apr 2018.

[339] P. G. Krastev and B.-A. Li, "Imprints of the nuclear symmetry energy on the tidal deformability of neutron stars," *Journal of Physics G: Nuclear and Particle Physics*, vol. 46, no. 7, p. 074001, 2019.

[340] E. R. Most, L. R. Weih, L. Rezzolla, and J. Schaffner-Bielich, "New constraints on radii and tidal deformabilities of neutron stars from GW170817," *Phys. Rev. Lett.*, vol. 120, no. 26, p. 261103, 2018.

[341] B. P. Abbott *et al.*, "GW170817: Observation of Gravitational Waves from a Binary Neutron Star Inspiral," *Phys. Rev. Lett.*, vol. 119, no. 16, p. 161101, 2017.

[342] P. Danielewicz, R. Lacey, and W. G. Lynch, "Determination of the equation of state of dense matter," *Science*, vol. 298, pp. 1592–1596, 2002.

[343] C. Fuchs, A. Faessler, E. Zabrodin, and Y.-M. Zheng, "Probing the nuclear equation of state by k^+ production in heavy-ion collisions," *Phys. Rev. Lett.*, vol. 86, pp. 1974–1977, Mar 2001.

[344] W. Lynch, M. Tsang, Y. Zhang, P. Danielewicz, M. Famiano, Z. Li, and A. Steiner, "Probing the symmetry energy with heavy ions," *Progress in Particle and Nuclear Physics*, vol. 62, no. 2, pp. 427–432, 2009.

[345] R. Negreiros, L. Tolos, M. Centelles, A. Ramos, and V. Dexheimer, "Cooling of small and massive hyperonic stars," *The Astrophysical Journal*, vol. 863, no. 1, p. 104, 2018.

[346] C. Greiner, P. Koch, and H. Stöcker, "Separation of strangeness from antistrangeness in the phase transition from quark to hadron matter: Possible formation of strange quark matter in heavy-ion collisions," *Phys. Rev. Lett.*, vol. 58, pp. 1825–1828, May 1987.

[347] C.-J. Xia, T. Maruyama, N. Yasutake, T. Tatsumi, H. Shen, and H. Togashi, "Systematic study on the quark-hadron mixed phase in compact stars," *Phys. Rev. D*, vol. 102, no. 2, p. 023031, 2020.

[348] E. S. Fraga, M. Hippert, and A. Schmitt, "Surface tension of dense matter at the chiral phase transition," *Phys. Rev. D*, vol. 99, no. 1, p. 014046, 2019.

[349] B. W. Mintz, E. S. Fraga, G. Pagliara, and J. Schaffner-Bielich, "Nucleation of quark matter in protoneutron star matter," *Phys. Rev. D*, vol. 81, p. 123012, 2010.

[350] B. W. Mintz, E. Fraga, J. Schaffner-Bielich, and G. Pagliara, "On thermal nucleation of quark matter in compact stars," *Journal of Physics G: Nuclear and Particle Physics*, vol. 37, no. 9, p. 094066, 2010.

[351] G. A. Lalazissis, J. König, and P. Ring, "New parametrization for the lagrangian density of relativistic mean field theory," *Phys. Rev. C*, vol. 55, pp. 540–543, Jan 1997.

[352] J. Carriere, C. Horowitz, and J. Piekarewicz, "Low-mass neutron stars and the equation of state of dense matter," *The Astrophysical Journal*, vol. 593, no. 1, p. 463, 2003.

[353] B. Frois, J. B. Bellicard, J. M. Cavedon, M. Huet, P. Leconte, P. Ludeau, A. Nakada, X. H. Phan, and I. Sick, "High Momentum Transfer electron Scattering from Pb-208," *Phys. Rev. Lett.*, vol. 38, pp. 152–155, 1977.

[354] M. Wang, G. Audi, A. Wapstra, F. Kondev, M. MacCormick, X. Xu, and B. Pfeiffer, "The ame2012 atomic mass evaluation," *Chinese physics C*, vol. 36, no. 12, p. 1603, 2012.

[355] I. Angeli and K. P. Marinova, "Table of experimental nuclear ground state charge radii: An update," *Atomic Data and Nuclear Data Tables*, vol. 99, no. 1, pp. 69–95, 2013.

[356] D. H. Youngblood, H. L. Clark, and Y.-W. Lui, "Incompressibility of nuclear matter from the giant monopole resonance," *Phys. Rev. Lett.*, vol. 82, pp. 691–694, Jan 1999.

[357] M. Uchida, H. Sakaguchi, M. Itoh, M. Yosoi, T. Kawabata, Y. Yasuda, H. Takeda, T. Murakami, S. Terashima, S. Kishi, *et al.*, "Systematics of the bimodal isoscalar giant dipole resonance," *Physical Review C—Nuclear Physics*, vol. 69, no. 5, p. 051301, 2004.

[358] T. Li, U. Garg, Y. Liu, R. Marks, B. Nayak, P. M. Rao, M. Fujiwara, H. Hashimoto, K. Kawase, K. Nakanishi, *et al.*, "Isotopic dependence of the giant monopole resonance in the even-a sn 112–124 isotopes<? format?> and the asymmetry term in nuclear incompressibility," *Physical review letters*, vol. 99, no. 16, p. 162503, 2007.

[359] T. Li, U. Garg, Y. Liu, R. Marks, B. Nayak, P. Madhusudhana Rao, M. Fujiwara, H. Hashimoto, K. Nakanishi, S. Okumura, *et al.*, "Isoscalar giant resonances in the sn nuclei and implications for the asymmetry term in the nuclear-matter incompressibility," *Physical Review C—Nuclear Physics*, vol. 81, no. 3, p. 034309, 2010.

[360] D. Patel, U. Garg, M. Fujiwara, T. Adachi, H. Akimune, G. Berg, M. Harakeh, M. Itoh, C. Iwamoto, A. Long, *et al.*, "Testing the mutually enhanced magicity effect in nuclear incompressibility via the giant monopole resonance in the 204,206,208 pb isotopes," *Physics Letters B*, vol. 726, no. 1-3, pp. 178–181, 2013.

[361] S. Weissenborn, D. Chatterjee, and J. Schaffner-Bielich, "Hyperons and massive neutron stars: vector repulsion and SU(3) symmetry," *Phys. Rev. C*, vol. 85, no. 6, p. 065802, 2012. [Erratum: Phys.Rev.C 90, 019904 (2014)].

[362] O. Hashimoto and H. Tamura, "Spectroscopy of Lambda hypernuclei," *Prog. Part. Nucl. Phys.*, vol. 57, pp. 564–653, 2006.

[363] A. Gal, E. V. Hungerford, and D. J. Millener, "Strangeness in nuclear physics," *Rev. Mod. Phys.*, vol. 88, p. 035004, Aug 2016.

[364] G. Shao, M. Colonna, M. Di Toro, Y. Liu, and B. Liu, "Isoscalar-vector interaction and hybrid quark core in massive neutron stars," *Physical Review D—Particles, Fields, Gravitation, and Cosmology*, vol. 87, no. 9, p. 096012, 2013.

[365] R. C. Pereira, J. Moreira, and P. Costa, "The strange critical endpoint and isentropic trajectories in an extended pnjl model with eight quark interactions," *The European Physical Journal A*, vol. 56, no. 8, p. 214, 2020.

[366] B. Mohanty and J.-e. Alam, "Velocity of sound in relativistic heavy-ion collisions," *Phys. Rev. C*, vol. 68, p. 064903, Dec 2003.

[367] L.-N. Gao and F.-H. Liu, "On pseudorapidity distribution and speed of sound in high energy heavy ion collisions based on a new revised landau hydrodynamic model," *Advances in High Energy Physics*, vol. 2015, no. 1, p. 184713, 2015.

[368] J. Adam *et al.*, "Centrality dependence of the pseudorapidity density distribution for charged particles in Pb-Pb collisions at $\sqrt{s_{\mathrm{NN}}} = 5.02$ TeV," *Phys. Lett. B*, vol. 772, pp. 567–577, 2017.

[369] S. Gandolfi, A. Y. Illarionov, K. E. Schmidt, F. Pederiva, and S. Fantoni, "Quantum Monte Carlo calculation of the equation of state of neutron matter," *Phys. Rev. C*, vol. 79, p. 054005, 2009.

[370] I. Tews, T. Krüger, K. Hebeler, and A. Schwenk, "Neutron matter at next-to-next-to-next-to-leading order in chiral effective field theory," *Phys. Rev. Lett.*, vol. 110, no. 3, p. 032504, 2013.

[371] B. Liu, V. Greco, V. Baran, M. Colonna, and M. Di Toro, "Asymmetric nuclear matter: The role of the isovector scalar channel," *Physical Review C*, vol. 65, no. 4, p. 045201, 2002.

[372] A. L. Watts *et al.*, "Colloquium : Measuring the neutron star equation of state using x-ray timing," *Rev. Mod. Phys.*, vol. 88, no. 2, p. 021001, 2016.

[373] L. Adamczyk *et al.*, "Global Λ hyperon polarization in nuclear collisions: evidence for the most vortical fluid," *Nature*, vol. 548, pp. 62–65, 2017.

[374] D. E. Kharzeev and D. T. Son, "Testing the chiral magnetic and chiral vortical effects in heavy ion collisions," *Phys. Rev. Lett.*, vol. 106, p. 062301, Feb 2011.

[375] Y. Jiang, X.-G. Huang, and J. Liao, "Chiral vortical wave and induced flavor charge transport in a rotating quark-gluon plasma," *Phys. Rev. D*, vol. 92, p. 071501, Oct 2015.

[376] Z. Zhang, C. Shi, X. Luo, and H.-S. Zong, "Chiral phase transition in a rotating sphere," *Physical Review D*, vol. 101, no. 7, p. 074036, 2020.

[377] E. Blanquier, "Color superconductivity in the Nambu-Jona-Lasinio model complemented by a Polyakov loop," *Eur. Phys. J. A*, vol. 53, no. 6, p. 137, 2017.